MICROCOPY RESOLUTION TEST CHART

NATIONAL BUREAU OF STANDARDS-1963-A

AFWAL-TR-81-2122

ANALYTICAL AND EXPERIMENTAL INVESTIGATIONS OF SODIUM HEAT PIPES
AND THERMAL ENERGY STORAGE SYSTEMS

Mechanical and Energy Systems Engineering
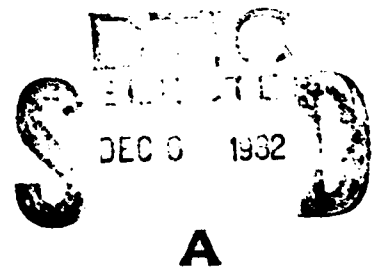Arizona State University

January 1982

Final Report for Period October 1980 – September 1981

Approved for public release; distribution unlimited

A

AERO PROPULSION LABORATORY
AIR FORCE WRIGHT AERONAUTICAL LABORATORIES
AIR FORCE SYSTEMS COMMAND
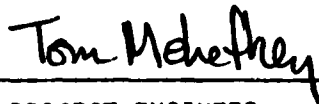WRIGHT-PATTERSON AIR FORCE BASE, OHIO 45433

PROJECT ENGINEER

DONALD P. MORTEL
Chief, Energy Conversion Branch
Aerospace Power Division
Aero Propulsion Laboratory

FOR THE COMMANDER

JAMES D. REAMS
Chief, Aerospace Power Division
Aero Propulsion Laboratory

REPORT DOCUMENTATION PAGE		READ INSTRUCTIONS BEFORE COMPLETING FORM
1. REPORT NUMBER AFWAL-TR-81-2122	2. GOVT ACCESSION NO. AD-A122093	3. RECIPIENT'S CATALOG NUMBER
4. TITLE *(and Subtitle)* SODIUM HEAT PIPES AND THERMAL ENERGY STORAGE SYSTEMS		5. TYPE OF REPORT & PERIOD COVERED October 1980 – September 1981
		6. PERFORMING ORG. REPORT NUMBER
7. AUTHOR*(s)* Dean Jacobson		8. CONTRACT OR GRANT NUMBER*(s)* F33615-77-C-2059
9. PERFORMING ORGANIZATION NAME AND ADDRESS Mechanical and Energy Systems Engineering Arizona State University, Tempe, Arizona 85281		10. PROGRAM ELEMENT, PROJECT, TASK AREA & WORK UNIT NUMBERS 2308S802
11. CONTROLLING OFFICE NAME AND ADDRESS AERO PROPULSION LABORATORY (AFWAL/POOC-2) AIR FORCE WRIGHT AERONAUTICAL LABORATORIES WRIGHT-PATTERSON AFB OH 45433		12. REPORT DATE January 1982
		13. NUMBER OF PAGES 213
14. MONITORING AGENCY NAME & ADDRESS*(if different from Controlling Office)*		15. SECURITY CLASS. *(of this report)* Unclassified
		15a. DECLASSIFICATION/DOWNGRADING SCHEDULE

16. DISTRIBUTION STATEMENT *(of this Report)*

Approved for public release; distribution unlimited.

17. DISTRIBUTION STATEMENT *(of the abstract entered in Block 20, if different from Report)*

18. SUPPLEMENTARY NOTES

19. KEY WORDS *(Continue on reverse side if necessary and identify by block number)*

Sodium Heat Pipes   LiF Thermal Storage
Thermal Energy Storage   Corrosion and Life Testing
Inconel 617

20. ABSTRACT *(Continue on reverse side if necessary and identify by block number)*

(See reverse side)

DD $_{1\ JAN\ 73}^{FORM}$ **1473**   EDITION OF 1 NOV 65 IS OBSOLETE

ABSTRACT

Eight work elements for FY 1981 are reported on. A brief evaluation of the limits of arterial heat pipes is presented followed by the post life examination of two Inconel 600, sodium heat pipes which failed by pin hole corrosion through the evaporator. Nearly 12,000 hours of operation was sustained by one of the heat pipes prior to failure.

A parametric test station for a thermal train including a 15-foot Inconel 617-sodium heat. A secondary sodium heat pipe with integral LiF thermal energy storage capsules and a sodium thermal transfer joint is discussed.

A series of fiftenn 18-in. long by 0.5 in. diameter Inconel 617, sodium heat pipes are being prepared for parametric and life tests.

A 12-in. long, 1-in. diameter Inconel 617 container filled with the thermal energy storage salt 64LiF- 30 MgF_2-6KF was tested to determine latent heat of fusion (782 J/gm), melting point (710°C), freezing point (671°C) and diffusivity (0.00799 cm^2/sec) of the salt.

The post life test results of a series of nine salt-Inconel 600 capsules, including LiF-MgF_2, LiF-MgF_2 -KF, and LiF-MgF_2-NaF are presented.

A 321 stainless steel, sodium heat pipe containing three LiF thermal energy storage units has a total of over 10,700 hours of operation and 3426 cycles of life testing.

FOREWORD

The information presented in this report was generated during the performance of the Analytical and Experimental Investigations of Heat Transfer, Materials and Thermodynamics Problems contract, SCEEE Contract No. F33615-77-C-2059. The work was carried out at Arizona State University, Mechanical and Energy Systems Engineering and at Air Force Wright Aeronautical Laboratories, Aeropropulsion Laboratory, Thermosciences Laboratory.

During FY 1980 nine tasks were performed as outlined in the Table of Contents. A number of the tasks were performed partly at ASU and partly at AFWAL/POOC Thermoscience Laboratory. The various tasks dealt with sodium heat pipes, wicking, performance, corrosion and life testing; with thermal energy storage analysis, performance testing, compatibility and life testing. One Master's Thesis was completed on Thermal Energy Storage while two others are in progress relating to Sections 4 and 7. Section 6 is from the Thesis. Six senior projects were also derived from the work reported. Personnel contributing to various sections are listed as follows.

Section	Name	Level
1	A. Carstens	Senior
2	W. Moddoman, U. of Dayton R.I.	Ph.D
3	J. Beemer, M. Tehan, L. Wilson	Senior
	C. Poure	Grad. Student
4	D. Stella	Grad. Student
5	M. Whitehead	Senior
	R. Ponnappan	Grad. Student
6	R. Ponnappan	M.S. Thesis
7	N. Moraga	Grad. Student
8	A. Kiefer	SCEEE Investigator
Appendix	T. Lamp	Hughes Aircraft Co.

This is the final report for FY 1981.

The program was sponsored by AFOSR under Task 2308S8 and AFWAL under Project 3145 with Dr. E.T. Mahefkey of AFWAL/POOC-2 as technical monitor.

iii

TABLE OF CONTENTS

TABLE OF CONTENTS

(continued)

TABLE OF CONTENTS

LIST OF ILLUSTRATIONS

LIST OF ILLUSTRATIONS

(continued)

LIST OF ILLUSTRATIONS

LIST OF TABLES

NOMENCLATURE

A	Surface area
Å	Angstrom
C	Specific heat
D	Diameter
E	Thermal capacity
F_o	Fourier number
G	Reciprocal Stefan number
H	Biot number
K	Permeability
L	Length
L	Latent heat of fusion
M	Mesh number
N_L	Liquid transport number
P	Pressure
$\dot{Q}$	Heat flow rate
$\bar{R}$	Gas constant
R_H	Resistance to heat transfer
R_H^*	Dimensionless R_H
St	Stefan number
T	Temperature
$\tilde{T}$	Dimensionless temperature
V	Volume
W	Uncertainty
Z	Heat pipe length
a	adiabatic
c	condenser
d	diameter
e	evaporator
g	acceleration of gravity
h	height
h	heat transfer coefficient
$\bar{h}$	average heat transfer coefficient
k	thermal conductivity
l	length

NOMENCLATURE (Con't)

m	mass
ṁ	mass flow rate
r	radial distance
r̄	dimensionless radius
t	time
τ̄	Fourier number
v	velocity
z	$2\pi/r_c$

α	Thermal diffusivity
γ	Specific heat ratio
δ	Annular gap
ε	Porosity
ε	Location of liquid-solid interface
ε̄	Dimensionless location
η	Hydraulic diameter
θ	Contact angle
λ	Latent heat of vaporization
μ	Viscosity
ρ	Density
σ	Surface tension
ν	Viscosity (kinematic)
∅	Inclination angle from horizontal
	Weight

Subscripts

C	capillary
c	cold surroundings
CAL	calorimeter
cw	cooling water
D	diametral
eff	effective
F	fusion

f	fusion
f	friction
G	gravity
h	surface pore hydraulic
i	inside
L	liquid
l	liquid
m	melting
o	outer
P	pressure
PCM	phase change material
r	radiative
S	sonic
s	solid
v	vapor
W	wall
ww	wick wall

Abbreviations

DSC	Differential scanning calorimeter
DTA	Differential thermal analysis
PCM	Phase change material
TES	Thermal energy storage
TESC	Thermal energy storage container

I. WICKING LIMITS OF SODIUM IN HEAT PIPES AT 1000K

1.1 Introduction

The heat pipe can be used for many applications, has no moving parts and has an effective conductance hundreds of times that of conventional heat exchangers. Sodium is the most widely used working fluid in the operation of the heat pipe between the temperatures of 800K and 1300K and has the very high liquid transport number of 2.1×10^{12} W/M^2. Many different fluids are used, however, according to design requirements and at operating temperatures ranging from 4K to 2300K. Design requirements also designate the choice of the numerous conventional and composite wicks, although manufacturing technology, cost, and the self-priming requirement limits the use of the high performance composite wicks. Sodium at 1000K requires a maximum wicking height in the artery one half that of its static wicking height because of the self-priming requirement. Although wicking is usually the major limitation in the operation of the heat pipe, the sonic and entrainment limitations can also cause severe reduction in performance because of high vapor velocities in the core. The heat flux limitation is also a serious problem that affects heat pipe performance, especially since no method has been developed to eliminate it.

Heat pipe theory was first suggested in 1942 by R.S. Gaugler, but the heat pipe was not developed until it was independently invented by G.M. Grover in 1962. The basic form of the heat pipe, shown in Fig. 1.1, consists of an evaporator, a condenser, a wick network and an enclosed, thin-walled tube, which is evacuated except for the working fluid. Capillary forces in the wick draw liquid from the condenser to the evaporator, where a heat source vaporizes the liquid, filling the inner core of the heat pipe with vapor. This fluid travels back to the condenser, where it liquifies, thereby transferring energy from the heat source to a heat sink under a very efficient (virtually constant pressure and temperature) operation. For high temperature operation, fluids such as sodium are often used as the working fluid since they allow very high heat transfer rates because of their high heats of vaporization and thermal conductivities.

Wick structures are categorized into two types: conventional and composite. The use of a particular wick depends on the design requirements. Since sodium is a commonly used and highly documented working fluid, many wicking analyses and experiments have been accomplished for sodium.

1
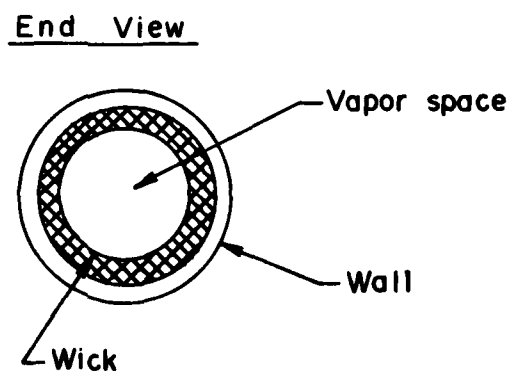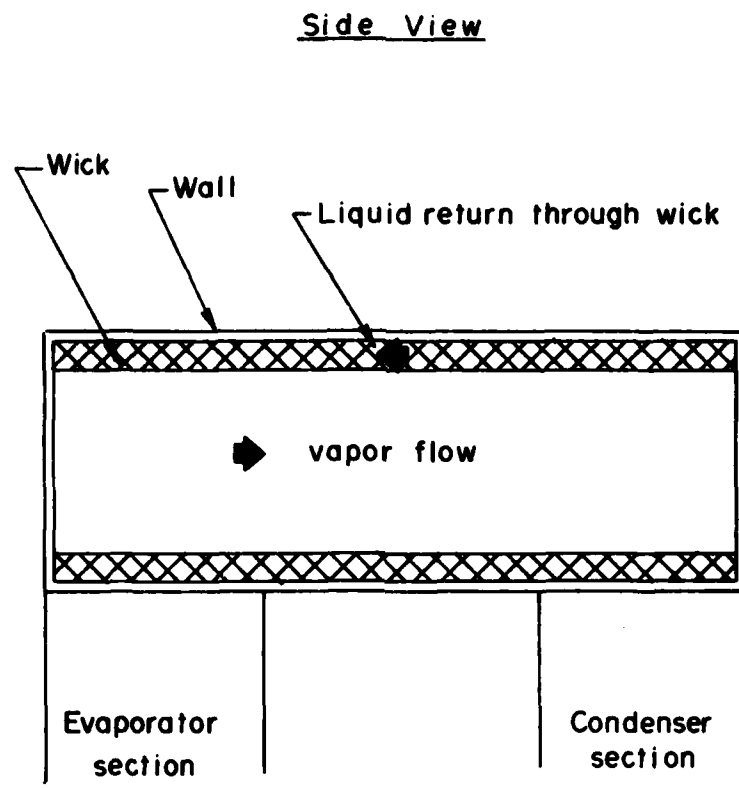
Fig. 1.1. Cylindrical Heat Pipe Structure

1.2 Working Fluids

Heat pipe theory was first presented by Cotter in 1965 [1.1]. The heat pipe has been applied widely using a number of working fluids, containment materials and designs. It is possible to construct a heat pipe for use at operating temperatures ranging from 4K to 2300K if a suitable working fluid is chosen [1.2]. For purposes of classification, however, heat pipes can be broken into three types according to the temperature of operation; these are listed as cryogenic (4-122K), moderate-temperature (122-628K), and liquid-metal (628-2300K).

Besides their respective operating temperature ranges, the most distinct difference in the three types of heat pipes is their maximum capabilities in transporting energy and their temperature drops at the same energy transport condition with similar geometries [1.3]. For example, sodium (liquid metal) has a maximum energy transport capability three orders of magnitude greater than the cryogenic nitrogen fluid, and one order of magnitude greater than the moderate-temperature ammonia fluid, even when operating at their respective optimum operating temperatures. On the other hand the temperature drops for nitrogen and ammonia, from evaporator to condenser, are much greater than that of sodium again under similar conditions. The reason for the higher performance of sodium as a working fluid is due mainly to the high thermal conductivity and the high liquid transport number, N_L. The high thermal conductivity is desirable for minimizing the temperature drop through the wick at both the evaporator and condenser. The liquid transport number is defined as:

$$N_L = \frac{\sigma \lambda}{\nu_L}$$

where, σ – Surface tension

λ – Latent heat of vaporization

ν_L – Liquid viscosity

which is a measure of the capillary pumping capabilities as well as the energy transport capabilities. Since sodium is relatively low cost, is in wide abundance, and has an extremely high N_L among the liquid metals over the temperature range 600K to 1000K, it is the most commonly used fluid for that range [1.4]. Comparative data is shown in Fig. 1.2.

3
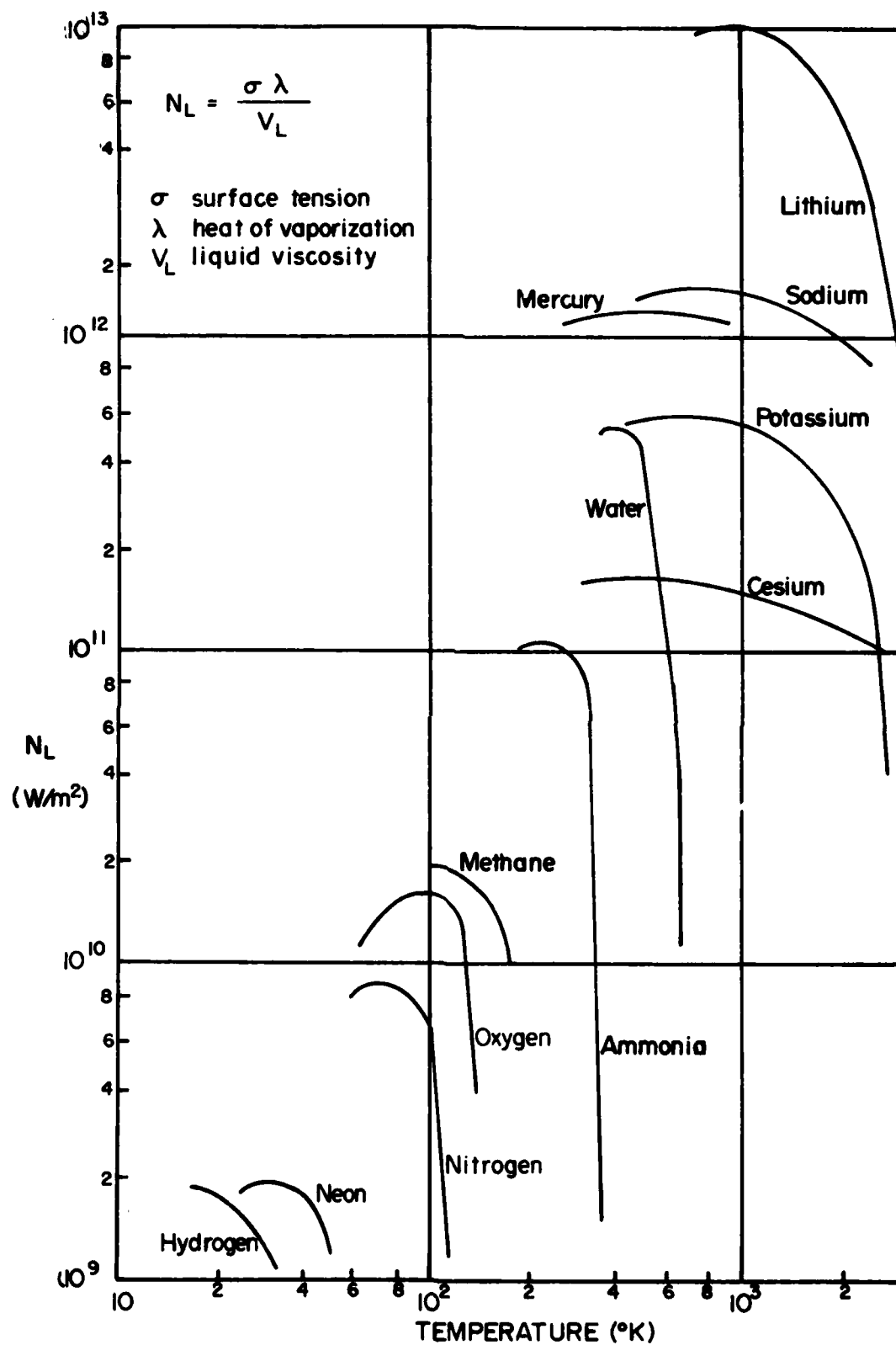
Fig. 1.2. Liquid Transport Numbers of Various Fluids Versus Temperature

4

1.3   Wick Structures

The wick structure of the heat pipe is usually attached to the inner wall of the heat pipe, depending on the particular design requirements. The primary purposes of the wick are (1) to provide the necessary liquid flow path from the condenser to all parts of the evaporator, (2) to supply enough pores at the liquid-vapor interface for developing the required capillary pumping pressure, and (3) to provide a heat flow path of minimum resistance from the heat pipe inner wall to the liquid-vapor interface [1.5]. A selection of these types are shown in Fig. 1.3.

Probably the most common wick is the wrapped screen. The flow resistance of the working fluid can be reduced, thus allowing a greater heat flux through the heat pipe by wrapping the screen more loosely, but by doing so this reduces the capillary pumping ability, causing a reduction in wicking height [1.6]. Along with the annular geometry wick, the wrapped screen also offers the highest resistance for heat flux through the wick [1.7].

The axial groove wick which is machined or etched in the inner wall of the heat pipe offers very low heat flux across the wick. However, separate control of liquid flow and capillary pressure is difficult to achieve with the present manufacturing techniques.

Artery wicks are considered high performance wicks since they were developed to reduce heat flux through the wick and flow resistance of liquid in the wick. For both conventional and composite artery wick structures, however, care must be taken that they are properly primed so that sufficient wicking height and optimum performance is achieved.

Composite wicks differ from conventional wicks in that they consist of two or more separate structures rather than a single structure [1.8]. These are labeled transport wicks and pumping wicks. The reason for using composite wicks is to provide sufficient pumping capabilities by using fine mesh screen, while still allowing the liquid to flow with minimal resistance, to the evaporator by using arteries, grooves, coarse mesh or other open passage ways. The major problem with composite wicks is that they must be able to self-prime during start-up or after burn-out. This process can take as long as several hours [1.9]. In some cases the heat pipe orientation must be changed to prime the artery. The self-priming requirements are (1) that the transport wick provides a static wicking head as high as the wick structure, and (2) that the energy transfer capabilities of the transport wick is not exceeded, without

5

CONVENTIONAL WICKS
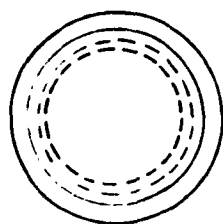
wrapped screen
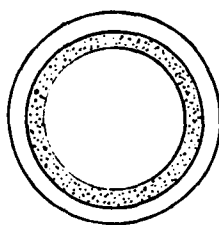
sintered metal
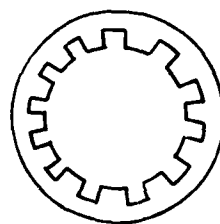
axial groove
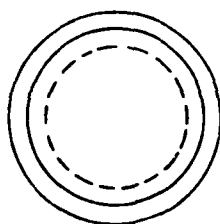
annular
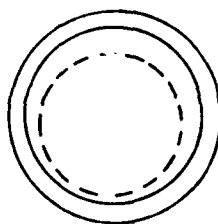
cresent
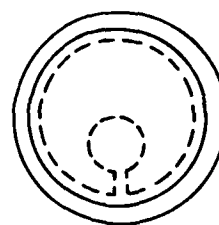
open artery

COMPOSITE WICKS
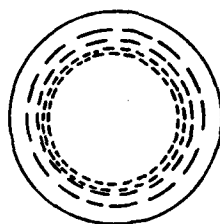
composite
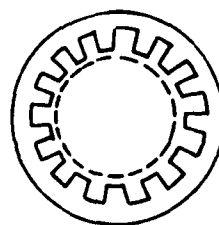
screen covered groove
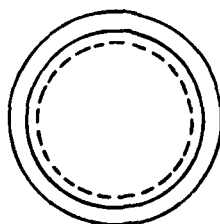
annular
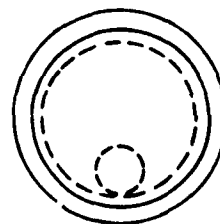
closed artery

Fig. 1.3. Selected Wick Structures

the aid of the pumping capillaries. From the self-priming requirements, it is possible to calculate the maximum artery diameter or annulus gap allowable in a 1-g environment. The maximum artery radius is given by:

$$r_{max} = \left(h^2 + \frac{8\sigma}{\rho_L g} \right)^{1/2} - h \qquad (1.1)$$

The maximum permissible annulus gap is:

$$\delta max = \frac{2\sigma \cos\theta}{\rho_L g D_i} \qquad (1.2)$$

Where, h – Height of artery

ρ_L – Liquid density

g – Acceleration of gravity

θ – Angle formed at the liquid-vapor interface

D_i – Inside diameter of the heat pipe

These equations are illustrated in Figs. 1.4 and 1.5 for sodium at 973K.

Tests performed on heat pipes with grooves covered with 400 mesh screen with sodium as the working fluid have shown that the wicking height is only one fourth of maximum height when improperly primed [1.10]. Composite wicks are less reliable and there is thus little performance data available. Manufacturing techniques have not been fully developed for inexpensive production [1.11].

1.4 Heat Pipe Theory

The principle for the proper operation of the heat pipe lies in the pressure balance of the fluid flow within the heat pipe. As shown in Fig. 1.6, the driving pressure in the wick, due to surface tension force, must overcome the pressure drops of the fluid in the liquid and vapor phases and the pressure drop due to gravity in order to circulate the liquid back to the evaporator. The vapor pressure drop, ΔP_v, and the pressure drop due to gravity, ΔP_G, are independent of wick geometry and can be written as:

$$\Delta P_v = \frac{128 \, \nu_v Z}{\pi D^4} \, \dot{M} \qquad (1.3)$$

$$\Delta P_G = \rho_L g Z \cos \phi \qquad (1.4)$$

7
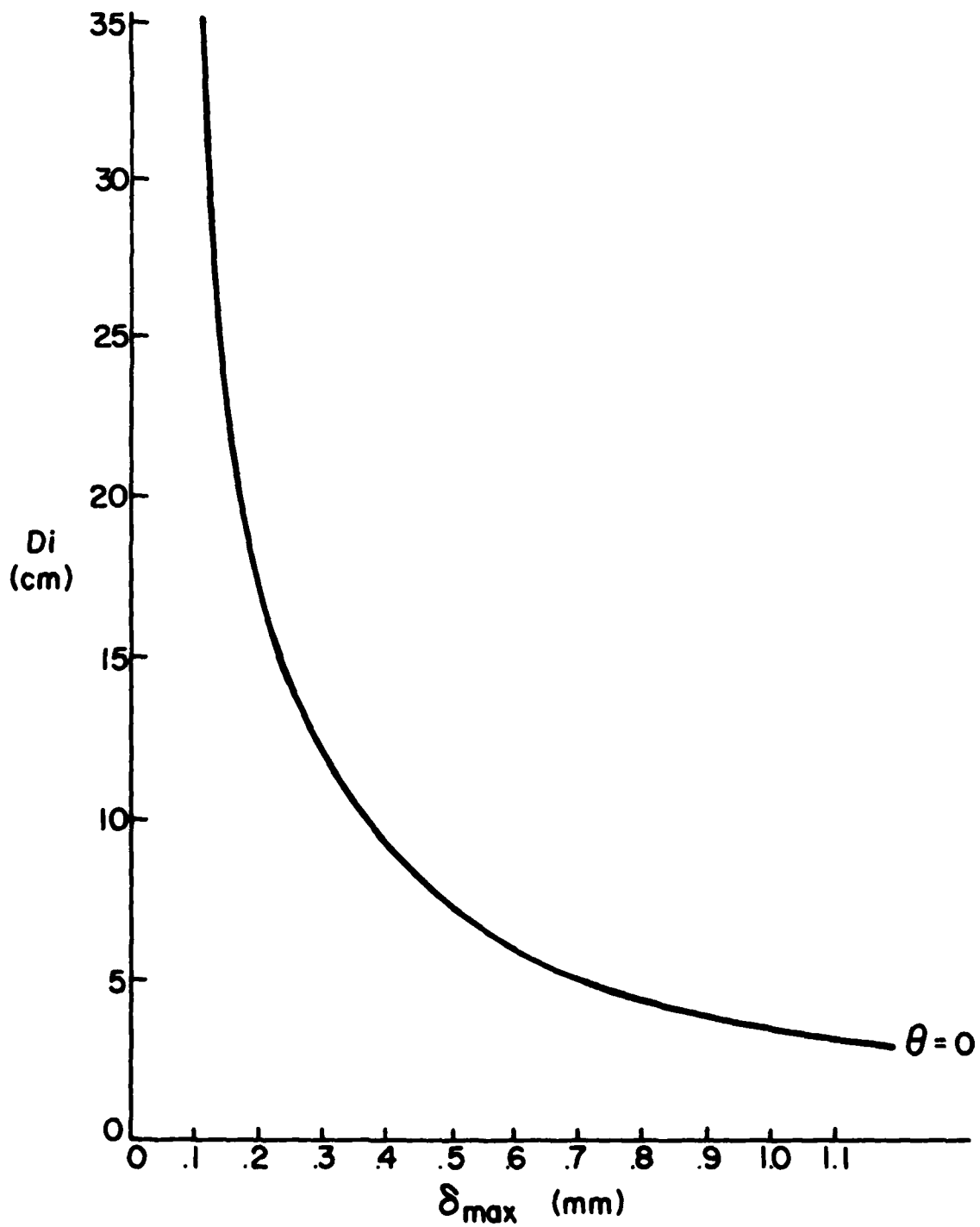
Fig. 1.4. Maximum Permissible Annular Gap to Meet Self-Priming
Requirement of Composite Wicks
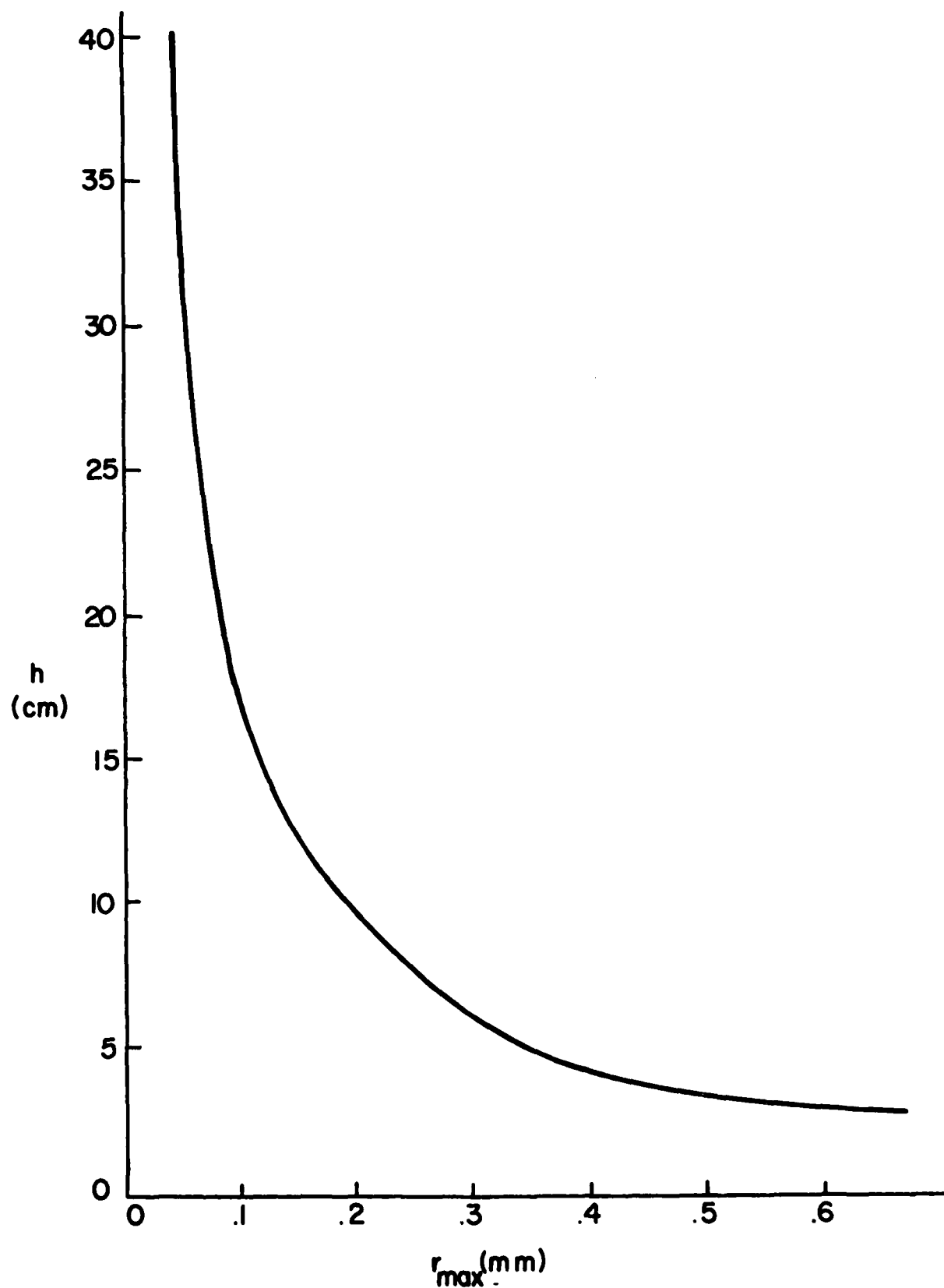
Fig. 1.5. Maximum Artery Radius for Self-Priming Requirements of
Composite Wicks

Fig. 1.6. Pressure Balance in a Heat Pipe
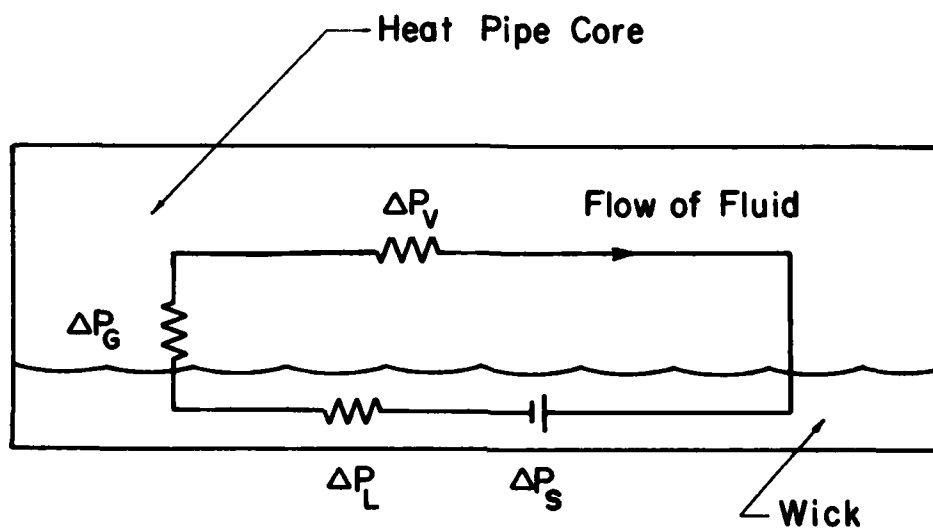
$$\Delta P_S = \Delta P_L + \Delta P_G + \Delta P_V$$

ΔP_S = Driving Pressure Developed in Wick

ΔP_L = Liquid Pressure Drop in Wick

ΔP_G = Gravitational Pressure Drop

ΔP_V = Vapor Pressure Drop in Core

Where, $\dot{M}$ — Mass flow rate of fluid

D — Diameter of heat pipe

Z — Length of heat pipe

ν_v — Vapor viscosity

$\emptyset$ — Angle of liquid flow with vertical

The driving pressure, ΔP_C, and the liquid pressure drop, ΔP_L, are both dependent on the wick geometry but can be written in general as:

$$\Delta P_C = \frac{4\sigma}{d\eta} = \frac{2\sigma}{r_p} \tag{1.5}$$

$$\Delta P_L = \frac{32 \ \nu_L^2 \rho_L Z}{d\eta^2} \tag{1.6}$$

Where, $d\eta$ — Hydraulic diameter

$$d\eta = \frac{4 \ x \ (x\text{-sect area})}{\text{wetted perimeter}} = 2 \ r_p$$

r_p — Effective pore radius

The pressure balance equation then becomes:

$$\Delta P_C = \Delta P_L + P_G + \Delta P_V \tag{1.7}$$

but ΔP_V is insignificant for small vapor flow rates and is often neglected.

A circular capillary (or artery) structure, has been chosen to solve for the maximum wicking height in terms of energy transport per capillary, capillary radius, and fluid properties. Reducing the above equations and neglecting the vapor terms yields:

$$h = \frac{2\sigma}{r \left[\rho_L g + \frac{8\nu_L \dot{m}}{\pi r^4} \right]} \quad . \tag{1.8}$$

Where h = Z

This relation is illustrated for sodium at 973K in Fig. 1.7. For comparison, we see from Fig. 1.8 that the static wicking height of sodium under no heat input conditions (q = 0). Also for comparison, we note that the wicking height reduces as q increases. This corresponds to the reduced wicking heights (from the static condition) due to the self-priming condition
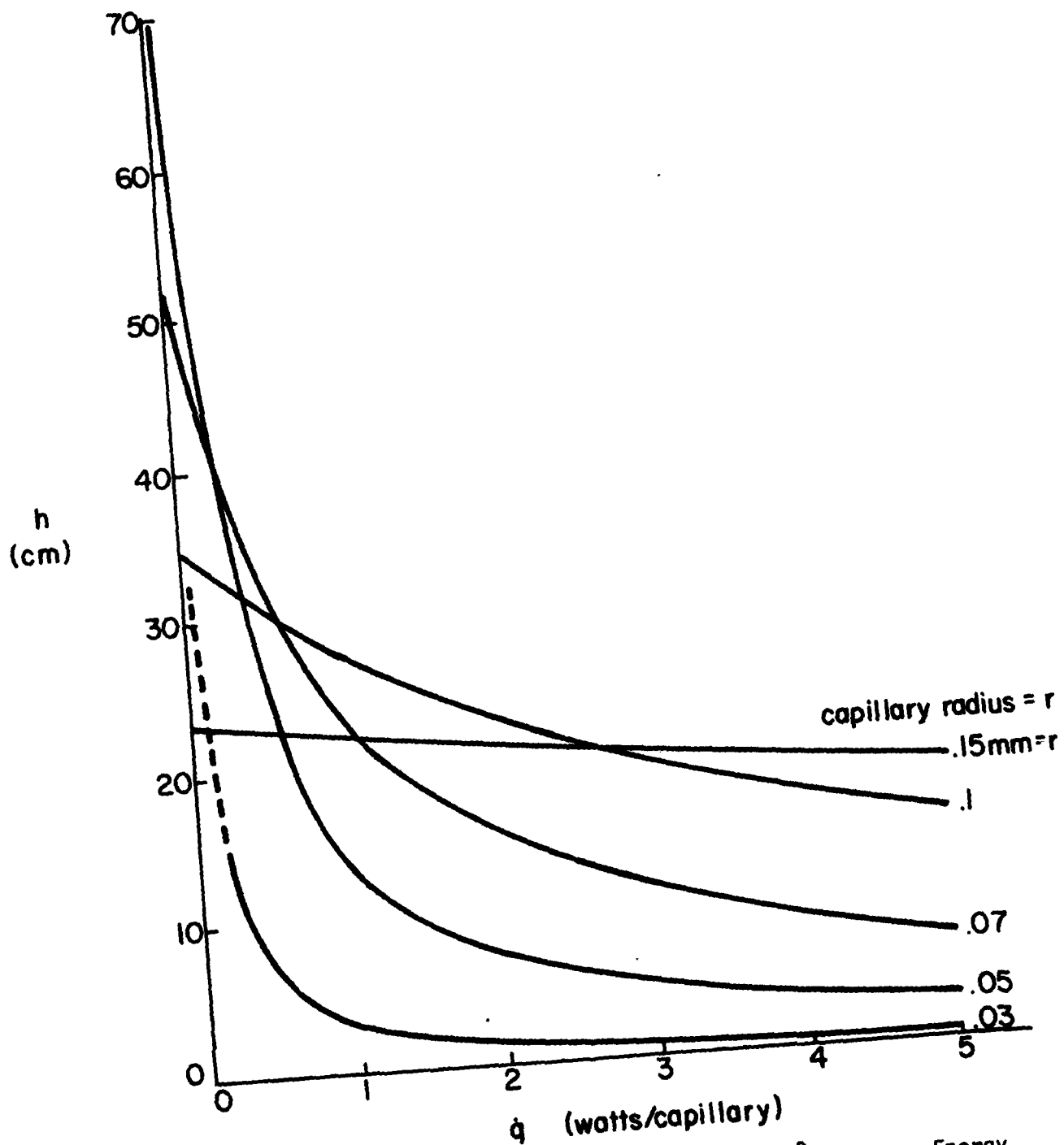
Fig. 1.7. Wicking Height of Liquid Sodium at 700° C Versus Energy Flux Transferred Per Capillary For a Circular Geometry Capillary

12
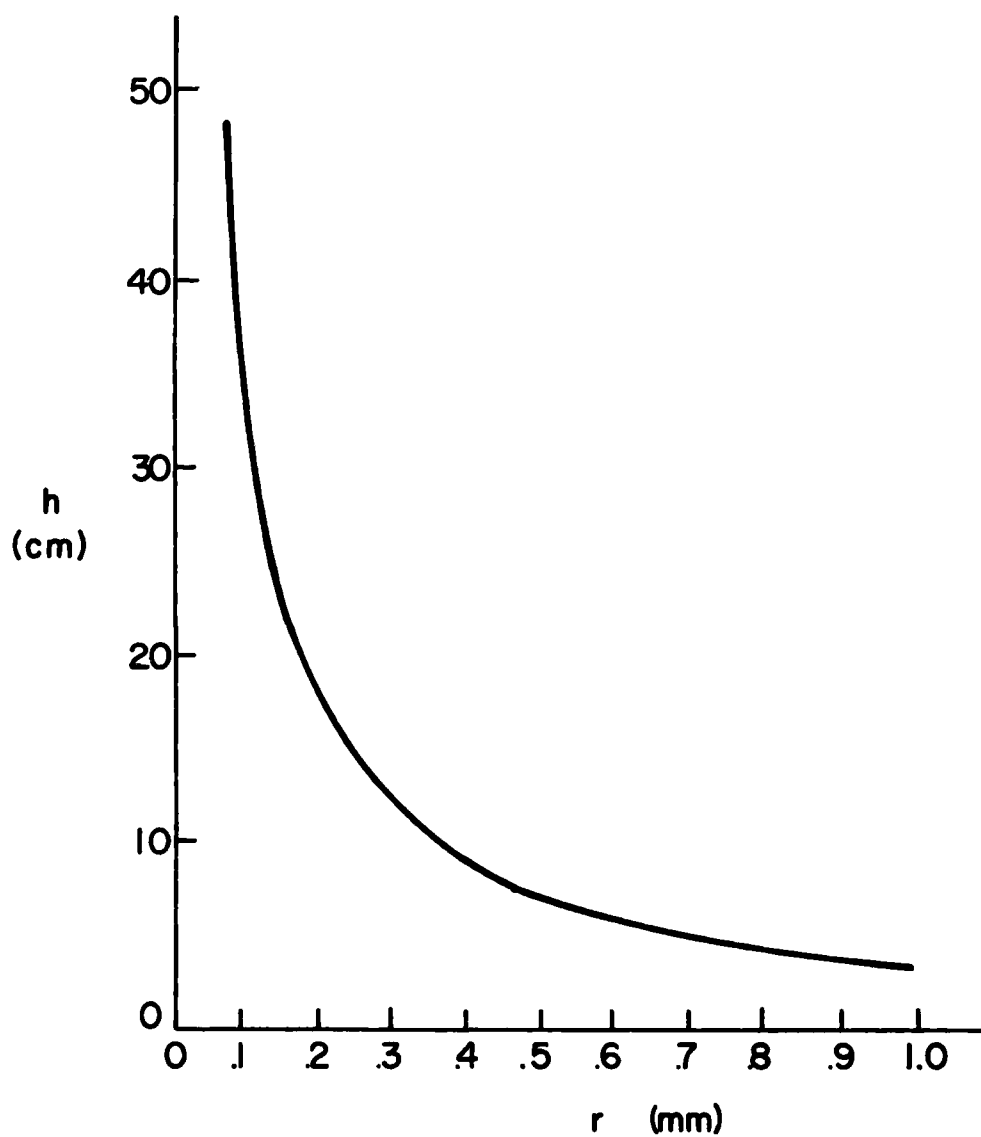
Fig. 1.8. Static Wicking Height of Liquid Sodium at 700° C Circular Capillary

(Fig. 1.5). In fact, the self-priming requirement reduces the maximum possible (static) wicking height by more than a factor of two. In order to increase the wicking height it is necessary to use a smaller radius capillary, but this in turn will reduce the heat transfer capabilities. This trade-off, coupled with the problems of exceeding the other heat pipe limitations (sonic, entrainment and boiling), makes the designing of the heat pipe an iterative and sometimes a very tedious process.

1.5   Heat Pipe Limitations

The four limitations involved in the operation of the heat pipe are: the wicking, the sonic, the entrainment and the boiling (or heat flux). These are illustrated in Fig. 1.9 for a typical heat pipe.

The most commonly encountered limitation in heat pipe operation is the wicking limitation [1.12].   This limit was discussed earlier in terms of wicking heights and heat transport capabilities. If the capillary pressure is insufficient to overcome pressure losses in the wick, then no liquid will be delivered to the evaporator resulting in local burn-out (or dry-out) of the evaporator.

If the velocity of the vapor in the heat pipe core exceeds mach .2, then the compressibility of the vapor is a significant factor causing a reduction in the heat transport capacity [1.13]; and if vapor velocities reach mach 1, then the heat transport cannot be increased regardless of wicking capabilities. As seen in Fig. 1.9, the sonic limitation is most commonly encountered during start-up of the heat pipe, when the temperature is lower than the operating temperature [1.14].   Even though heat pipes are not generally designed to operate with high vapor velocities, high velocities are attainable during start-up due to lower temperatures and pressures at the exit of the evaporator than at the beginning. The maximum heat flux allowable because of the sonic limitation can be shown as:

$$\frac{\dot{Q}}{A_v} = \frac{\rho_v \lambda v_S}{\left[2(\lambda+1)^{1/2}\right]}$$

Where, v_S – Sonic vapor velocity

$v_S = \sqrt{\gamma RT}$

γ – Specific heat ratio

A_v – Area of vapor flow
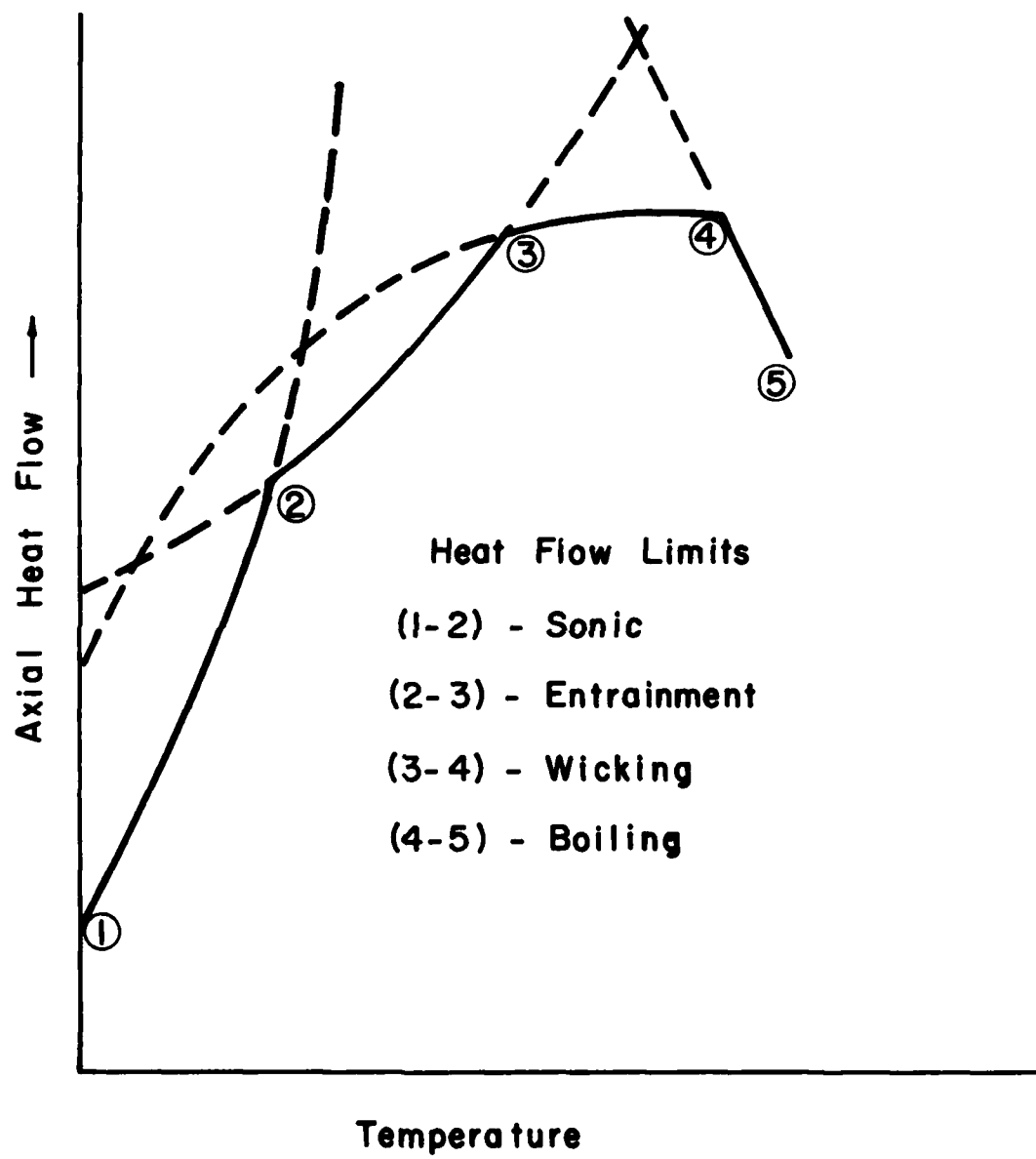
Fig. 1.9. Typical Plot of Heat Pipe Limitations

Heat Flow Limits

(1-2) - Sonic

(2-3) - Entrainment

(3-4) - Wicking

(4-5) - Boiling

Axial Heat Flow ⟶

Temperature

15

The entrainment limit is realized when the vapor velocity is such that liquid droplets are torn from the wick and ''entrained'' in the vapor. This condition reduces the heat transport capability of the heat pipe proportional to the amount of liquid entrained. The onset of entrainment occurs when the Weber number, We, reaches one.

$$We = \frac{\text{inertial forces of the vapor}}{\text{tension forces in the liq. surface}} = 1$$

$$= \frac{\rho_v V_v^2}{\sigma r_p}$$

This leads to the maximum heat flux of:

$$\frac{\dot{Q}}{A_v(max)} = (\rho V \lambda^2 \sigma r_p)^{1/2}$$

Entrainment is the least severe of all limitations and is circumvented by using a small pore radius at the liquid vapor interface [1.15].

The boiling limitation occurs in the wick at the evaporator in which the working fluid boils in the wick before reaching the evaporator. The bubbles that form in the wick reduce the flow area, thus causing a reduction in the heat transport capability. This limitation is the most severe next to the wicking limitation, and complete treatment has not yet been developed for fluid boiling in the wick [1.16]. For this reason most design work is empirical.

1.6   Conclusions

Heat pipe technology, though not fully developed, has expanded the use of the heat pipe into many areas which require operating temperatures ranging from 4K to 2300K. Sodium is the most widely used working fluid over the temperature range of 800K to 1300K because of its desirable properties and low costs. When used in the artery of a wick structure, the wicking height of sodium is limited to less than one half of its static wicking height if the self-priming requirement is to be met; this is true for all composite wicks.

The capillary force of the fluid in the wicks must be sufficient to overcome all viscous and gravitation forces for the proper circulation of the working fluid. This is the major limitation in heat pipe operation. However, high vapor velocities in the heat pipe core cause sonic and entrainment limitations of heat transport capabilities, and excessive heat flux input can

cause a boiling limitation at the evaporator, which can also reduce performance of heat pipe operation.

1.7 References

[1.1]   Heat Pipe Design Handbook, Part I. Cockysville, Md.: Dynatherm, 1974.

[1.2]   Dunn, P.D., and D.A. Reay. Heat Pipes, 2nd Ed., Great Britain: A. Wheaton and Co., 1978. p. 3.

[1.3]   Chi, S.W. Heat Pipe Theory and Practice, Washington, D.C.: Hemisphere Publishing Corp., 1976. p. 3.

[1.4]   H.P. Design Handbook, p. D-35.

[1.5]   Chi, op. cit, p. 5.

[1.6]   Kemme, Joseph, E., J.E. Deverall, E.S. Keddy, J.R. Phillips, and W.A. Rankin. Performance Tests of Gravity-Assist Heat Pipes with Screen-Wick Structures. Los Alamos, N.M.: Univ. of Calif. Los Alamos Lab., 1974. p. 5.

[1.7]   Chi, op. cit., p. 6.

[1.8]   H.P. Design Handbook, p. D-49.

[1.9]   Dunn, op. cit., p. 179.

[1.10] Reactor Technology. Los Alamos, N.M.: Univ. of Calif., Los Alamos Lab., Oct.-Dec., 1978. p. 32.

[1.11] H.P. Design Handbook, p. D-41.

[1.12] Ibid., p. T-18.

[1.13] Ibid., p. D-29.

[1.14] Space Electric Power R and D Program, Part I. Los Alamos, N.M.: Univ. of Calif. Los Alamos Lab., 1969. p. 4.

[1.15] H.P. Design Handbook, p. T-32.

[1.16] Ibid., p. D-30.

II.   INCONEL 600 SODIUM HEAT PIPE POST LIFE TEST ANALYSIS

2.1   Introduction

In a 1974 report, Electro Optical Systems described the design, manu-
facturing and partial results of 6 sub-scale heat pipes built for the Solar
Collector Thermal Power System Program for the USAF, WPAFB, AFAPL [2.1]. The
heat pipes consisted of Inconel 600 bodies with nickel screens and sodium
working fluid. The lifetime of the Solar Collector Thermal Power System
hardware was anticipated to be a minimum of three and a maximum of five years.
These heat pipes were built in order to demonstrate the lifetime of this
system as one of the components of this larger system. Of major concern in
this heat pipe program was the compatibility of the sodium with the
containment material and wick. Specific problems anticipated involved the
basic solubility limits between various elements of the system and complex
mechanisms in which contaminants, particularly oxides, play an active role in
the corrosion between sodium and nickel based alloys. The heat pipe is a
cyclic device and therefore corrosion cycles can possibly be established
whereby material picked up in the condenser region of the heat pipe may be
carried through the wick to the evaporator. When the sodium evaporates,
impurities may be left behind and accumulate in the evaporator region, which
is the hottest portion of the heat pipe. Containment wall corrosion may
result as well as loss of capillary structure and blockage of the wick by
material which is deposited in the evaporator. When wicking capabilities are
lost in the evaporator, the heat pipe will fail to function.

The life tests were designed to operate with pre-calculated heat transfer
conditions which represented the range as required for anticipated flight
hardware designs.

2.2   Heat Pipe Description

The six heat pipes fabricated were identical in design and numbered one
through six. The heat pipes consisted of one inch outside diameter Inconel
600 tubing which was 12 in. in length. The tube wall was 0.0625 in. in
thickness. The evaporator length was 1.25 in. in length with the condenser 5
in. in length. The heat pipe wick consisted of a double wrap of 60 mesh
nickel screen spot welded around the internal circumference of the heat pipe.
A diametral wick structure extended along the longitudinal axis which provided

18

for the liquid return from the condenser to the evaporator. The diametral
wick was 0.25 in. in width, 0.21 in. in cross-sectional area. The diametral
wick was formed from 24 layers of folded screen held between two 0.025 in.
Inconel straps, by twelve 1/8 in. diameter nickel stakes on 1 in. centers.
Heat pipe number two had a diametral wick fabricated from 40 mesh nickel
screen. The remaining four units incorporated 38 mesh Inconel bolting cloth.
The nominal diametral wick dimensions were 0.25 in. wide by 0.806 in. high by
11-3/8 in. long.

A 2 in. long by 0.8 in. wide by 0.001 in. thick zirconium foil was placed
between the centerfold of the evaporator end of each diametral wick.
Zirconium has a higher activity for oxygen than the other components in the
heat pipe and as a getter it is intended to clean up the oxygen to eliminate
the possibility of oxygen corrosion in conjunction with the sodium in the heat
pipe.

It is known that minimizing the oxygen content of the sodium in the heat
pipe is very important to eliminate corrosion. It is not known what the
actual cleanliness of the sodium was, except that it was reported as MSA high
purity sodium. High purity sodium can mean anywhere from ten to fifty parts
per million. It is recognized that five to ten parts per million is probably
the limit for long lifetime sodium heat pipes [2.2].

The heat pipe heaters were fabricated from Nichrome V Inconel sheath
resistance heaters. These sheated heater wires were close-wound around the
heat pipes and vacuum furnace brazed to the evaporator sections. Braze alloy,
82 gold, 18 nickel, designated ASTM-B-260-BAU-4 was used to braze the heater
wires to the heat pipes. Four Inconel sheathed Chromel-Alumel thermocouples
were attached by resistance spot welding Inconel tabs to the heat pipe outside
diameters. For heat pipes 1, 3, 4, 5 and 6 the thermocouple sensing tips were
torch brazed with the same alloy, to the heat pipe, for good thermal contact.
Heat pipe 2 did not have brazed thermocouples.

2.3   Heat Pipe Processing and Evaluation

The heat pipes were loaded with sodium and self-processed by venting to a
vacuum at temperature. The processing consisted of vacuum lines from the heat
pipes to a vacuum system with high vacuum valves. All connections were
helium-leak checked and the heat pipe transfer lines in reservoirs were vacuum

baked to 424K (300°F). The sodium was transferred at 424K (300°F) from the sodium container with argon as a driving gas. Thirty-five grams of sodium was transferred into each of the individual heat pipes. The heat pipes were heated to 1144K (1600°F) to self-process the sodium allowing any buried noncondensible gases to accumulate in the vapor space. The temperature was then lowered to 1034K (1400°F) and the heat pipe was opened momentarily to the vacuum system to remove any gases which might have accumulated. After this processing the heat pipes were closed using an electrode fusion weld to crimp and weld the filled tubes.

The cleaning procedures used prior to heat pipe fabrication were identified as TRW Specification PR2-2J Level 1. It is unknown at this time what this particular specification is. Following welding of this structure, a thermal vacuum step was performed simultaneously as the heater wires were brazed to the heat pipe. It is again unclear what the oxygen or carbon levels of the MSA sodium used in the heat pipes were and the sodium was apparently not distilled or gettered.

2.4   Heat Pipe Testing

The heat pipes were tested at (1144K) at a power input of 600 watts into the evaporator. The heat pipes were operated in air with natural convection cooling in an exhaust hood. Other operating conditions for the heat pipe design were evaporator heat input flux, 150 watts per square inch, condensor heat flux, 34.6 watts per square inch, and axial mass transport flux, 6 pounds per hour per square inch. The heat loss from the particular operational system was 90 watts per foot.

The results of the early endurance testing were that after several hundred hours of operation Units 1, 4 and 5 had heater failures. The brazed-on heaters of Units 1 and 4 were subsequently ground off and it was determined that pinhole failures existed in the heat pipe in the region of the evaporator where the heater wires were ground off. One to two millimeter diameter pinholes were found accompanied by sodium leakage. The brazed-on heaters on all of the heat pipes deteriorated and ultimately most of them failed and were subsequently ground off of the the heat pipes. Heat Pipes 3 and 6 malfunctioned in the sense that they ceased to operate as heat pipes, although pinholes and sodium leakage were not found. It was determined that during heater shortage, as power was continually increased to obtain the operating

TABLE 2.1

Life Test Times

Heat Pipe	Hours at TRW	Hours at ASU
1	672	
2	8760	3015
3	4368	
4	720	
5	840	
6	4848	

conditions required for the heat pipe, localized overheating may have occurred. It was assumed that Heat Pipes 1, 4 and 5 failed because of heater failure and that the heat pipe wall penetration, which was only in the area of the heaters, was considered as evidence that the heaters were the prime cause of heat pipe failure. At the end of the testing period, only Heat Pipe 2 had not had complete failure. The total test time at that point on Heat Pipe 2 was 365 days.

Conclusions which were drawn from the metallographic and microprobe analysis were that the failed region and the reacted zones showed a large amount of grain boundary chromium carbide. The Inconel tube at the zero flow point was apparently undergoing both trans-granular and inter-granular attack. The micro-chemistry of the tube inside diameter was substantially different from that of the bulk of the parent material. The failures were not to be related to the diffusion of the gold-nickel braze into the heat pipe. Other conclusions from the report that were found were that based upon Heat Pipes 3, 4 and 6 performance, the basic long term compatibility between the sodium and the Inconel 600 was good. The failures of Heat Pipes 1, 4 and 5 were attributed to runaway shorted heaters. The termination of testing of Heat Pipes 3 and 6 was simple heater degradation and not related to the heat pipes themselves.

2.5   Continued Life Testing at Arizona State University

Two of the TRW heat pipes were subsequently sent to Arizona State University through Electro Optical Systems for continued life testing. The heat pipe number 2 was placed in a tube furnace. A ceramic tube protected the heat pipe from direct radiation from the heater wires of the furnace. The longitudinal temperature profile of the furnace was not controllable and from thermocouples mounted on the heat pipe, a temperature difference of between 10-12°C was noted between the heat pipe ends. Three thermocouples were placed on the heat pipe surfaces, one at each end and one at the middle. The temperature of the midsection thermocouple was recorded continuously on a strip chart recorder. Many times the furnace or strip chart recorder was defective, causing interruptions in the progress of the test.

The heat pipe was heated to 993K. It was usually left at that temperature continuously during the week and shut off over the weekends. The temperature remained at approximately 993K ± 10K during the heating period.

The cycle time between minimum and maximum temperature was on the order of 30 minutes. The total number of heating cycles was 31 and the system was at the operating temperature of 993K during the total time of 3,400.5 hours. Near the end of this period the thermocouple indicators of the heat pipe showed that the temperature profile, which had always been essentially flat within the experimental area of the thermocouples themselves, began to change. It was noted that a relatively large temperature difference from end to end was beginning to persist. Removal of the heat pipe from the test furnace revealed a yellowish-white emission from the side of the heat pipe in the vicinity of what had once been the brazed heater area. There appeared to be more than one possible pinhole where the sodium was coming out of the heat pipe.

The second heat pipe was then put on test and within a very short period of time it was found to demonstrate the same performance characteristics as the first one which had failed. Upon removal of the second heat pipe from the furnace, it was noticed that sodium was also coming from pinholes very similar to those in the first heat pipe.

2.6   Failure Analysis of Sodium Inconel 600 Heat Pipes

The first heat pipe tested at ASU, number 2, was sectioned into 6 sections so that the evaporator and condenser could both be examined in a number of different ways. The sodium was removed from the heat pipe parts by immersing the pieces in water. It was noted immediately upon cross-sectioning that the evaporator section of the heat pipe was nearly destroyed. The double layer of nickel screen in the evaporator section was nearly completely ''dis-solved'' into the wall of the evaporator. Where the nickel could be pulled away from the wall, very deep impressions of the screen were left in the wall. In some spots the screen was hardly discernible at all. The remains of the evaporator are shown in photo Fig. 2.1. It appeared that the only sodium returning from the condenser probably was coming through the diametral wick and not through the double layer nickel screen on the circumference of the heat pipe. The diametral wick appeared to be in fairly good shape and intact. The circumferential wick in the condenser portion of the heat pipe also appeared to be in relatively good condition. The area of effluence of sodium on the external heat pipe wall was observed to have a highly corroded area adjacent on the inside of the heat pipe.

23

Fig. 2.1 Na-Inconel 600 Post Test Section
of Evaporator Wall Wick and
Diametral Wick Section

2.7 Auger Analyses of Sodium Heat Pipe Life Test Samples

Various parts of a sodium heat pipe structure were studied using Auger Electron Spectroscopy (AES). Experiments using AES were initiated in order to determine specifically the corrosion effects that the sodium has on the wick and container material. The AES technique is suited to this task because of its surface sensitivity (AES detects only those elements within ~ 30Å of the sample surface) and its ability to detect all elements with the exception of hydrogen and helium.

The samples which were analyzed using AES include the following:

1) Inside surface of heat pipe at evaporator end

2) Inside surface of heat pipe at condenser end

3) Surface of polished cross section of heat pipe

4) Nickel screen from evaporator end

5) Nickel screen from condenser end

6) Residue from the sodium heat pipe

An AES scan of a polished cross section of the heat pipe is shown in Figure 2.2. Prior to recording this spectrum, the sample was argon-ion etched for 30 minutes (~ 500Å of material removed) in order to remove both the residual contamination from the polishing process and the thin surface oxide which was present due to exposure to the atmosphere. This scan, which is representative of the bulk alloy composition, shows that the chief metallic constituents were chromium, iron, and nickel. The relative levels of these metals indicates that this was an Inconel alloy although the exact alloy could not be ascertained because of the inability of AES to detect some of the minor constituents. The scans of the evaporator and condenser end surfaces of the heat pipe are shown in Figs. 2.3 and 2.4 respectively. Both of these scans show that the surface was oxidized and that sodium and several other impurities were present on both surfaces. The scans taken after ion-etching these surfaces for 60 minutes (~ 1000Å of material removed) are shown in Figs. 2.5 and 2.6. These figures show that the ion-etching process removed the surface sulfur, chlorine, carbon, and sodium contamination as well as most of the surface oxide.

The scans shown in these figures allow an approximate determination of atom percent composition and these are given in Table 2.2. One obvious

Figure 2.2: Polished cross-section of sodium heat pipe after 30 minutes of argon ion etching.

ELECTRON ENERGY, eV.

$\frac{dN}{dE}$

26

30 min sputtered 1KV; 6 mA

SPECIMEN polished cross-section Na heat pipe

$E_p = 5$ keV $I_p = 3 \mu A$

$V_{MOD} = .10$ $V_{MULT} = 1500$

RC = 0.3   SENS = 2

DATE 9/14/79 BY ____
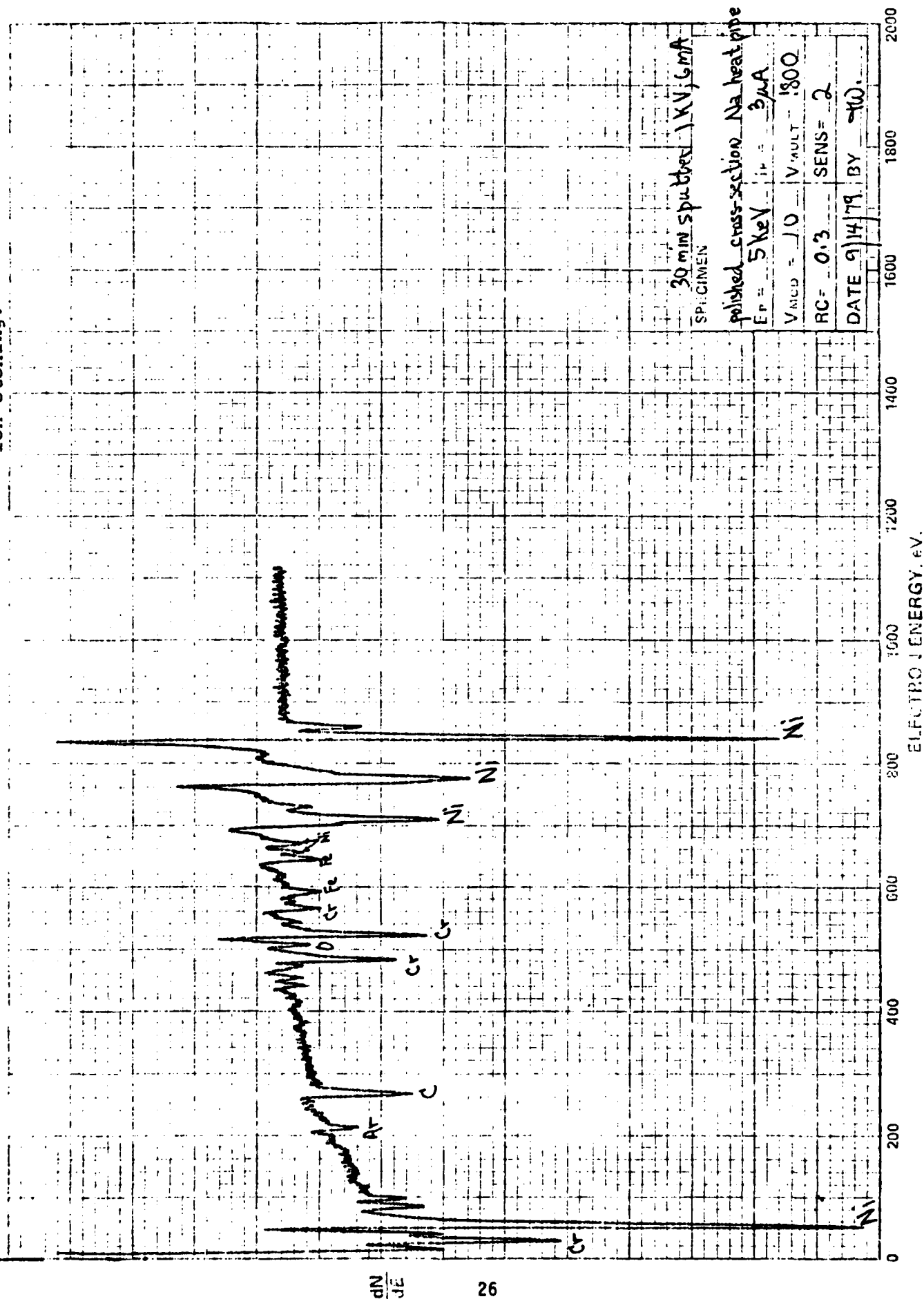
Figure 2.3: Evaporator end surface of sodium
heat pipe

27
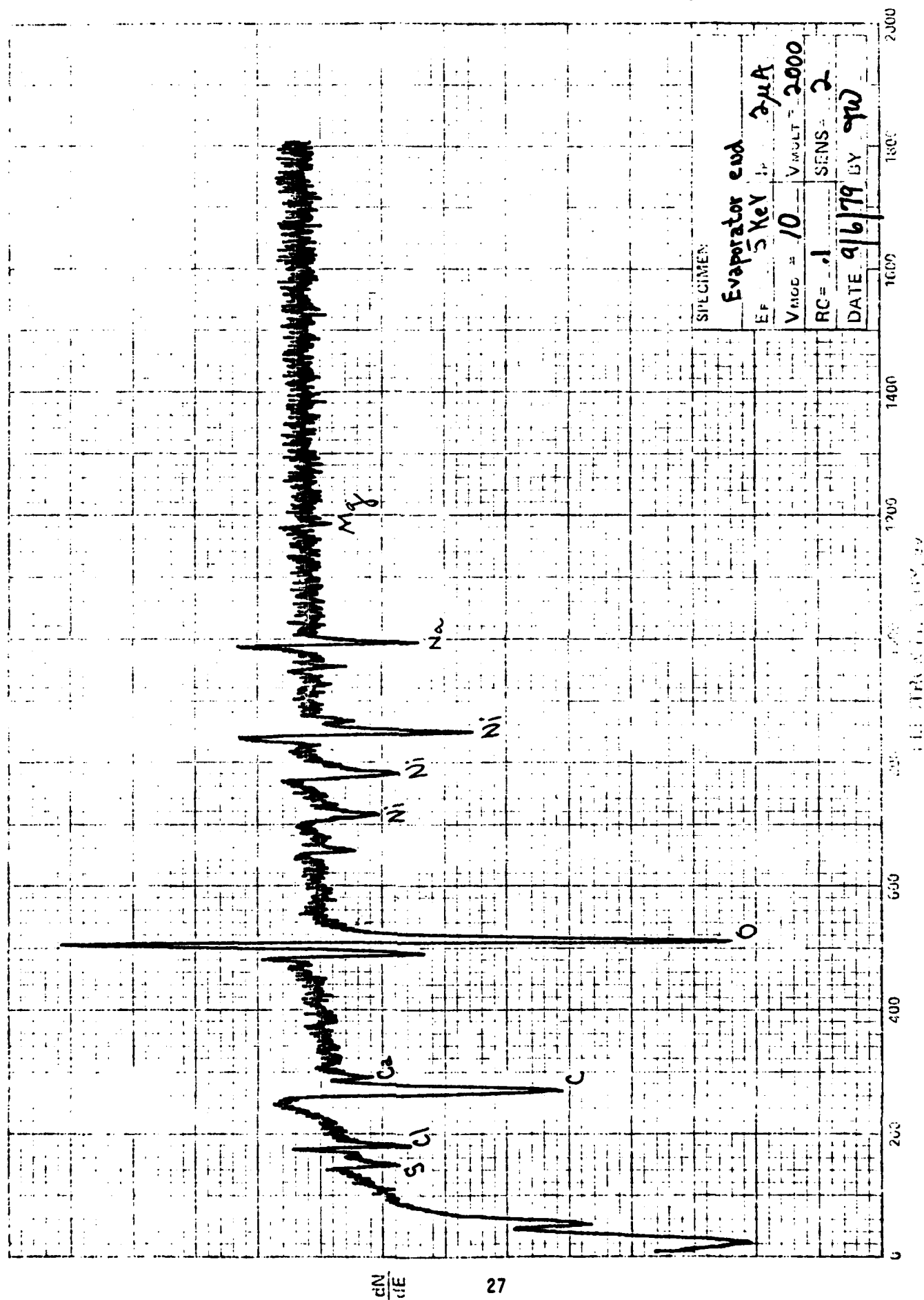
Figure 2.4: Condensor end surface of sodium heat pipe

28
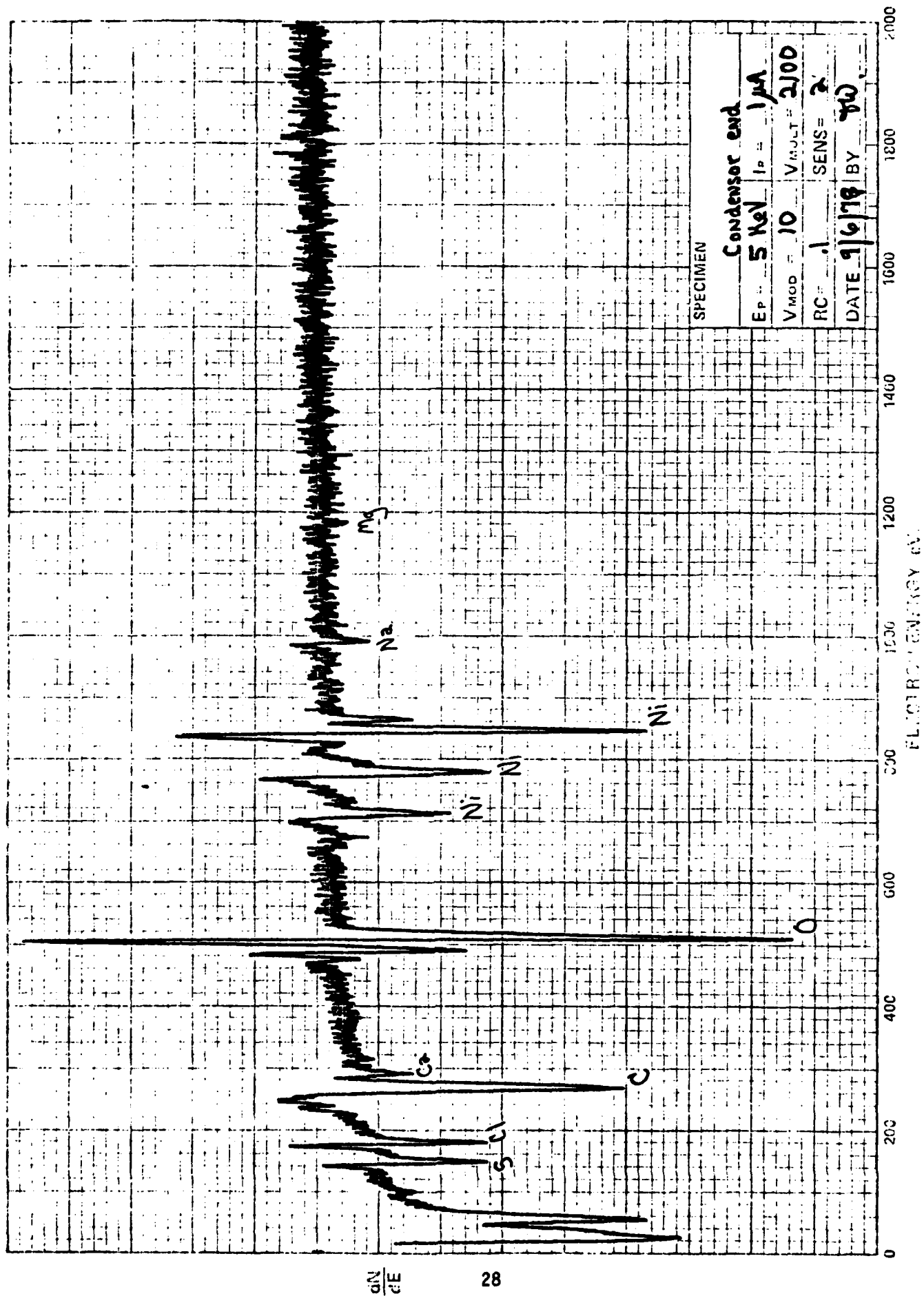
Figure 2.5 : Evaporator end of sodium heat pipe after 60 minutes of ion-etching

29
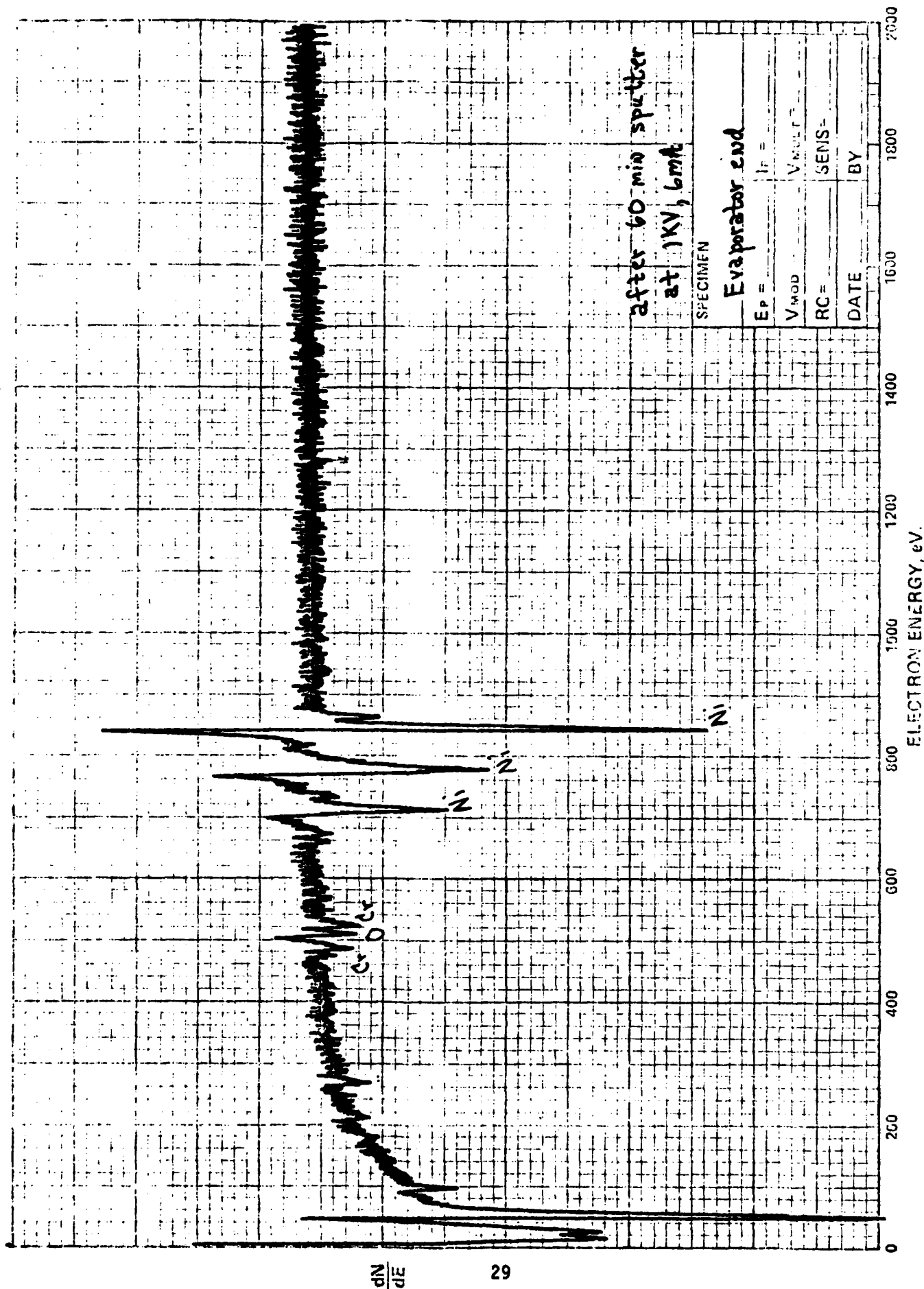
Figure 2.6: Condensor end of sodium heat pipe after 68 minutes of ion-etching
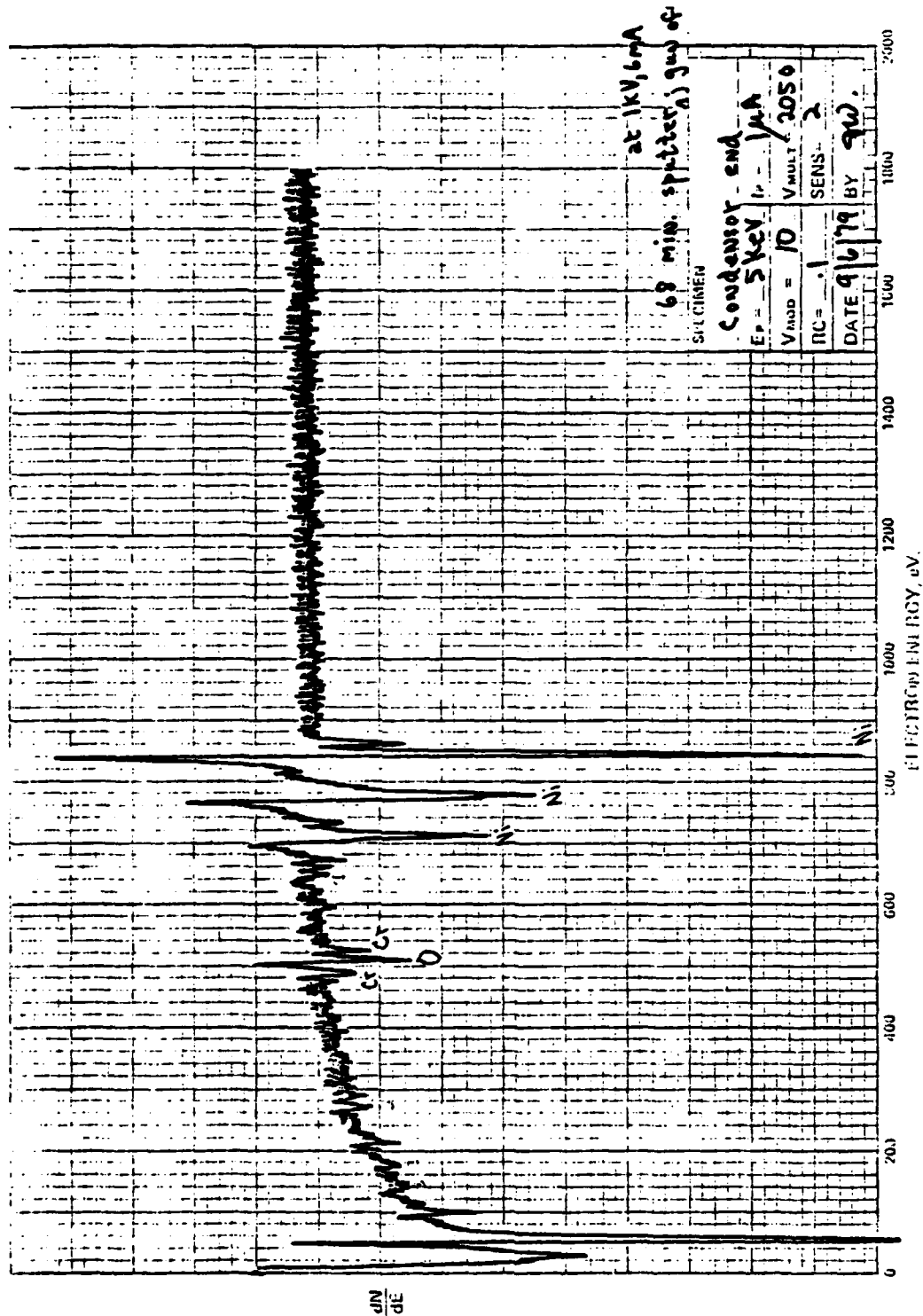
TABLE 2.2: APPROXIMATE ATOM % COMPOSITION FOR
SODIUM HEAT PIPE SURFACES

	S	Cl	C	O	Cr	Fe	Ni	Na
Condensor end -surface	5	14	39	18	<1	<1	17	4
Evaporator end -surface	2	10	41	20	<1	<1	10	15
Condensor end -after ion-etching $\sim 1000\text{Å}$	1	3	8	8	4	4	70	<2
Evaporator end -after ion-etching $\sim 1000\text{Å}$	1	2	12	5	4	<4	69	<3
Heat pipe cross-section -after ion-etching $\sim 500\text{Å}$	<1	<1	23	2	13	5	54	<2

conclusion that can be drawn from examination of this table is that the evaporator and condenser end surfaces of the heat pipe were depleted in chromium and iron compared to the bulk.

Scans are given in Figs. 2.7 and 2.8 of nickel screen samples which were taken from both the evaporator and condenser ends of the heat pipe. Both of these scans were taken after ion-etching the particular sample for ~ 30 minutes. At the evaporator end, the AES scan of the nickel screen shows that some chromium is present. No chromium was detectable, however, at the condenser end. A piece of the residue which was present in the heat pipe was also analyzed (a scan of this is shown in Fig. 2.9) and was found to contain a high level of nickel. It is interesting to note, however, that chromium and iron could not be detected in this residue sample despite the fact that these elements appear to have been depleted from the inner surface of the heat pipe.

In summary, then, the AES data has shown that:

1) chromium and iron were depleted from the inside surface of the heat pipe

2) chromium has been deposited on the nickel screen at the evaporator end

3) nickel is present in the residue inside the heat pipe

2.8   Conclusions

The conclusions reached by TRW in the earlier report were that three of the heat pipes that had failed, exhibiting pinholes with sodium effluent, had failed because of shorts from the heater wire to the heat pipe wall. Subsequent failures in the two heat pipes at Arizona State University, one of which had an additional exposure of 3,015 hours exhibited a similar pinhole type failure. In the ASU test setup, heating was done strictly by radiation with no contact between the heat pipe with anything except the alumina tube. The similarity of failures would indicate that the failures might not have been due to the heater wires at all, but rather to corrosion mechanisms internal to the heat pipe. Overheating of the heat pipe by the brazed-on heater wires might have been an important factor in the failure. It is very possible that a high oxygen or carbon content level in the sodium, especially at elevated temperatures, might have been the primary contributing factors towards corrosion failure of the heat pipes. As evidenced by the Auger

32

Figure 2.7: Nickel screen from evaporator end after 30 minutes of ion-etching.

33
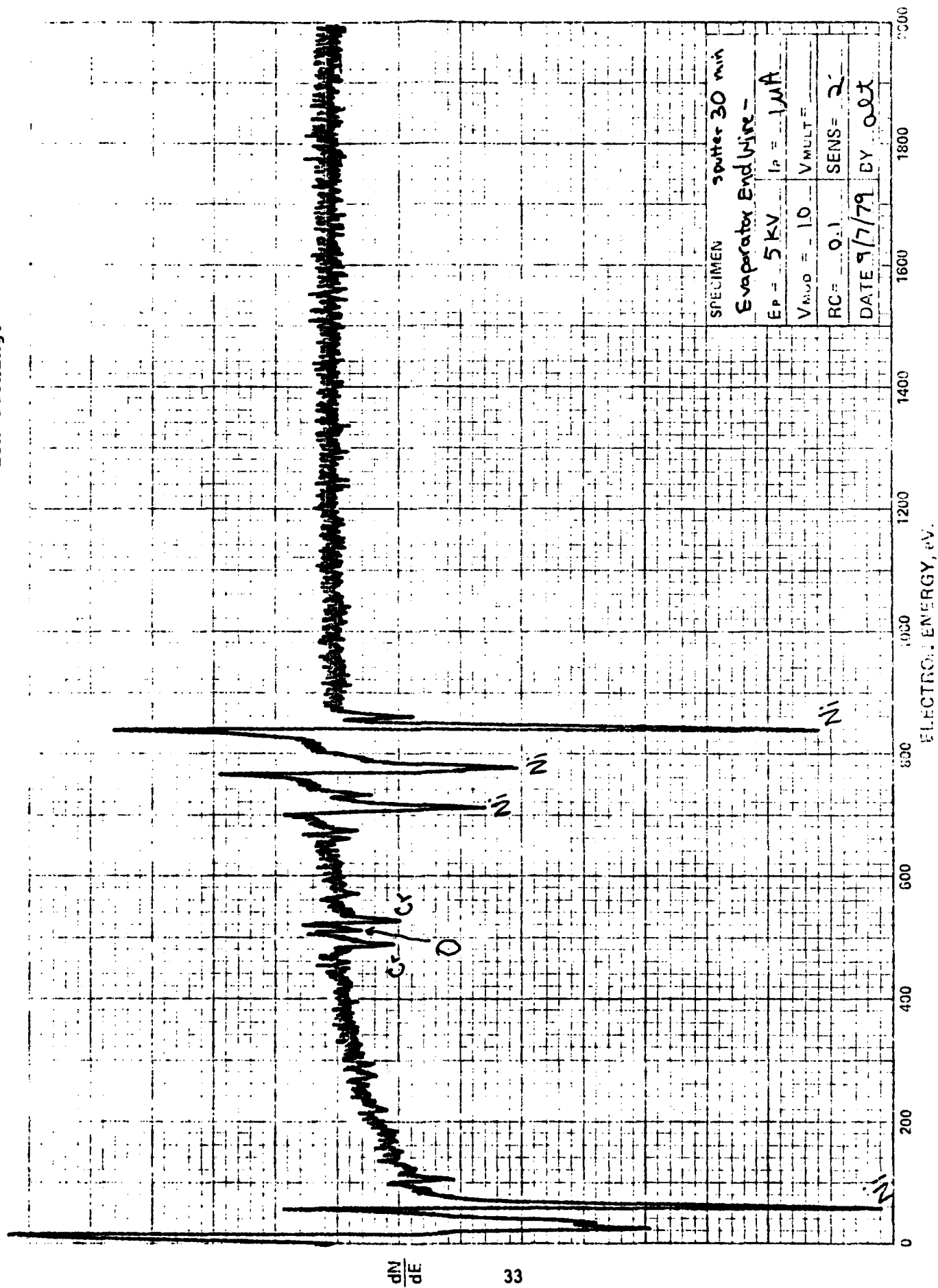
Figure 2.8: Nickel screen from condenser end after 30 minutes of ion-etching.

34
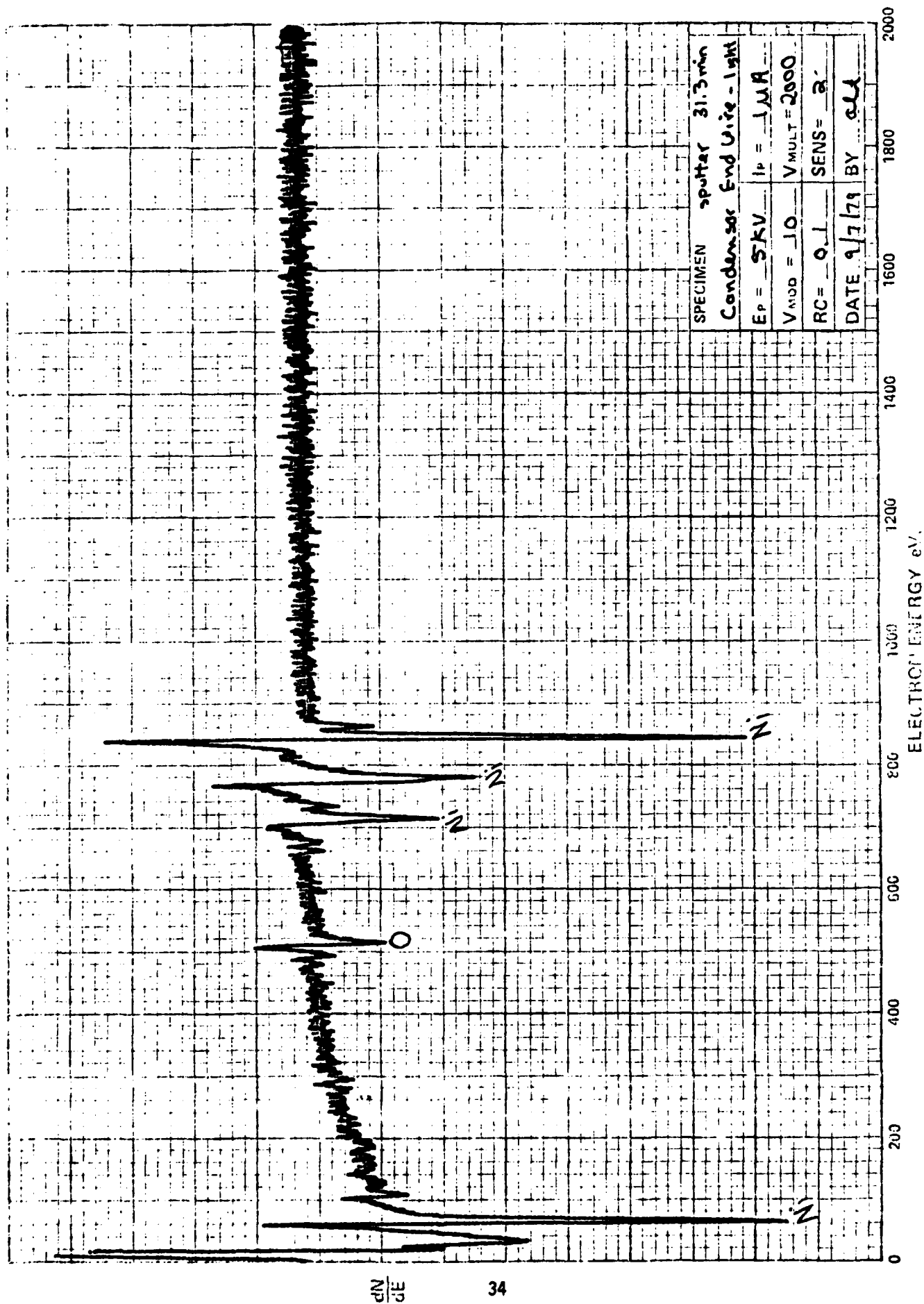
Figure 2.9: Residue from sodium heat pipe.
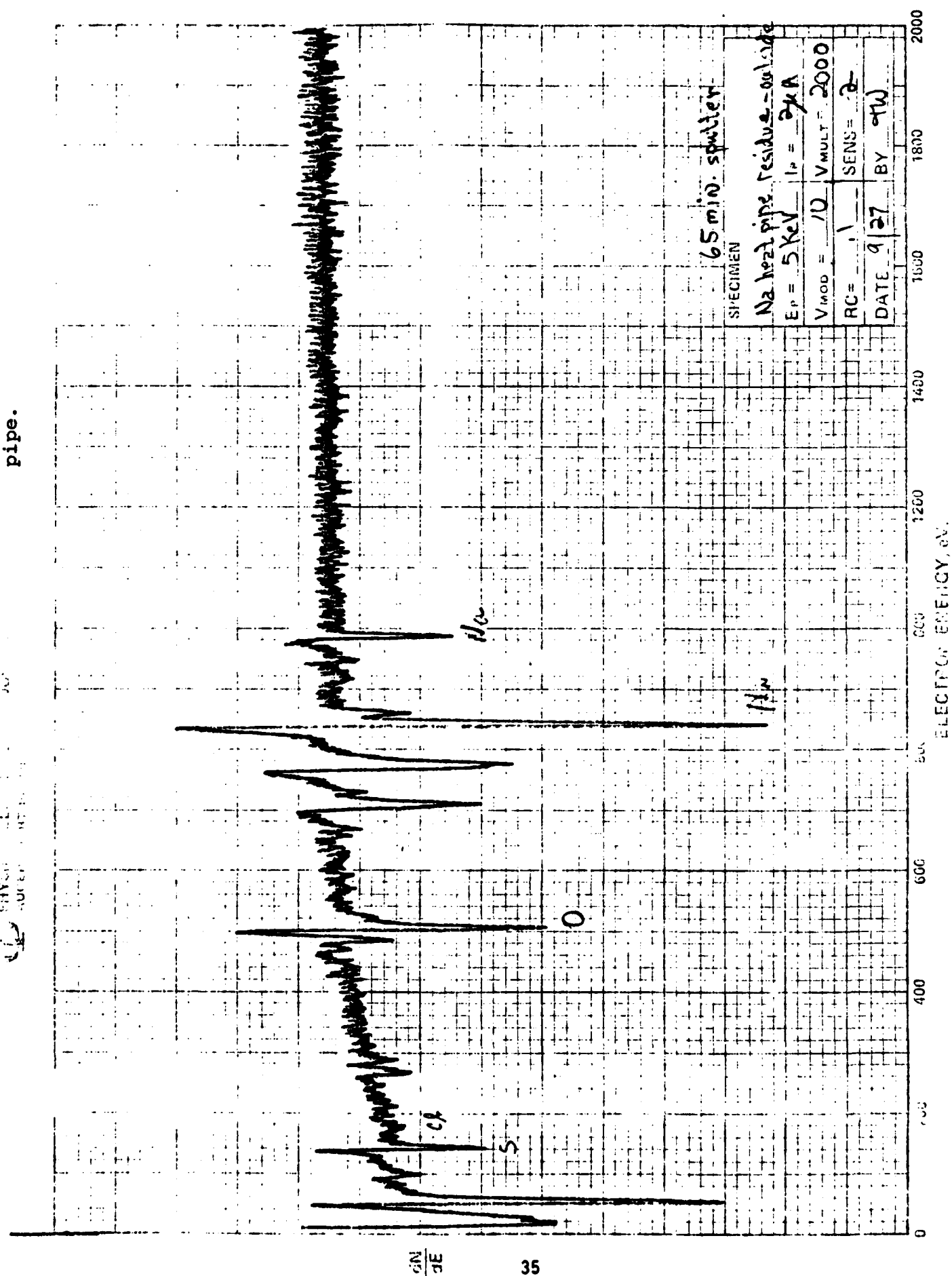
results there was a good deal of mass transfer of some of the primary elements constituting the Inconel 600 alloy. It is also unknown what kind of transferral might have occurred of some of the important secondary elements which tend to stabilize the structure and give it its important high temperature qualities.

It seems obvious that extensive, very high quality life test situations must be set up in order to determine the compatibility of sodium with various alloy systems operating in the heat pipe mode. This process has been initiated by the Air Force through a series of heat pipes built by Hughes. As these heat pipes are tested and then analyzed, great care must be taken to evaluate mass transfer, and therefore material compositions in different zones of the heat pipes, and also to evaluate the purity of the working fluid sodium before and after testing.

2.8   References

[2.1]   Richter, R., Solar Collector Thermal Power Systems, AFAPL-TR-74-89, Vol. III, Nov. 1974. p. 39.

[2.2]   Jacobson, D.L., Material Selection Considerations for Fluoride Thermal Energy Storage Containment in a Sodium Heat Pipe Environment, AFAPL-TR-77-9, May 1977.

III. THERMAL POWER TRAIN EXPERIMENTS

3.1 Introduction

3.1.1 History

The thermal power train, now located at ASU in the Engineering Center, was initially developed by Xerox Corporation/Electro-Optical systems as part of a Solar Collector Thermal Power System Program. The thermal power train was an integral part of a system to supply thermal energy from a solar collector to a Vuilleumier cryo-cooler on board a BMS (Background Measurement Satellite). Mission considerations dictated the use of a system that could perform thermal energy transmission as well as storage and thermal management. Furthermore, the system was to operate in a region between 980K and 1200K and provide 3 kilowatts of continuous thermal energy to a load at between 810K and 980K. Performance and life testing was accomplished by Xerox, and the unit was transferred to Arizona State University to continue extended thermal cycling life test.

3.1.2 Power Train Background

Figure 3.1 is a schematic of the thermal power train located in the Thermionics Lab. The power train consists of three main components. These are (1) a primary sodium heat pipe which is fifteen feet long, (2) a secondary heat pipe with a Lithium Fluoride (LiF) thermal energy storage system (TESS), and (3) a rotary radiation heat transfer joint. Of these components, the primary heat pipe is the heart of the thermal power train. Virtually all of the information developed by the Xerox Corp. about the thermal power train is devoted to the design, fabrication, and testing of the primary heat pipe [3.1].

The primary heat pipe was designed to operate with a maximum power input of 6kW and has three major sections in its design. These are (1) the evaporator section, (2) the adiabatic section, and (3) the condenser section. The evaporator section is 20 in. long, the adiabatic section is 122.5 in. long, and the condenser section is 27.5 in. long. The actual heat pipe is constructed of Inconel 617 alloy and has a wall thickness of .065 in. The outside diameter of the primary heat pipe is 2.25 in. The wick material, used to transfer the condensed fluid from the condenser to the evaporator, is 50 mesh

37

ROTARY HEAT TRANSFER JOINT
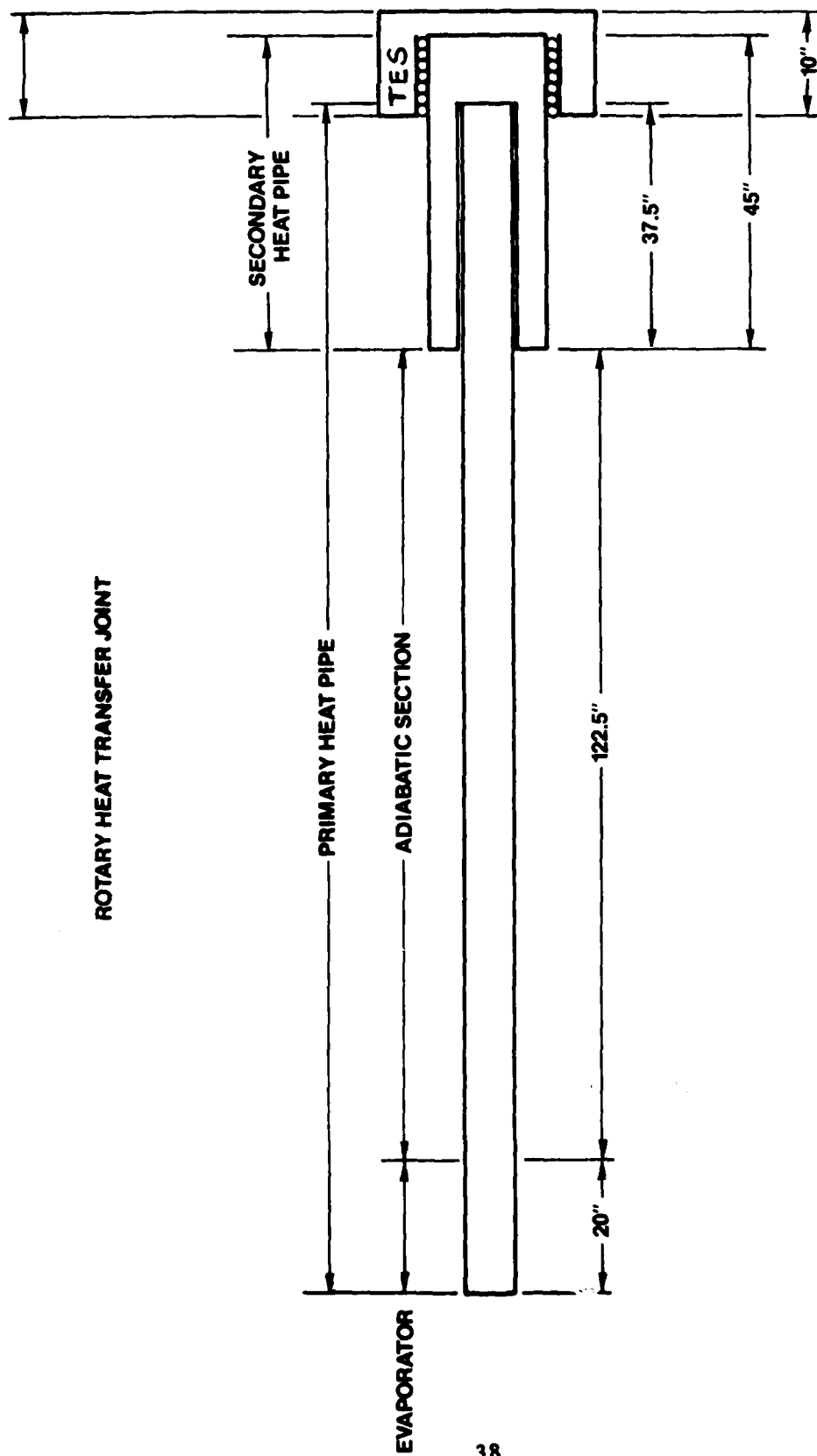
Fig. 3.1. THERMAL POWER TRAIN

38

bolting cloth. The wick consists of both a diametral wick and a wall wick as shown in Fig. 3.2. The working fluid used in the heat pipe is sodium. An 11.5 lb. fill was determined to be sufficient to keep the entire volume of the wick ''wetted'' during start up. Table 3.1 gives a complete list of parts and materials for the fifteen foot heat pipe [3.2].

Surrounding the condenser end of the primary heat pipe is the secondary heat pipe and the LiF storage material. This assembly was designed to supply energy to the cooler on the satellite. During periods of energy collection, the primary heat pipe would supply energy for both recharging the storage medium and running the cooler. When energy collection did not occur, the primary heat pipe would cease to operate and the storage medium would supply the energy required to run the cooler. This apparatus is shown in Fig. 3.3.

The lip of the secondary heat pipe is welded to the flange of the primary heat pipe. The small annular space between the two heat pipes is filled with sodium to insure proper heat transfer. Nine LiF energy storage cylinders are placed around the inside of the secondary sodium heat pipe. The secondary heat pipe is 45 in. long and has the same internal characteristics as the primary heat pipe.

Placed on the end of the secondary heat pipe is a rotary radiation heat transfer joint. The design function of this joint was to provide a degree of freedom between the thermal power train and the cooler, and to regulate the amount of energy transferred to the cooler. In the test setup, the rotary joint is used as a calorimeter with water circulating through cooling coils. Surrounding the entire thermal train is 1.5 in. of Min-K insulation that is under 2 in. of Cerafelt 800 insulation.

3.1.3 Experimental Use of the Power Train

The present efforts were directed towards preparing the entire thermal power train for experimental use. The thermal power train was first inspected to determine what work had to be done in order to prepare it for experimentation. It was found that a large number of tasks had to be accomplished to make the thermal power train operational. Five major areas were identified for preparing the power train for testing: (1) heat pipe stand, (2) power supply to run the test heaters, (3) cooling at the radiation heat transfer joint, (4) instrumenting the heat pipe for temperature control, and (5)

39
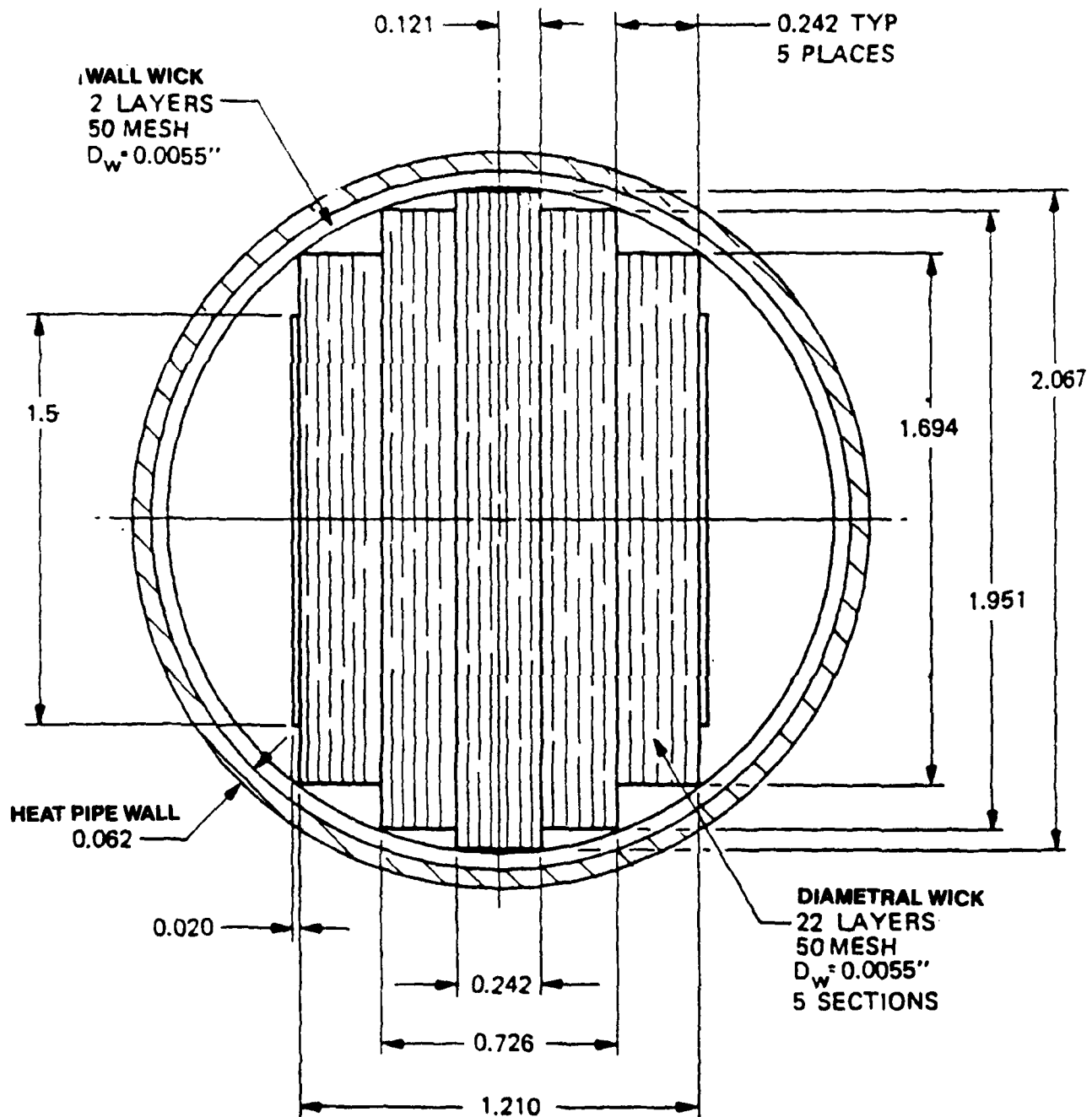
Fig. 3.2. **HEAT PIPE WICK CROSS SECTION**

40

Table 3.1 Ref.[3.3]

Fifteen-Foot Heat Pipe Materials

Item	Type/Size	Material
Diametral Wick	38-mesh bolting cloth 0.0065 inch wire diameter	Inconel 600
Wet Finger and Circumferential Wick	60-mesh screen 0.007 inch wire diameter	Nickel 200
Diametral Wick Retainer	Sheet 0.025 inch thick	Inconel 600
Diametral Wick Connectors	6-32 NC round head screw and nut	Inconel 600
Getter	Foil 0.001 inch thick	Zirconium
Tube	2.250 inch o.d. by 0.063 inch wall	Inconel 617
End Caps and Flange	Sheet 0.250 inch thick	Inconel 617
Fill Tubes	0.250 inch o.d. by 0.035 inch wall	Inconel 600
Heat Pipe Fluid	Bulk	MSA High Purity Sodium
Start and Processing Heaters	Semicylindrical heaters Model 50242, Type 2718-KSP	Lindberg Hevi Duty
Thermocouples	CR-Al 1063K6E, CR-Al 1063K12E	Sheathed Inconel 600
Braze Material	Rod	82% Au-18% Ni
Valves	Nupro SS-4TG	Satellite Tip
Insulation	Sheet 36 by 36 by 3/8 72 by 36 by 3/8	J-M Flex-Min-K

LiF ENERGY
STORAGE MAT'L

2.349 DIA.

5.432 DIA.

SECONDARY
HEAT PIPE
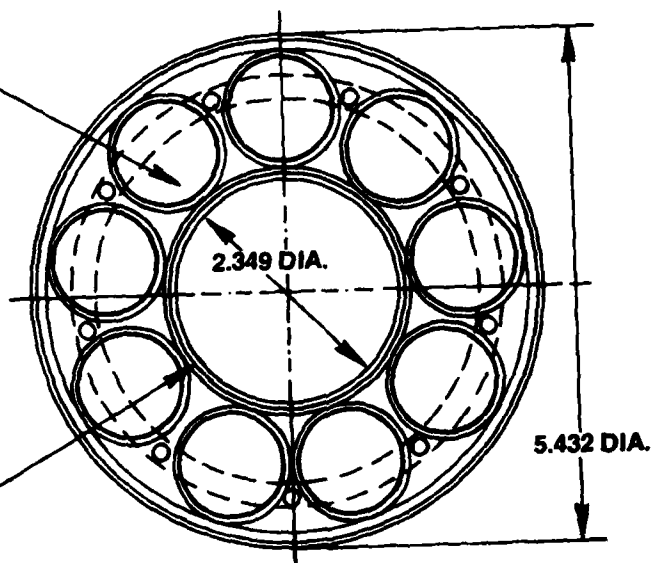
Fig. 3.3   ENERGY STORAGE MATERIAL
SURROUNDING SECONDARY HEAT PIPE

42

constructing a purge volume to recharge the heat pipe. These five steps are explained in the next section.

3.2   Design and Development

3.2.1   Setup

When the thermal power train was maneuvered into the Thermionics Lab, uncrated, and inspected, it was determined that the wooden crate support would be totally inadequate for high temperature operation and permanent installation. A stand was designed and fabricated that would hold the power train securely and yet insure minimum conduction losses. The stand consists of two pieces of square steel tubing that run the length of the power train. These steel rails are supported by five wooden trestles that give the stand lateral stability. The thermal power train is elevated from the rails by several sets of refractory fire brick, and is secured to the stand assembly by two small wire bands. The design is shown in Fig. 3.4.

3.2.2   Power Requirements

Investigation of the Electro—Optical systems reports [3.1] revealed that there are several heaters installed on the thermal power train. The primary heater, which provides power input to the evaporator, consists of three Calrod Tubular Inconel sheathed heaters each rated at 3 kW at 240 volts. These Calrod units are coiled tightly around the outer diameter of the heat pipe and are connected electrically in parallel. The secondary heater consists of two similar Calrod units rated at 1 kW at 110 volts. These heaters are placed along the adiabatic section of the heat pipe and are used to quickly bring the entire thermal power train to a uniform working temperature. The steady—state losses for the power train ranged from 1200 to 1500 watts depending on the working temperature and the state of the thermal energy storage unit and the insulation. Based on this information, 5 kW of power was requested to be supplied for the primary heater. This is more than enough to overcome losses and provide for testing of the thermal train with power transfer. In addition, since the thermal power train is a one—of—a—kind prototype and has been successfully operated at its design input power of 6 kW, the use of 5 kW provides the factor of safety prudence dictates. No other special power is required; the wall circuits in the Thermionics Lab are adequate to run the
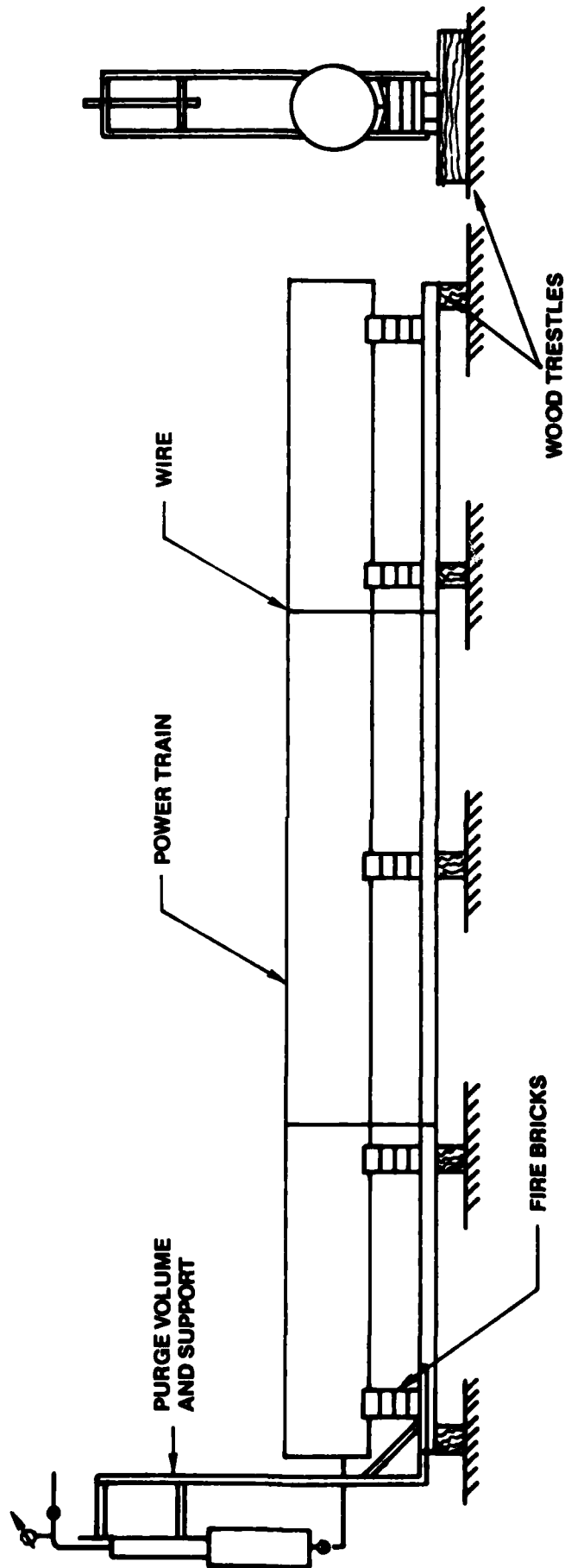
Fig. 3.4. POWER TRAIN SUPPORT STAND

secondary heaters. Two separate Variacs are required to control the power input to the primary and secondary heaters.

3.2.3 Calorimeter

Power extraction at the condenser end of the thermal power train is facilitated by a tubular heat exchanger calorimeter and the radiation heat transfer joint. This system is made up of four cooling coils installed in the joint. If water is used as the coolant, the amount of power extracted at the condenser can be determined from the mass flow rate of the water, its specific heat, and temperature rise. To increase the efficiency of the cooling operation, the coils can be supplied with coolant in a counterflow; coolant runs into two coils from the upstream side and into two from the downstream side of the thermal power train.

A schematic of the cooling system is shown in Fig. 3.5. The 25 gallon tank is located on a ledge formed by the second floor of the lab. A feed line and overfill line can maintain the tank fill at a constant level of 12 feet. The simplest way to determine the mass flow rate of the cooling water is with an orifice and upstream and downstream pressure gauges. A valve located at the base of the tank controls the mass flow rate so the thermal power train can be operated under varying power extraction conditions. The cooling coils on the radiation heat transfer joint have been fitted with inlet and exit tubing, a glass rotometer, and two flow rate control valves. Fig. 3.6 photo shows the calorimeter. The Rotometer calibration is given in Fig. 3.7. If the mass flow rate of coolant is carefully decreased until the heat exchanger efflux is just vaporizing, the power extraction can be determined fairly accurately by measuring the mass flow rate and the inlet and exit water temperatures. A graph of the pressure drop across the orifice versus mass flow rate would then serve as a quick reference of power extraction for various test conditions.

One method for power extraction is that measurements be taken with low enough coolant flow rates to allow coolant at the exit to reach a superheated state. This would allow errors in temperature measurement to propagate into very small errors in power extraction measurements. After a square-sum-root error analysis however, it was determined that this method might not be acceptable because at high power levels the coolant flow rate has to be determined within ± 0.05 gm/sec to give a power transfer value of at least 10%
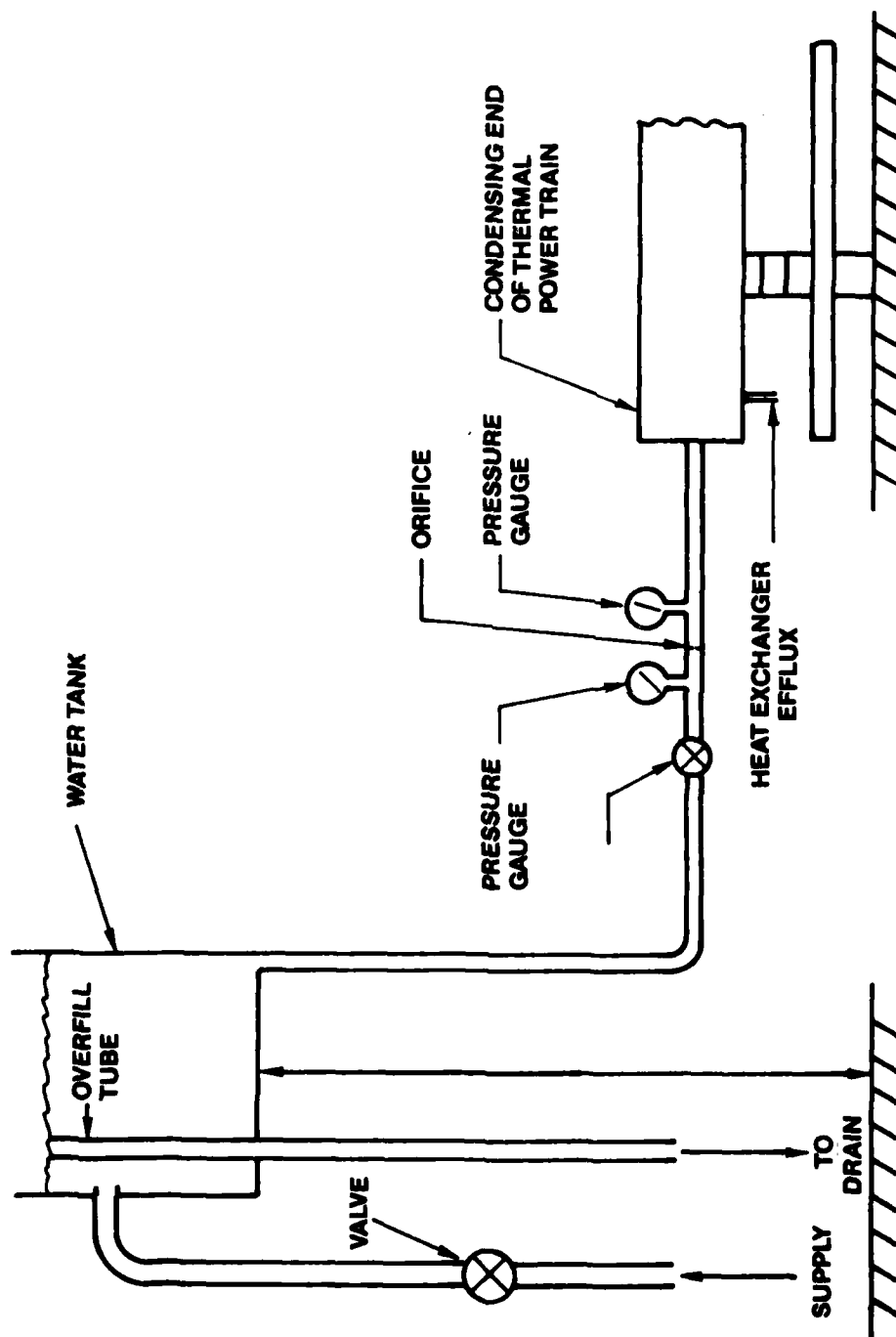
Fig. 3.5.   COOLING SYSTEM SCHEMATIC

46

WATER FEED LINE
FROM CONSTANT
LEVEL TANK

GLASS
ROTOMETER

SECONDARY
HEAT PIPE
CONDENSER
SECTION
(INSULATED)

ROTARY
RADIATION
HEAT TRANSFER
JOINT (INSULATED)

COOLING COIL
EXIT LINE
TO DRAIN

COOLING COIL

COOLANT FLOW RATE
CONTROL VALVES
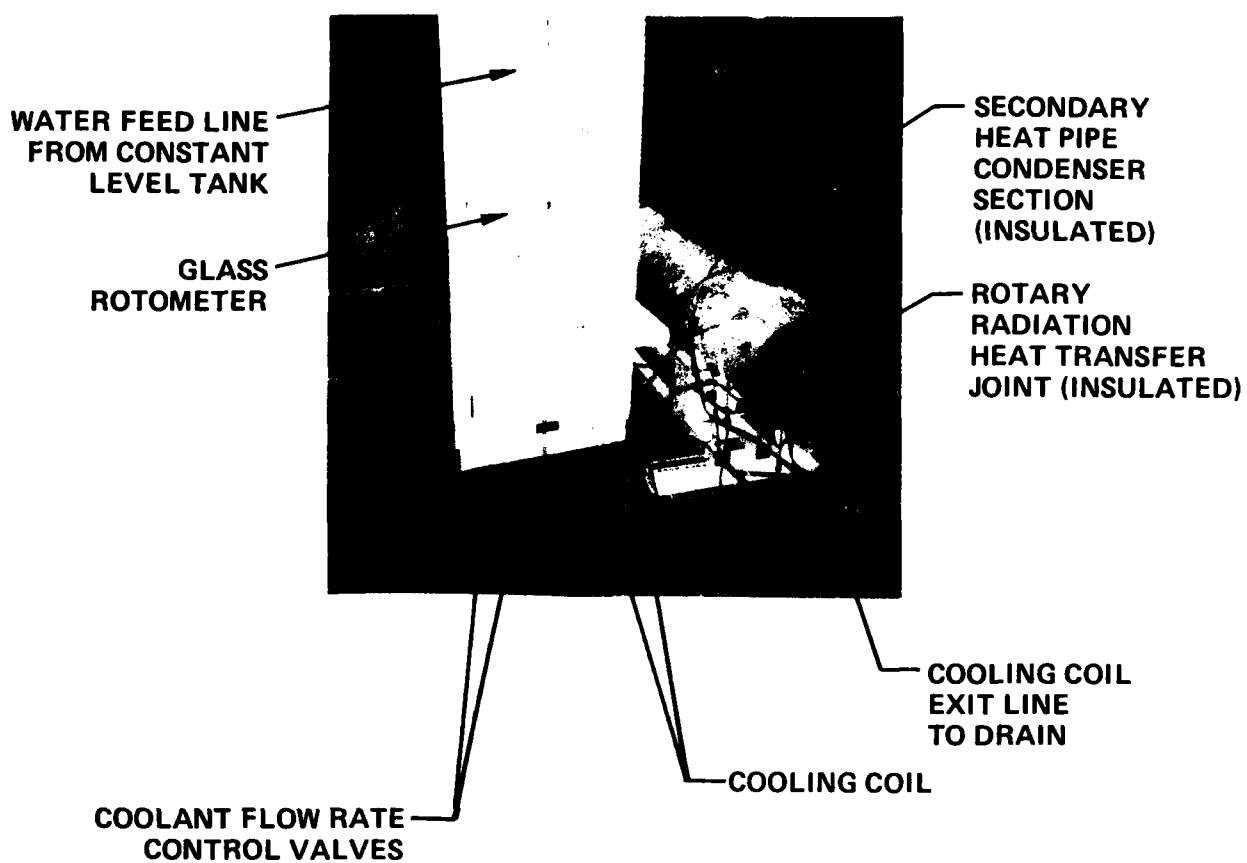
Fig. 3.6   CALORIMETER SET-UP

47
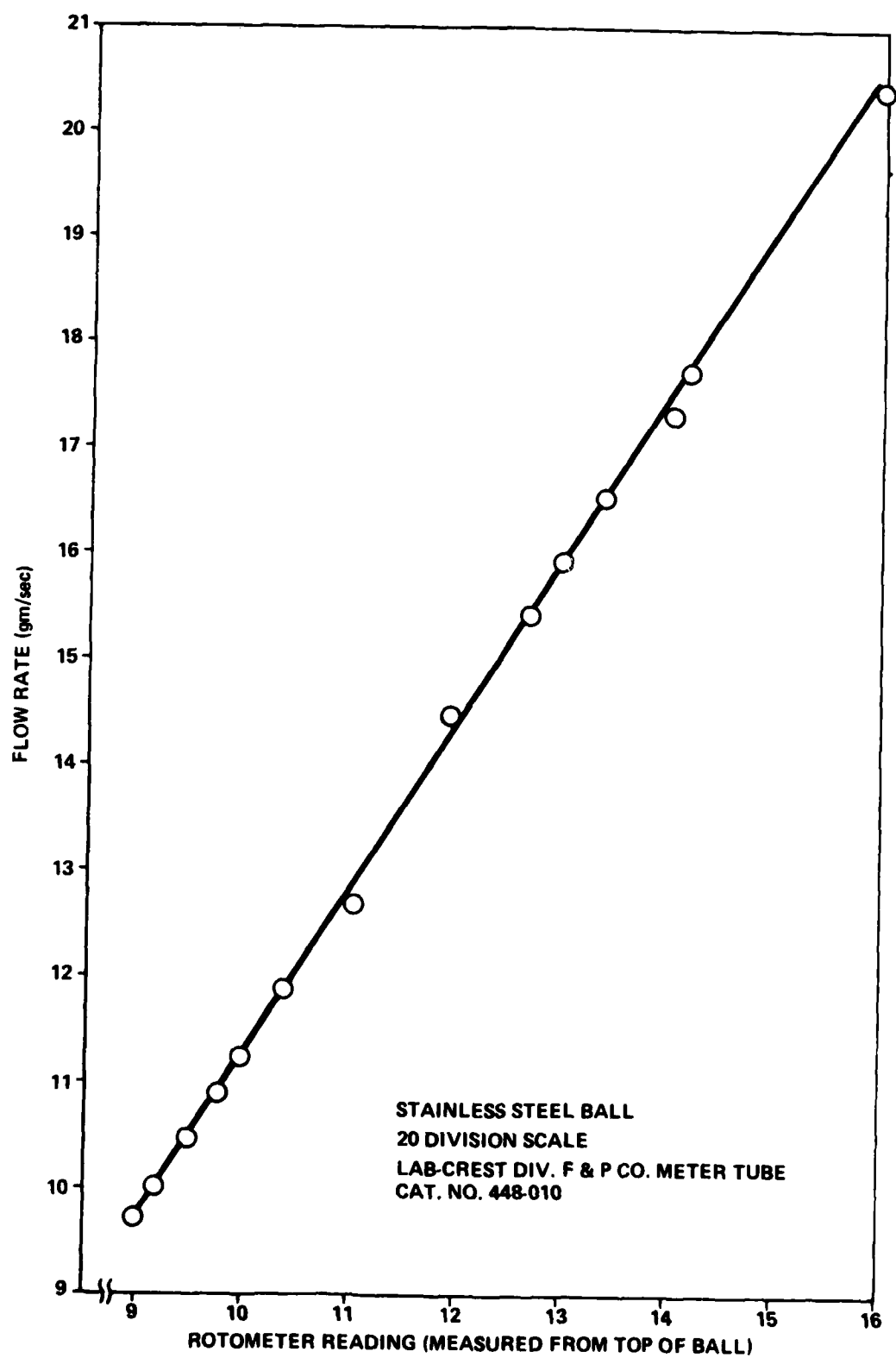
Fig. 3.7. **3/8" ROTOMETER CALIBRATION**

The figure plots FLOW RATE (gm/sec) on the vertical axis (from 9 to 21) against ROTOMETER READING (MEASURED FROM TOP OF BALL) on the horizontal axis (from 9 to 16). Annotation on the plot reads:

STAINLESS STEEL BALL
20 DIVISION SCALE
LAB-CREST DIV. F & P CO. METER TUBE
CAT. NO. 448-010

uncertainty. Because of the unavailability of a precise enough flow meter to perform this task, it was decided to use much higher coolant flows to reduce error. The uncertainty in the power extraction is given by:

$$W_{\dot{Q}} = \frac{QW_{\dot{m}}^2}{\dot{m}} + \frac{(W_{T_i}^2 + W_{T_o}^2)^{1/2}}{(T_o - T_i)^2}$$

where: $\dot{Q}$ = thermal power extracted

$\dot{m}$ = mass flow rate of cooling water

T_i = temperature of inlet cooling water

T_o = temperature of exit cooling water

$W_{\dot{Q}}$, $W_{\dot{m}}$, W_{T_o}, W_{T_i} = the uncertainties of $\dot{Q}$, $\dot{m}$, T_o, T_i, resp.

With the rotometer presently installed on the calorimeter, the mass flow rate can be determined within ± 0.2 gm/sec. At a mass flow rate of 10 gm/sec, and assuming the water temperature can be determined within $\pm 2K$ at a 72K differential, the error in the thermal power determination will be less than 5%. Figure 3.7 shows the calibration curve for the rotometer.

3.2.4 Instrumentation

The thermal power train is equipped with 30 Chromel/Alumel thermocouples located at various positions along its entire length. These thermocouples terminate in standard OST male thermocouple connectors. In order to utilize as much of the original instrumentation as possible, the thermocouple circuits are extended with the attachment of female connectors and Chromel/Alumel leads running to barrier strips on the heat pipe stand. In order to accommodate the large number of thermocouples, two manual thermocouple switches are required. An automatic switch, an Omega ice point reference chamber, two Hewlett-Packard 3440B digital voltmeters, and a Hewlett-Packard 5050A digital recorder are also necessary for the temperature instrumentation. Figs. 3.8 and 3.9 show the thermocouple layout and numbering system as it actually exists on the thermal power train.

Other instruments required include the voltmeters and ammeters that correspond to the Variacs used to control the power input to the heaters. Three 0 to 110 voltmeters and three 0 to 10 amp ammeters are required for the instrumentation of the secondary heat pipe heaters and the two heating systems on the purge volume. One 0 to 240 VAC voltmeter and one 0 to 25 amp ammeter

Fig. 3.8   THERMOCOUPLE LAYOUT AND NUMBERING

TO VACUUM PUMP
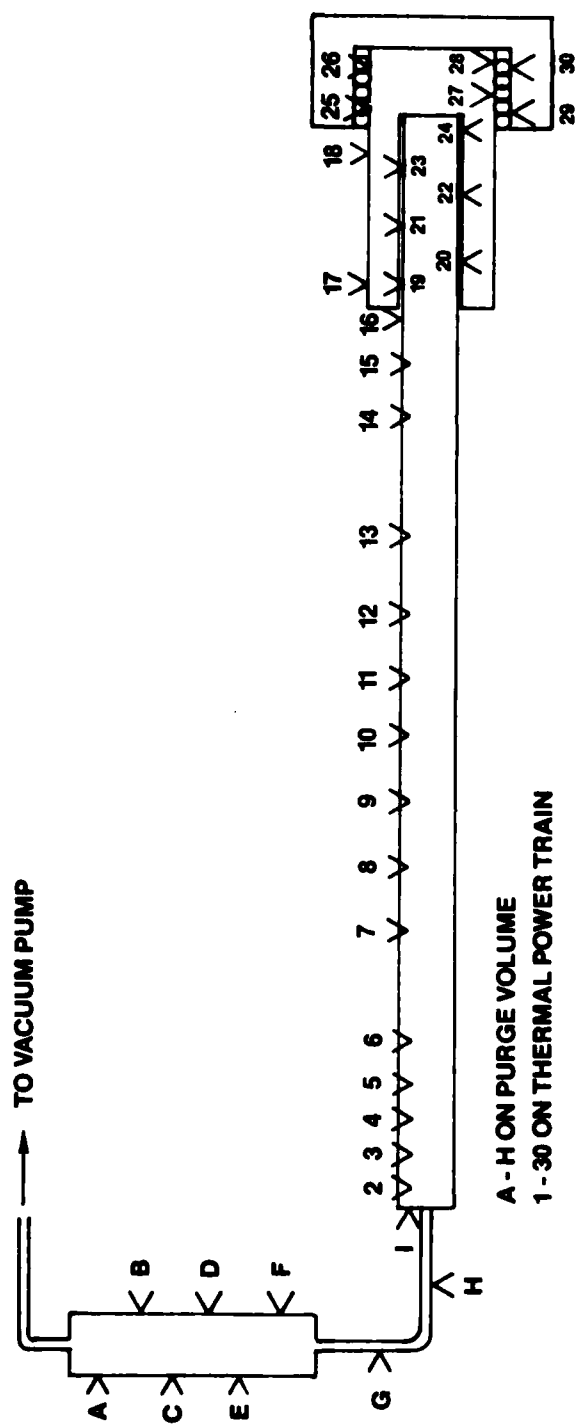
A - H ON PURGE VOLUME
1 - 30 ON THERMAL POWER TRAIN
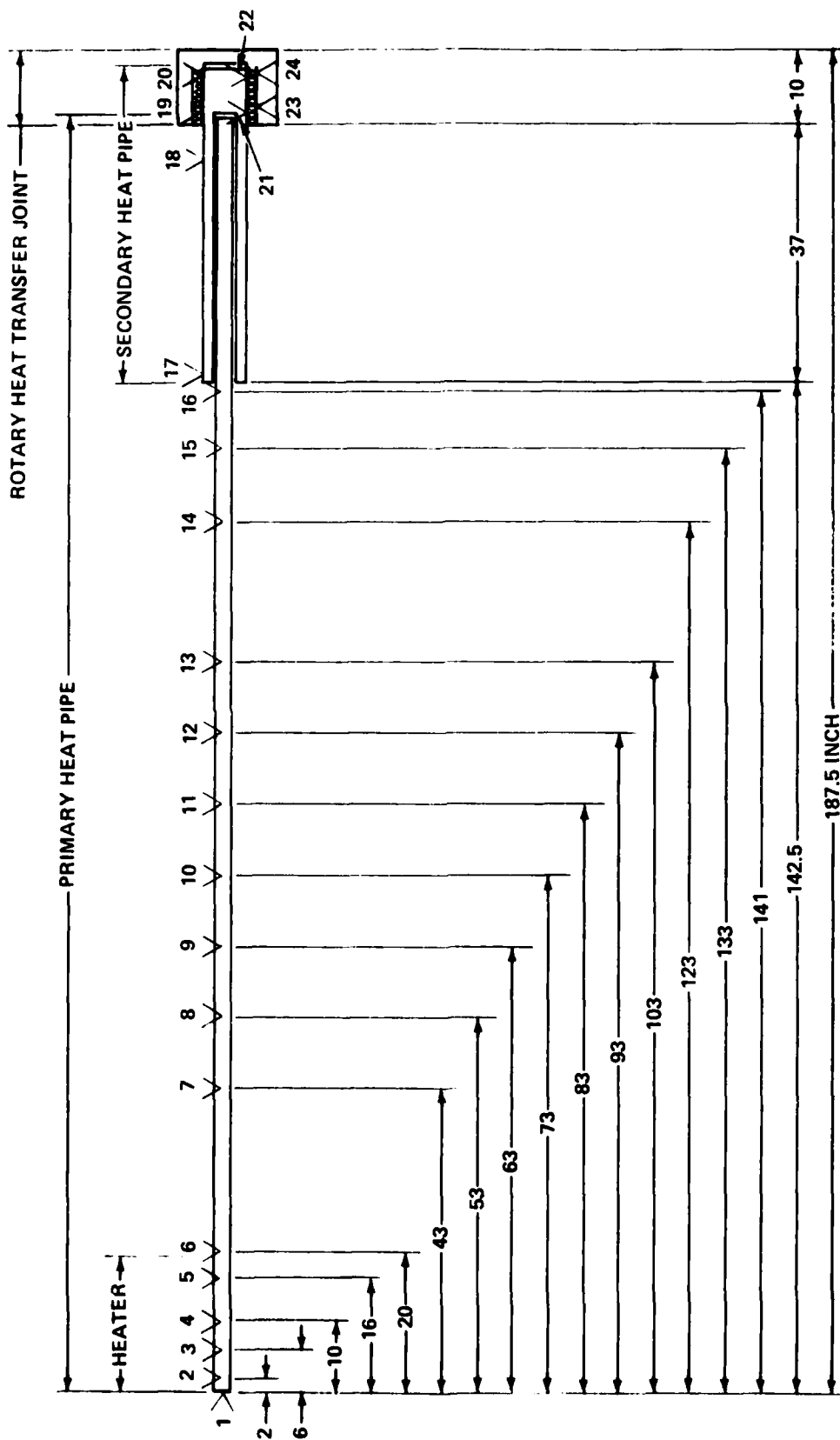
Fig. 3.9. THERMOCOUPLE LOCATIONS

51

are required to instrument the primary heater on the heat pipe. These four systems can be adjusted to obtain the desired power input conditions.

3.2.5 Purge Volume

A purge volume had to be designed in order to decontaminate the primary heat pipe. The heat pipe has not operated for six years and has been open to the atmosphere at some point in time. For proper operation, all excess gases and contaminants must be purged until the heat pipe is filled only with pure sodium. This is essential to assure proper operation of the heat pipe.

The purge volume was designed to be attached to the evaporator end of the heat pipe with the heat pipe fill tube as the attachment point. Basically, the purge volume consists of the supply line, valves, collection chamber, pressure gauge, and vacuum pump. The final design of the purge volume is shown in Fig. 3.10 with the schematic shown in Fig. 3.11. The supply line is .25 in. O.D. stainless steel tubing with a wall thicknes of .035 in. This was used to be consistent with the existing fill lines and connections. The purge chamber is 3 ft. long and is made of AS 304 stainless steel. It has a 2 in. I.D. and a 2.25 in. O.D. On each end of the chamber, .25 in. thick stainless steel flats are welded to form a closed cylinder. The welds must be made in an inert gas atmosphere to minimize the chance of outgassing from the welds. All fittings for valves, tees, and connections to the purge chamber are of the Swagelok type to allow for easy assembly and disassembly.

The purge chamber was designed to contain 3 lbs. of sodium at the highest operating temperature the chamber would reach. This provides 50% greater capacity than the original EOS designed purge chamber. The chamber was treated as a thick walled cylinder in the design analysis. The support structure for the purge volume was made of .125 in. thick steel box tubing. The purge chamber is connected to the support using two large hose clamps.

Six thermocouples placed on the outside of the purge chamber and two thermocouples placed on the .25 in. feed line sense temperature fluctuations during operation. Tape heater circuits around the feed line and the purge chamber insure proper temperature distribution during the purging process. Insulation added to the lower half of the purge volume and feed line keep the heat losses in this area to a minimum. This area will always have an elevated temperature to insure that the sodium can flow back to the heat pipe as a liquid.
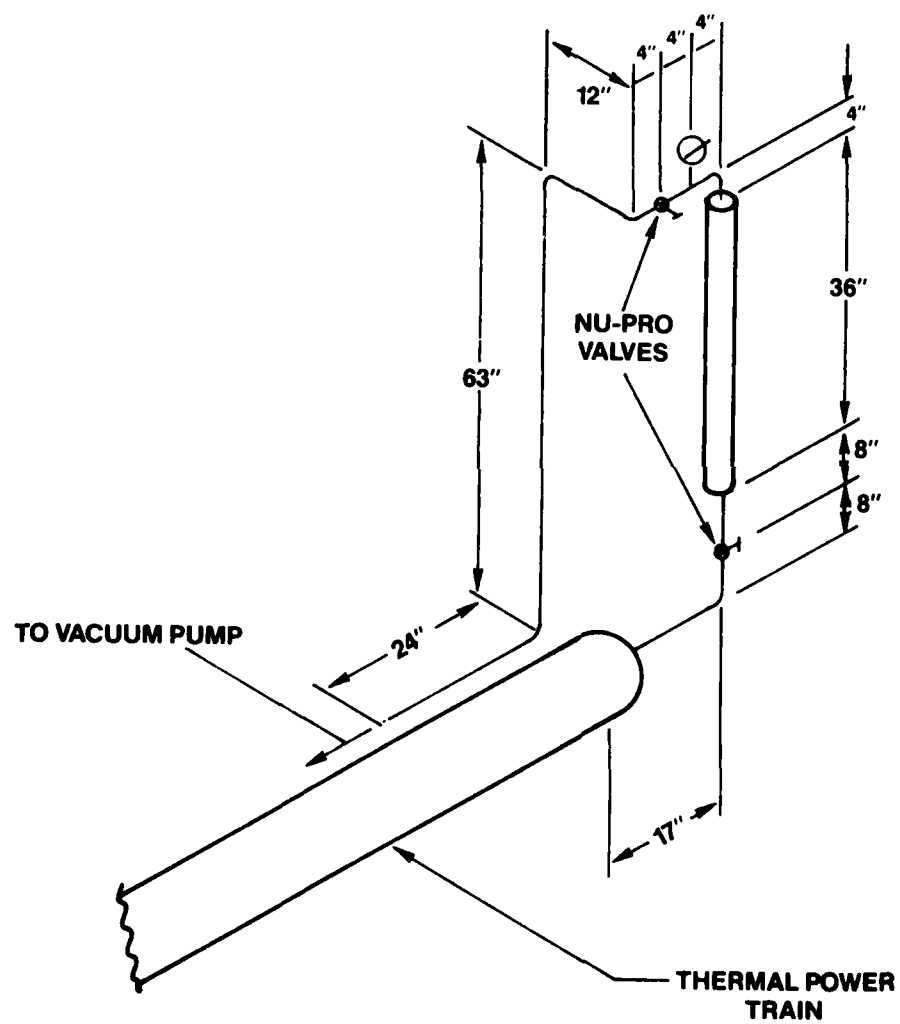
Fig. 3.10. PURGE VOLUME DESIGN
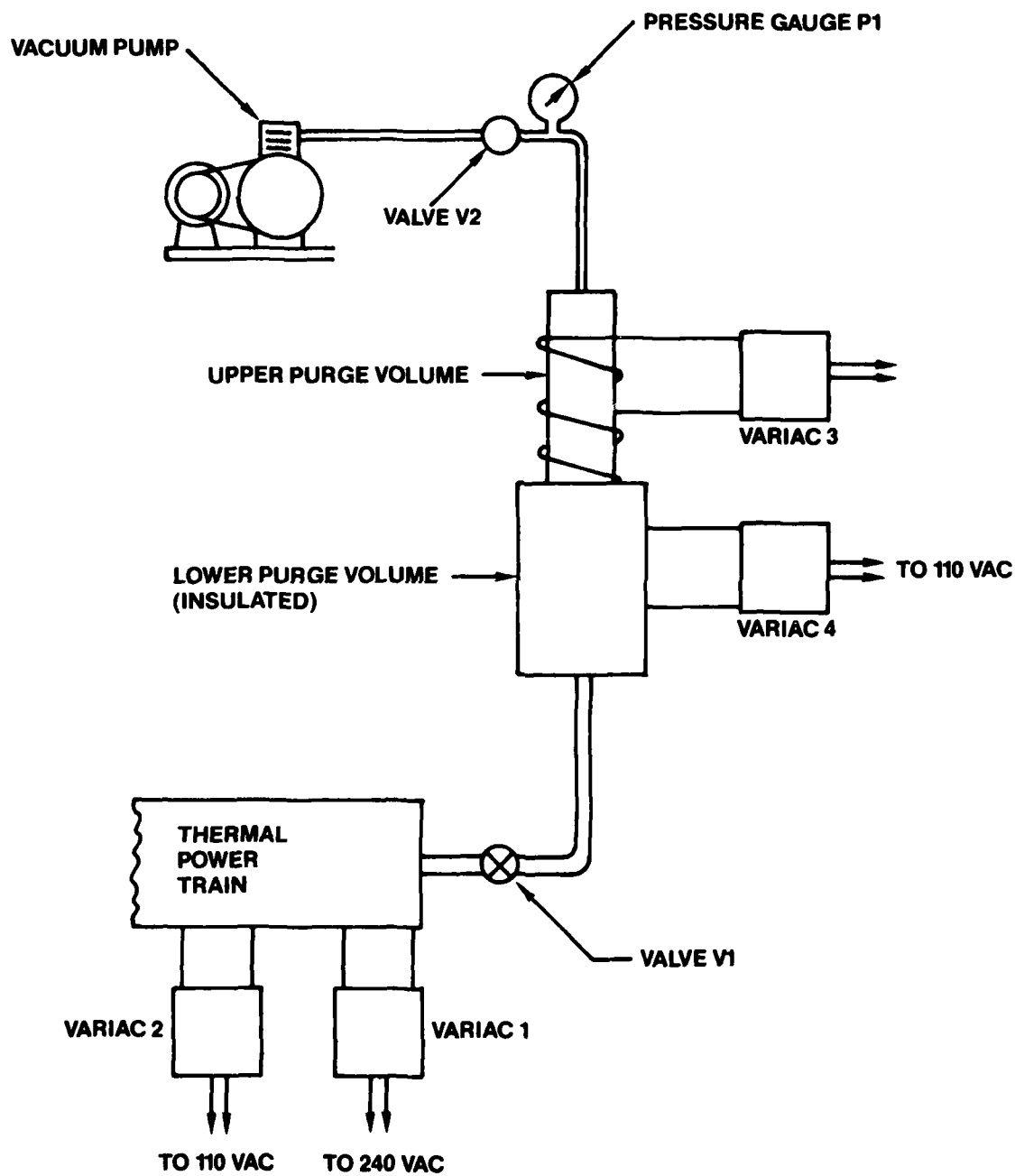
Fig. 3.11. PURGE VOLUME SCHEMATIC

54

3.2.6 Vacuum Ion Pump

The vacuum ion pump has two preliminary purposes in the test setup.

1) To evacuate the sodium gap at the primary-secondary heat pipe interface to allow for sodium expansion during operation.

2) To create the vacuum required during the contaminant purging of the primary heat pipe.

The ion pump setup for evacuating the sodium gap is shown in photo Fig. 3.12. Evacuation is accomplished by first pumping down to 10^{-3} torr with a mechanical roughing pump and then operating the vacuum ion pump. Since evacuation of the sodium gap was the first time use of the ion pump, the following procedure was used to additionally determine the integrity of the pump, fill lines, valves, and ion pump vacuum chamber:

1. Cap-off and close valve V1.
2. Fill reservoir with liquid nitrogen to prevent mechanical pump oil from entering vacuum chamber.
3. Start mechanical roughing pump and run until a 10^{-2} torr vacuum is established in vacuum chamber as read from meter 1.
4. Start Vac-ion pump and shut off mechanical pump.
5. When 10^{-8} torr vacuum is reached in the vacuum chamber (as read from meter 2), shut off ion pump.
6. Read pressure for one-half hour to detect leaks in vacuum chamber.
7. Uncap V1 (closed) to detect valve leaks.
8. Connect fill line to V1 and close V2.
9. Open V1 to detect leaks in the fill line and V2.
10. Restart ion pump, oven V2 and evacuate sodium gap.
11. When 10^{-7} torr is achieved, shut off ion pump and read pressure again from meter 2 to determine leaks in the sodium gap.
12. Close V2, disconnect fill line, and cap-off V2.

During initial attempts at this procedure, Murphy's Law predominated and step 5 was never reached. After resealing the vacuum chamber, the pressure sensor for meter 1 was replaced and after resealing the vacuum chamber, a vacuum of 10^{-7} torr still could not be achieved. This problem was probably

VALVE 1

VACUUM ION PUMP

VACUUM CHAMBER

FILL LINE

LIQUID NITROGEN RESERVOIR

VALVE 2

MECHANICAL ROUGHING PUMP

THERMAL POWER TRAIN

PRESSURE METER 2

PRESSURE SENSOR FOR METER 1

PRESSURE METER 1
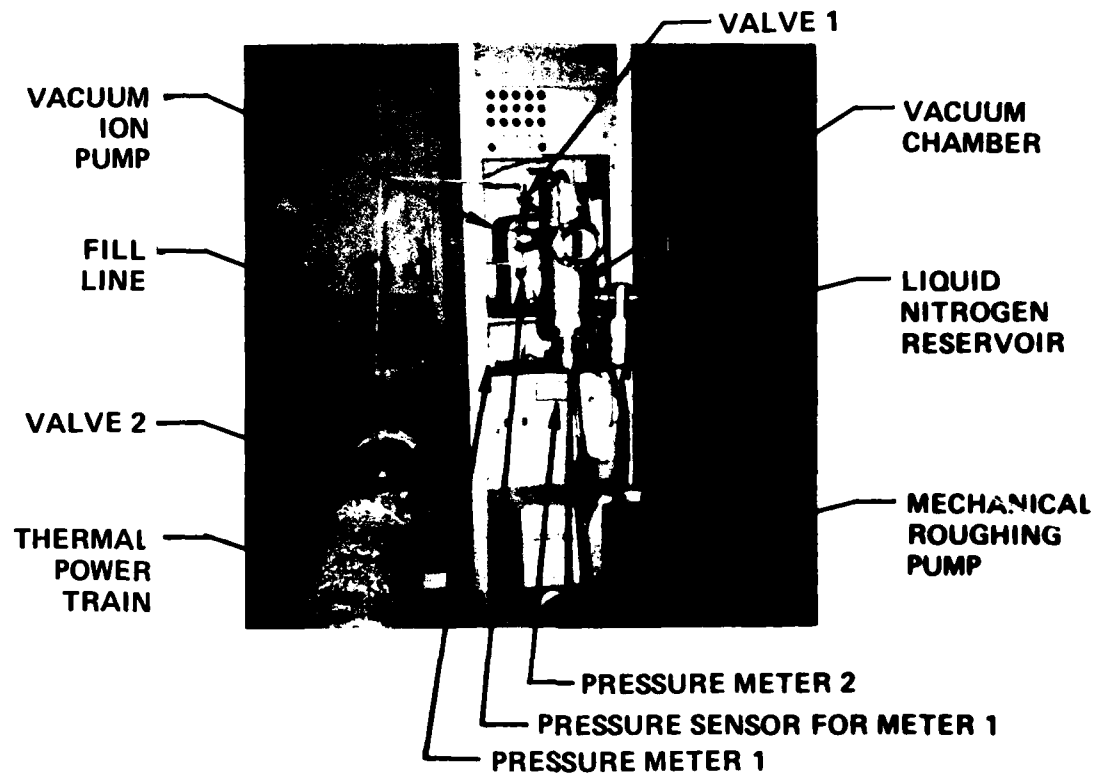
Fig. 3.12

ION PUMP SET-UP FOR SODIUM GAP EVACUATION

largely due to the construction of the ion pump-vacuum chamber connection. The vacuum chamber, which is of considerable weight, is totally supported by the front flange of the ion pump. This large moment created on the flange most probably is the cause of the vacuum chamber leakage.

3.3   Start Up

The following start-up procedure, in conjunction with the purge volume and equipment described in the design and development section, has been developed to prepare the thermal power train for use after its long period of inactivity.

The general concept of the purging process is to draw liquid sodium from the heat pipe and introduce it to the evacuated purge volume by means of a vacuum pump and two control valves. The temperatures of the upper half and lower half of the purge volume can be varied independently; thus, the lower half can be maintained at a temperature higher than the melting point of the sodium, while the upper half is held at a temperature less than the melting point. This should insure that no liquid sodium is drawn into the vacuum pump. With the sodium in a liquid state, the heat pipe is allowed to outgas for about 4 hours. The liquid sodium is then drained back into the heat pipe and the valve between the purge volume and the heat pipe is closed. The procedure is repeated 3 or 4 times.

3.3.1 Start Up Procedure

Refer to Fig. 3.11 for schematic of purge volume apparatus.

1) Close valves V1 and V2.   Turn vacuum pump power switch to ON position.

2) Heat thermal power train to a uniform overall temperature of approximately 930°F by adjusting VARIAC 1 (input power to primary heater) and VARIAC 2 (input power to adiabatic section heater).

3) Heat upper and lower purge volume sections to a temperature of approximately 590K by adjusting VARIAC 3 (input power to upper purge volume heater) and VARIAC 4 (input power to lower purge volume heater).

4) Open valve V2. Observe vacuum reading on pressure gauge P1.

5) Decrease thermal power train overall temperature to approximately 620K by adjusting VARIAC 1 and VARIAC 2.

6) Decrease upper purge volume temperature to approximately 366K by adjusting VARIAC 3. Maintain lower purge volume temperature at approximately 590K.

7) Close valve V2.

8) Open valve V1. Observe change in pressure reading on P1.

9) Open valve V2. Observe vacuum reading on P1.

10) Allow thermal power train to outgas for 4 hours. Maintain specified temperatures on thermal power train and purge volume.

11) Close valve V2.

12) Increase upper purge volume temperature to approximately 590K by adjusting VARIAC 3. Entire purge volume should now be at about 590K.

13) Decrease thermal power train overall temperature to approximately 480K by adjusting VARIAC 1 and VARIAC 2.

14) With the thermal power train stabilized at about 480K, let any liquid sodium present in lower half of the purge volume drain into the power train for 10 minutes. Close valve V1.

15) Increase thermal power train overall temperature to approximately 620K by adjusting VARIAC 1 and VARIAC 2.

16) Decrease upper purge volume temperature to approximately 366K by adjusting VARIAC 3. Maintain lower purge volume temperature at approximately 590K.

17) Repeat steps 8 through 16 three times to insure thermal power train is completely purged.

18) Make sure all valves are firmly closed. Turn vacuum pump power switch to OFF position.

3.4 Maximum Performance Estimations

Maximum heat transfer capability calculations were performed on the primary heat pipe to verify the maximum design value of 6kW at 1145K predicted by Xerox. These calculations were based on a strictly steady state analysis of several physical limitations that occur during heat pipe operation. These include (1) sonic limitations, (2) entrainment limitations and (3) capillary limitations, and are shown as a function of input temperature in Fig. 3.13.

58
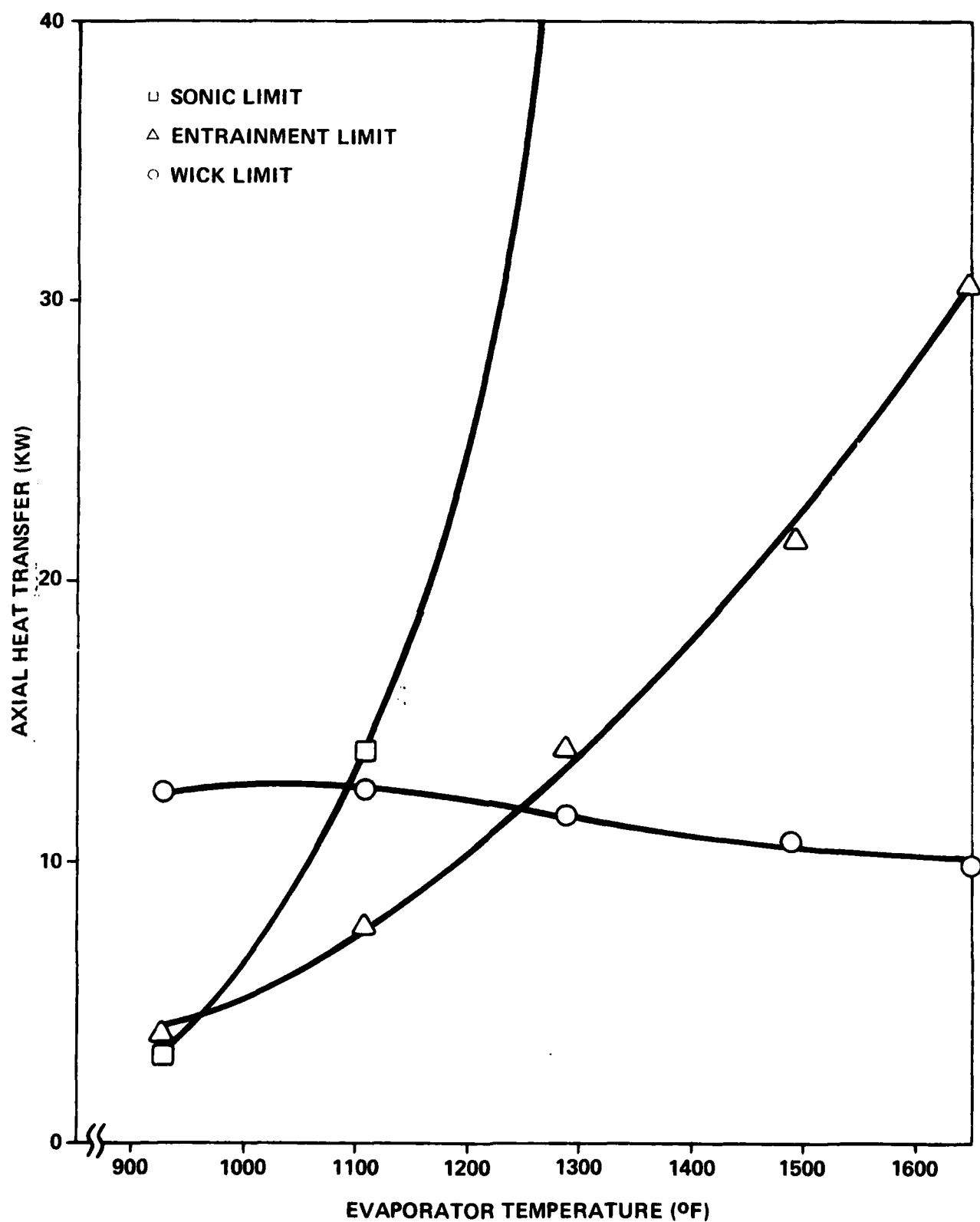
Fig. 3.13. **PRIMARY HEAT-PIPE HEAT-TRANSFER LIMITATIONS**

Sonic limitations during heat pipe operation result from variations of vapor velocity that occur because of vapor addition in the evaporator and removal of vapor in the condenser. Because of this acceleration of the vapor, the resulting back pressure in the evaporator section can cause the vapor to reach supersonic speeds, and consequently sonic choking of the vapor stream to the condenser. This condition causes decreasing condenser temperatures and reduced heat transfer.

Another condition caused by high vapor flow rates is the entrainment limitation. When this condition occurs, liquid working fluid at the wick-vapor core interface is ripped off the wick by the high speed vapor passing by, causing a reduction in liquid working fluid returning to the evaporator. This causes the evaporator to eventually become ''starved'' of liquid working fluid, and consequently wick dry-out occurs at the evaporator. During operation this condition can be detected by the sound of liquid droplets entrained in the vapor striking the evaporator.

The major heat transfer limitation of the heat pipe at elevated operating temperatures is the capillary limitation. Liquid working fluid transport in the wick is caused by capillary pressure which is attributed to the wick structure and working fluid surface tension characteristics. The capillary pressure, which is greatest at the condenser end and lowest at the evaporator end, must be great enough to overcome frictional pressure drops incurred by fluid flowing in the wick and vapor flowing in the vapor core. Xerox reports on the primary heat pipe design indicating the failure of a previous primary heat pipe was the result of a wick structure with high fluid flow resistance [3.1]. This was caused by the lateral over-compression of a diametral wick structure, which resulted in reduced permeability. Because the equations used to calculate the capillary limitation curve do not take wick compression into account, it is recommended that further investigation be made in this area. Changes in heat transfer capillary limitations shown in Fig. 3.13 are basically the result of variances in the working fluid's viscosity, density, and surface tension with varying temperature. The effects of vapor flow frictional drops are very small in comparison to fluid flow pressure drops, and were neglected.

Overall, it can be seen from the curves in Fig. 3.13 that the capillary limitation is dominant at the higher temperatures. At 1170K, the maximum heat

transfer capability of the primary heat pipe is 9.96kW, well above the maxim
design value of 6kW.

The equations, assumptions and dimensions used in calculating the
limitation curves are included in the following sub-sections.

3.4.1 Primary Heat Pipe Dimensions [3.1]

Pipe:

Material: Inconel 617

d_o = outside diameter = 2.25 in.

d_1 = inside diameter = 2.1875 in.

L = length = 180 in.

L_a = adiabatic section length = 122.5 in.

L_c = condenser section length = 20 in.

L_e = evaporator section length = 37.5 in.

Wick:

M = mesh number = 50 in.$^{-1}$

d = wire diameter = 0.0055 in.

A_D = diametral wick cross sectional area = 15.277 cm^2

A_{ww} = wall wick (circumferential) cross sectional area = 0.902 cm^2

A_v = vapor core area = 8.068cm^2

3.4.2 Performance Limitation Calculations [3.3]

Sonic Limitation:

$$Q_{Smax} = A_v \rho_v \lambda \left(\frac{\gamma v R_v T_v}{2(a_v+1)} \right)^{1/2}$$

Where: Q_{Smax} = maximum axial heat transfer limited by sonic choking

A_v = vapor core cross-sectional area (m^2)

T_v = vapor temperature at upstream end of the evaporator (K)

λ = latent heat of vaporization (J/Kg)

ρ_v = vapor density at T_e (Kg/m^3)

R_v = R/M = 361 J/Kg-K for sodium

$$\gamma_v = \text{specific heat ratio} = 5/3 \text{ for monotomic sodium}$$

Assumptions:

1) properties of vapor follow the ideal gas law

2) inertial effect dominates

3) frictional effects may be neglected

4) $T_o \approx$ temperature on outside wall of evaporator

3.4.3 Entrainment Limitations:

$$Q_{emax} = A_v \lambda \left[\frac{\sigma \rho_v}{2 r_h} \right]^{1/2}$$

Where: Q_{emax} = maximum axial heat transfer limited by entrainment (W)

λ = latent heat of vaporization (J/kg)

σ = surface tension (N/m)

ρ_v = vapor density (kg/m³)

r_h = surface pore hydraulic radius

$\quad$ = $1/2$ wire spacing in wick = $1/2(1/M-d)$

$\quad$ = 1.8415×10^{-4} m

3.4.4 Capillary Limitations:

$$Q_{Cmax} = \frac{(2\sigma/r_c - \rho_L g d_i) K A_w \rho_L \lambda}{\mu_L \left[\frac{L_e}{2} + L_a + \frac{L_c}{2} \right]}$$

Where: Q_{Cmax} = maximum axial heat transfer limited by capillary pressure (W)

σ = surface tension (N/m)

ρ_L = liquid density (kg/m³)

μ_L = liquid viscosity (kg/m·sec)

λ = latent heat of vaporization (J/kg)

L_e = evaporator length (m)

L_a = adiabatic length (m)

L_c = condenser length (m)

d_i = inside heat pipe diameter (m)

A_w = total wick cross-sectional area = 1.618×10^{-3} (m)

r_c = capillary radius = $1/2(1/m-d)$ = 1.8415×10^{-4} m

62

$$K = \text{wick permeability} = d^2\varepsilon^3/122(1-\varepsilon)^2 = 1.65 \times 10^{-9} \ (\text{m}^3)$$

$$\varepsilon = \text{wick porosity} = 1 - (\pi M d/4) = 0.7840$$

3.4.5 Results

Assumptions:

1) heat pipe is in a horizontal position

2) vapor flow frictional losses are negligible

T_{evap} °C	T_{evap} °F	Q_{Cmax}(kW)	Q_{Smax}(kW)	Q_{emax}(kW)
500	932	12.47	3.12	3.91
600	1112	12.49	13.96	7.67
700	1292	11.76	54.66	14.03
800	1492	10.75	149.59	21.48
900	1652	9.96	351.42	30.61

3.5 Conclusions and Recommendations

The scope and amount of work required to restore the thermal power train to experimental usefulness far exceeded original expectations. A visit by Robert Richter from JPL revealed that the condition of the power train was much worse than when he had left it. The valves located on the sodium fill lines, for instance, had been removed thus contaminating the heat pipe. The permanent stand used for the power train was also missing. Designing a stand and purge volume, and developing a startup procedure thus became small projects in themselves.

Several projects that need to be completed before a test can be run include:

1) Completion of the purge volume and its instrumentation (near completion)

2) Programming of the data acquisition system for thermocouple monitoring

3) Purging of the primary heat pipe sodium fill (ready to be performed)

Prior to further operation of the vacuum ion pump, it is recommended that a support stand for the vacuum chamber on the ion pump be designed and constructed.

In evaluation of the primary heat pipe performance, it seems apparent that a better correlation between diametral wick compression and permeability is needed for reliable capillary limitation estimates on maximum heat pipe heat transfer capability. An experiment to determine such a correlation would make an important project for heat pipes with diametral wicks.

3.6 References

[3.1]   Richter, R., _Solar Collector Thermal Power System_, AFAPL-TR-74-89, Vol. II, Vol. III, Air Force Aero Propulsion Laboratory, Nov. 1974.

[3.2]   Richter, op. cit., Table IV.

[3.3]   S.W. Chi, _Heat Pipe Theory and Practice_, (McGraw-Hill, 1976).

IV.   HAC SODIUM-INCONEL 617 HEAT PIPE TESTS

4.1   Introduction

Hughes Aircraft Co. (HAC) fabricated twenty Sodium-Inconel 617 heat pipes for WPAFB. The heat pipes were manufactured for the purpose of life testing in accordance with a predetermined test matrix so that the compatibility of Inconel 617 with sodium can be determined. The Manufacturing methods and processing is documented in the Appendix. The eventual life test results will be correlated to these processes where possible.

Heat pipe tests will be carried out at WPAFB, AFWAL, POOC Thermal Laboratory and at Arizona State University, Mechanical Engineering Thermoscience Laboratory.

4.2   HAC Report Summary on Fabrication

The complete Hughes Aircraft report is presented as the Appendix. The following subsections paraphrase and comment on some aspects of the report.

4.2.1 Heat Pipe Parameters

Important heat pipe and wick parameters are as follows:

Heat Pipe Length	18 in.
Heat Pipe I.D.	0.500 in.
Heat Pipe O.D.	0.404 in.
Heat Pipe Body	Seamless Inconel 617 tube
Heat Pipe End Caps	Cut from 0.50 in. rod
Wick	100 mesh Inconel 617 screen
Wire Diameter (d)	0.0045 in.
Wick Permeability (Measured)(K)	$4.2 \times 10^{-10} M^2$
Wick Capillary Radius (r_c)	$1 \times 10^{-4} M$
Wick Porosity (ε)	0.702 - 0.724

The relationship for permeability for HAC calculations was:

$$K = \frac{d^2}{122} \cdot \frac{\varepsilon^3}{(1-\varepsilon)^2}$$

r_c was measured microscopically (rather than by wick rise tests) and ε was determined experimentally.

4.2.2 Pre-Assembly Cleaning Procedures

The tubing, or envelope, was cleaned in the following manner:

1) Toluene scrub and rinse
2) Acetone rinse
3) Ultrasonic acetone clean (5 min.)
4) Freon vapor degrease (5 min.)
5) Air dry
6) Dry hydrogen fire at 1273K for 10 min.

Step six resulted in oxidation of the tubes. The oxides were removed by honing with 240 grit silicon carbide and the cleaning procedure was repeated.

The wick and end caps received treatments 3 and 4 but were not hydrogen fired to avoid the oxidation problem encountered with the tube.

4.2.3 Vacuum Firing and Welding

Vacuum firing was done by resistance heating of the envelope. Tantalum foil lead straps were also supports for the tubes. Reportedly no cold zones were left at the interface ends, although the temperature at the ends was not measured.

During vacuum firing at approximately 3×10^{-7} torr, heavy deposits were produced in the vacuum chamber walls when temperatures were at 1273K or above. It is guessed in the report that aluminum was the most likely material evaporated. The residue was not evaluated. It is very possible that corrosion resistance could be adversely affected by depletion of certain elements and alteration of the surface stoichiometry. The heating times above 1273K varied over the range from 0 to 56 minutes. Accompanying pressures were normally in the 10^{-5} torr range.

4.2.4 Vacuum Firing Sodium Charging

Prior to sodium loading, each heat pipe envelope was vacuum fired. Deposits were again produced. Heat pipes 001 through 004 were loaded with fired titanium sponge (Alpha Lot 120478). These envelopes were fired above 1370K to break down any titanium oxides. Heavy evaporative deposits were again produced.

After firing all heat pipes are argon filled, mechanically capped and transferred to a glove box for sodium loading. It is not clear if any oxygen contamination occurs during this transfer. The sodium is transferred from a glass ampoule to the heat pipes by a syringe. Once again argon cover gas and a mechanical cap close the heat pipe while it is transferred to the processing vacuum chamber. The purity of the sodium is designated Alpha t 3N5, and the

oxygen and carbon content are not given in the material certification. It is expected that the oxygen content of the sodium alone is on the order of 30 to 50 ppm.

4.2.5 Processing and Closure

Processing was done in vacuum by resistance heating the bottom half of the heat pipe until uniform temperature is obtained (through heat pipe action). Then, the process pin was fusion welded into the fill part of the process end cap.

Heat pipe 001 was fabricated with a valve and the loading and processing procedures were somewhat different. The 001 valve end cap was machined from Inconel 617 bar stock such that the cap and 1.5 in. long tube were a continuous piece of metal. The tube end was then heliarc welded to the stainless steel valve tube. Final closure for the other pipes was a pinch-off and weld with argon in the tube above the valve and vacuum on the heat pipe side.

4.2.6 Testing

A preliminary performance test was made to assure the operation of each heat pipe. Power input was approximately 1000 watts producing surface temperatures of 1200K.

4.3 ASU Analysis Applied to HAC Heat Pipes

4.3.1 Heat Transfer

Heat can be transmitted into and out of the heat pipe by conduction from a heat source/sink, by convection and by thermal radiation. The test setup in question transmits heat by thermal radiation for both the evaporator and condenser sections. To better understand the heat transfer that takes place, an evaluation at the evaporator region of the heat pipe will be made. First, for low values of heat flux, the heat will be transported to the liquid surface partly by conduction through the wick and liquid and partly by natural convection [4.1].

For high values of heat flux, the liquid will become superheated and bubbles will form on the surface of the pipe. The formation of bubbles creates very high heat transfer rates with small temperature changes. Also the heat is transported as latent heat and convective heat transfer from

67

bubble nucleate sites. It is important to note that if bubble populations become too high, a continuous vapor film forms and the condition is known as burnout [4.2]. Burnout is when the wick structure of the heat pipe dries out and the heat pipe will no longer function.

The heat transfer in the condenser is slightly less complicated. The vapor will condense on the liquid surface in the condenser and through surface evaporation a small temperature drop and thermal resistance will occur [4.3]. The total temperature drop in the condenser is calculated by summing up the equivalent thermal resistances and applying the appropriate relations.

4.3.2 Capillary Limit

In order for the heat pipe to operate, the capillary pumping heat must be greater than the total pressure drop in the pipe. The total pressure drop (ΔP_c) is made up of three different pressure drops which are [4.4]:

1) The pressure drop ΔP_L (in liquid phase) required to return the liquid from the condenser to the evaporator.

2) The pressure drop ΔP_v (in vapor phase) necessary to cause the vapor to flow from the evaporator to the condenser.

3) The gravitational head ΔP_g which can be zero, positive or negative.

$$\Delta P_c \geq \Delta P_v + \Delta P_L + \Delta P_g$$

If the above condition is not met, the wick structure will dry out and the heat pipe will not operate. Therefore, it is important to choose the right materials which make up the heat pipe to create a larger capillary head than total pressure drop across the heat pipe. The parameters which play the most important role in the operation are the properties of the working fluid. They are the density, surface tension, enthalpy of vaporization or latent heat and the viscosity of the liquid working fluid. It is important to note that in the calculations and the results that follow in a later section, the vapor pressure drop ΔP_v is neglected. The ΔP_v is neglected because it becomes negligible in the evaporator and condenser sections by radial flow due to evaporation and condensation.

4.3.3 Sonic Limit

When the sodium heat pipe is first put into operation, the vapor velocity

can easily reach sonic values. This is caused by a change in mass flow rate of the vapor from the evaporator to the condenser. In this case, we must take into account compressibility effects and the limiting of the maximum heat transport capability of the heat pipe. The heat pipe can be modeled as a diverging-converging nozzle. When the vapor velocity becomes sonic, choked flow conditions exist at the exit of the evaporator. It is significant to point out that when the condenser temperature drops and sonic velocities are reached, the mass flow rate does not increase for a decrease in condenser temperature.

4.3.4 Entrainment

Another important parameter in design of heat pipes is the limit of maximum heat transport due to entrainment. At the interface between the wick surface and the vapor, the latter will exert a shear force on the liquid in the wick [4.5]. The magnitude of the shear force will depend on the vapor properties and the velocity of the flow. This action will entrain droplets of liquid and transport them to the condenser end. Entrainment limits the performance of the heat pipe to such an extent that it no longer effectively transp rts heat.

4.3.5 Viscous Limit

The last limitation to heat transport is the effect of viscosity. At low temperatures of operation, viscous forces become predominant over the vapor flow in the heat pipe. The axial heat flux rapidly increases as the pressure in the condenser is reduced and the maximum heat flux occurs when the pressure is reduced to zero.

4.4 Test Apparatus and Instrumentation

The test apparatus for the proposed work was donated by the NASA-Lewis Research Facility. The test equipment shown in Fig. 4.1 consisted of an ion pump with a capability of 10^{-9} torr, a water cooled vacuum chamber, a PS1000 control unit for chamber pressure and a Variac transformer with a power input range from 208V/34.6 amps to 13V/540 amps. A major portion of the work was directed to getting the equipment in one instrument rack and all electrical connections and accessories attached. Because of the nature of the equipment,

69
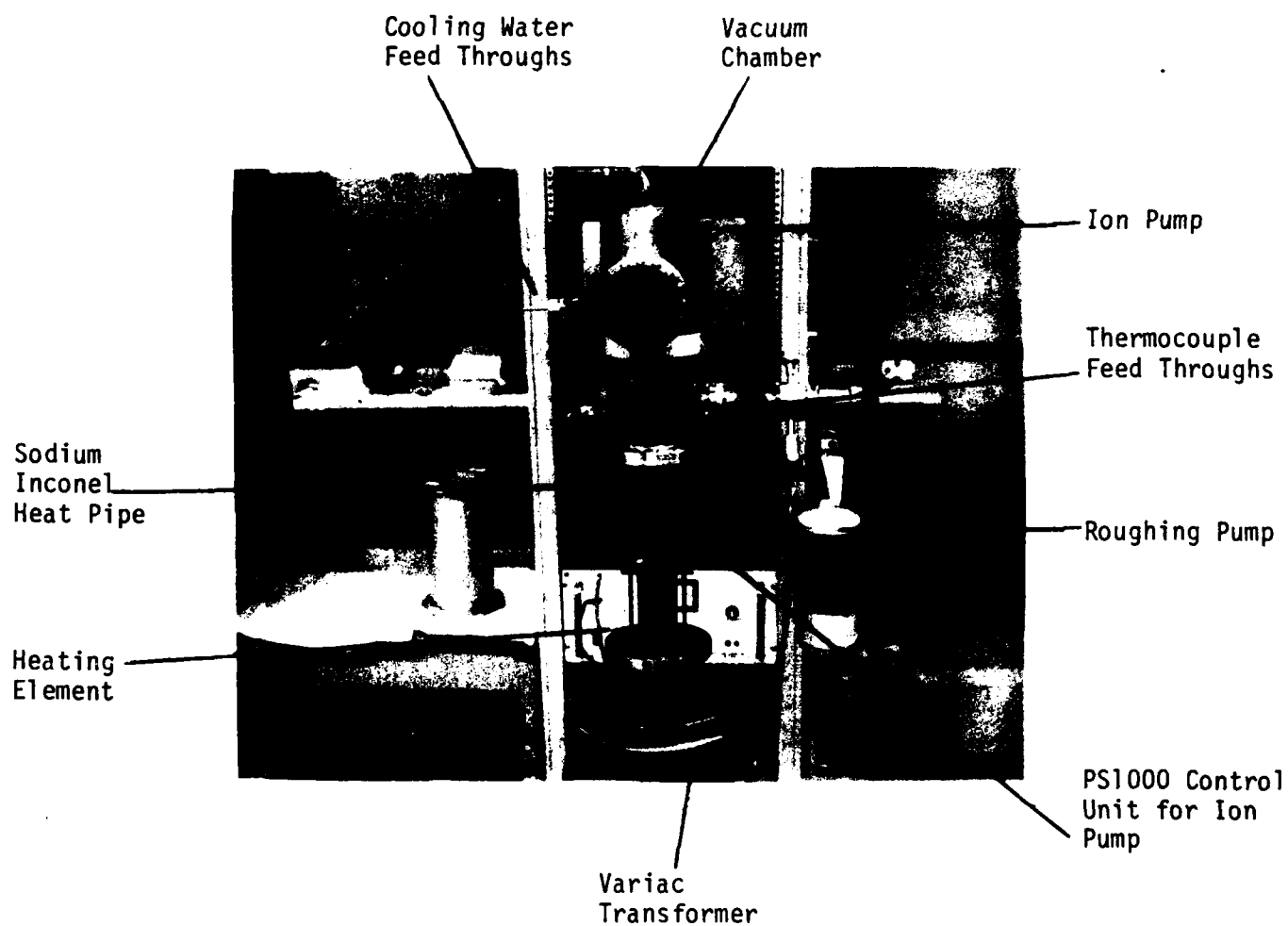
Fig. 4.1 Laboratory Test Setup

70

there was no electrical schematic for the test rack, therefore considerable time was spent trying to understand the electrical schematics and general operation. The power requirements for the experiment is approximately 12KV for start up. The Thermosciences Lab did not have the capability to operate at these high power levels. A 400 amp bus bar was installed in the Lab which became operational in April. One of the objectives of the work was to lay out the temperature measurement and the roughing pump attachments. The power and instrumentation schematic is shown in Fig. 4.2. In this schematic, the power inputs are shown with special attention to the roughing pump. The roughing pump is a device which is attached to the vacuum chamber and is used in the initial vacuum process. The roughing pump evacuates the air in the chamber to approximately 10^{-3} torr where the ion pump becomes effective enough to begin pumping down to the operational vacuum of 10^{-9} torr. For this experiment, special attention was given to the temperature measurement set up.

As seen in Fig. 4.2, thermocouples are fed through the connectors adjacent to the roughing pump connection. It was determined that ten type K Chromel/Alumel thermocouples would be spaced down the length of the 18 in. heat pipe as shown in Fig. 4.3. Because of the high operating temperatures (1300K), the thermocouples have to be shielded by ceramic tubing. Therefore, from the inlet to the vacuum chamber and to the locations around the heat pipe, the thermocouples are insulated. A 20 channel input with a paper print-out in millivolts records the thermal data. The temperatures are then found from type K thermocouple tables. A recorder reserved from the development shop was to be picked up on May 1 for installation. However, for some reason it was lent out to someone else. Therefore, at the time of this report the test setup was without a temperature recorder although the problem is being adressed. One last item to be discussed in the test setup itself is the Variac transformer. The purpose of the transformer is to input power to the tantalum heating element in the vacuum chamber. With the Variac, it is possible to input varying amounts of power to study the performance of the heat pipe.

The test setup was originally designed for 12-in long heat pipes; therefore, the vacuum chamber had to be extended to accommodate the 18-in. long HAC heat pipes. To do this an extension flange was ordered to lengthen the chamber so as to accommodate up to 26-in. long heat pipe. The extension flange is still on order.
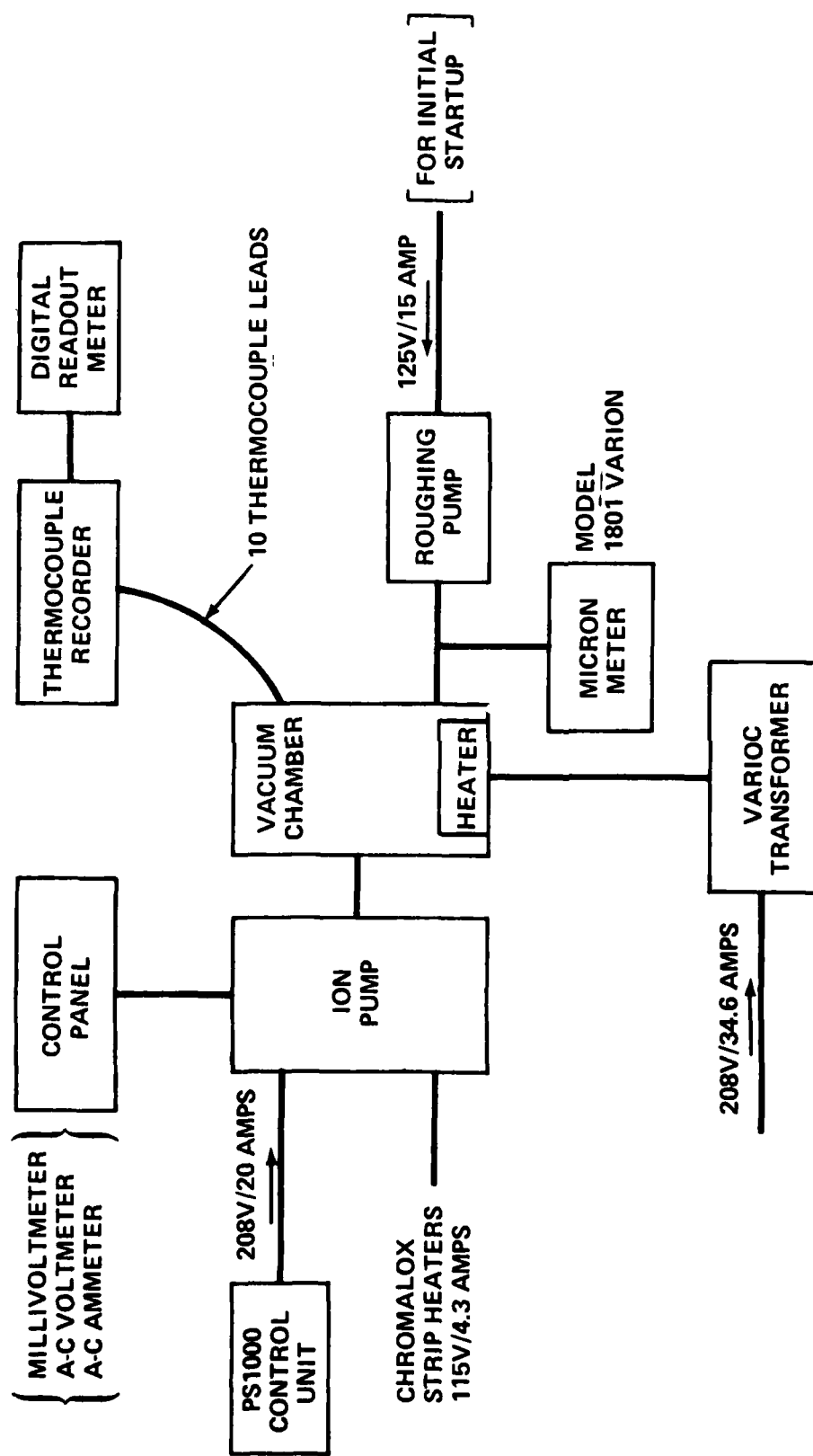
POWER AND INSTRUMENTATION SCHEMATIC

FIGURE 4.2

72

EVAPORATOR   ADIABATIC SECTION   CONDENSER
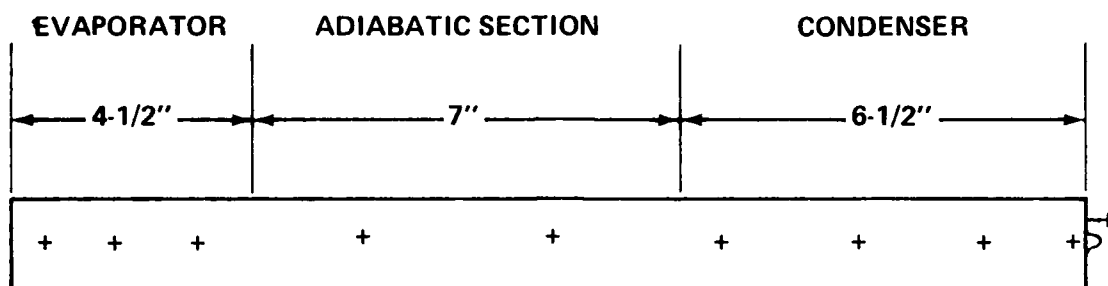
NOTES:

1. DRAWING NOT TO SCALE

2. + - ARE LOCATION THERMOCOUPLES
   WHICH ARE APPROXIMATE

FIG. 4.3 **LOCATION OF THERMOCOUPLES**

4.5   Calorimeter Design

A calorimeter is being designed to fit inside the vacuum chamber and cool the condenser section. The heat transfer chosen was radiation, although an argon convection system is being considered in order to vary the rejection load at the condenser.

The calorimeter design proposed to be built is shown in Figure 4.4. The calorimeter consists of a coiled 14 in. copper tubing, 7-1/2 in. long. Note that the condenser section of the heat pipe was fixed at 6-1/2 in. At the top of the calorimeter, a flat copper plate, 1/4 in. thick, and 3 in. in diameter, is screwed to the cooling coils. Also below that a 1/2 in. diameter solid copper rod is welded for the support of the tantalum shielding as shown in Fig. 4.5. The removable copper plate on the coils will make it easier to add tantalum shielding to insure no heat loss from the end of the condenser. The heat pipe will be tested at different orientations, and it thus had to be pinned at the top of the condenser with a ceramic threaded rod. The support for the calorimeter comes from the feed-through connection at the top of the calorimeter. The weight of the entire calorimeter can be supported by the inlet and outlet tubing. A complete list of the materials needed for the construction of the calorimeter is as follows:

1. 14 ft. of 1/4-in. copper tubing

2. Ceramic rod 1-3/4 in. long, 1/2 in. diameter

3. 8-1/2 in. of 3/8 in. diameter solid copper rod

4. 3-Tantalum shields 2-5/8 in. diameter

5. 2-3/4 in. long steel threaded screws (27/in.)

4.5.1 Calorimeter Cooling Water Calculations

To insure proper operation of the calorimetr, a small experiment was conducted to find the flow rate of water from the constant head water tank. A graduated cylinder was placed at the same height above the floor as are the feed-throughs for the calorimeter. After several trials, a value of 20.3gm/s was established as the actual water flow rate.

FIG. 4.4   CALORIMETER DESIGN

75

TOP VIEW

1-1/2"

FRONT VIEW

1/2"

CERAMIC THREADED FIXTURE
18 THREADS/IN

1/8"

1-3/4"

3/4"

SCREW
27 THREADS/IN

3/8"

1/4"

1/8"

3/16"

COOLING WATER COILS

SOLID COPPER TUBING 3/8"
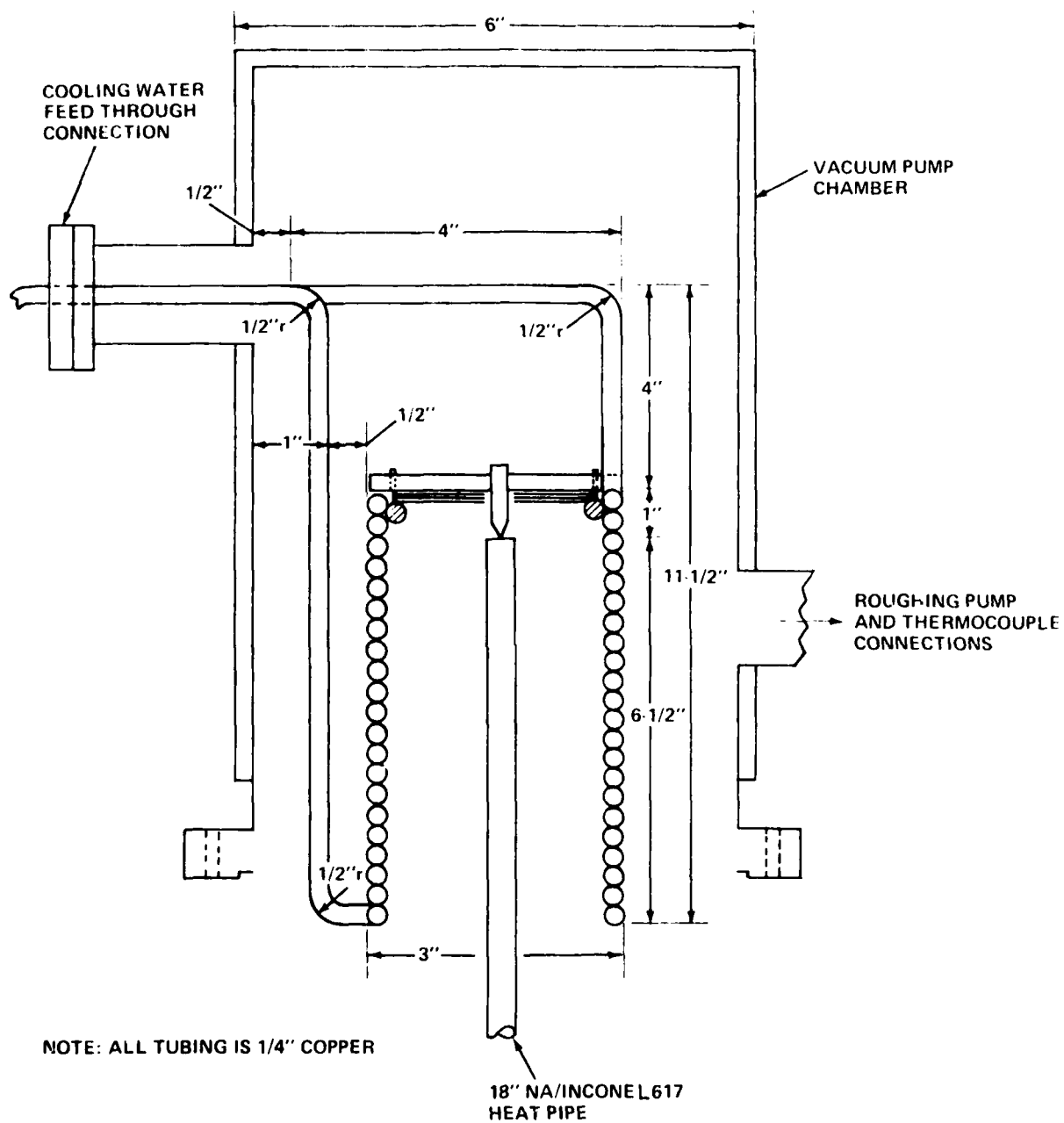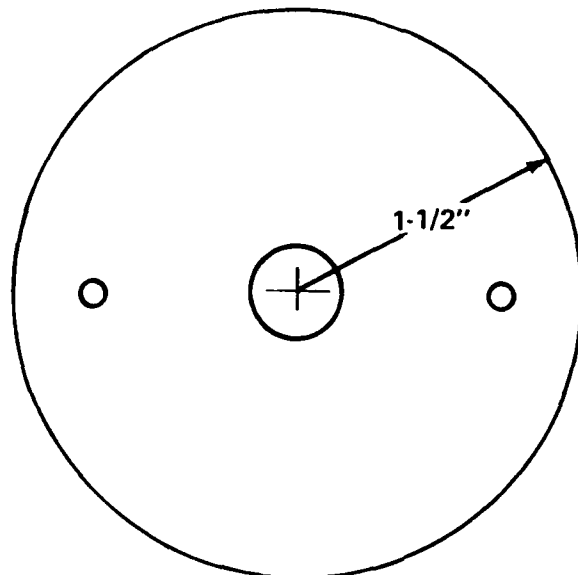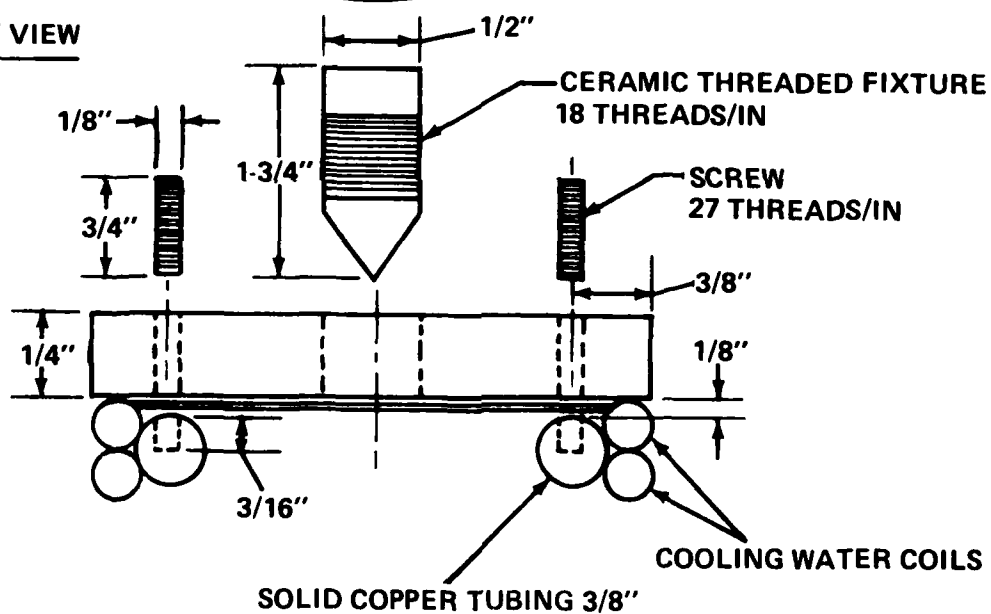
FIG. 4.5 DETAILS OF CALORIMETER

4.5.1.1 Mass Flow Rate Required for Maximum Heat Transport

$$Q_{max} = 2000W$$

If $\Delta T_{water} = 90-25^{\circ}C$

$$= 65^{\circ}C \text{ or } 65K$$

Then,

$$\dot{m}Cp\Delta T = 2000W$$

$$\dot{m} = \frac{2000W}{1cal/gmK(65)K}$$

$$\dot{m} = 7.33gm/s$$

4.5,1.2 Friction Loss

The model of the calorimeter will be a straight tube as shown:

Tube: ID = 0.375 in. or 9.53×10^{-3} m

OD = 0.540 in.

4.27m
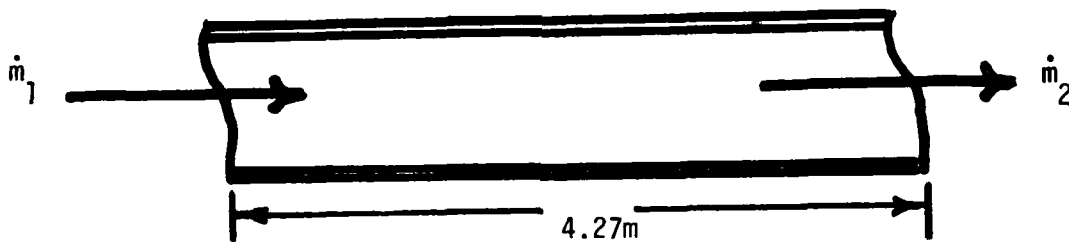
Now: $\dot{m} = \rho VA$

Solving for V

$$V = \frac{20.3}{\rho A} = \frac{20.3 \times 10^{-3}}{\frac{100kg}{m^3}(7.126 \times 10^{-5}m^2)}$$

where: $A = \frac{\pi D^2}{4}$

$A = 7.126 \times 10^{-5} m^2$

$$V = 0.285 \text{ M/S}$$

4.5.1.3 Reynolds Number

$$Re = \frac{Vd}{\mu} = \frac{(0.285M/S)(9.53 \times 10^{-3}m)}{1.006 \times 10^{-6}m^2/S}$$

$$Re = 2698 \quad (critical \text{ or transition})$$

Also

$$\frac{\varepsilon}{D} = \frac{0.046mm}{9.53mm}$$

$$\frac{\varepsilon}{D} = 4.83 \times 10^{-3}$$

4.5.1.4 From the Moody Diagram

$$f = 0.032 = \frac{h_f}{\frac{L}{D}\frac{V^2}{2g}}$$

$$h_f = 0.032 \left[\frac{(4.27m)\ (0.285M/S)^2}{9.53 \times 10^{-3}m\ (2)9.81m/S}\right]$$

$$h_f = 0.059m$$

The head loss from frictional effects is very small

The total head is: 2.134m

and the loss due to the fluid having to climb back up to the feed-through is: 0.3m

Therefore, total head available   = 2.134 − 0.3 − 0.059

                                   = 1.7698m

This is more than enough head to insure flow.

In order to be completely sure that the calorimeter would work as predicted, several simple calculations were made. In the Thermosciences Lab there is a constant head water tank available to be used for the cooling calorimeter. A 1/2 in. plastic tubing was run to the test setup and a small experiment was conducted with a graduated cylinder and a stop watch; the flow rate was found to be 20.3 gm/s. A check was made on the flow rate needed to handle the maximum heat transport of the heat pipe. The maximum heat transport is found to be approximately 2000W. From the relation in $c_p\Delta T = Q_{max}$, and assuming a ΔT of 65K the mass flow rate needed is 7.33 gm/s.

At first glance, the flow rate is of course more than enough, but the frictional losses must be accounted for. The calorimeter was modeled as a straight piece of copper tubing. The frictional head loss for straight tube 4.27m long was 0.06m and the loss in the geometry of the calorimeter was 0.3m. The total head available was 2.134m, so the head after losses was 1.77m, which is more than sufficient to insure proper operation to the proposed calorimeter.

The complete calculations are as follows.

4.6   Theoretical Calculations for Testing

4.6.1 Maximum Heat Transfer vs. Temperature

To insure proper operation of the heat pipe, it was important to verify the results of HAC test of maximum heat transport versus temperature. In the HAC test, the effective length of the heat pipe was 0.267m and the tilt angle was 0 degrees. The definition of effective length is the evaporator plus the condenser length divided by two, plus the adiabatic length of the heat pipe. ($\ell_{eff} = \ell_a + \dfrac{\ell_e + \ell_c}{2}$). In this experiment the effective length is 0.318m and the tilt angle from the horizontal is 0 degrees. Note that the curve to be verified from the Hughes Report is an actual test of a sodium/ Inconel 617 heat pipe that will be tested in this laboratory. The calculations and summary of the maximum heat transport versus temperature is as follows.

The maximum heat transport in a heat pipe at a ˉiven vapor temperature is found using the following equation:

$$Q_{max} = \dot{m}_{max} \lambda \qquad (1a)$$

where 8 $\dot{m}_{max}$ = max liquid flow rate in the wick

Now using a standard pressure balance, and neglecting the vapor pressure drop ΔP_L, yields

$$\Delta Pc = \Delta P_L = \Delta Pg$$

where $\Delta P_L = \dfrac{\mu \ell_{eff} \dot{m}}{\rho_\ell KAw}$

$\Delta Pg = \rho_\ell g \ell_{eff} \sin\emptyset$

$\Delta Pc = \dfrac{2T\ell\cos\theta}{rc}$

substituting,

$$\frac{2\sigma_\ell \cos\theta}{rc} = \frac{\mu \ell_{eff} \dot{m}}{\rho_\ell KAw} + \rho_\ell g1 \ell_{eff}\sin\emptyset$$

rearranging terms,

$$\dot{m} = \frac{\rho_\ell KAw}{\mu_\ell eff} \qquad \frac{2\sigma_\ell}{rc} \cos\theta - \rho_\ell g\ell_{eff}\sin\emptyset \qquad (1)$$

Properties of Sodium at 827°C

$$\rho_\ell = 757.3 \text{Kg/m}^3$$

$$\mu = 1.8 \times 10^{-4} \text{NS/M}^2$$

$$\sigma_\ell = 0.123 \text{ N/M}$$

$$K = 4.16 \times 10^{-10} \text{M}^2$$

$$\lambda = 3977 \text{ KJ/Kg}$$

Note: The above temperature of sodium is the first test point to be checked to verify the published values (curve) that 'Hughes Electron Dynamics Division' furnished with the heat pipes to be tested.

And,

$$\ell_{eff} = \ell_a + \frac{\ell_e + \ell_c}{2}$$

$$= 0.1778 + \frac{(-0.1143+0.165)}{2}$$

$$\ell_{eff} = 0.318 \text{m}$$

Also,

$$A_w = 3.71 \times 10^{-5} \text{m}^2 \qquad \text{where:} \quad A_w = \text{wick area}$$

$$r_c = 1 \times 10^{-4} \text{m} \qquad\qquad 100 \text{ mesh Inconel 617}$$

$$r_c = \text{pore radius}$$

Assuming perfect wetting ($\theta = 0°$)

And the angle of tilt ($\phi = 0°$)

Equation 1 reduces to

$$\dot{m} = \frac{\rho_\ell K A_w}{\mu \ell_{eff}} \quad \frac{2\sigma_\ell}{r_c} \tag{2}$$

Substituting values into equation (2) yields,

$$\dot{m} = \frac{(757.3 \text{Kg/m}^3)(4.16 \times 10^{-10} \text{m}^2)(3.71 \times 10^{-5} \text{m}^2)}{(1.8 \times 10^{-4} \text{S/m}^2)(0.318 \text{m})} \left[\frac{(2)0.123 \text{N/m}}{1.0 \times 10^{-4} \text{m}}\right]$$

$$\dot{m} = \frac{5.02 \times 10^{-4} \text{Kg}}{S}$$

Now substituting $\dot{m}$ into equation (1a),

$$Q_{max} = \dot{m}_{max} \, \lambda$$

$$5.02 \times 10^{-4} \frac{Kg}{S} \, (3.977 \times 10^6 \, \frac{J}{Kg} \, \frac{1 \, watt}{J/S}$$

$$Q_{max} = 1998 \, watts$$

Now check Q_{max} at the high temperature limit

$$T = 1077°C$$

Properties of Sodium at 1077°C

$$\rho_\ell = 690.8 Kg/m^3$$

$$\sigma_\ell = 0.095 N/n$$

$$\mu = 1.6 \times 10^{-4} NS/m^2$$

$$K = 4.16 \times 10^{-10} m^2$$

$$\lambda = 3.69 \times 10^6 J/Kg$$

Substituting these values into eqn (1)

$$\dot{m} = 3.98 \times 10^{-4} Kg/s$$

Therefore, $Q_{max} = \dot{m}\lambda = (3.98 \times 10^{-4} Kg/S)(3.69 \times 10^6 J/Kg) 1W/J/S$

$$Q_{max} = 1469 \, watts$$

To get a representative curve of maximum heat transport vs. temperature, Q_{max} is calculated for temperatures, 900°C, 1000°C

Properties of Sodium at 900 and 1000°C

T = 900°C	T = 1000°C
$\rho_\ell = 745.4 Kg/m^3$	$\rho_\ell = 725.4 Kg/m^3$
$\sigma_\ell = 0.113 \, N/m$	$\sigma_\ell = 0.104 \, N/m$
$\mu = 1.7 \times 10^{-4} NS/m^2$	$\mu = 1.6 \times 10^{-4} NS \, m^2$
$K = 4.16 \times 10^{-10} m^2$	$K = 4.16 \times 10^{-10} m$
$\lambda = 3.913 \times 10^6 J/Kg$	$\lambda = 3.82 \times 10^{6} \, K$

81

MICROCOPY RESOLUTION TEST CHART

NATIONAL BUREAU OF STANDARDS-1963-A

Note: These values are at zero degree tilt from horizontal

T = 900°C   T = 1000°C

$\dot{m}$ = 4.81x10^{-4}Kg/S $\dot{m}$ = 4.58x10^{-4}Kg/S

Q_{max} = 1882 watts Q_{max} = 1752 watts

Table: Q_{max} for varying Temp. $\theta = 0°$

Q_{max} Watts	Temperature °K
1998	1100°
1882	1173
1752	1273
1469	1350

It is shown in the calculations above that as the temperature of the sodium vapor increases, the maximum heat transport decreases. This phenomenon is illustrated in Fig. 4.6. The reason for this decrease in heat transport lies in the properties of liquid sodium. The increased temperatures change the density and the latent heat of vaporization significantly more than the liquid viscosity and the liquid surface tension. It is also worth pointing out that there is a limit to the amount of liquid the wick structure can handle which can play a part in the reduction in heat transport.

4.6.2 Entrainment

As discussed in the theory section of this report, an entrainment limit calculation was made to confirm that for all operational temperatures tested, the entrainment of liquid droplets in the vapor would not occur. The calculation shows that the entrainment limit heat flux is approximately 92 times higher than the highest heat flux to be tested. The calculations are as follows.
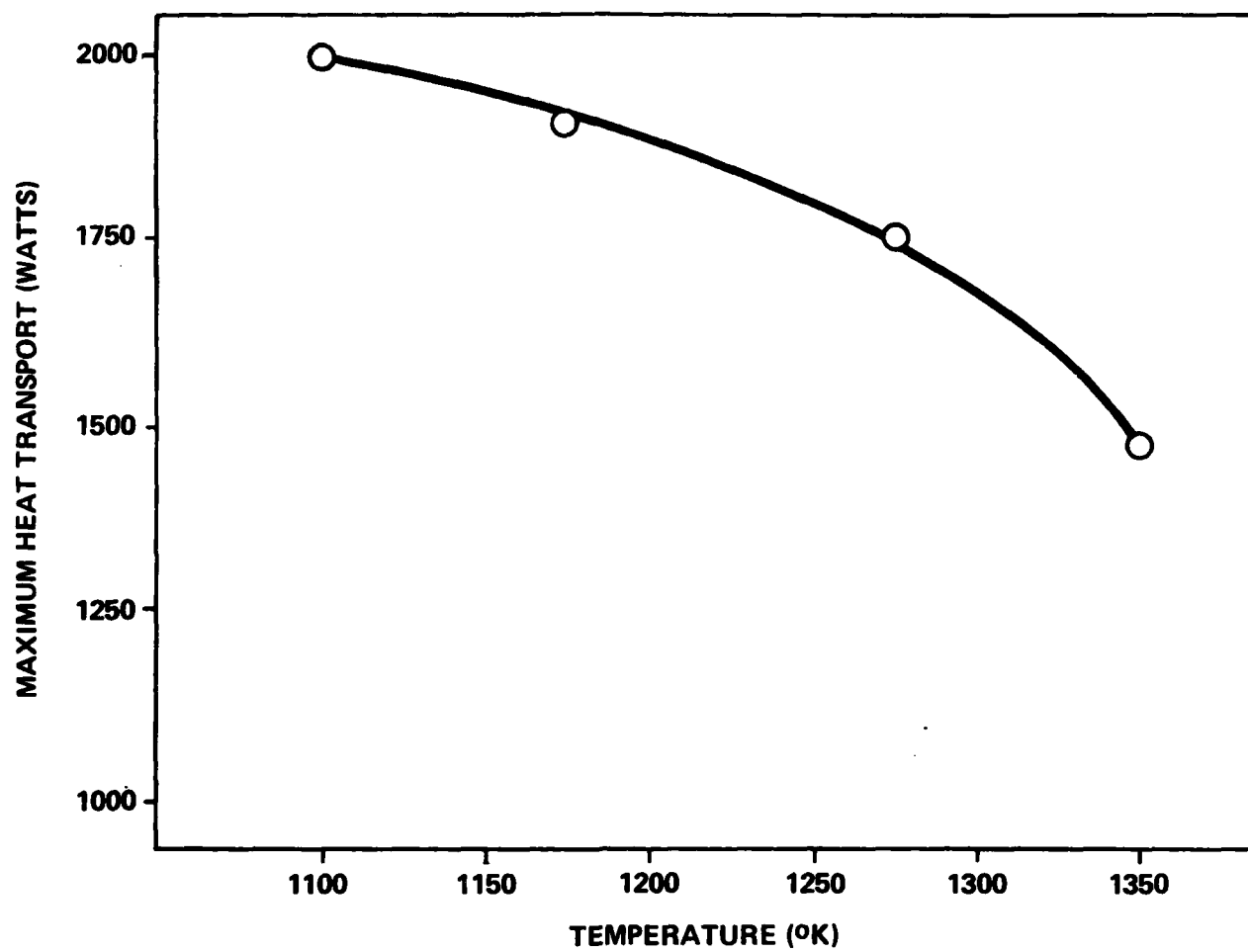
MAXIMUM HEAT TRANSPORT VERSUS TEMPERATURE

FIGURE 4.6

The entrainment limit is the maximum heat flux that can occur before entrainment of droplets from the wick structure are sheared into the vapor space.

$$q = \sqrt{\frac{2\pi\rho_v\lambda^2\sigma_\ell}{z}} \qquad \text{where:} \quad z = 2\pi/r_c$$
$$z = 0.0077$$

From Fig 2.24 ''Heat Pipes'' by Dunn and Reay [4.2], the merit number at 1200°C is $\rho_v\lambda^2\sigma_\ell = 2\times10^6 W^2/cm^3$

Therefore,

$$q = \sqrt{\frac{2\pi(2\times10^6W^2/cm^3)\frac{10^6-cm^3}{1m^3}}{0.0077m}}$$

$$q = 4.04\times10^7 w/m^2$$

This value is well above the q_{max} values calculated.

4.6.3 Effect of θ on Performance

One substantial area of investigation of heat pipe performance is the ability to transport heat at all angles of operation. Before these tests can be conducted, calculations of the maximum heat transport (Q_{max}), and the maximum axial heat flux (Q'_{lim}) for varying vapor temperatures must be made. These calculations are done at various angles from 0 to 90 degrees in 15 degree increments.

Recall that:

$$Q_{max} = \dot{m}\lambda$$

and

$$\dot{m} = \frac{\rho_\ell K A_w}{\mu \ell_{eff}} \left[\frac{2\sigma_\ell}{r_c}\cos\theta - \rho_\ell g \ell_{eff}\sin\theta\right]$$

Now calculate Q_{max}, for $\emptyset = 15°, 30°, 45°, 60°, 75°, 90°$

To conserve space, a sample calculation of $\emptyset = 30°$ will be shown here.

for
T = 827°C or 1100°K
$\emptyset = 30°$
$\theta = 0$

84

$$. \quad = \frac{(757.3Kg/m^3)(4.16x10^{-10}m^2)(3.71x10^{-5}m^2)}{(1.8x10^{-4}Ns/m^2)(0.318m)} \left[\frac{(2)0.123N/m}{1.0x10^{-4}m} \right.$$

$$\left. -757.3Kg/m^3 9.81m/s^2 0.38m sin30^\circ \right]$$

$$\dot{m} = 2.61x10^{-4}Kg/s$$

$$Q_{max} = \dot{m}\lambda$$

$$= (2.61x10^{-4}Kg/s)(3.977x10^6 J/Kg)1watt/J/s$$

$$Q_{max} = 1038 \text{ watts}$$

The calculations of the maximum heat transport (Q_{max}) found at different angles and temperatures. Also the heat flux can be calculated for an evaporator length of 4.5 in. which is shown in the table below.

	1100 K		1173 K		1273 K		1350 K	
Q	Q	Q'	Q	Q'	Q	Q'	Q	Q'
0	1993	$4.38x10^5$	1882	$4.13x10^5$	1752	$3.84x10^5$	1469	$3.22x10^5$
15	1501	$3.29x10^5$	1422	$3.12x10^5$	1336	$2.93x10^5$	1136	$2.49x10^5$
30	1038	$2.28x10^5$	993	$2.18x10^5$	947	$2.08x10^5$	825	$1.81x10^5$
45	641	$1.41x10^5$	624	$1.37x10^5$	613	$1.24x10^5$	559	$1.23x10^5$
60	336	$7.37x10^4$	341	$7.48x10^4$	356	$7.80x10^4$	354	$7.75x10^4$
75	145	$3.18x10^4$	164	$3.49x10^4$	195	$4.28x10^4$	226	$4.95x10^4$
90	79	$1.73x10^4$	103	$2.26x10^4$	140	$3.07x10^4$	182	$3.99x10^4$

$Q' = Q_{max}/A = Q/A$ 　　　　　 where: A = surface area

　　　　　　　　　　　　　　　　　　 A = πDL

　　　　　　　　　　　　　　　　　　 A = $\pi(0.0127)(0.1143m)$

example; for T = 1100°K, θ=0　　　 A = $4.56x10^{-3}m^2$

$$Q' = \frac{1998 \text{ watts}}{4.56x10^{-3}m^2}$$

$$Q' = 4.38x10^5 \text{ W/m}^2$$

For these angles and temperatures, a performance map can be made to predict all variations in values as shown in Fig. 4.7. The results were as expected; as the temperature is increased, the maximum heat transport and heat flux decrease. The tilt angle produces a negative term in the heat transport equation as shown below:

$$Q_{max} = \frac{\rho_\ell KA_w}{\mu \ell_{eff}} \left[\frac{2\sigma_\ell}{r_c} \cos\Theta - \rho_\ell g \ell_{eff} \sin\phi \quad \lambda \right]$$

At the temperature of 1100K the heat transport is reduced about 20 times as the angle is changed from 0° to 90°.

4.7 Conclusions and Recommendations

The calculations for the calorimeter design were very simple, but entirely adequate. The theoretical calculations performed for verification of data from the HAC Report were in good agreement. Also the calculations of performance of the heat pipe at different angles seems at the first glance a true approximation of what will occur. It is recommended that a closer investigation of the choked flow phenomenon as it relates to the sonic limitation of the heat pipe be carried out.

Additional information should be obtained from HAC in regard to heat pipe fabrication. These include the following:

1. r_c measurement
2. ε measurement
3. Hydrogen firing use and results
4. Purity of sodium
5. Metallurgical results obtained on weld cross sections
6. What material is the final seal ball
7. Process for port pin weld.

In order to perform adequate analyses some time in the future, the high temperature processing of the Inconel 617 must be determined. It is important that the elemental material depleted from the container and wick be known. Possibly a simulated experiment should be run to determine what the losses are. This could be very important in a post-test analysis of the heat pipes.
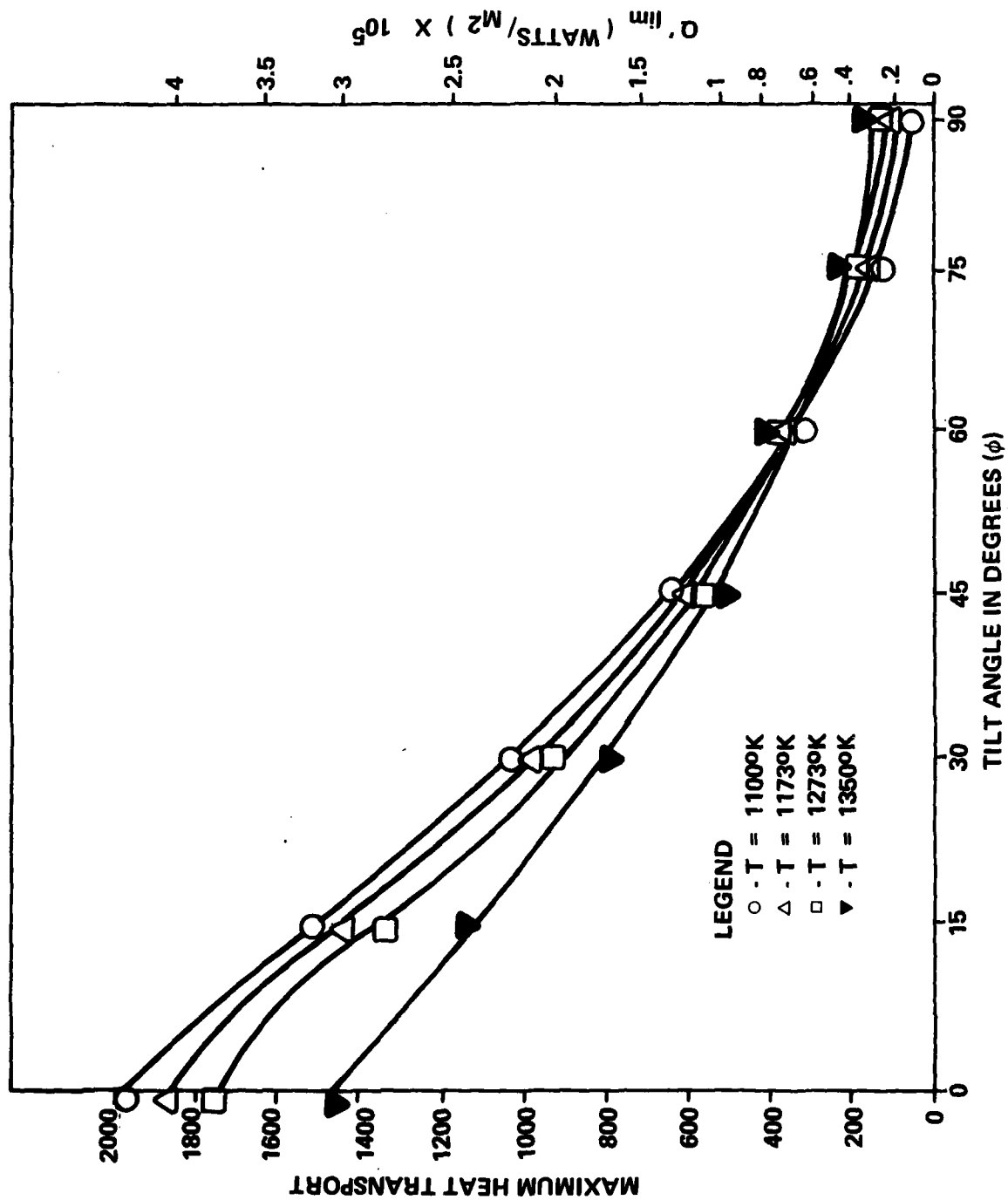
MAX. HEAT TRANSPORT AND HEAT FLUX VERSUS TILT ANGLE

FIGURE 4.7

87

Four heat pipes have titanium sponge which is not compatible with nickel. A more suitable getter should be identified for future Inconel 617 heat pipes.

4.8   References

[4.1]   Dunn, P.D., D.A. Reay, Heat Pipes, Pergamon Press, 2nd ed., 1978 Oxford, England, p. 56.

[4.2]   Ibid., p. 57.

[4.3]   Ibid., p. 77.

[4.4]   Ibid., p. 19.

[4.5]   Ibid., p. 53.

V. EUTECTIC FLUORIDE SALT THERMAL ENERGY STORAGE EXPERIMENTS

5.1   Introduction

Thermal Energy Storage (TES) Units consisting of eutectic composition of 64LiF-30MgF-6KF have very high phase change energy capacity and their applications as energy source for satellites and terrestrial uses have been investigated in the literature [5.1]. The research problems connected with these applications are broadly identified to be in two areas, namely, 1) material compatibility between the salt and container material; 2) performance evaluation of various TES device geometries. A clear and concise picture of the work carried out so far in the above areas is not available.

In the present study an attempt has been made to review and categorize the existing work in a more amenable way. The categorization includes a chronological arrangement of the past work done in the above mentioned areas and a comparative study to relate each piece of research work to its predecessor and successor such that a continuity is established.

Secondly, an experimental setup has been designed and assembled to investigate the performance of a cylindrical Thermal Energy Storage Capsule (TESC) filled with a eutectic mixture of fluorides of Mg, Li and K. Experimental results have been used to verify the melting point, and latent heat of fusion of the eutectic salt, in addition to evaluating the solidification and heat transfer resistance characteristics of the cylindrical TESC. Heating and cooling (with melting and solidification) cycles have been repeated several times in a vacuum environment to reveal any problem in material compatibility.

Analytically, the theoretical model of London and Seban for solidification in cylindrical configuration in the horizontal mode has been verified with the present setup. Experiments in the vertical mode have been carried out to investigate the effect of natural convection in the melt on the solidification and heat transfer characteristics.

The TES capsule tested was previously on life test by directly heating the container (clad). The life-cycle test is reported on in Section 9.

5.2   Experiments on the Eutectic Fluoride Salt Thermal Energy Storage Capsule (TESC)

5.2.1 Physical details of the sample (TESC)

The TES capsule shown in Fig 5.1 and 5.2 supplied to ASU by the Air Force Laboratory is 12 in. long and 1 in. in outside diameter. The capsule has been fabricated at University of Dayton Research Institute from Inconel alloy 617 stock of Huntington Alloy Products Division of the International Nickel Company, Inc. The capsule has a longitudinal seam weld and electron beam welded flat end caps machined from Inconel 617 bar stock and bears a serial number 12 disclosing its identity of origin referred to a batch of 13 TESC's fabricated at UDRI in 1975 [5.2]. According to this report, the TESC has been filled under extreme cleanliness conditions with 225.519 grams of the eutectic fluoride salt, $LiF-MgF_2-KF$ of composition 42.27%, 48.76% and 8.95% by weight, respectively.

The TESC had been stored in a vacuum dessicator so as to avoid atmospheric corrosion prior to the start of the present experiment and had a dark bluish coat on the body indicating its past heating cycles at Air Force Laboratory. The oxidized layer has been cleaned with emery paper (400 grit) until the surface appeared like a polished steel and in this condition the sample TESC has been assembled to the experimental setup, to be described in the next section.

5.2.2 Experimental Setup

A simple experimental unit was assembled using some of the hardware already available at ASU, which includes a 40 sec. varian vacion/vacsorb pump unit and an 8 in. diameter stainless steel cross chamber fitted with vacuum flanges and fittings. Minor but important items like thermocouple assemblies, ceramic tubing and beads, copper tubing, clam-shell electric heaters, varian gaskets and feed-throughs were purchased and used. Fabricational support has been given by the development shop and the assembly and installation were done at the Thermionics Lab, ASU.

The experimental unit consists of the following:

   i) A vacuum chamber hooked up to a vacsorb/vacion pumping unit to provide the vacuum environment, and

   ii) A calorimeter with the TESC sample, electric heater, thermocouple temperature measuring circuitry and instrumentation and a tap water circulated cooling coil.

FILLED WITH THE EUTECTIC SALT LiF - MgF$_2$- KF

1/16" WALL THICKNESS

12"

1" DIA

91
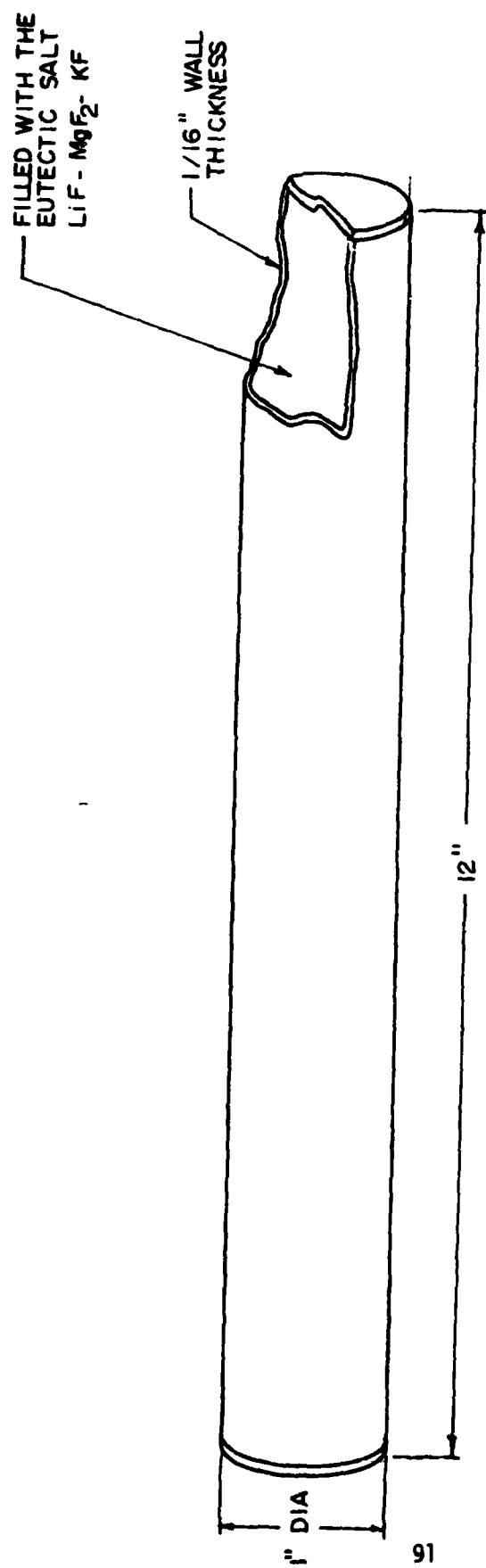
Fig. 5.1. CYLINDRICAL CONTAINER FOR EUTECTIC SALT (LiF-MgF$_2$-KF)
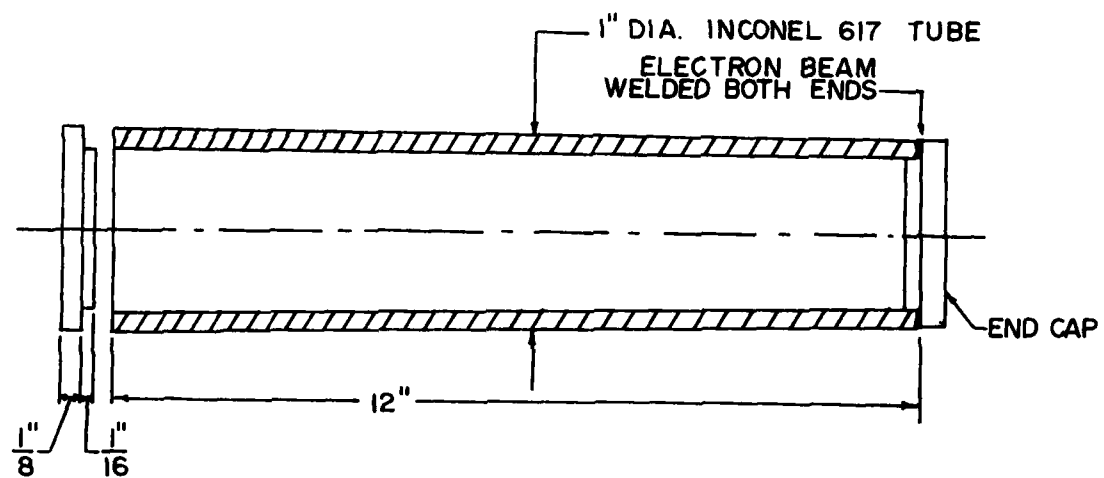
Fig. 5.2. TESC SAMPLE

The features of the test setup for measuring the latent heat fusion are
ttrated in Figs. 5.3 and 5.4. Figure 5.3 is a complete assembly drawing
ing all parts in their respective position places in the vacuum chamber.
₂ 5.1 is an indexed parts list to identify the items in Fig. 5.3.

Table 5.1 Vacuum Chamber Assembly Component List

1. Salt in Cylindric Container, Ref. Fig. 5.3
2. Heater
3. Cooling Coil, Ref. Fig. 5.8
4. Stand-Off Ring, Ref. Fig. 5.6
5. Heater Cap, Ref. Fig. 5.5
6. Compression Bolt, Ref. Fig. 5.7
7. Fastener for Cooling Coil, Ref. Fig. 5.7
8. End Radiation Shield
9. Longitudinal Radiation Shield
10. Vacuum Chamber, Ref. Fig. 5.9
11. Inlet and Outlet for Cooling Coil

Since it is required that all the heat radiated from the cooling salt be
·bed and consequently measured through the cooling coil, it is necessary
·ep to a minimum all points of contact that would be required to hold the
container rigidly in place, in this way reducing conduction losses. The
m chosen to accomplish this was two stainless steel 3/8 in. bolts that
  support a pair of stainless steel cups and, in turn, support the
iner for the salt at its ends. Figures 5.5, 5.6 and 5.7 are parts
ngs for the internal vacuum hardware. 304 stainless steel was chosen for
ow thermal conductivity property. The supporting cups were also designed
rve a dual purpose, that of supporting the heating element and the salt
₂. Note clearance conditions for the heater and the salt container were
that the salt container was under the compressive load delivered by the
'8 in. bolts while the heating element was simply cradled.

Calorimeter Design
·he purpose of a calorimeter is to supply measurable amounts of
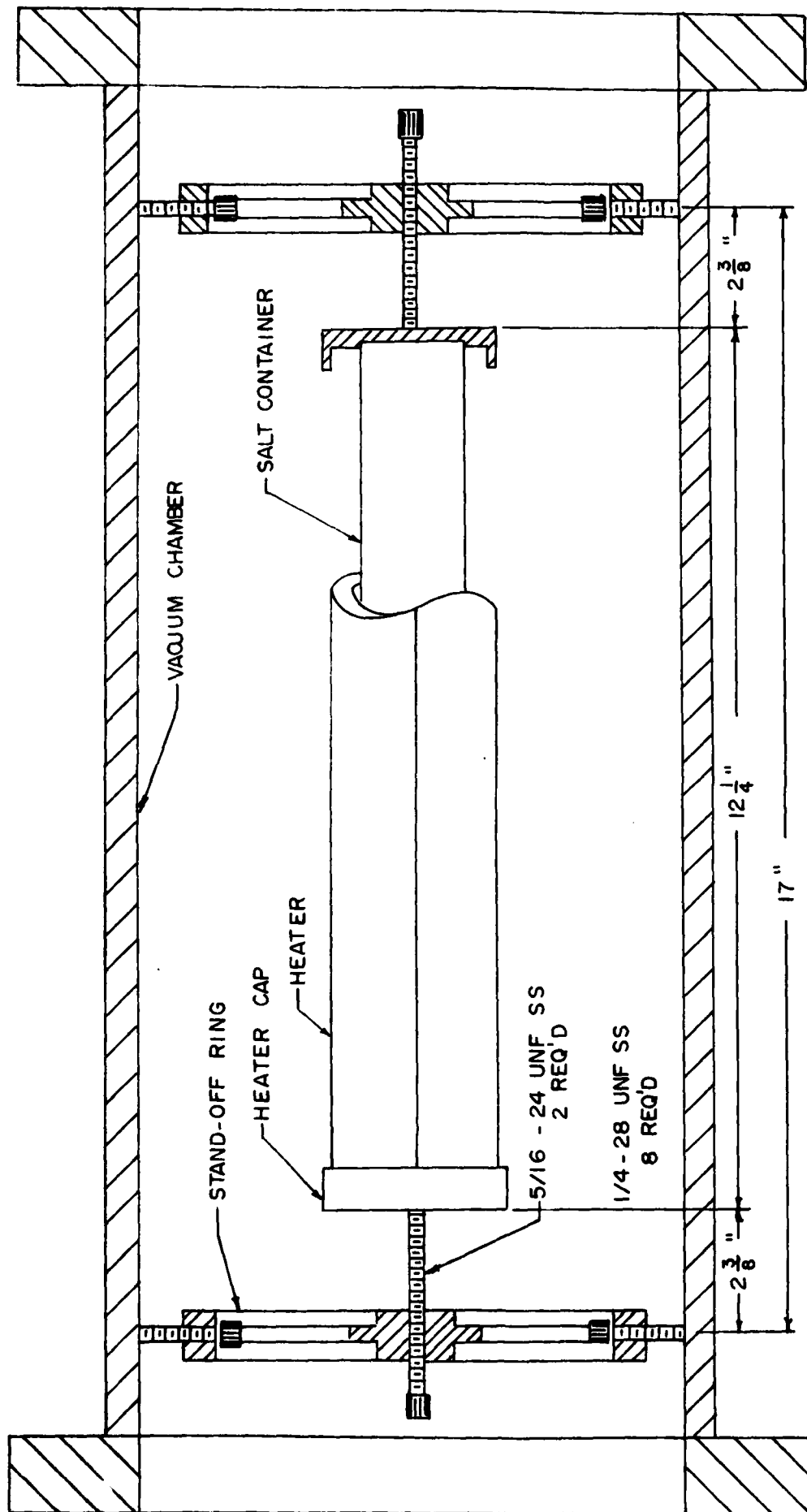
Fig. 5.3. VACUUM CHAMBER SUB ASSEMBLY
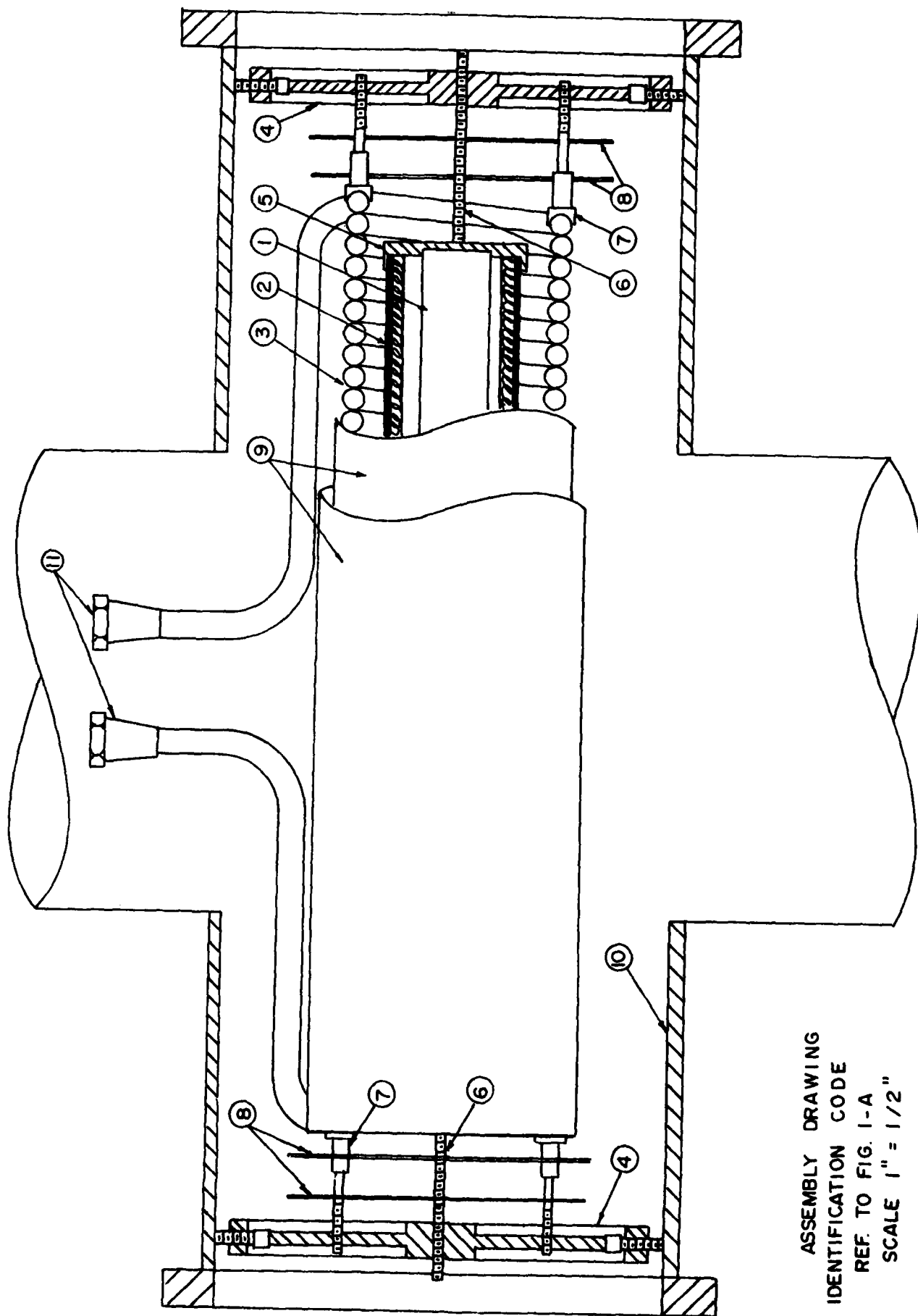
ASSEMBLY DRAWING
IDENTIFICATION CODE
REF. TO FIG. 1-A
SCALE 1" = 1/2"

Fig. 5.4. TESC EXPERIMENTAL SET-UP DETAIL

$\frac{5}{16}$ DIA. 8 HOLES
ON $1\frac{1}{4}$ DIA. CIRCLE

$2\frac{3}{8}$

$2\frac{1}{8}$

$\frac{3}{32}$

1/2

3/16

1/8

90°

SECTION A-A
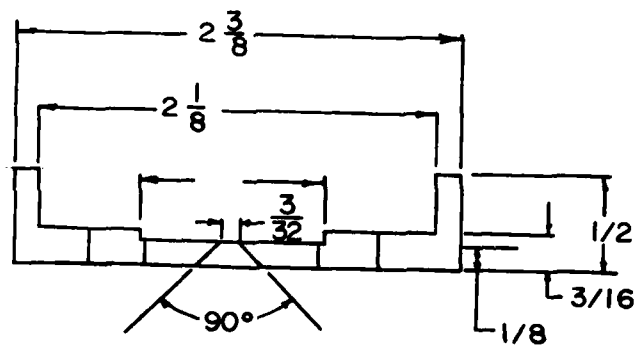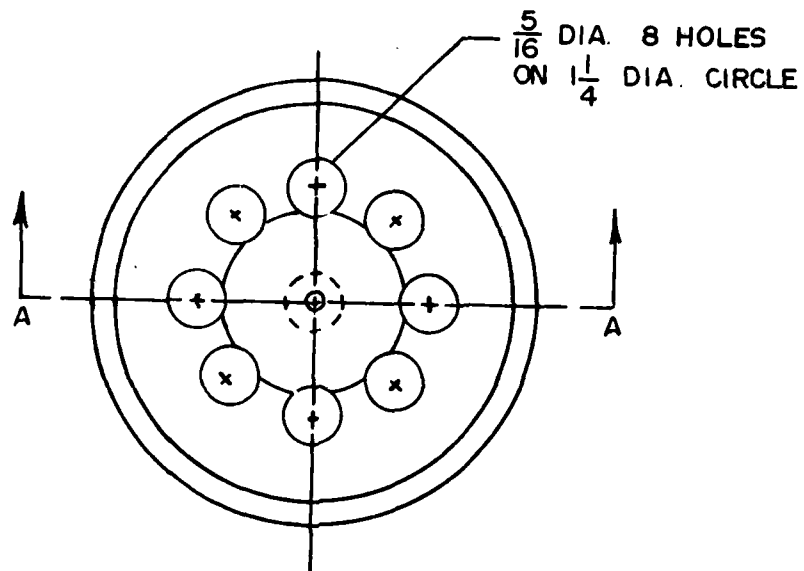
HEATER CAP
MAT'L. SS 304
QTY. TWO REQ'D
SCALE: FULL

Fig. 5.5. HEATER CAP

96

2" DIA. 4 HOLES ON 2" DIA. CIRCLE

TYP. 4 POSITIONS DRILL AND TAP FOR 1/4"-28 UNF

B — B

$6\frac{1}{2}$

6

1

1/2

1/8

DRILL AND TAP FOR 5/16-24 UNF
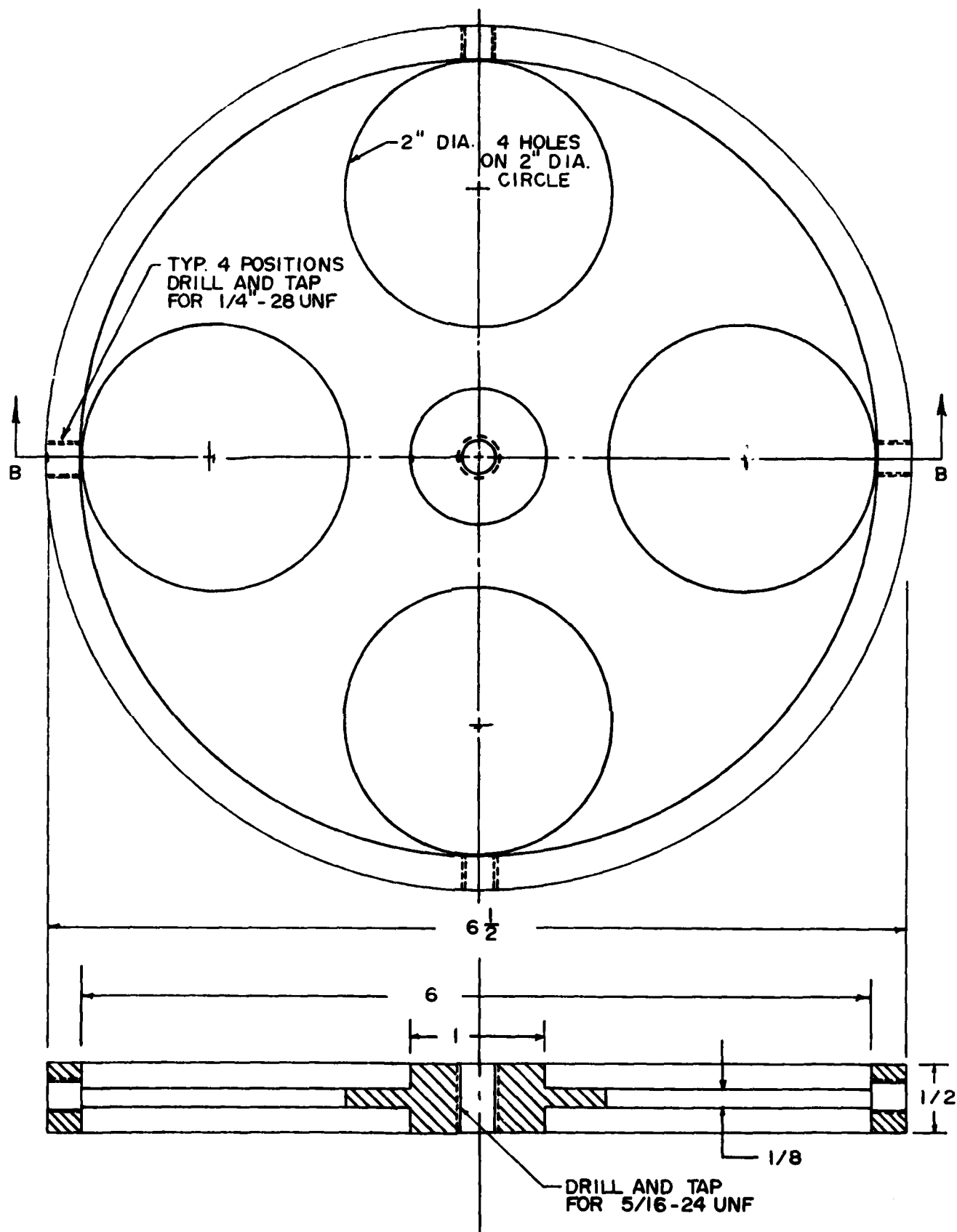
STAND-OFF RING
QTY: TWO REQ'D
MAT'L: AL 2024
SCALE: FULL

Fig. 5.6 STAND OFF RINGS

1/4" 24 SS.
4 REQ'D.

1 ½"   3/4"

2 ¼"

1/4" DIA.

5/8" - 24 UNF, SS
2 REQ'D.

4"

3/8" R

MAT'L   TEFLON
4 REQ'D

5/8"

3/4"   1/2"

1 ¼"

5/8"

3/4 DIA.   1/4" DIA.

5/8"
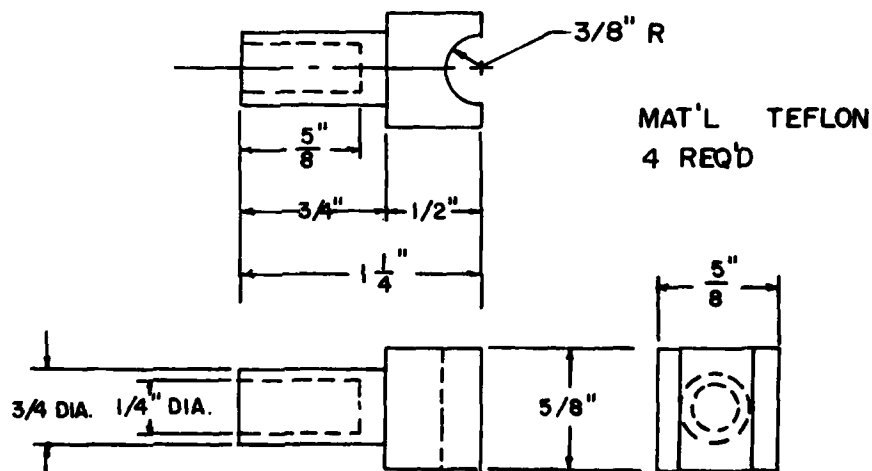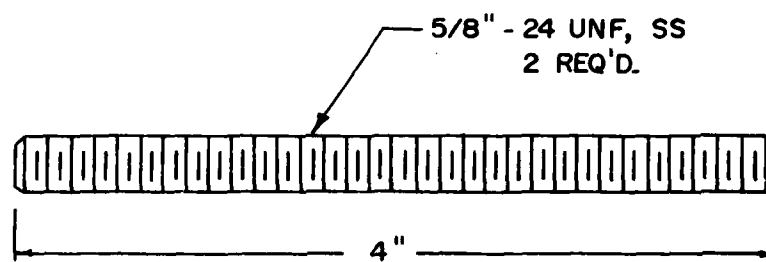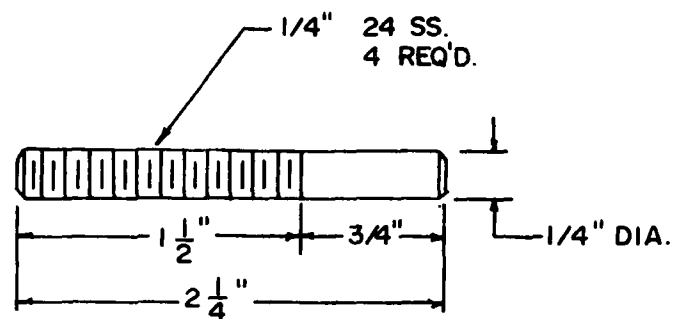
Fig. 5.7.   FASTENER   FOR   COOLING   COIL

thermal energy to the TESC while heating the sample to its melting point and to exactly meter the heat output during cooling. The calorimeter was designed to minimize heat losses and to maintain a uniform temperature throughout the length of the TESC. The particular design shown in Fig. 5.4 has an electric clam shell heater which is an annular hemi-cylindrical type heater. TESC, together with the thermocouples, is housed inside the annular region of the heater shells. The heater and TESC assembly is held concentrically between a close-coiled cooling water coil shown in Fig. 5.8 which in turn is kept inside the cross chamber. The electrical, water, and thermocouple connections are taken out through proper feed-throughs in the vacuum chamber. The cooling coil is insulated with stainless steel sheet and aluminum foil to prevent radiation loss to the outer wall. Convection loss is eliminated by evacuating the chamber. Radiation is the only mode of heat exchange allowed between the TESC and heater assembly and the cooling coil. The cooling coil is fitted with inlet and outlet temperature probes (thermocouples) and flow meter. This provides an accurate means for determining the heat radiated to it from the cooling salt. In order to keep the design and assembly simple, the cooling coil only encloses the longitudinal surface of the cylinder containing the salt. All heat radiated from the ends is minimized with radiation shields placed at both ends of the cooling coil. Radiation shields are also placed around the outer surface of the cooling coil to reduce heat flow from the coil to the surfaces of the vacuum chamber. All efforts were made to insure that all heat leaving the salt sample is absorbed by the cooling coil.

Additional hardware and fasteners were used to locate and support the cooling coil. The same consideration of minimizing contact points and reducing heat loss by conduction through the fasteners were used.

The design of the calorimeter required the calculation of suitable numbers for the following:

    1) Electric heater: capacity, type of dimension
    2) Cooling coil: flow rate and size

The calculations are given in the following sections.

3" INSIDE DIA.

14"

3"

MATERIAL COILED FROM
3/8" DIA. SOFT COPPER TUBING
I REQ'D
SCALE - NONE

Fig. 5.8. COOLING COIL

100

Physical details of TESC known/measured:

Length   = 12-1/4 inches

Diameter OD   = 1 inch (nominal)

Weight (gross)   = 571.2 grams

Weight of salt filling= 225.5 grams[2]

Material of container= Inconel 617

With the above data and the preceding data for MgF_2-LiF-KF eutectic salt and Inconel 617, the energy required to heat the TESC to the salt melting point (that is, from 298K to 988K), has been estimated to be **242.8 watt hour** assuming no heat losses. If a heat loss of equal amount is allowed from the outer surface of the clam shell electric heater (which was chosen for its ready availability and good vacuum functioning) and assuming about 45 minutes of heating time, the heater capacity is determined to be about 650 watts. Hence, the clam-shell, hemicylindrical heaters of 375 W, 115 V rating each could be readily used for this application. The length (12 in.), ID (1-1/4 in.), and OD (2-1/16 in.) match the heater dimensions. Each hemicylindrical half has 8 grooves to accommodate the heater coil which insures uniform heating.

The cooling water coil design was based on the criterion of maximum energy input to the TESC and minimum temperature differential between inlet and outlet water temperatures. Maximum output occurs when the TESC is maintained at steady state above the M.P. of the TES salt, approximately 725°C. A maximum temperature rise to 363K has been assumed in order to avoid boiling the water within the coil. With these values the radiated power which is absorbed by the cooling coil is approximately 905 watts and the cooling water flow rate necessary is 22 liters/hour. A constant heat water tank arrangement provided a maximum flow rate of 40 liters/hour which was adequate for the present experiment.

The cooling coil was formed out of annealed copper coil of 3/8 in. tube diameter and it has 37 close helix turns with 3.5 in. coil ID.

5.2.4 Vacuum Environment

A vacuum environment was necessary for this experiment for two reasons: (1) to avoid oxidation of the TESC wall when heated to high temperatures, and (2) to make the heat balance calculation simpler by eliminating the convection

101

mode of heat loss from the TESC assembly to the outside. However, conduction loss through the thermocouple and power load wires and through the mounting fixtures were not fully eliminated, but minimized.

The vacuum system shown in Fig. 5.9 employs a varian vacsorb/vacion pumping unit which provided a vacuum of 10^{-6} torr. The cross chamber with a 7 in. ID provides a good spacing and mounting arrangement for the TESC assembly. The chamber also provides enough flexibility in connecting various flanges and feed-through such that the experimentation of TESC in horizontal and vertical modes is possible.

5.3   Experimental Procedure

5.3.1 Power and Temperature Measurement

Electrical power (0-115 AC) to the heater was supplied through a variac and wattmeter and the input could be regulated depending upon the requirement. Power input readings on the wattmeter were cross-checked by precisely measuring the resistance of the heater coil in the steady state condition ($\approx 1000K$) and the voltage input ($V^2/R=$power).

Energy output through circulating water was obtained by measuring the inlet-outlet temperatures and the flow rate. The flow rate was measured by collecting a known quantity of water from the outlet in a measuring jar and by measuring the time required with a stopwatch. This method gave more reproducible readings that those with flow meter (rotameter type) in the water line.

Temperatures along the lengths of the TESC outer wall were measured with nine Cromel-Alumel thermocouples. These thermocouples were fabricated very carefully to obtain consistent beads and equal length wires were used to get uniform resistances. Thin high-temperature type ceramic beads were used to give rigidity and insulation for the thermocouples. Contact of the thermocouple beads with the TESC wall was insured by a strap of stainless steel strip which was spot welded around the TESC cylinder. In this way the TESC wall was not damaged. Apart from these nine, one thermocouple monitored the heater outer surface temperature and two others measured the circulating water temperature.   All the thermocouples were connected to the instrumentation through a junction box, switch, reference Celsius junction unit, digital

102

4 - 7" DIA. ACCESS PORTS
TO TWO VACUUM CHAMBERS

ALL MATERIAL STAINLESS STEEL
ALL PORTS FLANGE TYPE FITTING

8-1 $\frac{1}{2}$" DIA. EXIT PORTS

18"

9"

18"

9"
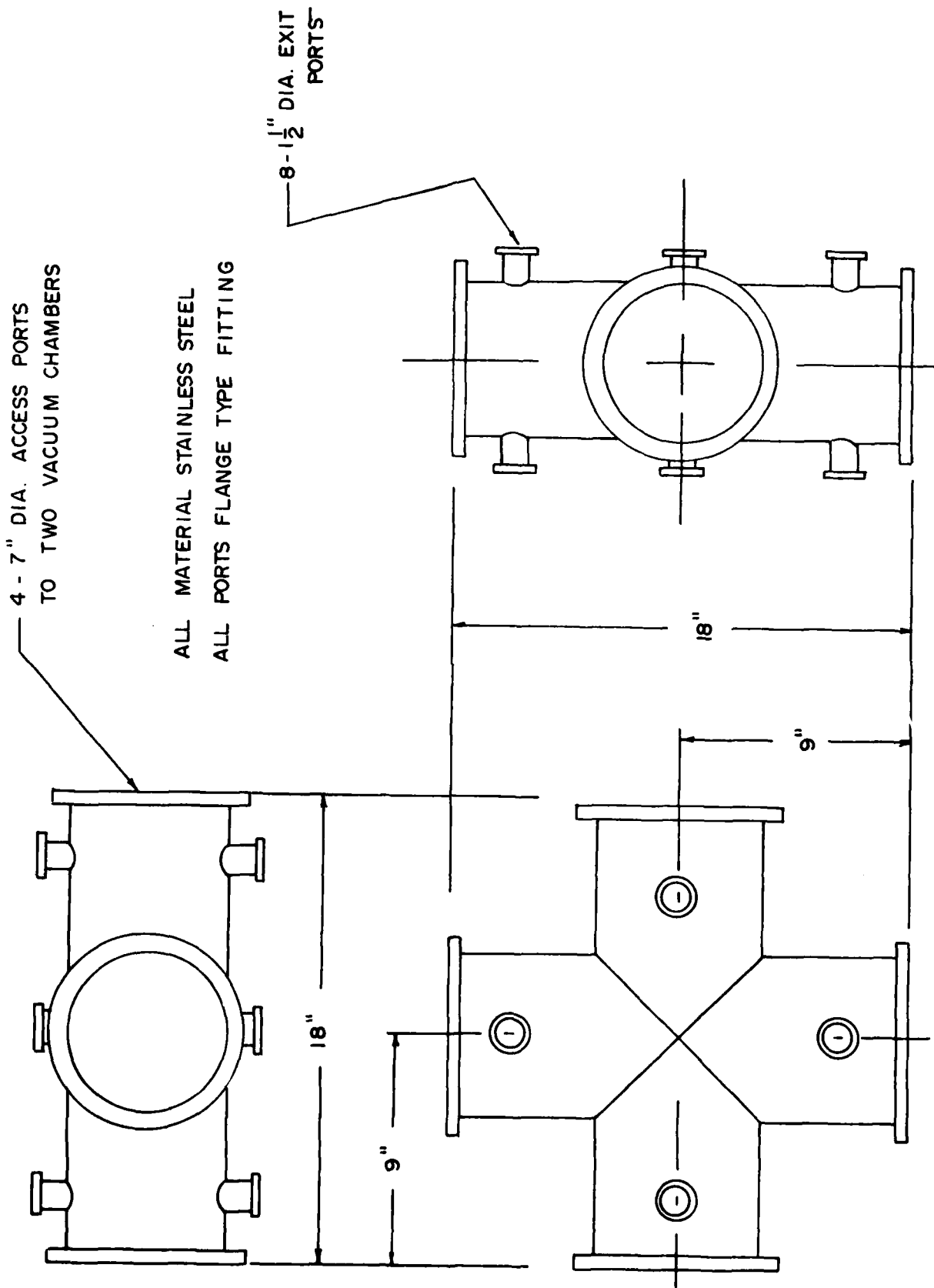
Fig. 5.9. VACUUM CHAMBER

103

voltmeter and to a printer. Omega company's reference junction unit maintained a constant zero Celsius bath which made the temperature measurement easy and reliable in comparison to an ice bath. The printer gave the millivolt output of each thermocouple which was in turn converted to Celsius with a calibration chart.

5.3.2 Melting and Solidification

The system was switched on by first starting the vacuum pump. A required vacuum of 10^{-5} to 10^{-6} torr was attained (actually a vacuum better than 20 millitorr would be sufficient to eliminate convection) by operating the vacsorb pump and the vacion pump after crossover at 10^{-4} torr. The vacion pump maintained a steady vacuum of 10^{-5} torr. Cooling water was circulated at a desired flow rate and the heater supply was switched on. Power input to the heater was increased slowly in steps of 25 watts in order to heat the TESC assembly at a slow rate. This was essential to avoid any uneven expansion of components, TESC sample, clamps, holders, etc. and any possible short circuiting of heater supply or slipping of the TESC from its pivotal supports within the vacuum chamber. When the TESC temperature surpassed 873K, a constant desired power input was set and the system was allowed to run continuously until it reached a steady state. A chart recorder recording the TESC centerpoint (TC #4C) temperature at a slow speed (chart speed = 1'/hr) indicated whether steady state had been attained or not.

The experimental procedure was divided into three sequential steps.

1) heating – sensible heat and latent heat addition and melting
2) steady state
3) cooling – latent heat and sensible heat removal

During heating, the thermal energy storage salt receives the sensible heat until the salt is brought to near its melting temperature and when the phase change or melting takes place, it receives the latent heat. Due to the cylindrical geometry of the TESC, melting cannot occur instantly. On the other hand, the ''melting front'', called the liquid-solid interface, advances radially inward. Likewise, in the reverse, when the system gives out its latent heat, a ''solidification-front'' advances radially inward to the center of the TESC. The time of complete melting or solidification for a given TESC

configuration depends on the salt composition and latent heat and the quantity of salt filled in. Since the latent heat of addition/removal takes place at nearly constant temperature, a melting or solidification curve will provide experimental verification for the latent heat value and melting point of a given eutectic salt.

In the present experiment, the following data are obtained:

1) Steady state loss of the system

2) Melting temperature of TES salt

3) Latent heat of fusion of the salt

4) Time for complete solidification of melt

5) Heat transfer resistance for the system (cylindrical two-way heat flow model)

5.4   Conclusions and Recommendations

The design of the test apparatus for determining the latent heat of fusion of the eutectic salt (LiF-MgF$_2$-KF) was strongly influenced by the fact that the salt was totally contained in a cylindrical envelope capped at both ends. Since the test sample could not be directly handled or seen, the technique of drop calorimetry for testing was ruled out. It was also felt the test should not damage the salt sample or its container, a consideration based on the possibility of future testing.

The approach taken for testing was that of heating the contained salt to some 20K past its melting point and the salt was then allowed to cool at a controlled and measurable rate. With the use of several thermocouples attached to the outer surface of the containing cylinder, a plot of the cooling curve for the salt is then constructed (temperature vs. time) as in Fig. 5.10. The cooling curve indicates the time interval in which the salt is passing through its phase change (liquid to solid) and giving up its latent heat of fusion. The phase change shows up on the cooling curve as the constant slope portion indicating there is minimum temperature change per unit time. With a means of measuring the outflow of heat during this unit of time, the latent heat of fusion for the eutectic salt is then determined.

This work preceded the Master's research of Mr. R. Ponnappan. The experimental setup was relatively successful and leads to useful information which is discussed in the following two sections.

105

SALT GOING THROUGH
PHASE CHANGE (LIQUID
TO A SOLID)

HEAT GIVEN UP DURING THIS TIME
PERIOD IS THE LATENT HEAT OF FUSION

TEMPERATURE °C

TIME
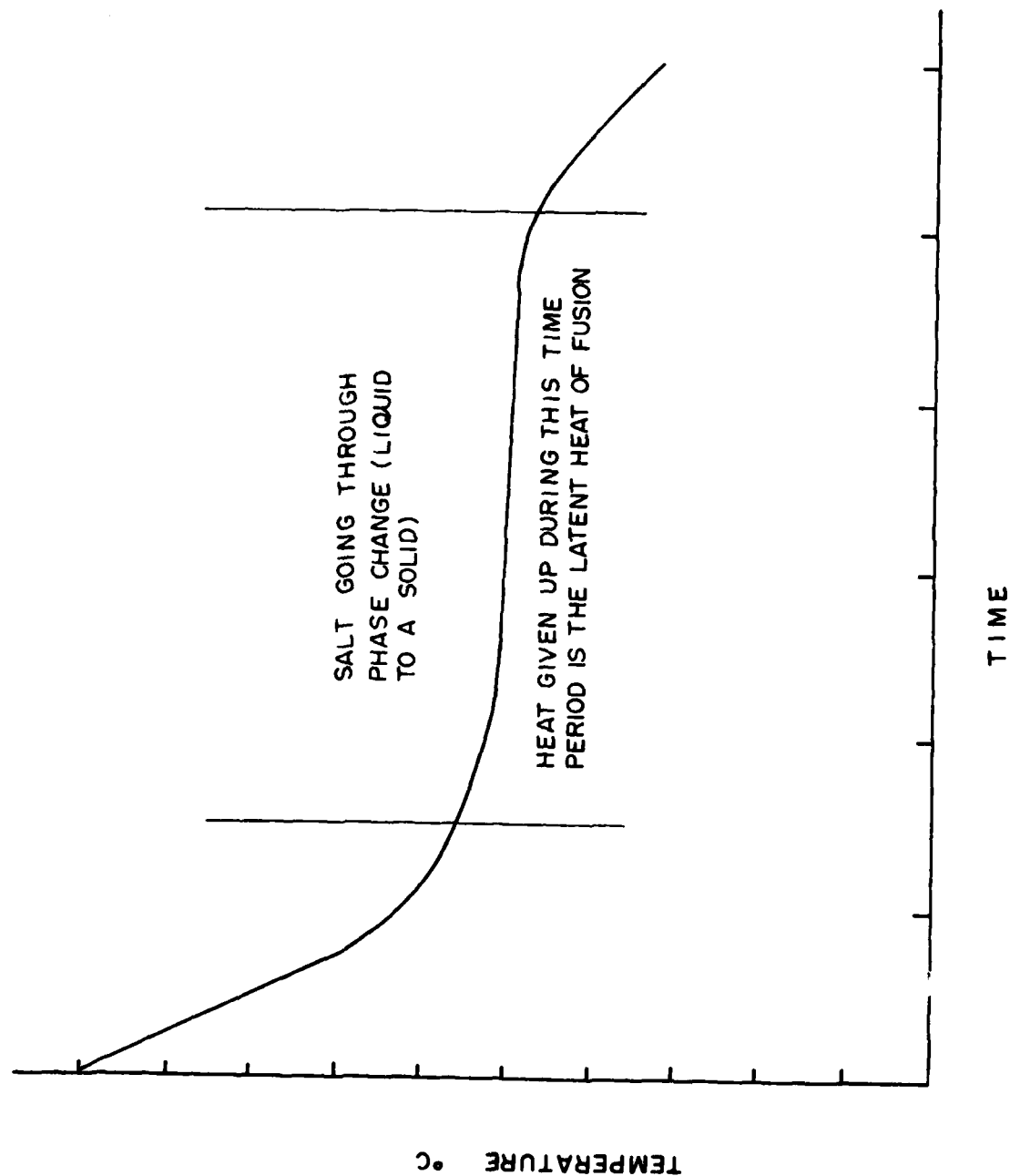
Fig. 5.10. TYP. COOLING CURE GOING THROUGH PHASE CHANGE (LIQUID TO SOLID)

References

Richter, R., Solar Collector Thermal Power System, AFAPL-TR-74-89, Vol. I, II, III, November 1974.

Davison, J.E., Evaluation of Eutectic Fluoride Thermal Energy Storage Unit Compatability, Part I. Survey of Thermophysical Property Data and Description of Clad/Salt Sample Preparation. AFAPL-TR-75-92, Part I, October 1975.

VI. PERFORMANCE OF A CYLINDRICAL PHASE CHANGE THERMAL ENERGY STORAGE UNIT

This Section is a paper from the M.S. Thesis of Mr. R. Ponnappan which has been accepted for presentation at the AIAA Aerospace Sciences Meeting in January, 1982 and will be submitted for publication in The Journal of Energy.

VI. PERFORMANCE OF A CYLINDRICAL PHASE CHANGE THERMAL ENERGY STORAGE UNIT

6.1 Introduction

The latent heat Thermal Energy Storage (TES) concept is attractive because of its high energy storage densities over a narrow temperature range. Promising applications both in space and terrestrial thermal system [6.1,6.2] are apparent. Eutectic mixtures of fluoride salts have been found to release energy on the order of $1.25-4.25$ GJ/m^3 in the temperature range of 900-1000K. The thermophysical properties of such high temperature Phase Change Materials (PCM) and the heat transfer characteristics of TES devices containing them are very important in the design of thermal systems.

The objective of the present work was to design and construct a calorimeter system capable of working in a vacuum in order to evaluate the performance of a given cylindrical TES unit made of Inconel 617 and filled with the eutectic mixture of $64LiF-30MgF_2-6KF$ salt. This setup was planned to measure the melting and solidification temperatures, and the latent heat of fusion of the fluoride salt.

The data obtained provided a means of verifying an analytical model for solidification time and surface temperature. The thermal diffusivity of the PCM at its fusion temperature was calculated from the experimental information. No other literature values were found for comparison.

6.2 Theoretical Considerations of Melting and Solidification in a Cylinder

Analytical methods of solving the moving phase boundary problems range from the general approximate method of London and Seban 1943 [6.3] to the Modified Heat Balance Integral (MHBI) method of Tien 1980 [6.4]. Some of the other significant works are the Heat Balance Integral method of Goodman 1958 [6.5], the generalized numerical method of Tao 1967 [6.6] and the Enthalpy Model of Shamsundar and Sparrow 1975 [6.7]. The recent work of Tien on the solidification of cylindrical samples is an appropriate model for the analysis of energy extraction for the present TES system.

6.2.1 Problem Formulation

The problem considered is the freezing of an infinitely long cylinder of molten PCM when the latent heat extraction takes place at its outer surface with a constant coefficient of radiative heat transfer for the cooling coil of

109

the calorimeter. The coordinate system and the boundary conditions of this problem are set as in Fig. 6.1.

The following idealizations are made in order to represent the experimental unit into a convenient mathematical model:

- the ends of the cylindrical TESC are adiabatic;
- energy leaving the TESC wall is purely radiative and is completely absorbed by the calorimeter cooling coil;
- the TESC wall has uniform emittance and an average heat transfer coefficient $\bar{h}_r$ can be obtained from steady state heat losses;
- energy loss through lead wires and mounting fixtures are negligible and can be accounted for experimentally;
- thermal capacitive effects of the heater blocks and the TESC wall are negligible;
- the material (PCM) behaves like a pure substance so that its liquid-solid transition occurs at a single temperature, that is the melting point;
- the liquid is at its melting point just at the start of solidification which means that there is no heat transfer within the liquid;
- physical properties (α, C_p, ρ, k) are temperature independent and they are constant for the solid and liquid phases;
- convection effects within the liquid are negligible;
- no supercooling occurs upon solidification.

Under these assumptions, the temperature distribution within the solid and the propagation rate of the liquid-solid interface (or freezing rate) are obtained from the one-dimensional heat conduction equation in cylindrical coordinates given by the normalized partial differential equation together with the initial and boundary conditions as follows:

PDE:
$$\frac{1}{\bar{r}} \frac{\partial}{\partial \bar{r}} \left(\bar{r} \frac{\partial \bar{T}}{\partial \bar{r}} \right) = \frac{\partial \bar{T}}{\partial \bar{t}} \qquad (6.1)$$

AT THE CENTER:
$r = 0$
$\bar{r} = 0$
$\bar{z} = 0$
$1 - \bar{z} = 1$

AT THE WALL:
$r = r_0$
$\bar{r} = 1$
$\bar{z} = 1$ (LOCATION OF FREEZING FRONT)
$1 - \bar{z} = 0$ (FROZEN SHELL THICKNESS)
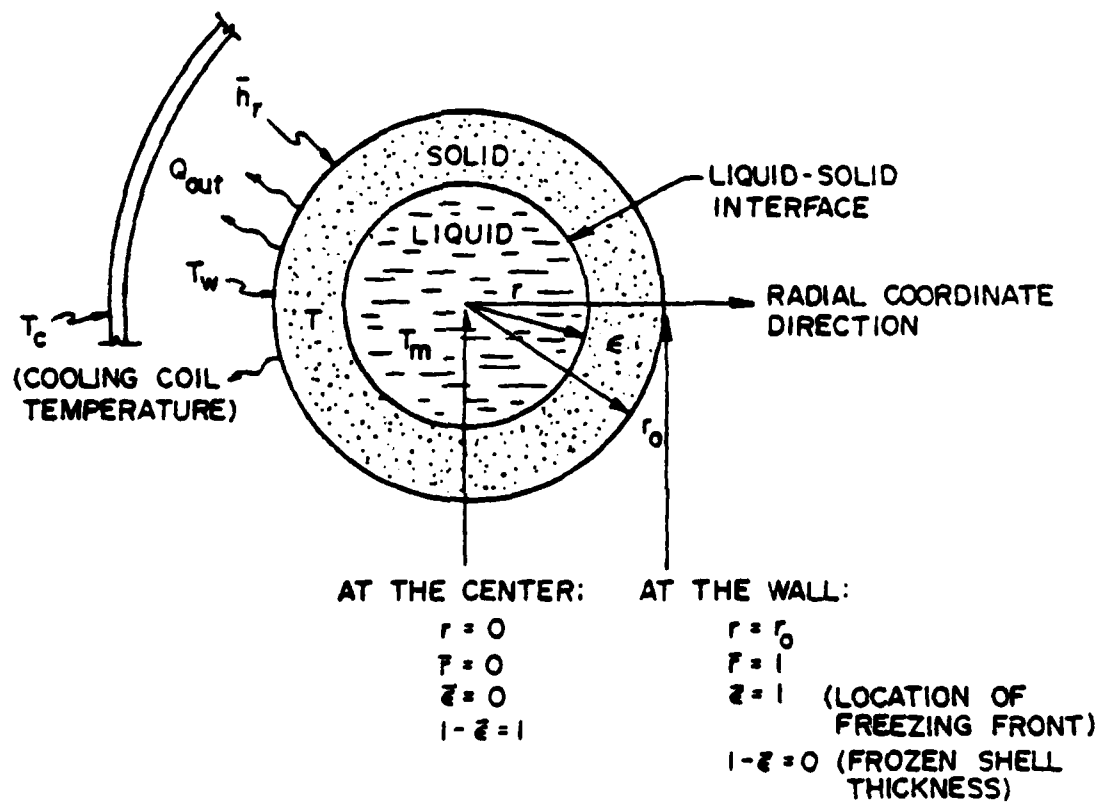
Figure 6.1 Coordinate System for the Cylindrical Geometry

$$\bar{T} = 1 \qquad\qquad \text{at } \bar{r} = \bar{\varepsilon} \qquad\qquad (6.2)$$

$$\text{B.C.:} \qquad \frac{\partial \bar{T}}{\partial \bar{r}} = G \frac{d\bar{\varepsilon}}{d\bar{t}} \qquad\qquad \text{at } \bar{r} = \bar{\varepsilon} \qquad\qquad (6.3)$$

$$\frac{\partial \bar{T}}{\partial \bar{r}} = -H\bar{T} \qquad\qquad \text{at } \bar{r} = 1 \qquad\qquad (6.4)$$

$$\text{I.C:} \qquad \bar{\varepsilon} = 1 \qquad\qquad \text{at } \bar{t} = 0 \qquad\qquad (6.5)$$

Where the normalization parameters are defined as,

$$T = \frac{T - T_c}{T_m - T_c} \;\; ; \quad \bar{r} = \frac{r}{r_0} \;\; ; \quad \bar{\varepsilon} = \frac{\varepsilon}{r_0} \;\; ; \quad \bar{t} = \frac{at}{r_0{}^2}$$

(Fourier Number)

$$H = \frac{\bar{h}_r \cdot r_0}{k_s} \;\; ; \quad G = \frac{L}{C_p(T_m - T_c)}$$

(Biot Number) $1/\text{Stefan Number} = \dfrac{1}{St}$

Integration of Eqn. 6.1 with respect to $\bar{r}$ between $\bar{r} = \bar{\varepsilon}$ and $\bar{r} = 1$ and using the boundary conditions gives,

$$\frac{d\Theta}{d\bar{t}} = -(1 + G)\, \bar{\varepsilon} \, \frac{d\bar{\varepsilon}}{d\bar{t}} - H\bar{T}_{\bar{r} = 1} \qquad\qquad (6.6)$$

where

$$\Theta = \int_{\bar{\varepsilon}}^{1} \bar{r}\bar{T}d\bar{r}$$

Equation 6.6 is the integral form of the heat-conduction equation which has to be solved for the temperature $\bar{T}$ and freezing front $\bar{\varepsilon}$ by suitable techniques.

6.2.2 Solution of the Heat Balance Integral

The method of Tien [6.4], MHBI has been used to transform Eqn. 6.6 into a second order ordinary differential equation with two initial conditions by assuming a quadratic function as the solution for $\bar{T}$ ($\bar{\varepsilon}$ ($\bar{t}$), $\bar{r}$). The initial value problem obtained has been solved numerically by using the fourth-fifth order Runge-Kutta method with an IBM-AMDAHL 360 computer system. A computer program was written and used in conjunction with a CAN-program called SUBROUTINE RKF45. The results of this computation are shown later in Figs. 6.10 and 6.11 and discussed under the results and analysis section along with the experimental results.

112

6.2.3 Heat Transfer Resistance

As soon as the solidification process begins, an interface of the solid and liquid PCM is created which moves away from the original heat exchange surface. The layer of solid PCM bounded by the wall and the interface offers a resistance which is a function of time, geometry and material. This resistance for the annular layer of the solid PCM shown in Figure 6.1 can be written as

$$R_H = \frac{\ell n\left(\frac{r_o}{\varepsilon}\right)}{2\pi k_s \ell} \tag{6.7}$$

This is non-dimensionalized by multiplying R_H by the factor $\frac{k_s A^2}{V}$ where A is the area of heat exchange and V is the volume of the PCM. Hence, the theoretical normalized resistance R_H^* is obtained as

$$R_H^* = R_H \frac{k_s A^2}{V} = -2\ell n(\overline{\varepsilon}) \tag{6.8}$$

which is a function of the location of the freezing front. R_H^* varies from zero at the start of the solidification ($\overline{\varepsilon} = 1$) to infinity towards the end ($\overline{\varepsilon} = 0$) and this provides the theoretical bound for an ideal cylindrical TES system.

The quantity $\overline{\varepsilon}$ in Eqn. 6.8 can be expressed in terms of a fraction ( ) defined as,

$$\chi = \frac{\text{weight of the annular layer solidified}}{\text{weight of the total PCM}}$$

or

$$\chi = \frac{r_o^2 - \varepsilon^2}{r_o^2} = 1 - \overline{\varepsilon}^2 \tag{6.9}$$

Therefore the relation Eqn. 6.8 can be expressed in terms of χ as

$$R_H^* = -\ell n(1 - \chi) \tag{6.10}$$

Further, in terms of energy extraction from the PCM, the fraction can be expressed as a time dependent function as

$$(t) = \frac{1}{\dot{m}_{PCM} L} \int_o^t \dot{Q}_{LH}(t)\Delta t \tag{6.11}$$

where the integrand represents the latent heat release from the start of solidification up to any instant of time t within the region of ''temperature

113

arrest''. Figure 6.9 will compare the theoretical and experimental resistance values.

6.3   Performance of a Cylindrical TESC

6.3.1 Physical Details of the Sample

The TESC sample is 12 inches long and 1 inch in diameter (OD) and its cross-section is shown in Fig. 6.2. The container has a longitudinal seam-welded body and electron beam welded flat end-caps, all made of Inconel 617. It has been filled under extreme cleanliness conditions with 225.519 grams of the eutectic fluoride salt and the total weight is 571.2 grams. The container design and filling details are given in Ref. [6.8].

6.3.2 Description of the Experimental Setup

The setup consists of a vacuum chamber – 8 inches in diameter (ID), cross-shaped stainless steel tubular chamber fitted with detachable vacuum joint flanges and feed-throughs and hooked to a Vacsorb/Vacion pumping unit of 40 liter/sec capacity and a calorimeter – comprising of the TESC sample, electric heater blocks of clamp-shell type in two cylindrical halves, Chromel-Alumel thermocouple temperature measuring circuitry and instrumentation and water circulated copper cooling coil. A schematic diagram of the experimental setup is given in Fig. 6.3.

The calorimeter was designed to minimize heat losses and to maintain a uniform temperature throughout the length of the TESC and had an electric heater of the semi-cylindrical annular-shell type. The TESC together with the thermocouples was housed inside the core region of the heater shells and this whole assembly was held concentrically inside a closely-coiled copper cooling water coil which in turn was inside the vacuum chamber. The water line, electrical and thermocouple lead connections were taken out through proper feed-throughs in the vacuum chamber. The cooling coil was insulated with stainless steel and aluminum foils to prevent radiation loss to the outer wall. Convection loss was eliminated by evacuating the chamber to at least 10^{-3} torr. The only mode of heat exchange allowed between TESC and heater assembly and the cooling coil was by radiation. Figure 6.4 gives the schematic diagram of the calorimeter.

114

ELECTRON BEAM - WELDED ON BOTH ENDS

END CAP

25.4-DIA. INCONEL 617 TUBE

1.58

304.8

1.58

3.175
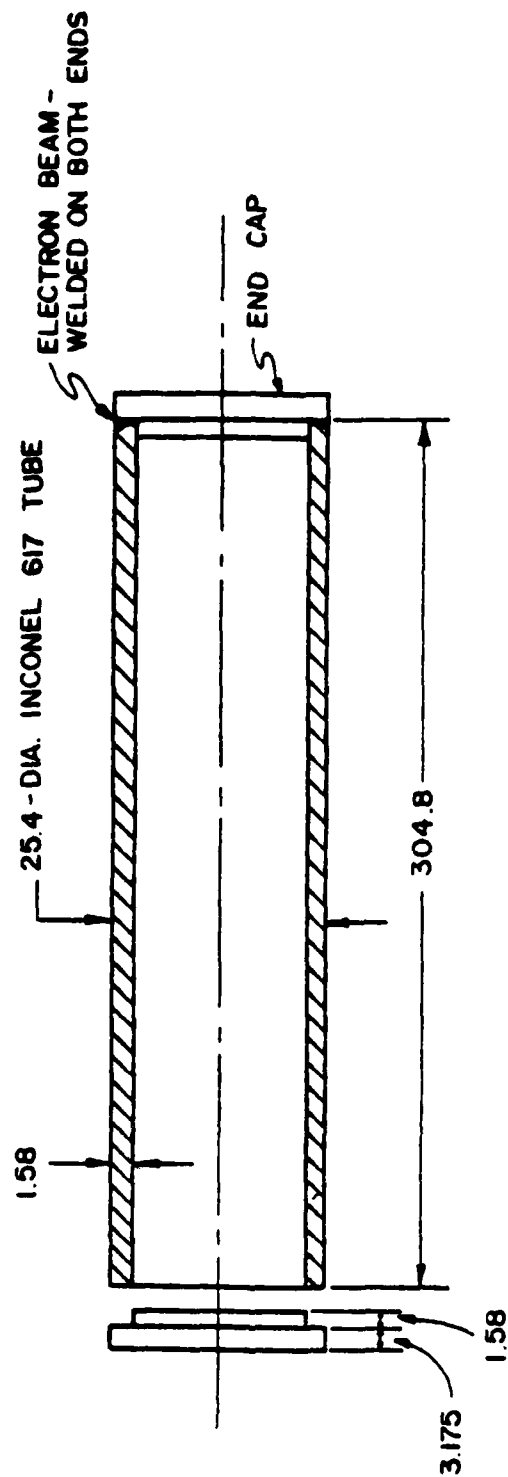
ALL DIMENSION IN mm ONLY

Figure 6.2 - TESC Sample
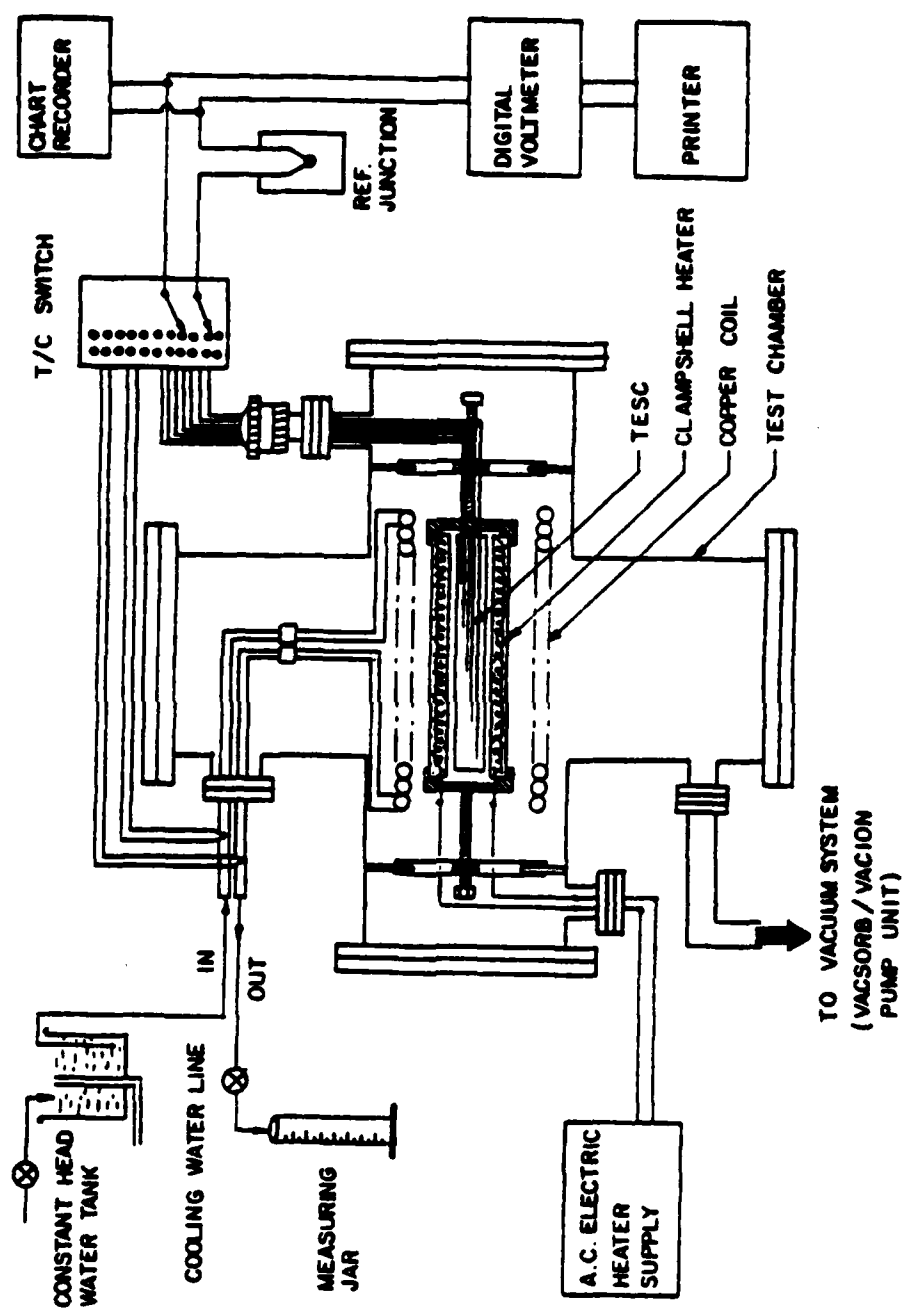
Figure 6.3   Schematic of the Experimental Set Up

116

COOLING WATER Q_{CAL}

IN ΔT_{CW} OUT

Q_{IN}

ELECTRIC
HEATER
INPUT

TESC

THERMO-
COUPLE
LEADS

Q_{SS}

RADIATION SHIELDS —

VACUUM CHAMBER

MIN-K INSULATION
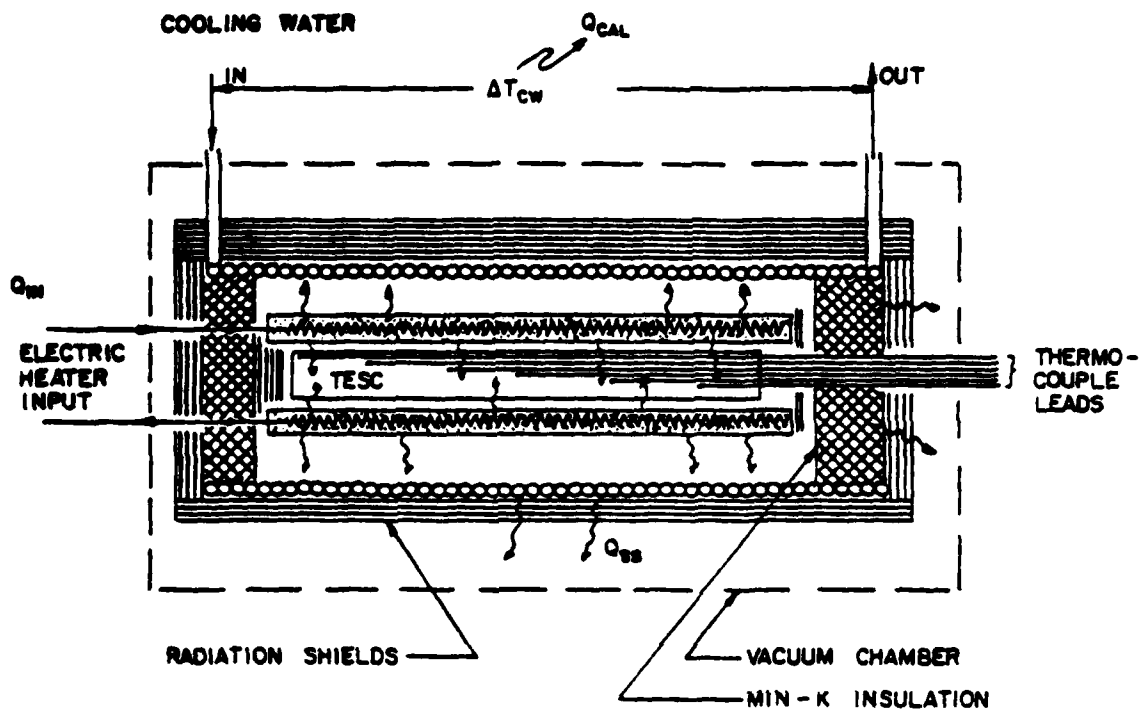
ENERGY BALANCE:

1.) STEADY STATE: $\qquad$ $Q_{IN} = Q_{CAL} + Q_{SS}$

2.) HEATING: $\qquad$ $Q_{IN} = Q_{CAL} + (SH + LH)_{TESC} + Q_{SS}$

3.) COOLING: $\qquad$ $Q_{IN} = 0$

$\qquad\qquad\qquad$ $Q_{SS} + Q_{CAL} = -(SH + LH)_{TESC}$

Figure 6.4   Schematic of the Calorimeter with Energy Balance

117

The energy required to heat the TESC to the salt melting point (that is from ambient to 710°C) was estimated to be 242.8 watt-hour assuming no heat losses. A heat loss equal to that from the outer surface of the electric heater during a 45 minute heating period produces a calculated power of 650 watts.

The water-cooling coil design was based on the criterion of maximum energy input to the TESC and minimum temperature differential between inlet and outlet water temperatures. Maximum output occurred when the TESC was maintained at steady state above the melting point of the salt (998K). A maximum temperature rise to 363K was assumed in order to avoid boiling of water within the coil. With these values, the radiated power absorbed by the cooling coil was 905 watts and the cooling water flow rate required was 22 liter/hour. A constant-head water tank arrangement provided a maximum flow rate of 40 liters/hour which was adequate for the present experiment. The cooling coil was formed out of annealed 3/8 in. copper tube with 37 closely-coiled helical turns with a 3.5 in. coil ID. Three to four layers of polished stainless steel sheet wrapped around the cooling coil provided the thermal insulation at the periphery while MIN-K type high temperature insulation together with two to three layers of aluminum foil shielded the ends.

A vacuum environment was necessary for this experiment in order to avoid oxidation of the TESC wall when heated to high temperature and to make the heat balance calculations simpler by eliminating convection heat losses from the TESC. However, conduction loss through the thermocouple and electric heater lead wires and through the mounting fixtures were not fully eliminated but minimized. The vacuum system was a Varian Vacsorb/Vacion pumping unit which provided 10^{-6} torr.

6.3.3 Experimental Procedure

Electrical power to the heater was supplied through a variac and watt-meter and the input could be regulated. The power input reading on the wattmeter was counter-checked by precisely measuring the resistance of the heater coil in steady state conditions (998K) and the voltage input. Energy output through circulating water was obtained by monitoring the inlet and outlet temperatures and the flow rate.

Temperatures along the length of TESC outer wall were measured with nine thermocouples of chromel-alumel type and 20 SWG size. Thin ceramic beads for

high temperature application were used to give rigidity and insulation for the thermocouples. Proper contact of the thermocouple bead with the TESC wall was ensured by a strap of stainless steel strip spot-welded around the TESC. The thermocouples were connected to the instrumentation consisting of a junction box, a switch, a thermoelectric reference junction, a digital voltmeter and a printer. A continuous charg recording of the TESC wall temperature at a slow speed of 1''/hour indicated whether steady state was attained or not.

6.4 Experimental Results and Analysis

6.4.1 Steady State Losses and Temperature Profiles

Steady state heat losses for the system were calculated by measuring the heater input and the calorimeter output powers when the temperatures of all the thermocouples remained steady. The difference between the input and output powers gave the steady state losses which account for the heat lost by conduction in thermocouple leads, heater electrical leads and the TESC support pivots and by radiation at the ends where no cooling coils were present. These measurements were made at different power input levels ranging from 150-600 watts. Tests were repeated several times with inputs sufficient to cause melting such that repeatability was ensured. Figure 6.5 shows the steady state losses as a function of TESC wall average temperature. The losses vary from 25 watts at 723 K to 50 watts at 1023K which is about 8-16% of the input power. Surface temperatures along the axial lengths of the TESC were monitored at different conditions of the cooling cycle. Figure 6.6 provides the representative axial temperature profiles of the horizontal mode test. The profiles indicate that the temperature remained fairly uniform at the center section while the end temperatures dropped below the average. The large gradient was due to the uncontrollable end and lead-losses of the system.

6.4.2 Melting and Freezing Points of the Salt

The melting point of the salt could not be directly measured since the salt was in a sealed container. Temperature measurements on the container wall during heating of the TESC provided an indirect method of obtaining the melting point. The melting curves plotted for two different heating conditions are shown in Fig. 6.7 and it can be seen that the Latent Heat
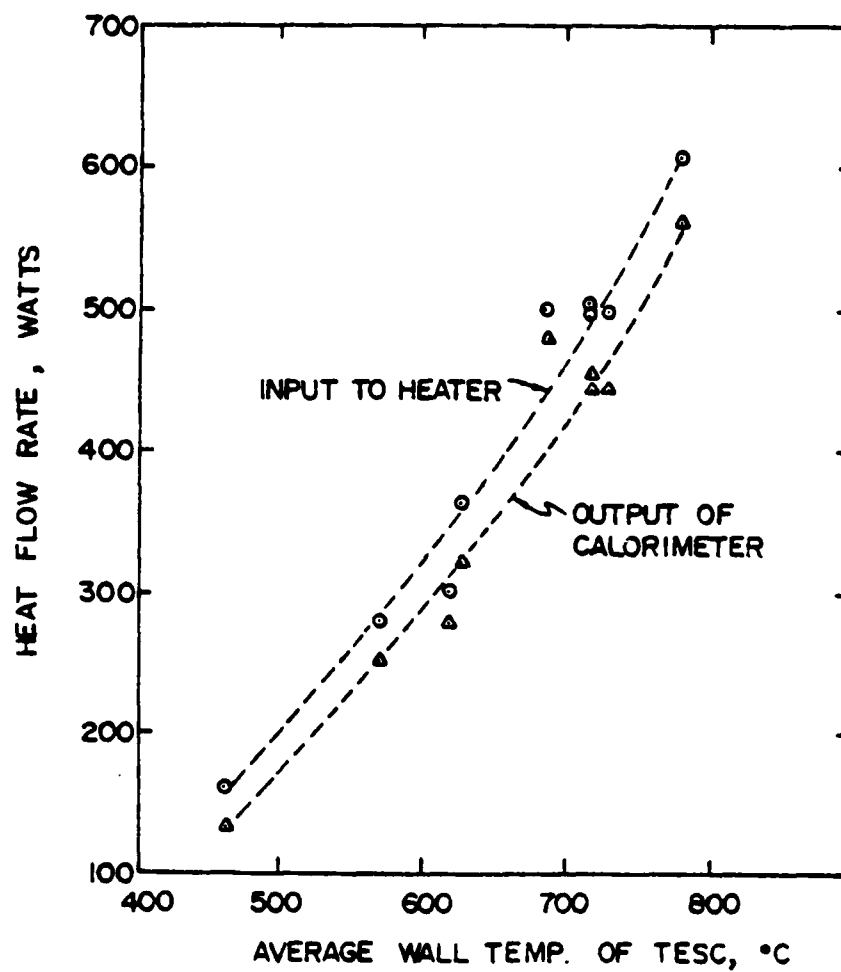
Figure 6.5 Steady State Heat Loss
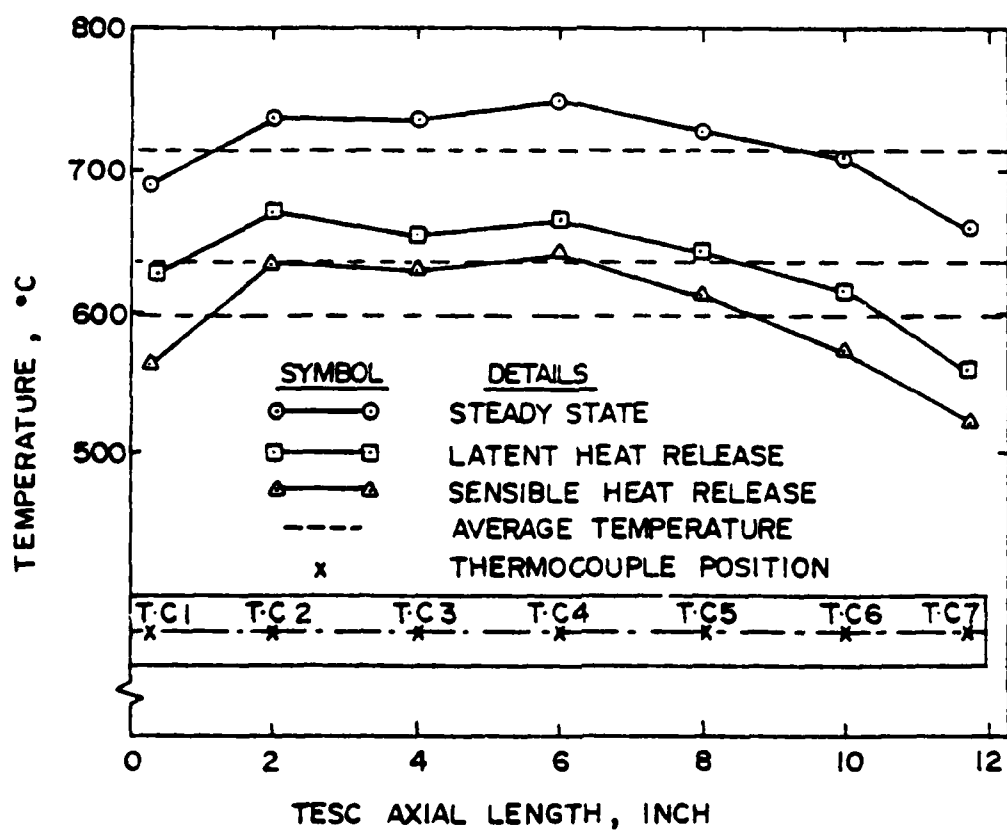
Figure 6.6   Axial Temperature Profile (Horizontal Mode Testing)
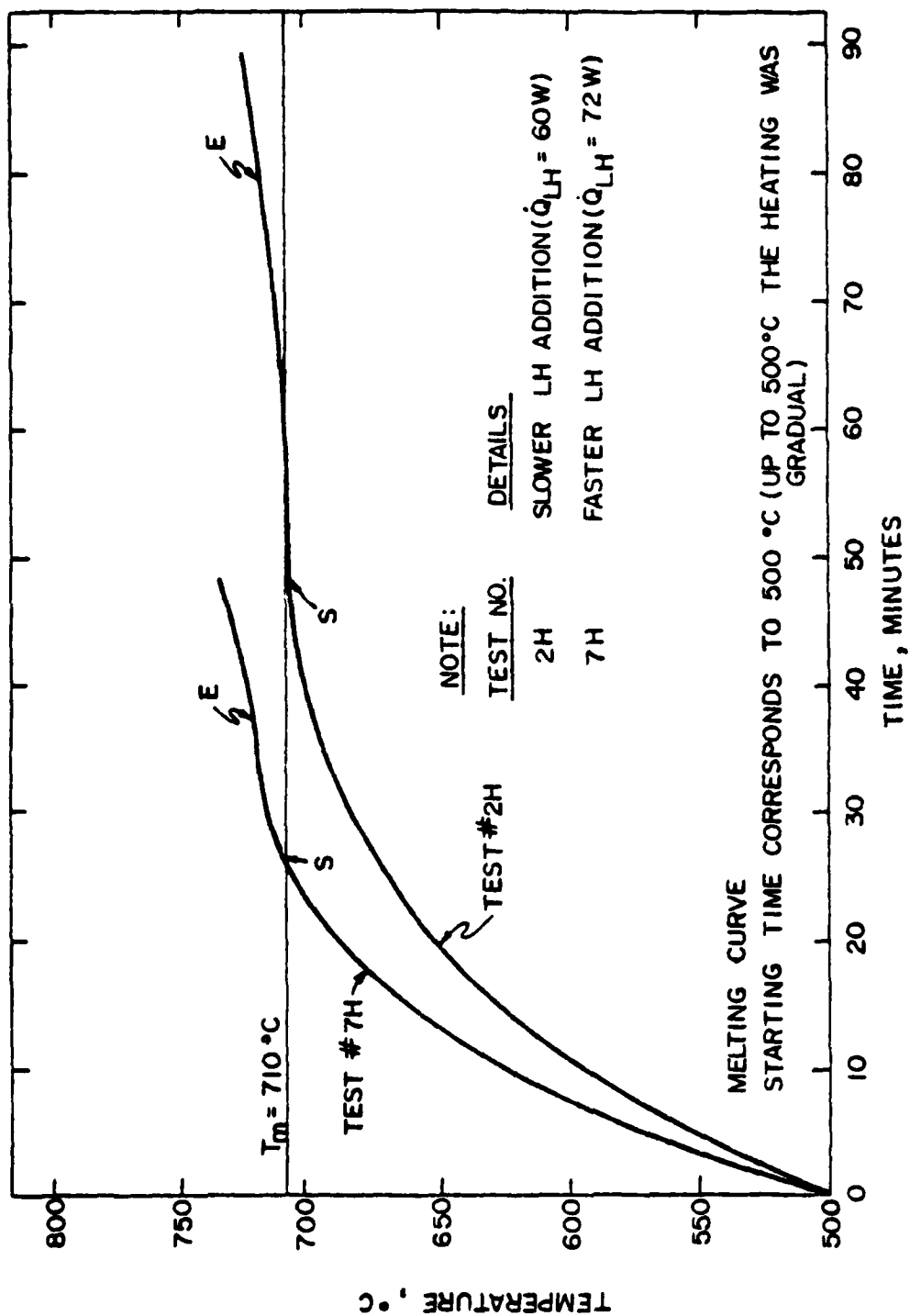
Figure 6.7 Melting Curves (Temperature Measured at T.C. #4)

122

addition takes place at fairly constant temperatures near 983 ± 2K which corresponds to the melting point. This agrees very well with the results of [6.9] 986K and of [6.10] 983K. An error of ± 5K is reasonable in this value in order to account for the measurement errors, the temperature drop across the TESC wall and the non-uniformity in the axial temperature of the unit.

6.4.3 Solidification Temperature

The freezing point may not be the same as the melting point. Differences arise because of subcooling and the effects of impurities. Melting points are generally reproducible but freezing points are often not. Figure 6.8 is a typical solidification curve. The freezing point is approximately the constant temperature region in which the latent heat release takes place. Due to the external temperature measurement and the loss of sensible heat from the solidified shell, the constant temperature region does not appear exactly constant. As soon as the solidification begins, a shell of solid PCM forms at the inside of the TESC wall around the core of the molten PCM. When the sol-idification proceeds with time, the TESC wall temperature cools down even though the molten core temperature remains constant at the melting point. In the present experiment it was observed that the solidification started when the wall temperature was approximately 944K and this value was reproducible during all the solidification tests (about 23 tests). The solidification temperature for the same eutectic mixture measured by direct method (Differential Scanning Calorimetry by Perkin-Elmer Corporation) has been reported as 955K [6.9] and by an indirect method similar to the present experiment, by [6.10] as 978K.

6.4.4 Latent Heat and Solidification Time

In the present experiment it was observed that the latent heat release took place over a temperature range of 25K and the duration of ''temperature-arrest'' was about 10.5 minutes as shown in Fig. 6.8. The latent heat release was estimated by the simple energy balance relation,

$$\dot{Q}_{out}\Delta t_f = \dot{m}_{PCM} L \qquad (6.12)$$

or
$$L = \frac{\dot{Q}_{out} \Delta t_f}{\dot{m}_{PCM}}$$ which yields L = 782.26 J/gm.

This value closely agrees with 793.50 J/gm reported in [6.9]. Table 6.1 compares the results of the present experiment with those from the literature.
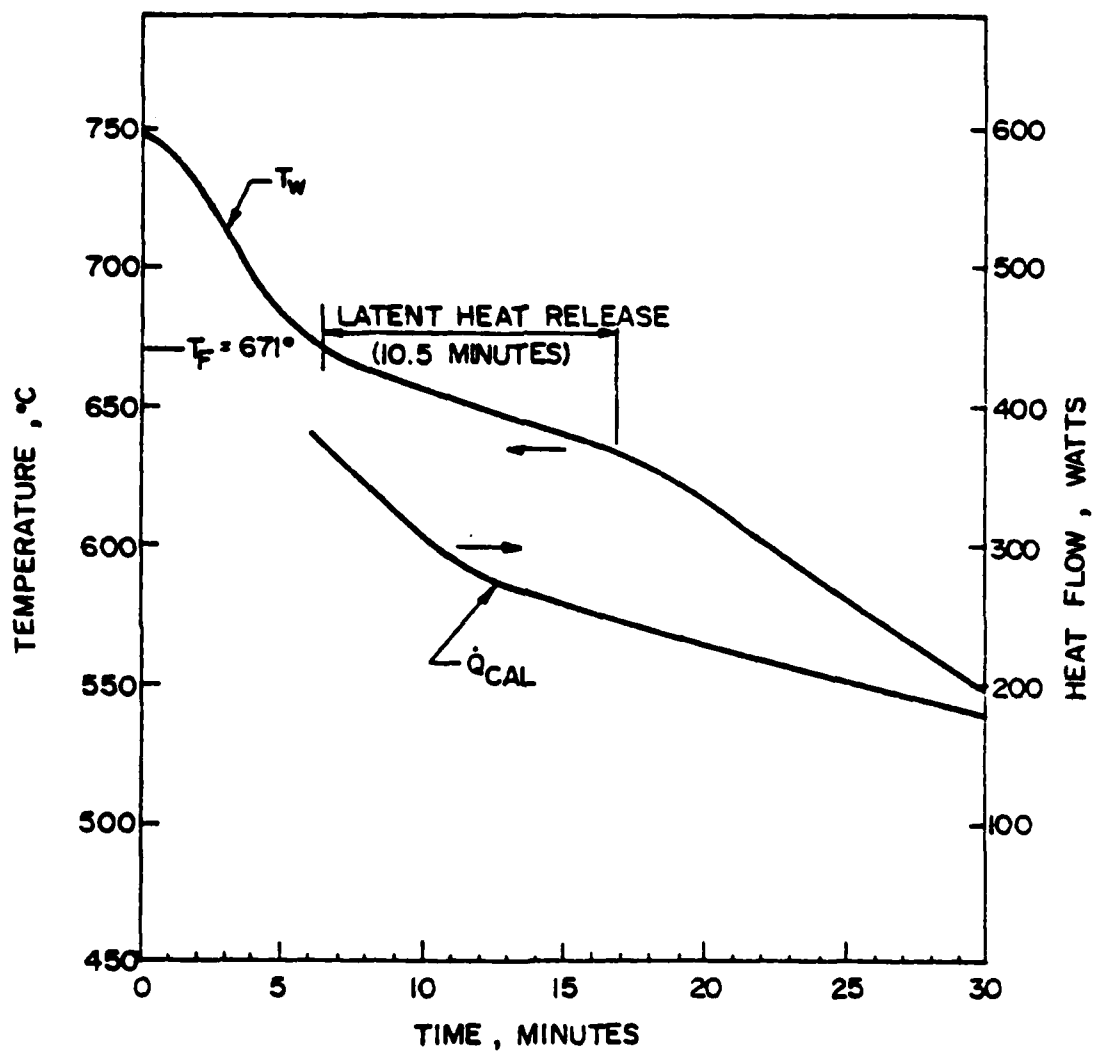
Figure 6.8   Solidification Curve (Test #15C)

TABLE 6.1

THERMOPHYSICAL PROPERTIES OF THE SALT (PCM)

Serial No.	Details			Data Source
1	Name of the salt: LiF-MgF$_2$-KF Eutectic mixture			
2	Composition, %: 63.5 - 30.5 - 6 (Molar)			[6.9, 6.13]
3	Density, gm/cm^3			
	solid at 25°C	:	2.918	
	liquid at 750°C	:	2.182 ±0.022	[6.13]
4	Conductivity, w/cm°C			
	at fusion temp.	:	0.0711	[6.11]
5	Specific heat, J/gm°C			
	solid at fusion temp.	:	2.025	[6.9]
	computed from other data:		3.638	[6.13]
6	Diffusivity, cm^2/sec			
	solid at 25°C	:	0.017	[6.13]
	solid at 455°C	:	0.009	
	solid at fusion temp	:	0.00799*	
7	Latent heat of fusion, J/gm			
	By DTA method	:	753.6	[6.13]
	By DSC method	:	793.5	[6.9]
	Method not known	:	814.12	[6.11]
	Present experiment	:	782.26*	
8	Thermal Events:			

	Melting Point K	Freezing Point K	Reference
By DSC method	986	955	[6.9]
By DTA method	981	976	[6.13]
Method Unknown	983	–	[6.11]
Present experiment	983+	944+	–

*Results of the present experiment

6.4.5 Heat Transfer Parameters

The TESC and the cooling coil are radiatively coupled since the test chamber was evacuated to 10^{-5} torr or better. When the capacitive effects of the heater shell on the heat transfer between TESC and the cooling coil were neglected, the overall heat transfer coefficient due to radiation was evaluated as:

$$h_r = \frac{\dot{Q}_{cal}}{A(\bar{T}_w - \bar{T}_{cw})} \qquad (6.13)$$

For the present setup, h_r varied from 31 to 42 w/m^2°C for $\dot{Q}_{cal}$ varying between 562 and 44 watts; $\bar{T}_w$ varied between 1052K and 735K while $\bar{T}_{cw}$ = 303K and A = 0.024322 m^2.

The dimensionless parameter representing the ratio of the internal to the external resistance of the TESC defined using the radius of the cylindrical TES as the significant dimension is the Biot Number and this was calculated as $B \simeq 0.065$ using the available literature value for k_s from Ref. [6.11]. The Stefan Number which gives the ratio of the heat of fusion to the sensible heat between the fusion point and the sink temperature was computed as $St \simeq 3.27$ or $G \simeq 0.305$. This number represents a property of the PCM, and PCMs generally have St values between 0 and 4 as noted in Ref. [6.12]. The Fourier Number representing the non-dimensionalized time required to solidify a given thickness of salt was the basis for estimating the thermal diffusibility of the salt.

6.4.6 Comparison of Experimental and Theoretical Results

The non-dimensionalized resistance to heat transfer R_H^* and the solidified or melted fraction of the PCM, X, are plotted (R_H^* as a function of X) in Fig. 6.9. In this figure, the resistance curves obtained for the melting and solidification processes at different heat flow rates are compared with the theoretical resistance for the cylindrical geometry. The resistance curves for solidification follow somewhat closely the theory and tend to merge only at the end of complete solidification. The reason for the deviation may be attributed to the possible non-uniform freezing within the cylinder as it is evident from the axial temperature profiles shown in Fig. 6.6. The uneven start of solidification directly violates the assumption of concentric solidification and hence results in larger resistance values in actual experiments. For the same solidified fraction (X), higher heat flow has
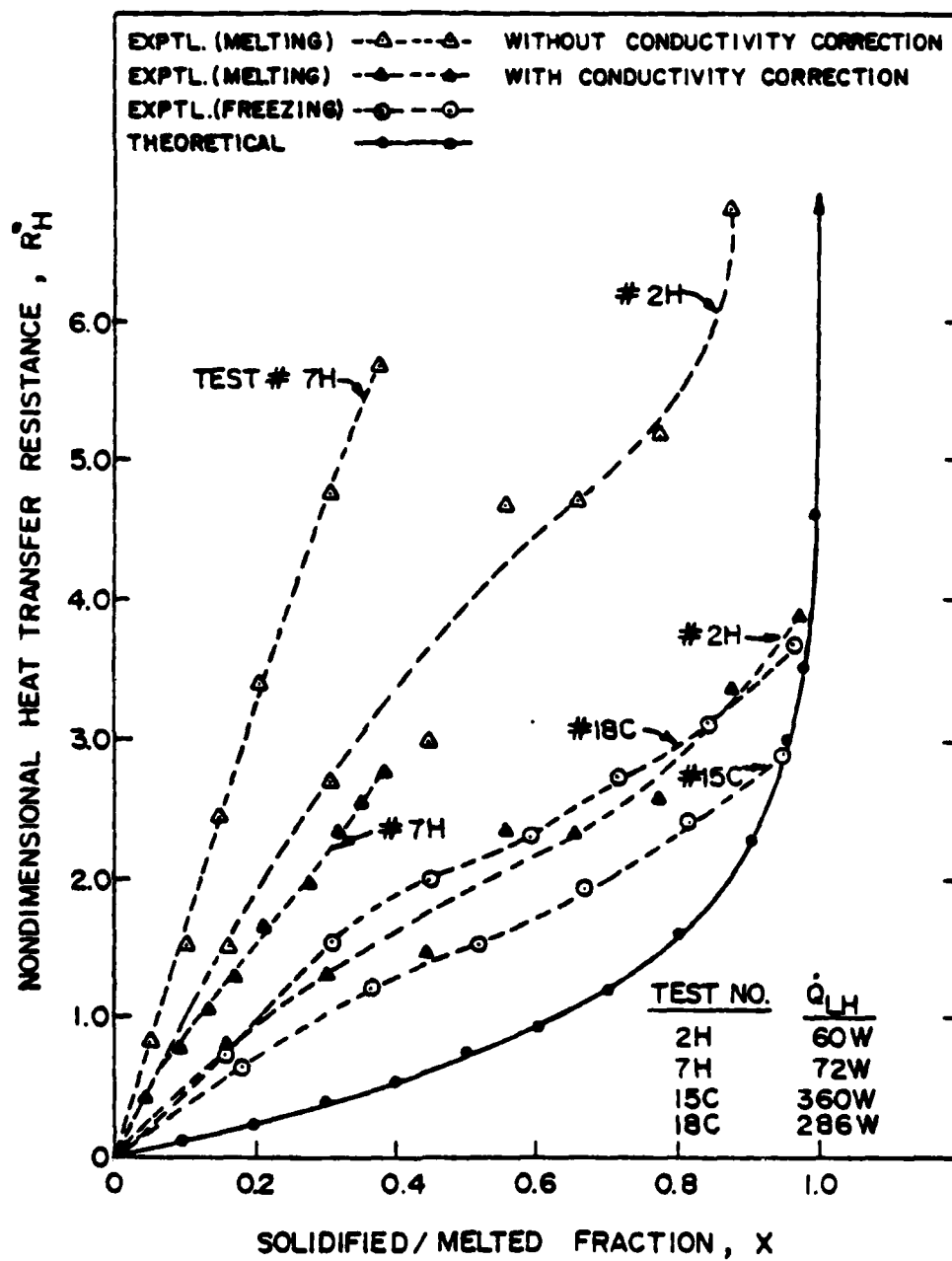
Figure 6.9 Heat Transfer Resistance of PCM During Solidification/Melting

lower resistance since the heat transfer occurs at nearly the same temperature differences.

The resistance curves for melting differ from the theoretical curve. This is due to the assumption of equal thermal conductivity for the solid and liquid phases ($k_s = k_\ell$) where in practice it is not true. There are no other published data for k_ℓ for this salt. Using the estimated value of k_ℓ, a correction could be applied in computing R_H^* for the melting cases as shown in Fig. 6.9. This correction brings the curves to that of solidification cases. For the same χ, higher heat flow has larger resistance contrary to the freezing case. This could be due to incomplete and non-uniform melting. If the thermal conductivity of the molten salt is accurately known, the resistance values of melting and freezing in a cylinder under identical heat flow can be estimated correctly. The resistance curves could assist in understanding the TESC behavior with respect to a given geometry and in general this would help determining proper size and shape.

The analysis for obtaining the location of the solid-liquid interface in the solidification process in a cylinder has been examined earlier and the result of the analysis for the present experimental parameters ($H = 0.065$; $G = 0.305$) is shown in Figure 6.10 and are compared with the results of Tien [6.4] for $H = 0.5$ and $G = 1.0$. It was determined that the computer program performed as projected in [6.4], and computations were repeated for the H and G values obtained here. It can be seen that the location of the freezing front or the solid-liquid interface depends on the H and G values while the initial slope of the curve at the start of solidification is determined from $\frac{d\bar{\varepsilon}}{d\bar{t}} = -\frac{H}{G}$ which is linear and constant for the given H and G. As demonstrated in [6.4], this computation accurately produces the time at which the freezing front would reach the center without encountering the problems faced by some of the earlier semi-analytical works [6.5, 6.6]. Since the solidification depends upon G (a physical property of the TES) and H (a parameter of the operating system), it is very easy to compute the freezing front and the time of complete solidification for any H and G combinations.

6.4.7 Surface Temperature and Freezing Rate

The computer program also allowed computation of the non-dimensional surface temperature $\bar{T}$ and freezing rate $-\frac{d\bar{\varepsilon}}{d\bar{t}}$ of the TES material as a function of frozen shell thickness $(1-\bar{\varepsilon})$. The curves obtained for the present
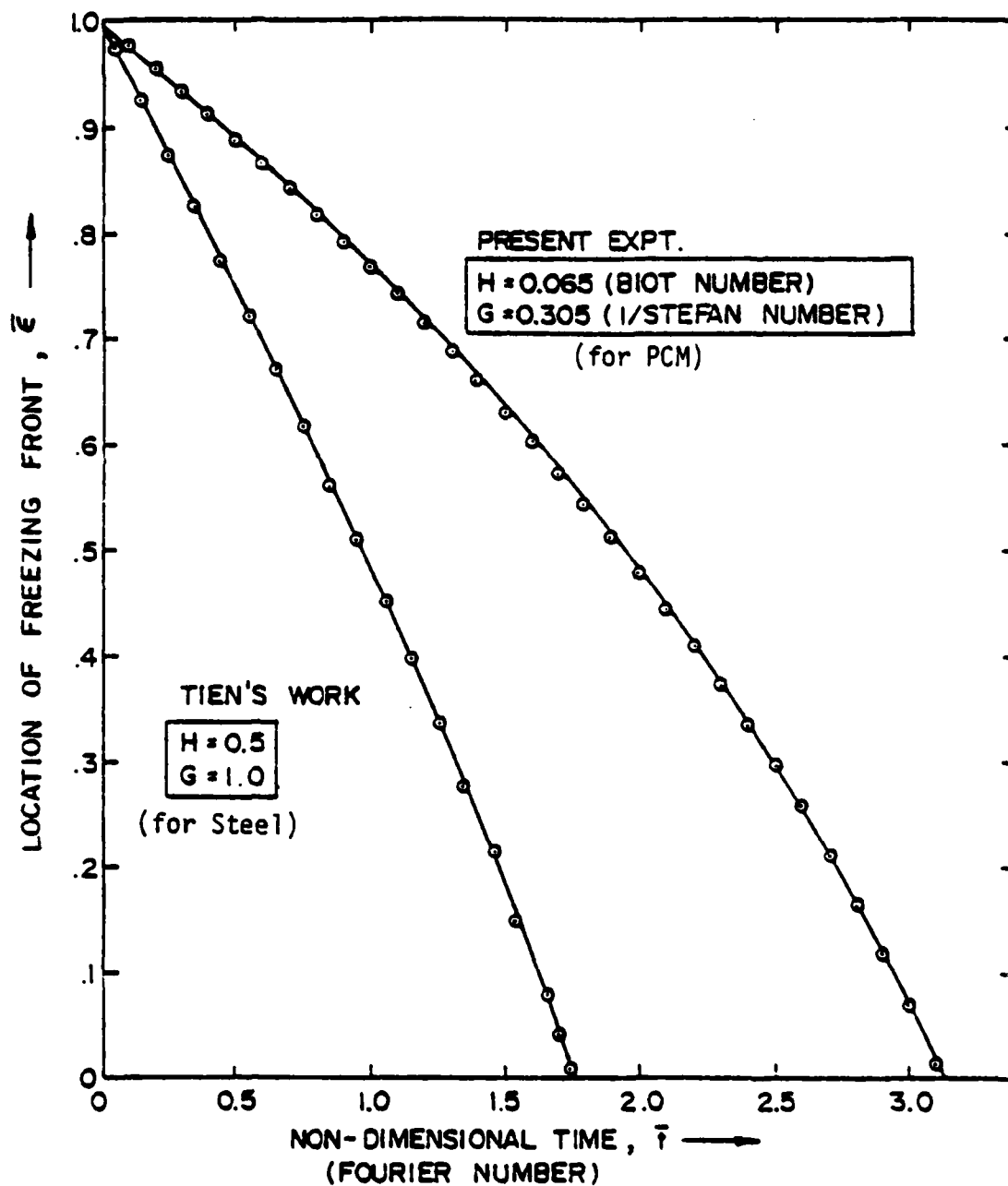
Figure 6.10   Location of Freezing Front with Time

experiment are shown compared with those of [6.4] in Fig. 6.11. In order to compare the numerically computed surface temperatures with the experimentally measured values, the cooling curve temperatures corresponding to the ''temperature-arrest'' region were plotted after normalizing in Figure 6.11. Since there was no possibility of experimentally measuring the frozen shell thickness $(1-\bar{\varepsilon})$, the abscissa for the experimental $\bar{T}$ was taken as the theoretical value corresponding to $\bar{t}$ from Fig. 6.10. The experimental surface temperature tends to drop more slowly than that of the analytical prediction towards the end of complete solidification. This deviation could be attributed to the unaccounted thermal-mass of the TESC metal wall and the heater blocks present in the system.

6.4.8 Thermal Diffusivity of TES Salt

The thermal diffusivity, α of the TES material was obtained from the relation $\alpha = \frac{r_o^2 \bar{t}}{t}$. Substituting the values obtained from Fig. 6.10 as $\bar{t} = 3.12$ for complete solidification and from Fig. 6.8 as $t = 10.5$ minutes, α for the 2.54 cm diameter TESC is determined to be 0.00799 cm²/sec. This value corresponds to the fusion temperature of 944K and it lies close to the value $\alpha_{728K} = 0.009$ cm²/sec reported in [6.13].

6.5 Conclusions

In the present work, a calorimeter system capable of working in vacuum was designed and assembled to evaluate the heating and cooling characteristics of a cylindrical Thermal Energy Storage container filled with a eutectic mixture of 64LiF-30MgF$_2$-6KF salt. Thermal data of the salt namely, melting/freezing points, latent heat of fusion and diffusivity were determined from the experimental data. The results were as follows:

- Melting temperature   = 983K
- Freezing temperature = 944K
- Latent heat of fusion = 782.26 J/gm
- Thermal diffusivity at the fusion temp. = 0.00799 cm²/sec

The first three values corroborated with literature values. Thermal diffusivity was not available.
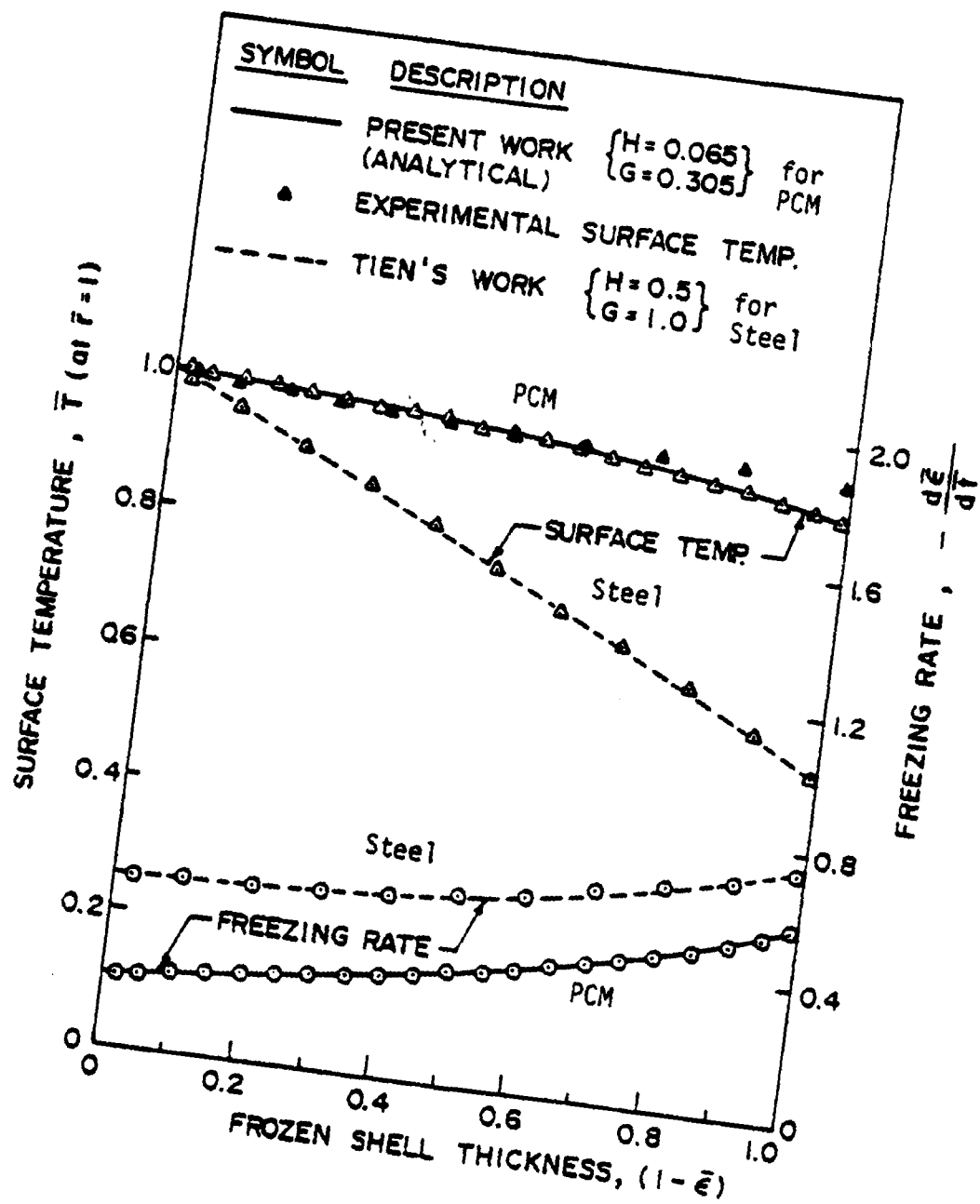
Figure 6.11 Non-Dimensional Surface Temperature and Freezing Rate

The Modified Heat Balance Integral method of Tien [6.4] was successfully used to predict the solidification time and the surface temperature of the cylindrical TES unit.

A dimensionless factor for heat transfer resistance (R_H^*) was defined for the cylindrical geometry and the experimental resistance factors for melting and freezing were evaluated and compared with that of the theoretical bounds.

It was demonstrated that the thermal diffusivity of the PCM could be computed from the Fourier number if the time for complete solidification was available from the experiment as well as from the analytical solidification model.

6.6   References

[6.1]   Charles Wyman, ''Thermal Energy Storage Applications: An Overview,'' Solar Energy Research Institute, Golden, Colorado, SERI/TR-34-089, March 1979.

[6.2]   Petri, R.J., Claar, T.D., and Tison, R.R., ''High Temperature Molten Salt Thermal Energy Storage Systems,'' DOE/NASA/0806-79/1 NASA-CR-159663, February 1980.

[6.3]   London, A.L., and Seban, R.A., ''Rate of Ice Formation,'' Transactions ASME, Vol. 65, 1943, pp. 771-778.

[6.4]   Tien, R.H., ''A Heat Transfer Analysis for Solidification of Rounds,'' Journal of Heat Transfer, Trans. ASME, Vol. 102, May 1980, pp. 378-379.

[6.5]   Goodman, T.R., ''The Heat-Balance Integral and its Application to Problems Involving a Change of Phase, '' Transactions ASME, Vol. 80, Feb. 1958, pp. 335-342.

[6.6]   Tao, L.C., ''Generalized Numerical Solutions of Freezing a Saturated Liquid in Cylinders and Spheres,'' AIchE Journal, Vol. 13, No. 1, Jan. 1967, pp. 165-169.

[6.7]   Shamsundar, N., and Sparrow, E.M., ''Analysis of Multidimensional Conduction Phase Change via the Enthalpy Model,'' Journal of Heat Transfer, Vol. 97, 1975, pp. 330-340.

[6.8]   Davison, J.E., ''Evaluation of Eutectic Fluoride Thermal Energy Storage Unit Compatibility Part I. Survey of Thermophysical Property Data and Description of Clad/Salt Sample Preparation,'' Wright-Patterson Air Force Base, Ohio, AFAPL-TR-92-Part I. Oct. 1975.

[6.9]   Richter, R., ''Thermal Energy Storage Demonstration Unit for Vuilleumier Cryogenic Cooler,'' Xerox Electro-Optical Systems, AFAPL-TR-77-65, Feb. 1978.

[6.10]   Feuermann, D., and Jacobson, D.L., ''Evaluation of a Sodium Heat
         Pipe/Thermal Energy Storage Unit Utilizing LiF-MgF$_2$-KF Phase Change
         Material,'' <u>AIAA 14th Thermophysics Conference</u>, June 4-6, 1979.

[6.11]   Bandow, H.E., Crisp, J.N., ''Analysis of Solidification in a
         Cylindrical Annulus with and without Internal Longitudinal Fins,''
         University of Dayton, School of Engineering, USDE TR 78-07, 1978.

[6.12]   Solomon, A., ''Melt Time and Heat Flux for a Simple PCM Body,'' <u>Solar
         Energy</u>, Vol. 22, 1979, pp. 251-257.

[6.13]   Davison, J.E., ''Feasibility Study of Inorganic Oxides for Thermal
         Energy Storage Applications,'' University of Dayton Research
         Institute, AFAPL-TR-77-70, Nov. 1977.

VII. PERFORMANCE OF A CYLINDRICAL PHASE CHANGE TES UNIT TO DETERMINE CONVECTIVE EFFECTS IN THE SALT

7.1 Introduction

This work is a direct follow-on to the M.S. Thesis research of R. Ponnappan presented in Section 6.

The thermal energy is stored in a cylindrical capsule of Inconel 617 alloy containing 225 grams of lithium fluoride, magnesium fluoride and potassium fluoride whose molar composition is 64 LiF-30MgF$_2$-6KF [7.1]. Melting and solidification cycles have been performed in the vertical and horizontal modes. The experimental setup consists of a vacuum chamber containing the storage unit and a calorimeter. The thermocouples record the capsule wall and cooling water temperatures at different locations.

The principal aim of this work is to present experimental results for the melting point, freezing point, solid-liquid phase change enthalpy (latent heat of fusion) and range of temperatures for change of phase for the capsule in the vertical and horizontal positions.

7.2 Analytical Model

A simple analytical model to obtain the heat capacity (ρc_p) of the unit is based on one dimensional, non-steady heat conduction approach, and assumed to be an infinitely long cylinder (30.5 cm in length, 2.54 cm in diameter) under constant heat flux conditions. The temperature distribution for the capsule before the change of phase is given by:

$$\frac{\partial T^*}{\partial F_o} = \frac{1}{r^*} \frac{\partial}{\partial r^*}\left(r^* \frac{\partial T^*}{\partial r^*} \right) \; ; \; \left.\frac{\partial T^*}{\partial r^*}\right|_{r^*=0} = 0 \; ; \; \left.\frac{\partial T^*}{\partial r^*}\right|_{r^*=1} = \frac{R}{k}\frac{q_{out}}{T_m-T_o} \quad (1)$$

Where the dimensionless parameters are defined according to

$$T^* = \frac{T-T_o}{\dfrac{R\; q_{out}}{k}} \; ; \; F_o = \frac{t\alpha}{R^2} \; ; \; r^* = \frac{r}{R} \quad (2)$$

The dimensionless temperature distribution for the surface $r^* = 1$ is

$$T^* = 2F_o + \frac{1}{4} - \sum_{n=0}^{\infty} \frac{2}{\lambda_n^2} e^{-\lambda_\eta^2\, F_o} \quad (3)$$

genvalues are given by $J_1(\lambda_\eta) = 0$. Numerical analysis 2 shows that for
r numbers (F_o) greater than 0.17 the series in (3) can be neglected and
·ror involved is smaller than 2%. For Fourier numbers greater than 1/8,
·nstant 1/4 can also be neglected and the dimensionless temperature dis-
ion at the surface becomes

$$T^* = 2F_o \; ; \; T(t) = T_o + \frac{1}{\pi R^2 L} \frac{q_{out}}{\rho c_p} \chi \, t \qquad (4)$$

;imple analytical linear model can be easily related with the experi-
response for heating and cooling processes where a linear relation
·n temperature and time has been found. From the comparison of analyti-
nd experimental slopes (E) the thermal capacity of the unit can be

$$M_e = \frac{1}{\pi R^2 L} \frac{q_{out}}{\rho c_{\rangle}} \; ; \; \rho c_p = \frac{1}{\pi R^2 L} \frac{q_{out}}{M_e} \qquad (5)$$

· calculations, axial conduction and free convection have been neglected.

Results

n the present experiments, melting and solidification points can not be
ly measured. Temperature measurements on the container wall during
g and cooling provide an indirect method of finding melting and freezing
Two melting curves for the unit in vertical and horizontal positions
·own in Fig. 7.1. It can be seen that the latent heat addition takes
at fairly constant temperature around 710°C which corresponds to the
g point.
ne solidification curve for the unit in the horizontal position and one
vertical position are shown in Fig. 7.2. The solidification temper-
·as found to be around 943K.
·e latent heat of fusion (2) was calculated from the energy balance:

$$L = \frac{q_{out} \, \Delta t f}{m} = \frac{315 \left|\frac{J}{s}\right| \, x \, 9.^2 \, \cdot 60[S]}{225.5[gr]} = 780[J/gr] \qquad (6)$$
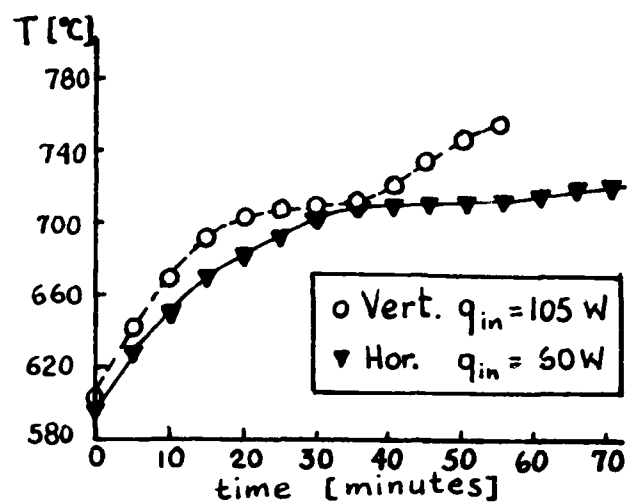
Fig. 7.1 MELTING CURVE
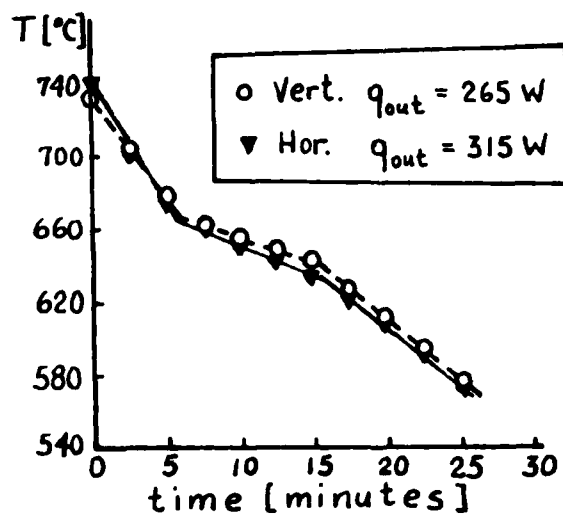
Fig. 7.2 SOLIDIFICATION CURVE

136

In the experiments, it was observed that the latent heat release takes place over a range of 30K. The thermal energy properties of this unit are presented in Tables 7.1 and 7.2.

Table 7.1   Solidification of 64Li-30MgF$_2$-6KF

Position	$\dot{m}_w$[1/hr]	q_{out}[w]	ΔT_{cp}[°C]	L[3/g4]	T_F[°C]	$(\rho C_p)_1$	$(\rho C_p)_{cp}$	$(\rho C_p)_s$
						ρC_p [KJ/m³ °C]		
Horizontal	7.1	315	34	781	668	2,650	10,160	3,410
Vertical	41.4	265	30	772	669	2,940	9,465	3,150

Table 7.2   Melting of 64LiF-30MgF$_2$-6KF

Position	$\dot{m}_w$[1/hr]	q_{in}[w]	ΔT_{cp}[°C]	T_m[°C]
Horizontal	22.9	60	6	708
Vertical	36.4	105	6	702

7.4   Conclusions

This study shows that the eutectic fluoride salt can be a good candidate for thermal energy storage at high temperatures, because it has a very high latent heat of fusion and small range of temperature change during phase change. The position of the unit does not effect the results for the solidification case; therefore, we can conclude that natural convection does not play an important role for this case. However, for the melting case, as the temperature becomes higher than the melting point, natural convection effects can be very important.

7.5   References

[7.1]   Richter, R., ''Thermal Energy Storage Demonstration Unit for Vuilleumier Cryogenic Cooler,'' Report No. AFAPL-TR-77-65, 1977.

[7.2]   Moraga, N., ''Analysis of an Experimental Correlation for a One-Dimensional Transient Conduction Problem of a Long Cylinder under Constant Heat-Flux,'' MEE 585 Class Assignment, 1980.

VIII. FAILURE EXAMINATION OF INCONEL 600 - EUTECTIC FLUORIDE THERMAL TEST CAPSULES

8.1 Introduction

Nine Inconel 600 capsules were fabricated and charged with fluoride salts. Each of the eutectic salts, $LiF-MgF_2$, $LiF-MgF_2-NaF$, and $LiF-MgF_2-KF$ were put into three capsules each, with the intent of life testing the array with a three fold redundancy for corrosion or failure comparisons. The capsules were 3 in. long and 1 in. in diameter. The capsules were fabricated and the salts were charged by the University of Dayton Research Institute. A complete report on capsule fabrication was not prepared, but similar work preceding this was reported in Ref. [8.1]. The main difference between the earlier report and the capsules tested here were that the material was changed to Inconel 600, and end caps were heli-arc welded rather than electron beam welded. The result was that the capsules contained an atmosphere of air on final weldment. The completed capsules were then put on life test at WPAFB, AFAPL Thermal Laboratory, in a superalloy-vacuum tube furnace. The temperature gradient from end to end of the furnace approximately matched the eutectic melting ranges of the three salts. The capsules were placed physically on a pure quartz ''boat'' which was a quartz tube cut in half lengthwise.

Following evidence of container failure, the entire system was evaluated visually and documented photographically. Failed capsules were cross-sectioned and examined metallographically including end caps, tube sections and weld zones. Salts remaining inside and outside the capsules were examined metallographically. As-received Inconel end cap and tube material was examined metallographically and by microprobe analysis. Unused salts were also examined by microprobe. Both containers and residue salts were evaluated extensively on the microprobe to determine impurities, metal porosity, diffusion and other high temperature related phenomenon.

8.2 Initial Post Test Observations

One hundred and two cycles and 315.4 test hours were completed when it was noted that thermocouple No. 7, at the cool end of the array (Fig. 8.1) was not producing a reasonable temperature reading. At that time the test was interrupted to examine the test samples and the failure of some of the
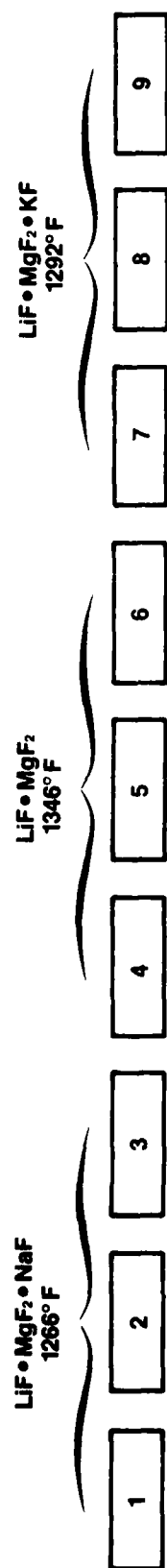
Fig. 8.1. SAMPLE ARRANGEMENT IN VACUUM TUBE FURNACE

139

capsules was discovered. LiF-MgF$_2$-NaF samples 1, 2 and 3 and LiF-MgF$_2$ samples 4 and 5 appeared to have lost salt through the containers by some mechanism.

In accordance with Fig. 8.1 from left to right, the sample array displayed the following characteristics which are also shown in the photographs.

Figure 8.2 Shows the TES capsules, thermocouple bundles and vacuum chamber end plate as removed from the vacuum chamber. Figure 8.3 shows that thermocouple bundles and radiation shield plate were covered with a pure white fine grain deposit. The deposit did not extend up to the first capsule though.

Figure 8.4 shows the leakage deposit which covers the end portions of Capsules 2 and 3. The region between 1 and 2 was also solid with deposit as well as that between 2 and 3. The residue wicked over much of the capsule length along the bottom and over one third of the length on top of Capsules 2 and 3. The heaviest deposit appeared between 2 and 3.

Figure 8.5 shows one section of the quartz boat in which the capsules were placed. The deposit from 2 and 3 is also evident here. The quartz was also etched uniformly. Capsule 4 showed no deposit while 5 and 6 appeared to have single small deposits on one end cap.

Samples 7, 8 and 9 in Fig. 8.5 had ''etched metallic appearing'' surfaces as compared to the usual darker capsule surfaces, and no deposits were observed. Samples 1, 2, 3, 4, 5 and 6 appeared to be lightly oxidized. At the right end of the chamber a hemispherical radiation shield seen in Figs. 8.3 and 8.6 was found with a heavy deposit similar to the thermocouple bundles at the opposite end. The deposit on the shield displayed two characteristic layers, a dark layer of about 1/64 in. on the shield followed by a pure white layer of similar thickness on the outside.

All thermocouples appeared to be firmly attached to the capsules. Thermocouples on 2 and 3 were encrusted in salt. Number 7 appeared undamaged and no salt was in the vicintiy of the contact area. Each of the fabricated capsules (tested and un-tested), had a noticeable doming effect on the end caps. Capsule design should have provided adequate allowance in the end cap fit so lack of tolerance could not have been a factor in the deformation. Internal hydrostatic pressure from the air remaining in the capsules during final end cap welding could be sufficient for doming. Salt volumes were sufficient to fill the capsules upon melting.

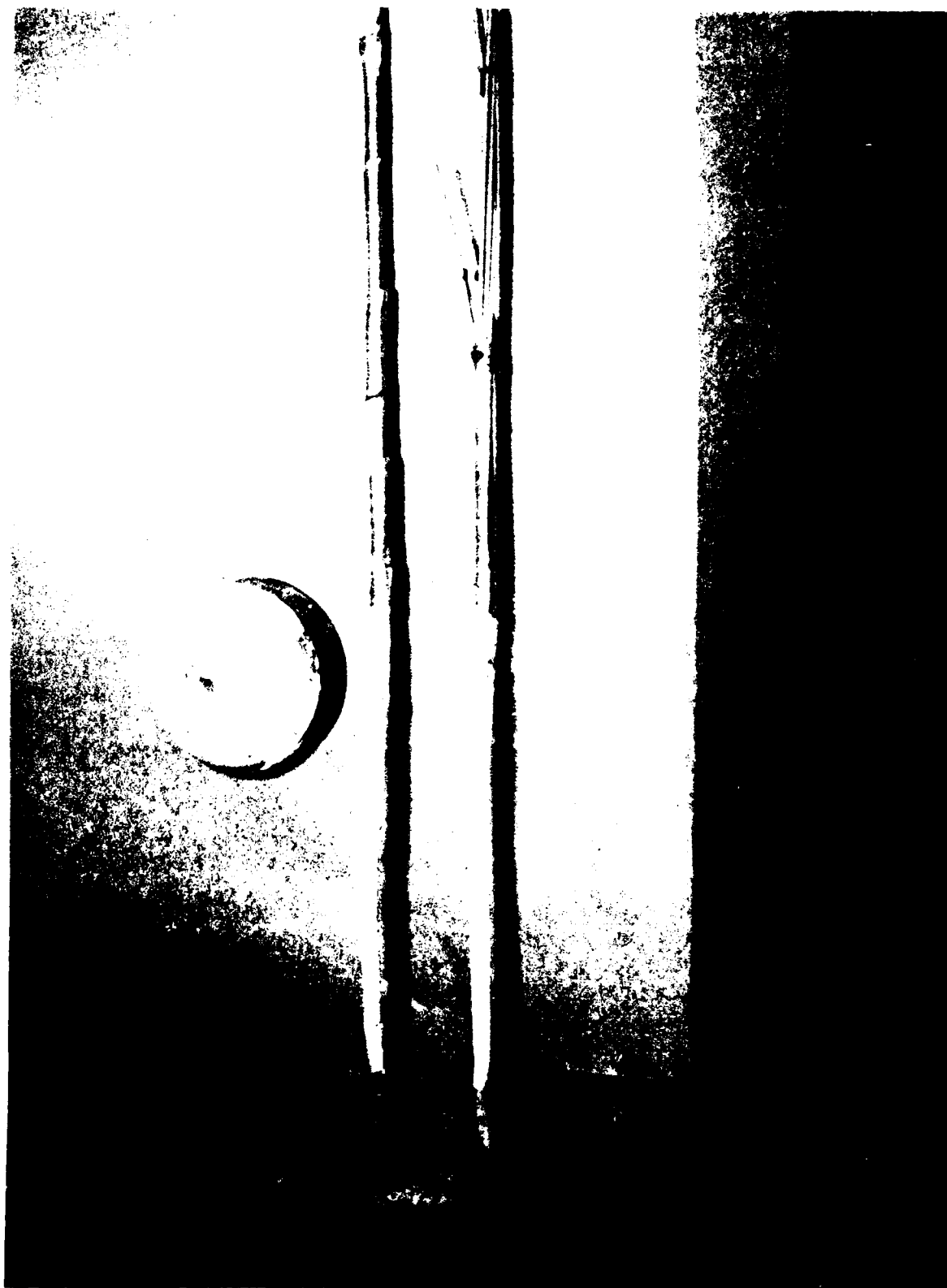Fig. 8.2 TES Capsules Array Removed From Vacuum Chamber

141

Fig. 8.3 Deposit on Thermocouple Bundles
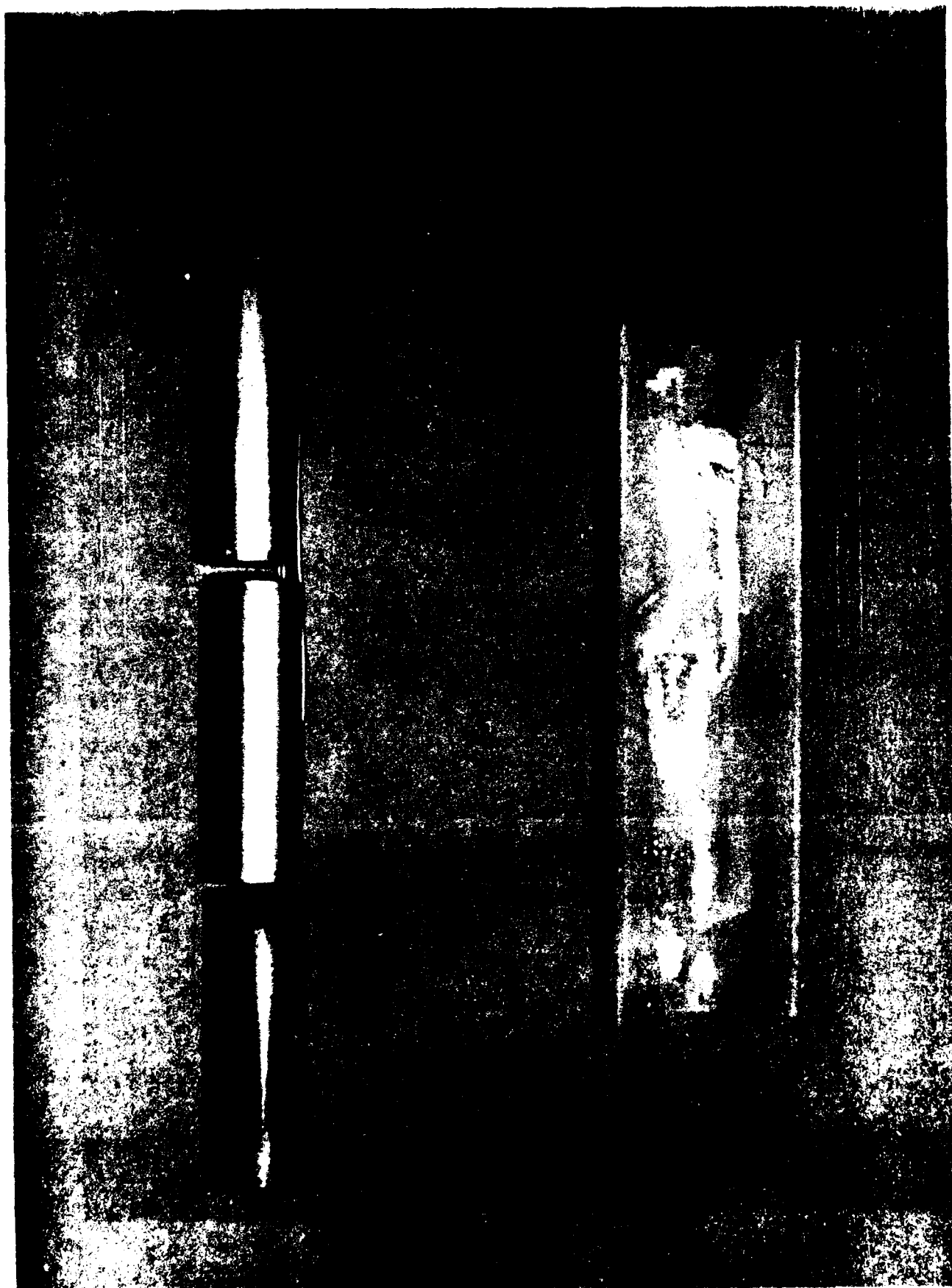and Radiation Shield

142

Fig. 8.4   Deposition on Capsules 2 and 3

143

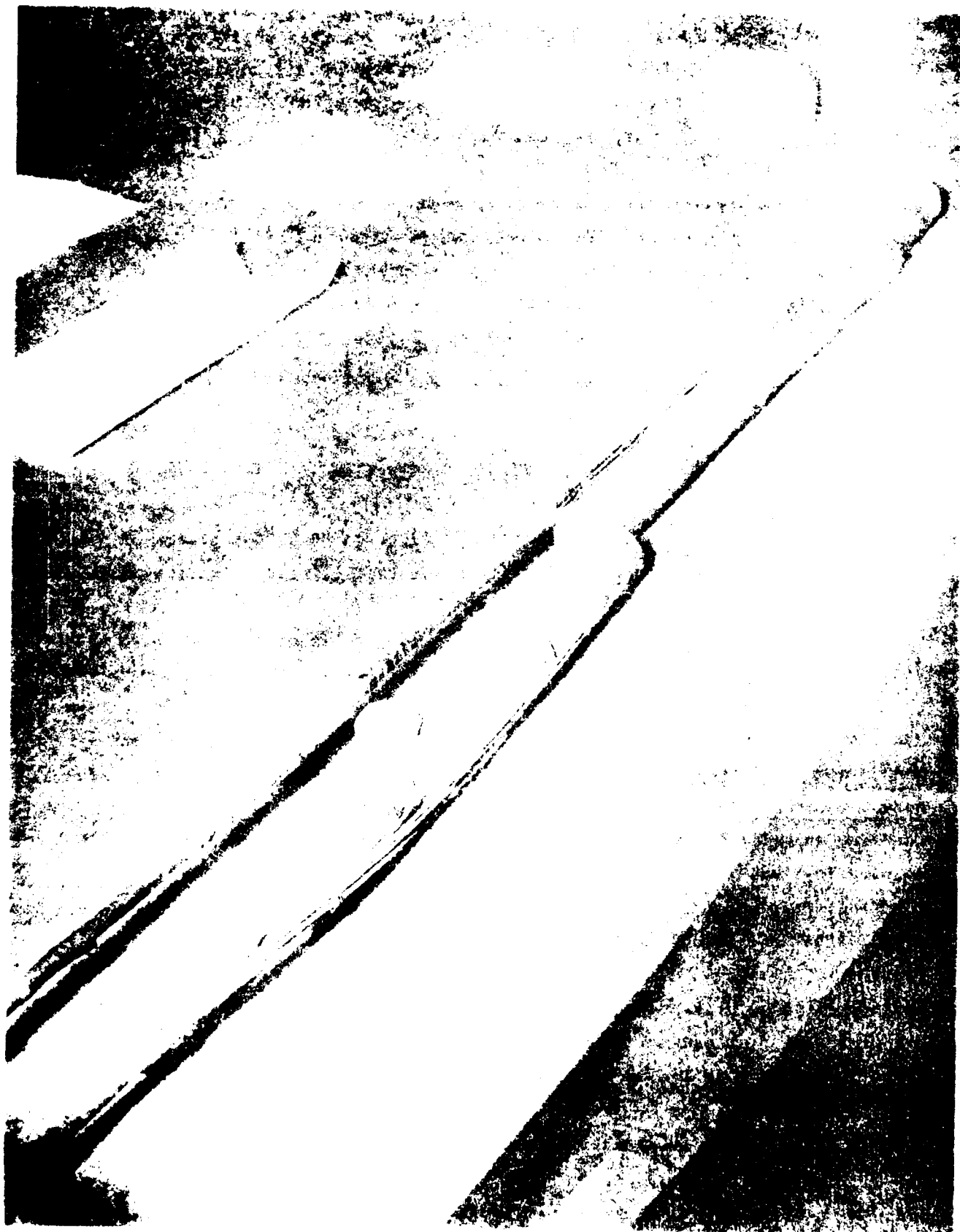Fig. 8.5 Quartz Boat Section with Salt Leakage

144

Fig. 4.6 Test Component Layout

145

Visual inspection of the capsule exteriors indicated failures of Capsules 1, 2, 3, 5 and 6. The pattern of the deposit on the capsules suggested pinhole failures in the end caps. There was also a bubble formation between the adjacent Capsules 2 and 3. Capsule ends are designated A (Right) and B (Left) in sequence 1 through 9. Macrograph 8.7 shows the left end of Capsule 1. The salt formation with the nodule in the center of the deposit strongly suggested pinhole failure. The right end of Capsule 1 in 8.8 shows a more general salt deposit as salt had wicked between and covered the right end of 1 and the left ends of 2, in Fig. 8.9. Figure 8.10 shows the right end of 2. The left end of Capsule 3, macrocraph 8.11, also shows a very ragged weld zone. Capsule 5 left end, shown in Fig. 8.12 also displays a salt deposit geometry which might lead one to suspect pinhole failure.

8.3 Sample Cross-Sectioning and Visual Examination

Each capsule was identified with an A (Left) for the end facing the thermocouple feed-through end plate. The B (Right) end is opposite.

Capsule 6 was sectioned immediately after the test and was cut by hacksaw on the diameter so that approximately 0.75 in. was left attached to the end caps. The center section remaining was then cut longitudinally into two equal pieces and the salts were removed. The cuts are shown in Fig. 8.13.

The other samples were sectioned either on a lathe with a cutting tool and the final cut-through was made with a hacksaw, or, the parts were cut with a hacksaw exclusively. Cutting fluid and increased temperatures by cutting were avoided. Some of the end caps were left intact and polished without mounting material. Smaller sections of weld areas and capsule walls were mounted in Bakelite for metallographic examination.

Specimens were ground with 120, 240, 320, 400 and 600 carbimet papers and with 2/0 and 4/0 emery papers. They were then polished with 6 micron diamond paste and final polished with .05 micron alumina with distilled water. Careful cleaning between each step was observed.

Existing etchants failed to reveal uniform microstructure and experimentation resulted in the following successful procedure:

1) 10% HCl solution immersion for one minute

2) Wash with distilled water and dry (This portion of the procedure activates the passive surface of this metal)
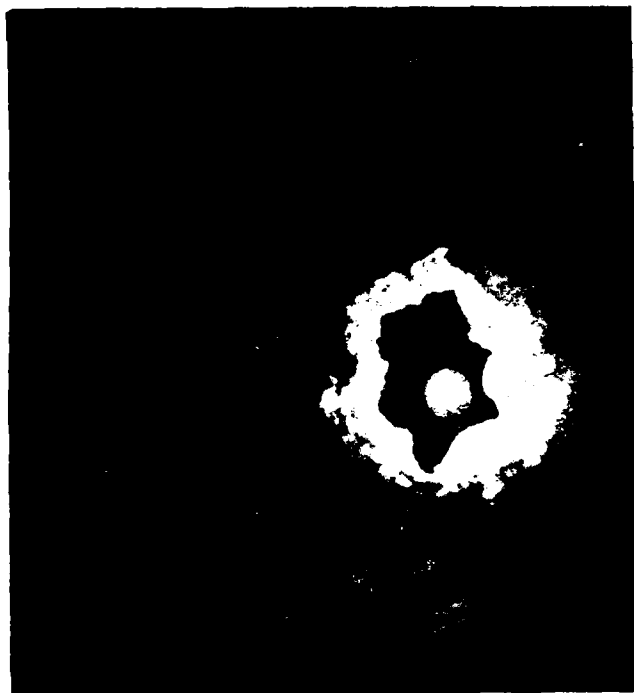
146

Fig. 8.7 Capsule 1 Left End (2.5X)

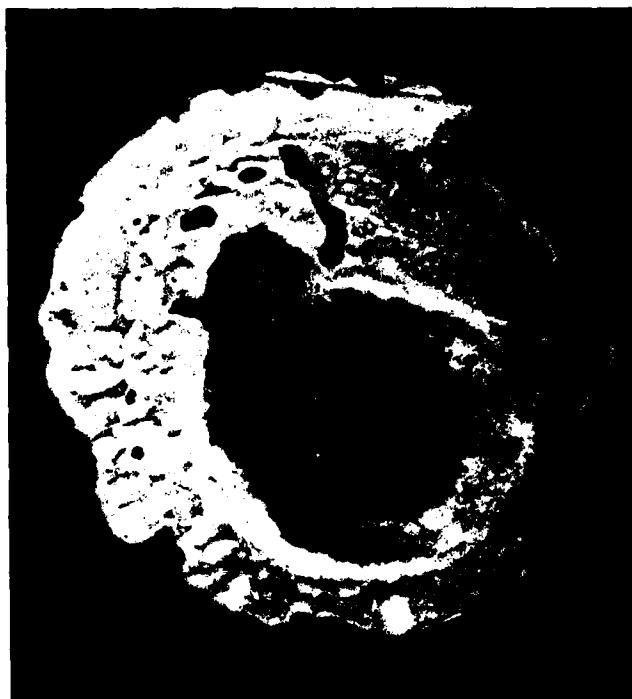Fig. 8.8 Capsule 1 Right End (2.5X)

Fig. 8.9 Capsule 2 Left End (2.5X)

Fig. 8.10 Capsule 2 Right End (2.5X)

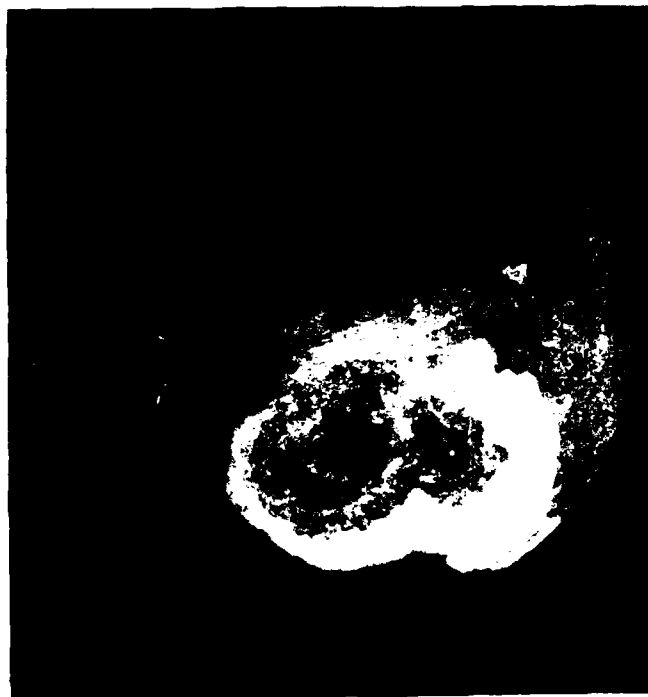Fig. 8.11 Capsule 3 Left End (2.5X)   Fig. 8.12 Capsule 5 Left End (2.5X)
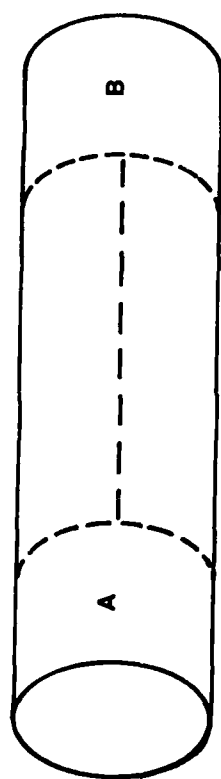
Fig. 8.13. CAPSULE SECTIONING FOR METALLOGRAPHY

3) 10 ml H_2O_2 (30% hydrogen peroxide), 6 drops HF (hydrofluoric acid) - this etchant requires 2-3 minutes on Inconel 600 in the ''as-received'' condition and 8-10 minutes on material which has been heat treated

4) Neutralize with 2% solution of sodium bicarbonate

5) Wash and dry specimen

It is advised to check the etching action every two minutes to obtain the degree of etching desired. This is a slow etchant but can be well controlled. Another half minute of 10% HCl wash might be necessary to activate the surface again before final results are obtained. This etchant provides a uniform, well defined and unstained microstructure.

The salts were removed from the capsules and samples were cold mounted in Buehler Plastic Powder #20-3552 mixed with Plastic Liquid #20-3554AB. No water was used during the grinding operations. The mounts were cleaned by wiping with clean soft lab towels and pressurized air. They were final polished with a very light spray of 1 micron diamond on Texmet paper followed by careful cleaning with ethanol. Water could be used on the salts in Capsules 1, 2, 3, 4, 5 and 6 without deterioration. When 0.05 alumina was used as a final polish, the structure was not as well defined. No etching was required.

8.3.1 Macroscopic Observations of Cross Sections

Internally, the frozen salts occupied from one half to two-thirds of the capsules. The single exception was Capsule 3 which was approximately 30% filled. Macrograph 8.14 is a cross section of Capsule 4 which shows that the capsule is somewhat greater than half full. Macrograph 8.15 shows the post-test salt remainder in Capsule 3.

Capsules 1, 2, 5 and 6 had continuous black deposits on the frozen salt surface. In all the salts except one there was a region of dark deposit at the bottom of the capsule. These deposits are shown in Fig. 8.16, Capsule 5 end B, and in Fig. 8.17, Capsule 7 end A. The bottom deposits ranged from 1/64 in. to 3/32 in. in maximum depth. Some of the bottom deposits appeared to have metallic inclusions and can be seen as dark spots in the dark layer in Macrograph 8.16.

Capsules 7, 8 and 9 had spotty dark deposits on the surface as seen in 8.17. These salts also appeared white with homogeneous ceramic-like surfaces
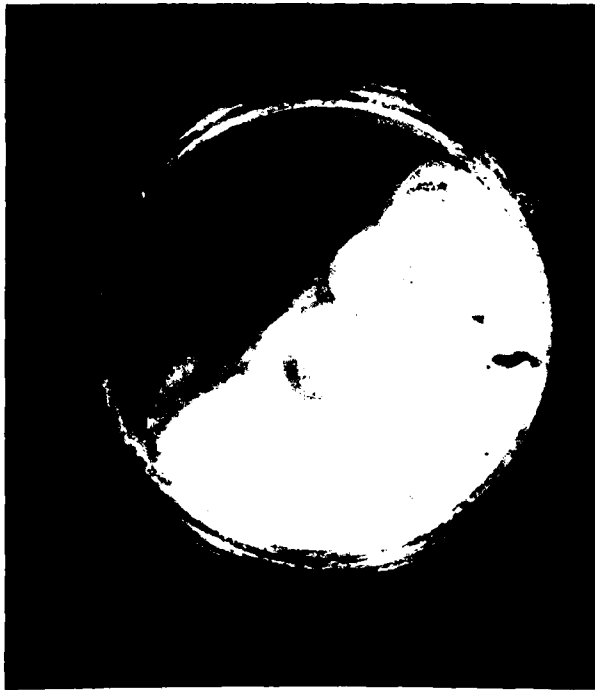
Fig. 8.14   Capsule 4 Left End (2.5X)

Fig. 8.15   Capsule 3 Right End (2.5X)

Fig. 8.16   Capsule 5 End B (3X)

Fig. 8.17   Capsule 7 End A (2.5X)

which formed voids during freezing. Macrograph 8.18 demonstrates the void formation quite visibly and also shows dendrite formation on both upper and lower surfaces of the void. The salts were also found to be extremely brittle.

The salts in 1, 2, 3, 4, 5 and 6 appeared gray, grainy and crystalline as shown in Macrographs 8.14, 8.15 and 8.16. Salts 4, 5 and 6 also displayed very large dendrites when the salts were viewed from the top as in Macrograph 8.19. Figure 8.20 shows the salt removed from the capsule and the dendrites are also evident. The black (bottom surface) layer is also clearly evident in the salt from Capsule 4 in this macrograph.

As stated in Section 8.2, the salt formations on some end caps would lead one to suspect pinhole failure. Subsequent polishing with removal of the surface salts did not reveal the anticipated ''holes''.

Radiographic x-rays were taken of all the end caps to determine weld integrity. Some of the welds were visibly rough and shallow and were suspect for possible leakage of the molten salts. End cap 3-A was an especially poor weld. The x-ray evaluation and inspection did not reveal any weld breach. Generally all the samples did demonstrate poor weld penetration.

The capsule walls and end caps were also tested with fluorescent dye penetrant. North American Dye Penetrant No. P6-F4 was used. In Figures 8.21, 8.22, and 8.23, the macrographs were taken under black light in order to show the penetrant indications. The dye sites are white on the photos. A red wax pencil was used to highlight the indications for metallographic precision grinding. The same dye penetrant was used hot at approximately 340K to further enhance and locate any ''continuous hole'' porosity. This testing failed to reveal any positive leak locations.

8.4   Microscopic/Microprobe Observations

Micrographs were taken on a Zeiss Bench Metallograph at magnifications from 100x to 1000x. Electron microprobe work of x-ray mapping, x-ray backscatter images, scanning electron microprobe images (SEM) and energy dispersive x-ray analysis were accomplished with an ETEC Autoprobe, X-Ray Energy spectrometer 5100C and Kevex Display Unit.

152

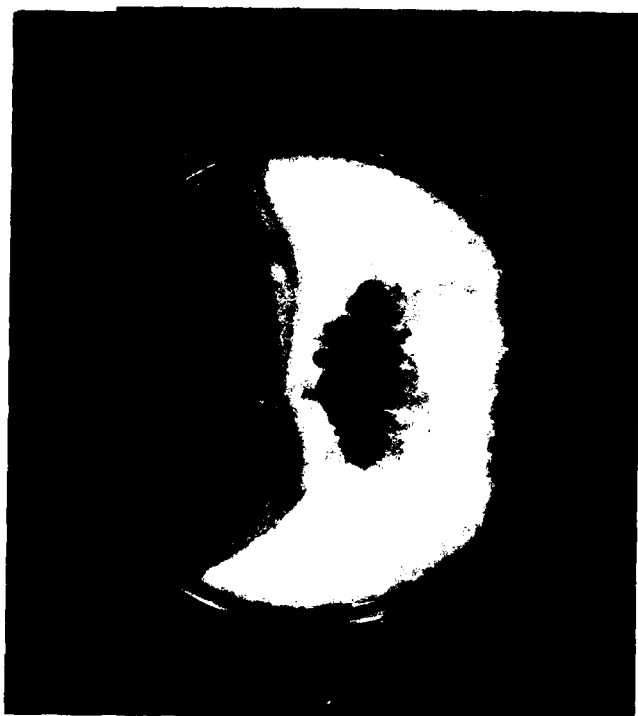Fig. 8.18   Capsule 8 Right End
(2.5X)

Fig. 8.19   Capsule 4 Top (3X)

Fig. 8.20   Capsule 4 Salt (Side)
(2.5X)

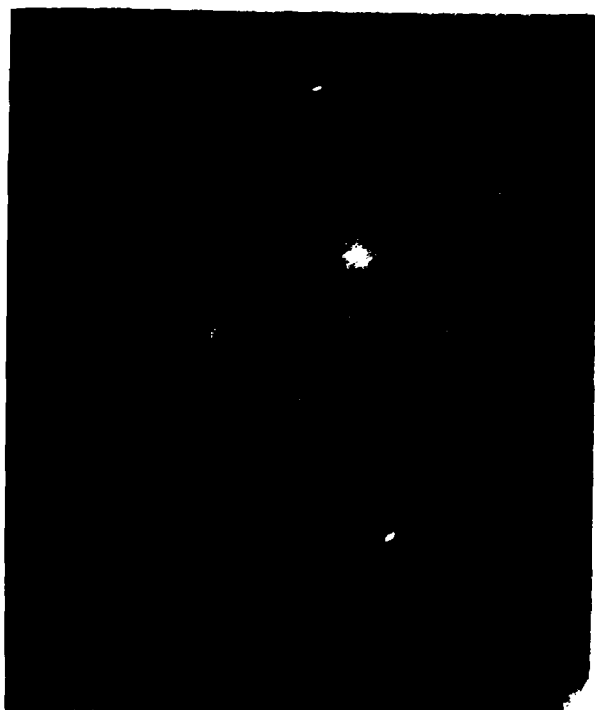Fig. 8.21   Pore Dye Penetration,
Capsule 5 Left End (2X)

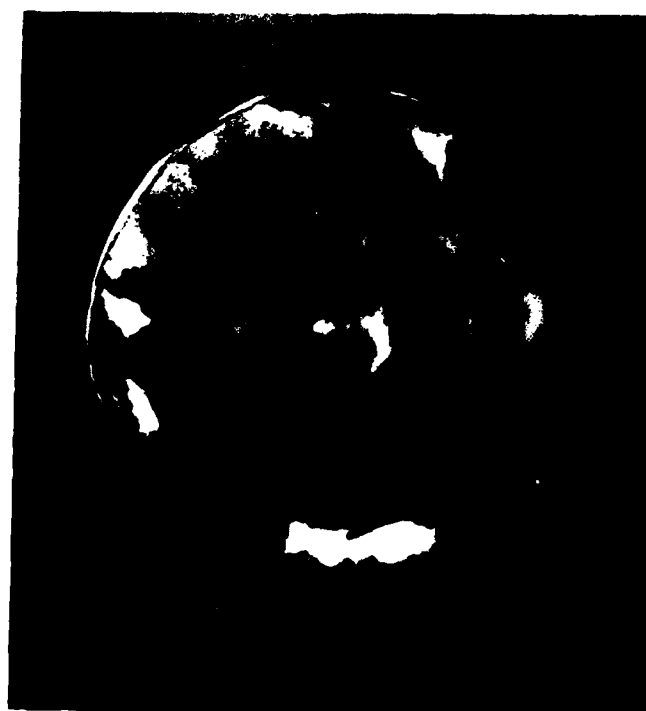Fig. 8.21A Pore Dye Penetration
Capsule 6 Right End (2X)

Fig. 8.22 Crack Dye Penetrant
Capsule 1 Right End (2X)
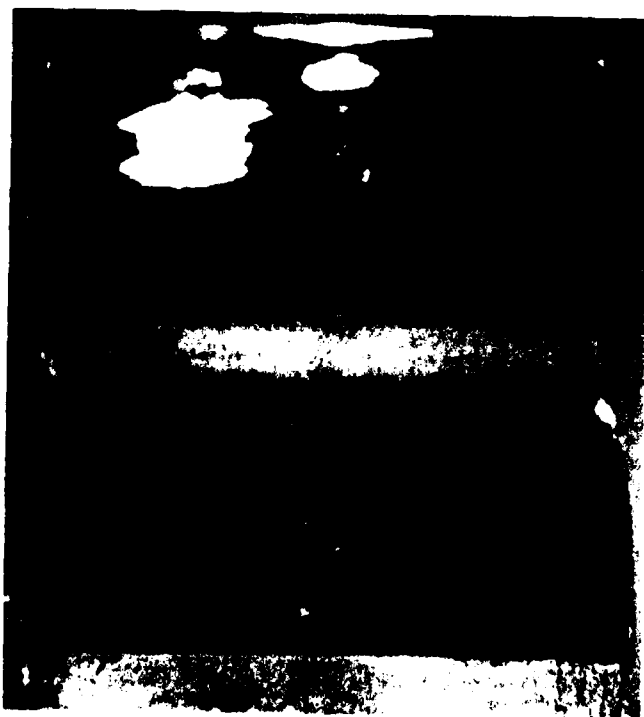
Fig. 8.23 Top: Capsule 9 Dye Penetrant (2X)
Bottom: Capsule 5 Black Light (2X)

154

8.4.1 Containment Material

The micrographs indicated a typical fine grained Ni-Cr-Fe solid solution Inconel 600 microstructure with particles of chromium carbide (globular) and titanium nitride (rectangular) inclusions. The carbides formed an almost continuous network at the grain boundaries. There was also notable porosity. Grain boundary and clustered carbides are shown in Figs. 8.24 and 8.25.

Metallographic and microprobe examination of the ''as-received'' material revealed the same characteristics as the fabricated pre-test samples and the post-test specimens. The un-processed bar stock and tubing had smaller but similar porosity and inclusions. The bar stock is shown in Fig. 8.26. Etching removed the carbide particles. There were larger grains on one side of the cross section than in the balance of the bar. This condition indicated an uneven cooling of the bar after processing. Further heat treatment would be required to ascertain uniform grain size in the end caps machined from this stock.

The porosity was seen throughout the capsule material. In the tested sample end caps this porosity increased in occurrence at approximately 1/8 in. from the edge. This concentrated defect could have been a result of elevated temperatures in the weld zone. The capsule wall cross sections showed more porosity than the end cap cross sections.

Micrographs 8.27 and 8.28 are from Capsules 2 and 3 at 100x and 160x. In Fig. 8.28 typical porosity and inclusions are shown while in 8.28 an isolated large void is seen. Similar micrographs as shown in Fig. 8.29 at 700x, were produced with the microprobe. The porosity in this material had various shapes: round, elongated and irregular. There seemed to be no location preference and some pores were clustered and some were found along grain boundaries and some were intergranular.

Part of the porosity could have been the result of inclusion removal during polishing. Fig. 8.30, for example, shows a nitride particle with an adjacent hole. Fig. 8.29 also shows the extensive array of carbide particles which have migrated to the grain boundaries. Both carbide particles and one large nitride particle are shown in Fig. 8.31. In this photograph twins are also evident in the grains.

The as-received tubing showed a typical microstructure. The inside surface appeared rough as well as the outside surface. There were also some small cracks near the edges of the cross section. Fig. 8.32 represents a

Fig. 8.24 Capsule 5 Left End
(160X)

Fig. 8.25 Capsule 5 Left End
(400X)

Fig. 8.26 Inconel 600 Bar Stock

Fig. 8.27 Capsule 2 Right End Cap
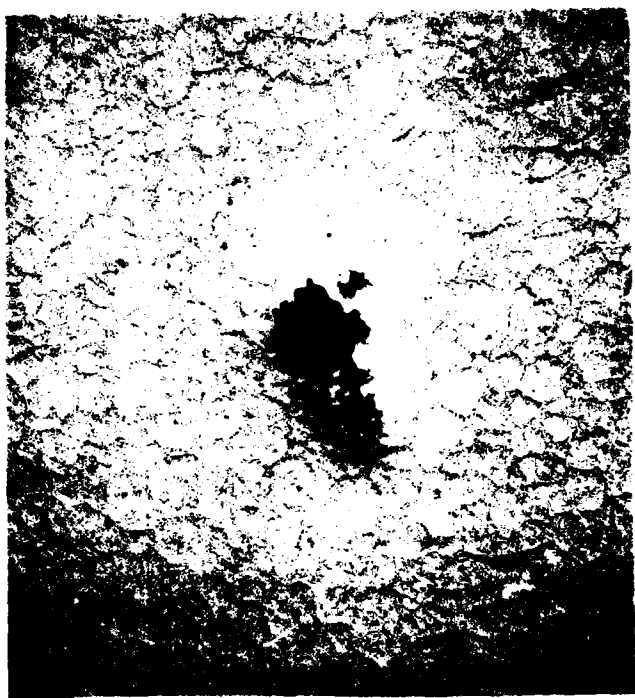(100X)

156

Fig. 8.28 Capsule 2 Right End Cap
(160X)
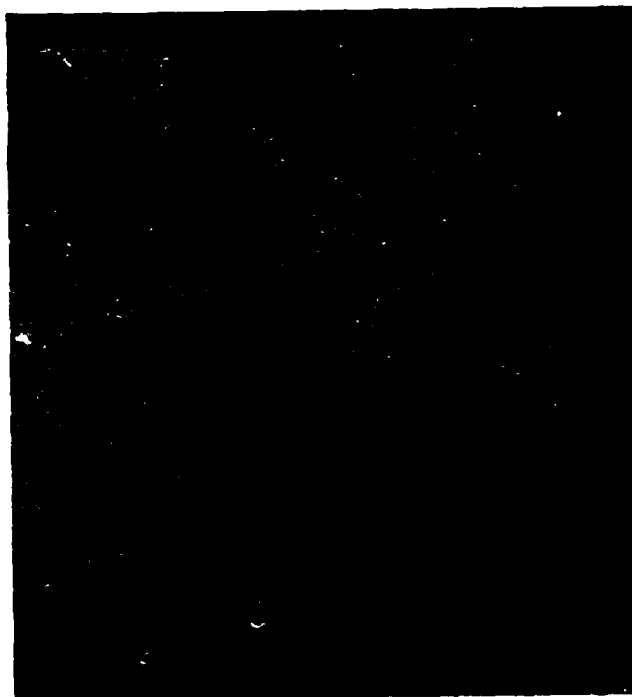
Fig. 8.29 Capsule 2 Left End
Microprobe (800X)
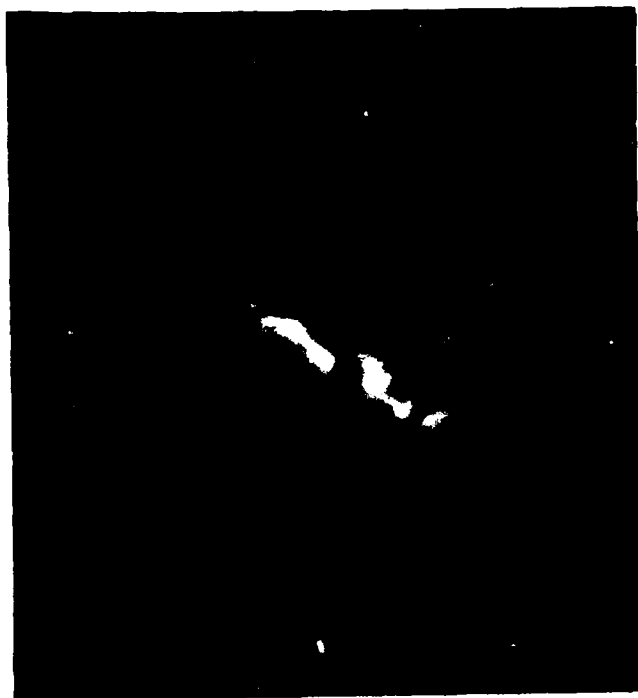
Fig. 8.30 Capsule 6 Left End Cap,
Microprobe (3000X)

Fig. 8.31 Capsule 2 Left End Cap,
Microprobe (3000X)

157
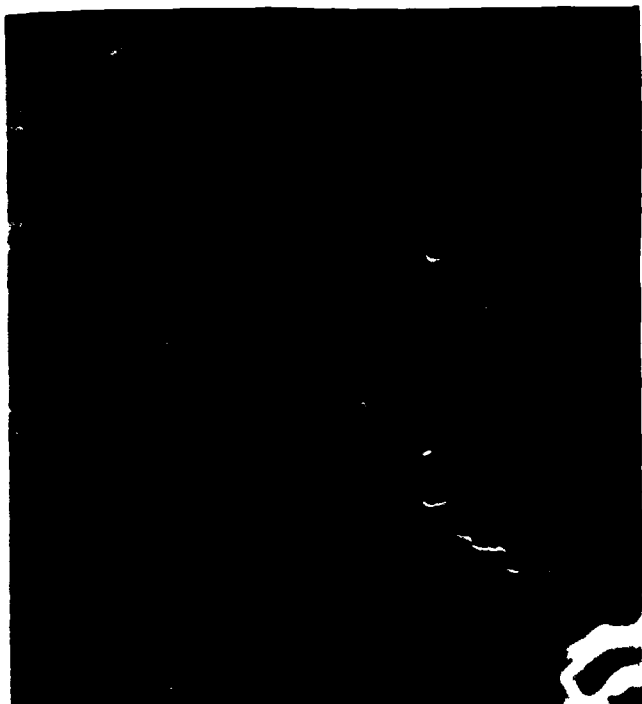
Fig. 8.32 As Received Tubing Edge,
Microprobe (1300X)

Fig. 8.33 Post Test LiF·MgF$_2$·
Capsule 6 (100X)

Fig. 8.34 Post Test LiF·MgF$_2$·
Capsule 6 (100X)

typical view of the inside edge. This rough surface could provide more salt corrosion initiation sites.

8.4.2 Eutectic Salts

The thermally cycled systems of eutectic salts have a unique and distinctive microstructure. Each of the three compositions can be individually identified. They do not show a complete homogeneity, but form typical eutectic microstructures.

There is a visible macroscopic and microscopic difference between the body of the salts shown in Figs. 8.33, 8.34 and 8.37 and the dark areas visible on the frozen surface or at the bottom of the specimens as shown in Figs. 8.34, 8.36 and 8.38. The grains in the dark areas are smaller and have a change in structure. There are also more numerous solid composition islands.

Micrographs of the LiF-MgF$_2$ salts in Capsules 4, 5 and 6 showed nodular and elongated magnesium grains with scattered solid composition irregular shapes as in Fig. 8.33. Capsules 1, 2 and 3 contained LiF-MgF$_2$-NaF salts as shown in Fig. 8.35. The salts formed a rectangular pattern of striated and dendritic type structures. The third system containing LiF-MgF$_2$-KF is shown in Fig. 8.37. These salts froze in a geometric dendritic and striated pattern.

8.5   Microprobe Evaluations and Analysis

Samples of the as-received, as-fabricated and as-tested capsules and salts were evaluated by microprobe.

The as-received material was quantitatively ascertained to be Inconel 600. In addition to the expected composition of Chrome-Iron-Nickel there was 0.2 Titanium and 0.2 Aluminum. Other trace elements were not quantified.

In each Inconel 600 sample calcium was found. This was associated with the pore or inclusion sites. Mounting material was changed from Bakelite to transoptic and polishing procedures were changed, but the Ca impurity was still present. Calcium is a solvent for nickel. This impurity in the Inconel 600 would affect the corrosion resistance in material subjected to thermal treatment and could have been one of the factors in the capsule failure.

The capsule end caps, sidewalls and weld sections were analyzed. The Ti nitrides, carbides and porosity along with the Ca impurity were photographed

159

Fig. 8.35 Post Test LiF·MgF$_2$·
NaF, Capsule 2 (100X)

Fig. 8.36 Post Test LiF·MgF$_2$·
NaF Capsule 2 (100X)

Fig. 8.37 Post Test LiF·MgF$_2$.
KF Capsule 9 (100X)

160
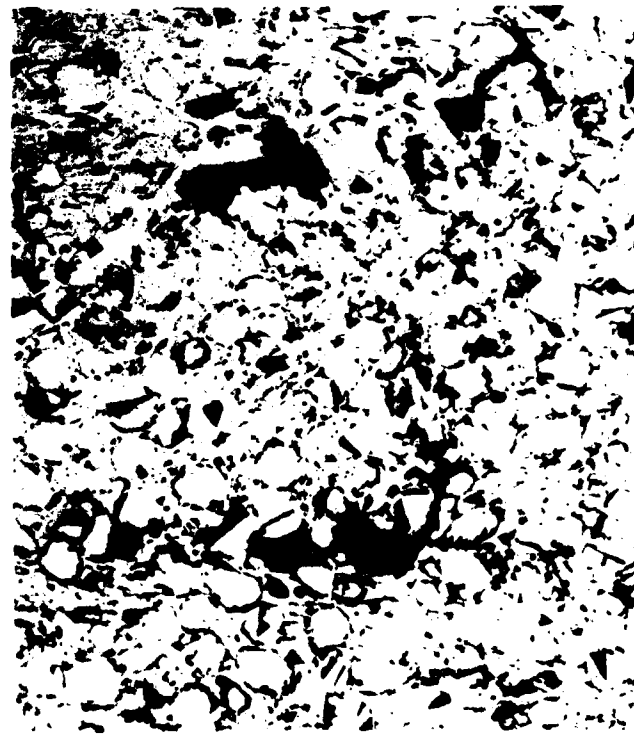
Fig. 8.38 Post Test LiF·MgF$_2$·
KF Capsule 9 (100X)

and documented on the image analyzer. X-ray scans were taken to note the elements present at specific sites. X-ray mapping delineated the type and amounts of selected elements in the pores.

The capsule inside walls were inspected for corrosion depth. As mentioned above, the final material processing left a rough surface and some grain damage. The salt corrosive action smoothed some of the walls but also penetrated the surface at the grain boundaries. The unpenetrated weld areas were filled with the salts. Salt elements were found two to three microns beyond the damaged grains.

It was determined by x-ray scans and x-ray mapping that the as-received, as-fabricated and as-tested salts contained a calcium contaminant. The calcium was found in the MgF_2 salts which was used in all the test samples. The calcium was found to be integral with, but not combined with, the magnesium. As stated above, calcium reacts with nickel; the calcium impurity was considered an important factor in the test results. Further testing will require ultra-pure salts.

Through the microprobe analysis it was determined that the dark band on the bottom of the salts contained Fe, Cr, and Ni. These main composition elements of the Inc-600 were leached from the capsule material and settled on the bottom as the salts froze.

A section of the quartz furnace shield, salt samples from the furnace thermcouples and other samples of the deposit inside the furnace were also analyzed. All the salt-like deposits contained Mg, F and Na. These were the salt components in the capsule group 1, 2 and 3.

8.6   Salt Leakage Path in Capsule 1 Left End Cap

As described earlier, the leakage salt patterns on the end caps suggested that a pinhole type failure was involved in the failures. Microscopes and microprobe examinations at high magnifications revealed a good deal of porosity, but no distinct ''hole'' as would be associated with a pinhole.

By shear luck, a cross section of Capsule 1 Left End Cap exposed what appeared to be a pinhole through the cap, as shown in Figs. 8.39 and 8.40

Extremely careful metallographic polishing procedures revealed a complete linear array of pores, completely through the end cap, providing conclusive evidence of the path for salt leakage from the capsule.
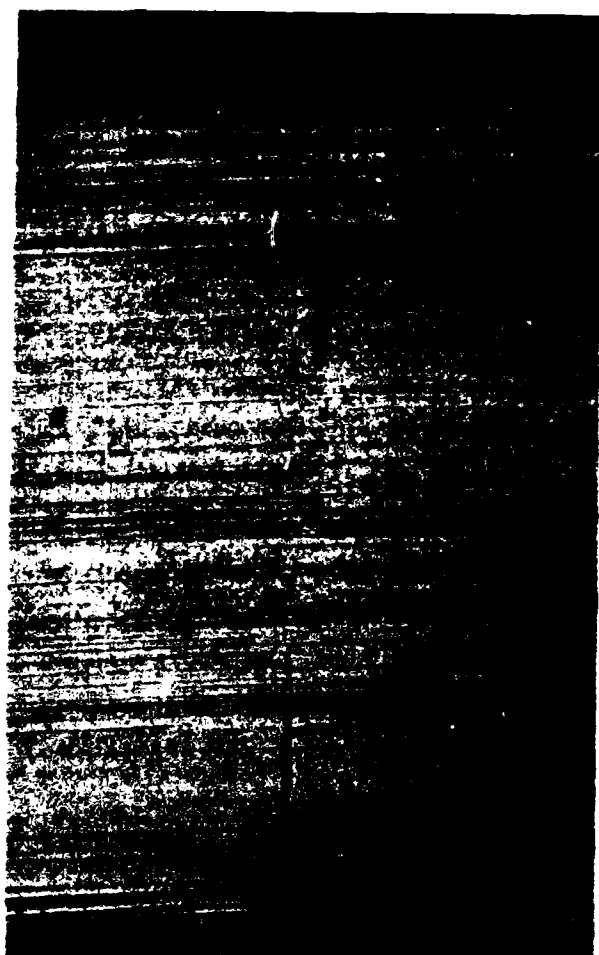
Fig. 8.39 As Sectioned Capsule 1
Left Eng Cap (10X)
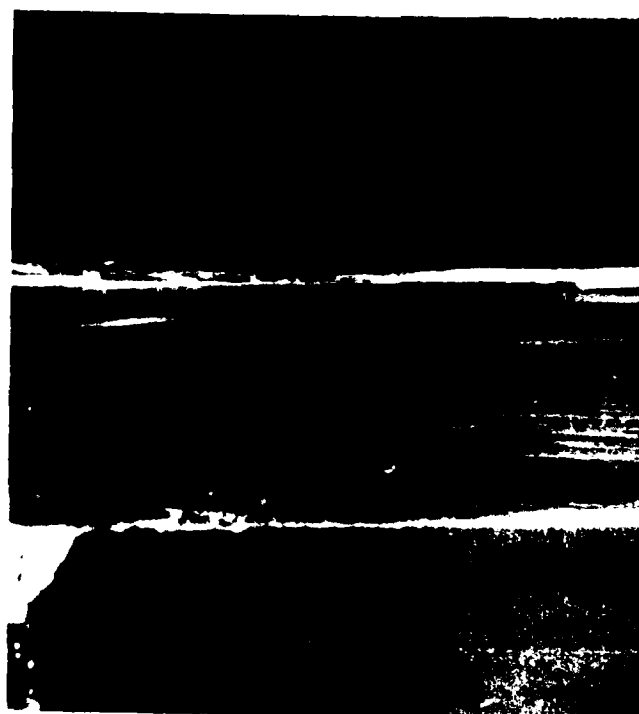
Fig. 8.40 As Sectioned Capsule 1
Left End Cap (25X)

Microprobe analyses are shown in Figs. 8.41, 8.42 and 8.43. Figure 8.41 backscatter picture showing the linear appearance of the system and also variation in grain apcarance near the fault as compared with the adjacent ix. Figure 8.42 is a microprobe micrograph of the failure at 1100x. This rly shows the interconnected pore network that constitutes the linear t. Figure 8.43 is a composite picture showing the complete path from one of the end cap to the other. It is interesting to note the macroscopi-y straight path formed by the microscopic voids. Other voids are apparent ther areas away from the fault, but clusters of such voids seem not to be ent elsewhere. The spread of the voids is also quite narrow and istently so, although more spreading is observed at the bottom edge.

It is not clear if this failure is due to manufacturing processes, a anically aligned array of impurities such as calcium particles, or a mal corrosion phenomenon.

If an internal corrosion mechanism were at fault, it would seem that the thin weld sections would be the first to fail. The tubes, or sidewalls demonstrated no apparent failures. The end caps thus become suspect for ons other than a pure metal corrosion failure. The short lifetime of 315 s would also suggest a nearly immediate failure considering the pore size the amount of salt rejected from the capsules.

Conclusions

The salt leakage path discovered in the end cap of Capsule 1 provides the ir to how the salt was leached from the capsules. The vacuum, external to ;apsules and the expansion of the salt upon melting probably accelerated alt removal. The high vapor pressure salts and components evaporated and nsed on the cooler portions of the system as determined visually and by probe analysis.

The existence of the pore path through which the salt passed is clear, he way in which this path came into existence is unclear. The multiple res which were found all appeared to be through the end caps. The end were all cut from the same wrought bar stock. It is possible that tho ity chain shown in Fig. 8.43 was the result of the manufacturing ises in drawing the bar stock or might have been a nonhomogeneous align-of a component (possibly calcium contaminant) which resulted in a live interaction with salt, providing the salt exit path. The extensive

163

Fig. 8.41 Capsule 1 Left End Cap Failure,
Microprobe Backscatter (80X)

Fig. 8.42   Capsule 1 Left End Cap Failure,
            Microprobe (1100X)

**Fig. 8.43 Capsule 1 Left End Cap Failure
Composite Microprobe (50X)**

porosity in the as-received material might point to the pre-existence of this pore path through faulty fabrication.

Another important consideration in the failure of the capsules reflects upon the manner in which they were fabricated. The salt filling procedure included melting the salt, in the capsule, in air. The final heli-arc weld was also completed in air. Oxygen has been demonstrated to create a highly corrosive environment with 304 stainless steel. The residual oxygen in the capsules could have been instrumental in the failure if it was corrosion related. The very thin metal thicknesses in the weld areas would seem to be likely locations for corrosion produced pinholes as opposed to the thick section of the end caps.

The microprobe analyses of the salt near the capsule walls showed that Fe, Cr and Ni were leached into the salt. It is not known how the oxygen or nitrogen might interact in this corrosion. It is also not possible to determine the extent to which this salt-wall leaching would proceed or how it would affect the lifetime of such a system, or its long term performance.

The Inconel 600 was contaminated with calcium, as well as some of the salts. Titanium oxides and carbides were also found in the metal. Calcium was associated with much of the porosity found and it is not known if or how the calcium might have been responsible for the porosity except that it is known that calcium will dissolve nickel. The magnesium fluoride as-received material was found to be contaminated with calcium; thus all capsules were contaminated since magnesium fluoride was part of each composition.

The capsule end caps were all buckled outward somewhat indicating that the expansion of the salt upon melting must have caused some deformation at operating temperature. It is not felt that this would have contributed to the failure.

Inconel 600 does not have the high temperature properties of such alloys as Inconel 617. It has good resistance to oxidizing and reducing and corrosive environments at high temperature. Inconel 617 has no iron but has additions of cobalt, molybdenum and aluminum. It has optimum high-temperature mechanical stability with excellent cyclic oxidation and carburization resistance to 1350K. Stress rupture resistance is good up to 1150K. The properties of Inconel 617 are superior to 600, but it is not clear that Inconel 600 would not be satisfactory for some applications. The corrosion and life capabilities of Inconel must be established conclusively. Ultra pure

salts should be used and welding procedures should be developed and refined to eliminate structural changes, contamination and mechanically weak sections. Highly controlled heli-arc inert gas or electron beam welding are suggested.

Processing of the salt should also be performed by providing a high vacuum (10^{-6} torr or less) atmosphere over the molten salt in the individual capsules. This can be accomplished following salt loading and end cap welding by supplying a valved appendage which is pinched and welded off following processing.

8.8   References

[8.1]   Davison, J.E., ''Evaluation of Fluoride Thermal Energy Storage Unit
         Compatability Part I'', Survey of Thermophysical Property Data and
         Description of clad/Salt Sample Prepartion, AFAPL-TR-75-92, October
         1975, pp. 20-22.

IX.   LITHIUM FLUORIDE-SODIUM HEAT PIPE THERMAL TRAIN SUBSYSTEM LIFE TEST

9.1   Introduction

A report entitled ''Thermal Train Subsystem for a Solar Collector Thermal Power System'' was prepared in December, 1971 by the General Electric Company for Electro Optical Systems. The report described the experimental evaluation of component performance of the thermal train subsystem for a solar collector thermal power system [9.1]. A series of heat pipe thermal storage units were constructed by General Electric and operated in air for 100 simulated cycles of 100-minute duration with 65/35 (sun/shade) periods. These tests consisted of a primary heat pipe coupled to a secondary heat pipe which contained thermal storage material (lithium fluoride) with a cylindrical container cartridge. The cylindrical cartridge geometry was designed for, and demonstrated as a method of, compartmentalizing the thermal storage material while permitting easily fabricated and loaded thermal energy storage capsules. Additionally, the thermal behavior of the system could be varied by changing the cartridge diameter in scaling up to larger storage capacity by increasing the number of cartridges. The ultimate goal of this program was to demonstrate the performance of the thermal energy storage sodium heat pipe subsystem with subsequent life testing of the systems to demonstrate compatibility of both the lithium fluoride and the sodium with their respective containment materials.

Subsequent tests with calorimetric measurement of power output were performed both by General Electric and later by Electro Optical Systems. A second category of testing with the different subsystems was to denote cartridge geometry optimization tests involving investigation of the cyclic thermal behavior of two heat pipe thermal storage units with different cartridge diameters. A further goal in the cartridge geometry test was to explain on a theoretical basis the variation in temperature observed during the heating and cooling portions of the cycle and to determine the dependence of that variation on both cartridge diameter and heat flux. These particular goals were met by General Electric and Electro Optical System in works which have been reported [9.1, 9.2]. The first report is primarily concerned with the further life testing of one of the units which has been going on for different periods through the last ten years.

One of the subsystem units which consisted of a sodium heat pipe with three lithium fluoride capsules inside the sodium heat pipe were tested by Arizona State University starting in June, 1978.

9.2   Subsystem Description

The subsystem tested by Arizona State University consisted of a sodium heat pipe 2.25 in. in outside diameter and 20 in. long. It was constructed of type 321 stainless steel. The heat pipe contained three lithium fluoride cartridges 0.81 in. inside diameter and 10 in. long. Each cartridge contained 134 grams of lithium fluoride so that the total quantity in the three cartridges was 402 grams. The latent energy of 402 gms of LiF is 4.2×10^5 Joules.

The wicking in the sodium heat pipe portion of the subsystem consisted of five layers of 100 mesh type 304 stainless steel screen which formed the main reflux wick lining the interior wall of the heat pipe. Each lithium fluoride cartridge was wrapped with three layers of 100 mesh screen. Fig. 9.1 shows the interior of this particular test unit showing the three lithium fluoride thermal storage cartridges and part of the wick structure surrounding those cartridges and connecting it to the larger heat pipe containment. Several wick layers were forced between the cartridges where they contacted each other, thus holding the cartridges against the outer wick. Short pieces of wick were then spot welded to the ends of the cartridges and to the wall wick to hold the cartridges in position. Two General Electric semi-cylindrical wire wound heaters, Lindberg Type 3708-SP, provided radiant heat input to an 8-in. length of the heat pipe. A number of thermocouples were attached to the heat pipe in order to determine the performance of the system during heating and cooling.

At Arizona State University thermal cycles were performed on a daily basis, heating in the morning and turning the system down in the evening. At General Electric and at Electro Optical Systems, thermal cycling of the test systems simulated a near earth orbit (400 NM) of a 100-minute period, with 65-minute solar illumination and 35-minute eclipse. At Arizona State the cycles were not performed in this manner.

On January 23, 1974, the thermal energy storage unit was shut down at GE. The unit had operated without interruption from February 14, 1973 to January 23, 1974. At the time of test termination the unit had gone through 3,150

Figure 9.1   Interior of TT3 Test Unit Showing Three LiF Thermal
Storage Cartridges. Heat Pipe OD Is 2.25 Inches

cycles of charging and discharging of the thermal energy storage material.
The initial cycles had lasted 206 minutes, while at the end of the test the
cycle time had stabilized at 70 minutes. During long duration tests, the
cycle time fluctuated between these two extremes. At the time of the shut
down all temperatures appeared to be consistent with the initially measured
temperatures. After the tests were terminated, radiographic pictures were
taken of the thermal energy storage capsules. No distortion of any of the
three capsules could be observed nor were there any indications that any one
of the capsules had sprung a leak. In the General Electric tests the opera-
ting temperature at melting was 1120K and at solidification 1117K. The
operating temperature difference between melting and freezing was approxi-
mately 14K.

9.3   Endurance and Cycle Tests at Arizona State University

The system was placed in a Lindberg heavy duty tube furnace. Three
regions of the furnace, the two ends and middle section, were independently
controllable. They were adjusted such that the system was uniformly heated
over its entire length. The temperature was controlled automatically by a
pyrometer, which is a built-in instrument of the furnace. During the heating
cycle the temperature was kept at 15K above the melting temperature of the
lithium fluoride which was determined to be 1122K. The system was heated up
in the morning and cooled in the evening. For several months this was
reversed, heating during the night and cooling during the day. This was done
to avoid overheating of the laboratory. In those cases the heating cycle was
much longer than the cooling cycle. The system was usually not operated
during weekends. One thermocouple was attached to the cylinder wall at the
midsection and the temperature was recorded continuously on a strip chart
recorder. Two thermocouples were attached to the two end sections of the
system. In the longintudinal temperature profile was periodically controlled
for uniformity. The furnace proved to be very stable and did not need
adjustments.

Since June 24, 1978, over 276 cycles have been performed on the
subsystem. This includes 2,862 hours of cumulative heating at 1122K.
According to GE data, time after the start of the cycle to the approximate
completion of extraction phase, during which the entire subsystem was in the
vicinity of 1122K, was on the order of 150 minutes. 150 minutes, therefore,

is used to determine the life test time for the 3,150 cycles which were accumulated. Thus each General Electric cycle had a duration of approximately two and one-half hours at 1122K for 3,150 cycles; the total time is 7,875 hours combined with the 2,862 hours at Arizona State University. The current total test time on the unit is 10,737 hours.

9.4 Conclusions

The thermal energy storage sodium heat pipe subsystem is examined visually occasionally between cycles at Arizona State University. The system appears to be performing the same as it always has. The life tests are continuing and will be continued as long as no failure appears. No damage has ever been observed except for a considerable amount of scaling of the outer wall due to oxidation. This observation was also made by General Electric and Electro Optical Systems during the time in which tests were being performed at those laboratories. Over 10,737 hours of operation and 3426 cycles have been completed on the unit at this writing.

9.5 References

[9.1]   Solar Collector Thermal Power system (SCTPS) First Interim Report, EOS Report 4074-I-1, January 14, 1972, Appendix E.

[9.2]   Solar Collector Thermal Power System (SCTPS) AFAPL-TR-74-89, Vol. III, Sect. IV, p. 89-160.

APPENDIX

Manufacturing Processes for
Sodium/Inconel 617 Heat Pipes

Contract No. F33601-79-C0158

Prepared By:

T.R. Lamp
Hughes Aircraft Co.
Electron Dynamics Division
P.O. Box 2999
Torrance, CA 90509

Prepared For:

Air Force Aero-Propulsion Laboratory
Wright-Patterson Air Force Base
Ohio 45433

August 20, 1980

A-1   INTRODUCTION

This report contains a description of the manufacturing processes and data pertaining to sodium/Inconel 617 heat pipes manufactured for Wright-Patterson Air Force Base in accordance with Contract No. F33601-79-C0158.

The units described herein are for use in compatibility experiments being conducted at the USAF/AFAPL laboratories. Manufacturing methods and processes are similar to those previously employed by HAC for stainless steel heat pipes.

The basic manufacturing sequence for liquid metal heat pipes is:

1) Ultrasonic followed by vapor degreasing.
2) Wick assembly.
3) Vacuum firing.
4) Electron Beam welding.
5) Leak test.
6) Final vacuum firing.
7) Loading with working fluid.
8) Hot processing under vacuum.

A-2   DESIGN AND PERFORMANCE ESTIMATES

A-2.1   Envelope

The heat pipe envelope is .500 dia. X .404 ID X 18 inches long. Tubing for the envelope is seamless Inconel 617. End caps were fabricated from .50 diameter rod stock. Prior to welding, each end cap was helium leak tested to 3×10^{-9} atm-cc/sec to check for porosity. Plate stock in Inconel 617 alloy was not available. Process and closure end caps were EB welded.

A-2.2   Wick

Wick material consists of 100 X 100 mesh square weave Inconel 617 screen. Wire diameter is .0045 inch.

The wick parameters of permeability (K) and capillary radius (r_c) were determined. Measured volumes for r_c ranged between 8×10^{-5} m and 1.14×10^{-4} m. A value of 1×10^{-4} m was used to establish performance estimates.

The permeability was determined by measuring the wick porosity which was
ı used in the equation:

$$K = \frac{d^2}{122} \frac{\varepsilon^3}{(1-\varepsilon)^2}$$

:e:

      d = wire diameter

      ε = porosity

ısity varied between .702 and .724 with estimated permeabilit;ıs of 4.16 X
·⁰ m² and 5.32 X 10⁻¹⁰ m², respectively. The lower value was used to esti-
: performance.

  Figure A-1 contains a plot of maximum axial heat transport versus temper-
·e for the selected wick design. Equations and fluid properties were taken
ı Reference [A-1].

END

FILMED

DTIC
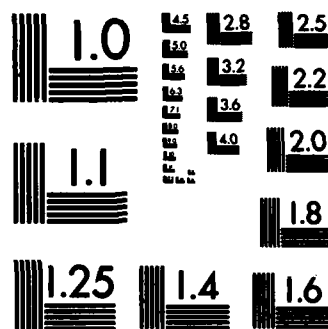
MICROCOPY RESOLUTION TEST CHART
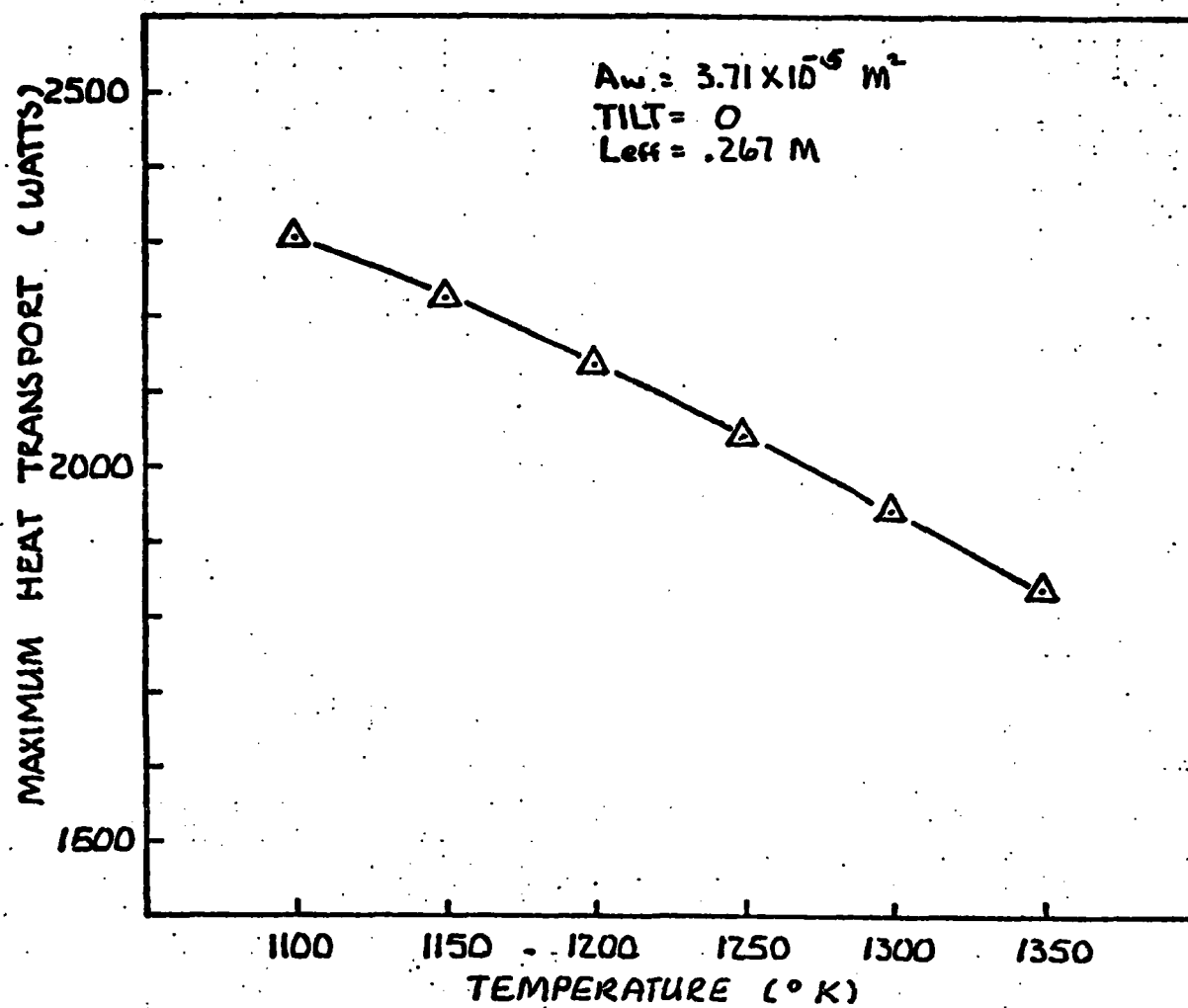NATIONAL BUREAU OF STANDARDS-1963-A

Fig. A-1   MAXIMUM HEAT TRANSPORT LIMIT VS TEMPERATURE

178

A-3 PREASSEMBLY CLEANING PROCEDURES

A-3.1 Envelope

The ''as received'' tubing material was cleaned per the following sequence:

1) OD and ID rinsed in reagent grade toluene solvent. During this rinse, the ID was scrubbed with nylon brushes.

2) OD and ID rinsed with clean reagent grade acetone. Several cleaning patches were run through the ID with the acetone until they came out clean.

3) Ultrasonic clean in clean reagent acetone for at least 5 minutes. Envelopes were suspended in a vertical position during the ultrasonic cleaning cycle.

4) Freon vapor degrease for a minimum of 5 minutes. Envelopes were suspended in a vertical position during vapor degreasing.

5) Air dry.

6) Each envelope was stored in a clean plastic tube with both ends capped. Cleaned parts were handled with gloves.

Following the above cleaning sequence, each envelope was fired in dry hydrogen at 1000°C for 10 minutes.

During this firing sequence, a furnace malfunction caused oxidation of the parts. A subsequent firing would not remove all oxides.

Short samples were taken and used to determine a cleaning procedure. Both chemical and mechanical methods were attempted. Successful cleaning was obtained by honing with 240 grit silicone carbide flex-hones. After honing, the initial cleaning sequences were repeated.

A-3.2 Wick

After cutting to size, each wick was cleaned in the following sequence:

1) Ultrasonic clean in reagent grade acetone for a minimum of 5 minutes.

2) Freon vapor degrease for a minimum of 5 minutes.

3) Cleaned wick material was stored in clean plastic containers. A layer of lint-free paper was placed between adjacent pieces of screen material. The wick material remained in the storage container when not in use. Gloves were used to handle the wick during all operations after cleaning.

179

A-3.3 Machined Parts

End caps and process pins were cleaned by acetone ultrasonic and freon vapor degreasing.

Cleaned parts were stored in plastic containers until needed for assembly.

Again, only gloves were used to handle clean parts.

A-4 WICK ASSEMBLY

Each wick was rolled on a .300 dia. mandrel (P/N DB703434). The rolling was performed while the mandrel was inserted in a .400 inside diameter die (P/N DB703433). See Figure A-2.

After rolling was completed, the heat pipe envelope was inserted into the .500 dia. X .75 deep counter-drill of the wick die. The wick was then driven into the envelope and the mandrel withdrawn. Wick ends were spot welded at each end of the envelope. Completed wick-envelope assemblies were returned to their storage containers.

A-5 INITIAL VACUUM FIRING

Each envelope-wick assembly was vacuum fired. Heating was by resistance heating of the envelope. Tantalum foil straps were used as both current input and supports for the envelopes. This assured that no cold zones were experienced at the ends of the envelope. Firing schedules for each assembly are contained in Table A-1.

Starting pressure for firing was between 2×10^{-7} and 4×10^{-7} torr. When the temperature of the envelopes reached approximately 980°C, the vacuum pressure would increase sharply. Maximum pressure listed in Table A-1 is the pressure at which the system peaked.

At temperatures above 1000°C, heavy deposits collected on the vacuum chamber surface. The amount of deposit did not appear to decrease during the final bake-out operation. The deposit was also observed at temperatures in the 800°C range, although they were not nearly as heavy.

Since the number of bake-outs did not appear to reduce the deposits, it is concluded that the deposits resulted from evaporation of one of the elements comprising the Inconel 617 material. The most likely candidate is aluminum. This phenomena may affect longevity of the heat pipes.

After firing, all envelopes were stored in glass tubes under high purity argon.
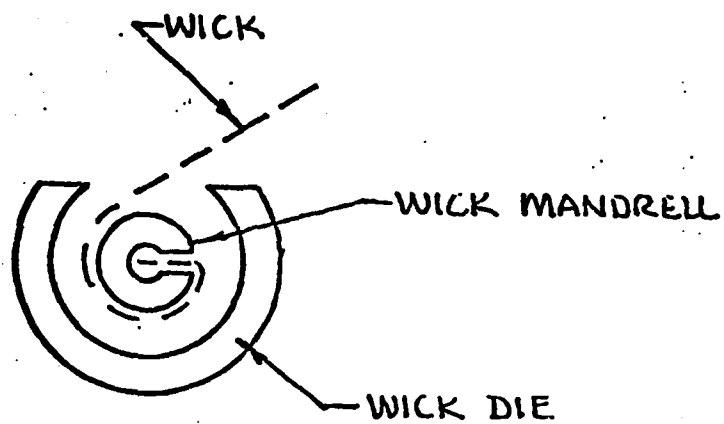
WICK MATERIAL DIM: 5.10 IN. WIDE X 18.0 IN.

Fig. A-2   WICK ASSEMBLY

Table A-1
INITIAL VACUUM FIRING SCHEDULES

S/N	Time (Min.) Above 1000°C	Max. Temp. (°C)	Max. Pressure (torr)
-001	13	1046	1.4×10^{-5}
-002	5	1001	1.5×10^{-5}
-003	5	1001	1.5×10^{-5}
-004	10	1110	1×10^{-4}
-005	25	1058	8.6×10^{-6}
-006	10	1091	7.4×10^{-5}
-007	27	1046	1.6×10^{-5}
-008	36	1035	1.1×10^{-5}
-009	24	1035	3×10^{-5}
-010	48	1028	9×10^{-6}
-011	10	1091	7.4×10^{-5}
-012	13	1080	1.4×10^{-5}
-013	56	1046	1.1×10^{-5}
-014	Not Used		
-015	56	1035	1.1×10^{-5}
-016	48	1023	9×10^{-6}
-017	23	1035	1.8×10^{-5}
-018	27	1046	1.6×10^{-5}
-019	23	1024	1.8×10^{-5}
-020	24	1046	3×10^{-5}

A-6   WELDING AND LEAK TESTING

Welding of end caps and envelopes was performed by Electron Beam Welding. Sample welds were made, cross-sectioned and micrographed to establish the proper welding schedule.

Figure A-3 shows a cross-section produced by the final weld schedule. Figure A-3 also shows the closure seal produced by the fusion weld technique.

After welding, each envelope was helium leak tested to 3×10^{-9} atm-cc/sec. Both the welder and leak detector were vented to high purity argon gas.

A-7   FINAL VACUUM FIRING

Immediately prior to loading with working fluid, each heat pipe envelope was vacuum fired. Table A-2 contains firing information for each envelope. During these firing sequences, the unknown deposits were again observed to collect on the chamber wall.

Envelope numbers -001 through -004 were loaded with titanium sponge. These envelopes were fired at higher temperatures (>1100°C) in order to break down titanium oxides. These firing operations produced deposits on the chamber wall which were almost opaque.

The titanium sponge was vacuum fired prior to loading in the envelopes. Table A-3 contains the firing schedule for the titanium sponge.
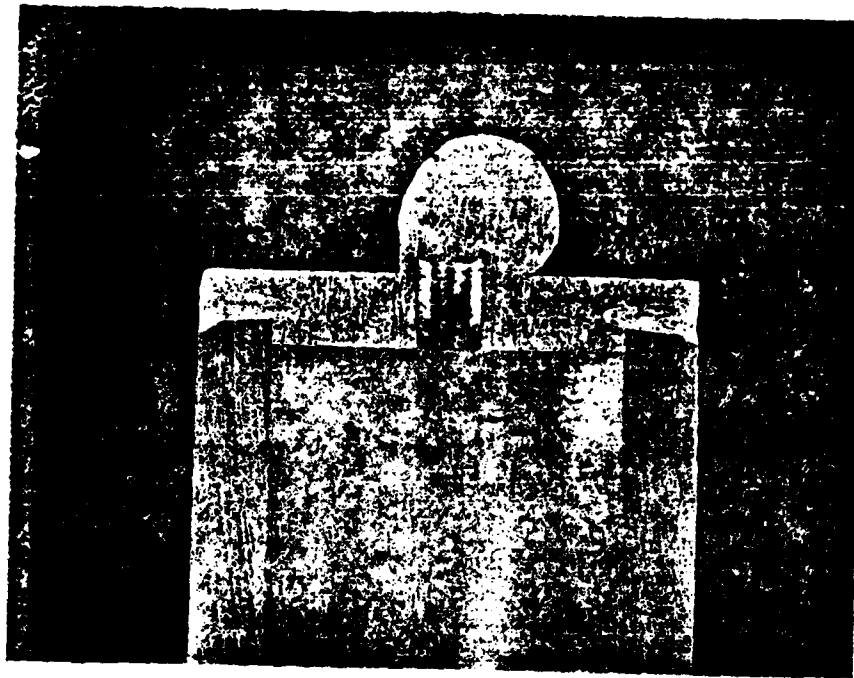
Weld Schedule:

Voltage	=	40 KV
Current	=	13.5 Ma.
RPM	=	36
Focus	=	Sharp
Time	=	2.7 sec.
Penetration =.		125%

Fig. A-3   MICROGRAPH OF EB WELD AND FUSION WELD

184

TABLE A-2

FINAL VACUUM FIRING FOR ENVELOPES

S/N	Time (Min.) Above 1000°C	Max. Temp. (°C)	Max. Pressure (torr)
-001*	43	1125	1.8×10^{-5}
-002*	25	1125	3.4×10^{-5}
-003*	43	1125	1.8×10^{-5}
-004*	25	1159	3.4×10^{-5}
-005	23	1058	1.3×10^{-5}
-006	15	1091	2×10^{-5}
-007	21	1012	1×10^{-5}
-008	8	1001	1.1×10^{-5}
-009	13	1001	1.5×10^{-5}
-010	36	1068	1.4×10^{-5}
-011	20	1001	1.5×10^{-5}
-012	8	1012	1.1×10^{-5}
-013	15	1103	2×10^{-5}
-014	Not Used		
-015	16	1069	2.6×10^{-5}
-016	21	1012	1×10^{-5}
-017	36	1091	1.4×10^{-5}
-018	20	1001	1.5×10^{-5}
-019	16	1069	2.6×10^{-5}
-020	13	1091	1.5×10^{-5}

* Contain Titanium Sponge

TABLE A-3
FIRING DATA FOR TITANIUM SPONGE

(Alfa Lot #120478)

Time	Temperature (°C)	Pressure (torr)
1222	1103	1.8×10^{-5}
1227	1137	8×10^{-6}
1233	1170	4.6×10^{-6}
1246	1170	3.4×10^{-6}
1248	1159	3.4×10^{-6}
1251	700	1.3×10^{-7}

After firing, both the envelopes and the sponge were soaked under argon for a minimum of one hour before opening the chamber. This assured complete cooling and saturation with the argon.

After opening the vacuum system, the envelopes were capped and transferred immediately to the glove box for loading.

A-8   LOADING AND PROCESSING

Loading of the heat pipes is performed inside an inert gas glove box. The inert gas (argon) is purified by passing it through a Precision Gas Products purifier model no. PGP-1.

All tools used in the glove box are vacuum baked-out to at least 250°F. During bake-out the tools are held in a deep stainless container which holds the argon when the vacuum chamber is opened. The bake-out container is then closed and transferred to the glove box.

Loading of the heat pipes is accomplished by drawing the melted sodium directly from its ampoule into a glass syringe. The sodium is then injected into the heat pipe. After loading, a long capillary tube is inserted into the heat pipe and a continuous flow of purified argon covers the working fluid until it has cooled and been placed in the process chamber.

After the process chamber has been evacuated, the bottom half of the heat pipe is resistance heated until the entire heat pipe is isothermal. Once this is achieved, the process pin is fusion welded into the fill-port of the process end cap.

The fluid charge for the Inconel 617 heat pipes was estimated to be 7.35 grams. Overfill is desired to aid start of the heat pipes. Table A-4 is a summary of processing data.

TABLE A-4
SUMMARY OF PROCESSING DATA

S/N	Processing Temp. (°C)	Pressure (torr)	Charge (gm)	Sodium Lot No.
-001*(.82)	880		8.10	072678
-002*(1.11)	967	1.6×10^{-6}	7.60	072678
-003*(.46)			7.77	
-004*(.33)	979	2.2×10^{-6}	7.93	072678
-005	–	–	–	–
-006	956	2.6×10^{-6}	7.98	072678
-007	801	1.4×10^{-6}	7.45	072678
-008	746	2×10^{-6}	7.57	122177
-009	856	1.6×10^{-6}	7.80	122177
-010	900	3×10^{-6}	7.39	
-011	776	1.6×10^{-6}	8.82	122177
-012	746	4.5×10^{-6}	7.48	072678
-013	845	2.9×10^{-6}	7.67	072678
-014	–	–	–	–
-015	757	2.5×10^{-6}	7.55	072678 and 120177
-016	768	3×10^{-6}	7.80	072678
-017	1000	2×10^{-6}	8.00	072678
-018	834	5×10^{-6}	9.24	122177
-019	768	2×10^{-6}	7.64	072678
-020	845	2.8×10^{-6}	7.35	122177

* Contains Titanium Sponge, gm

During sealing of the process ports, molten material was ejected from the sealing area. This characteristic has not been observed with fusion welding of other materials; i.e., Hastelloy, Inconel 600, and 601, Haynes 188 or stainless steels. Great care had to be exercised during sealing to avoid destroying the seal. One heat pipe was lost because the material literally burst at the port-process pin interface. Again, it appears that material is rapidly evaporating from the Inconel 617 alloy.

Processing for the valved heat pipe (S/N -001) is shown in Figure A-4. For this unit, loading was accomplished by drawing the working fluid into the heat pipe by suction.

After loading, the heat pipe was attached to an outside port in the vacuum chamber. An argon gas plug was maintained in the process port in order to keep the port from plugging with working fluid.

The argon blanket was expelled from the pipe and replaced three times. The third time the heat pipe temperature was approximately 880°C up to the process port. This temperature represents the actual optical pyrometer reading with no correction. No correction value is available for oxidized Inconel 617.

When the processed pipe had cooled, the stainless steel tube connecting the valve to vacuum station was pinched off and welded. The volume above the valve contains argon in the event that the valve should develop a leak.

The fluid charge for S/N -001 is 8.1 grams. Working fluid for all heat pipes was purchased from Alfa division of Ventron Corporation. The sodium was packed under argon gas in glass ampoules. Purity of the sodium is t3N5. The Alfa lot numbers for the 50 gram ampoules are listed in Table A-4.

The processing temperatures listed in Table A-4 are the temperatures at which the heat pipes became isothermal. Once the pipe became isothermal, the temperature would rise sharply.

The amount of titanium sponge in heat pipes S/N -001 through -004 is indicated by the value in parentheses in Table A-4.

Figure A-5 shows S/N -006 as it appears after processing. Temperature is 830°C. The optical pyrometer could not detect any temperature difference between the heated zone and the end cap.
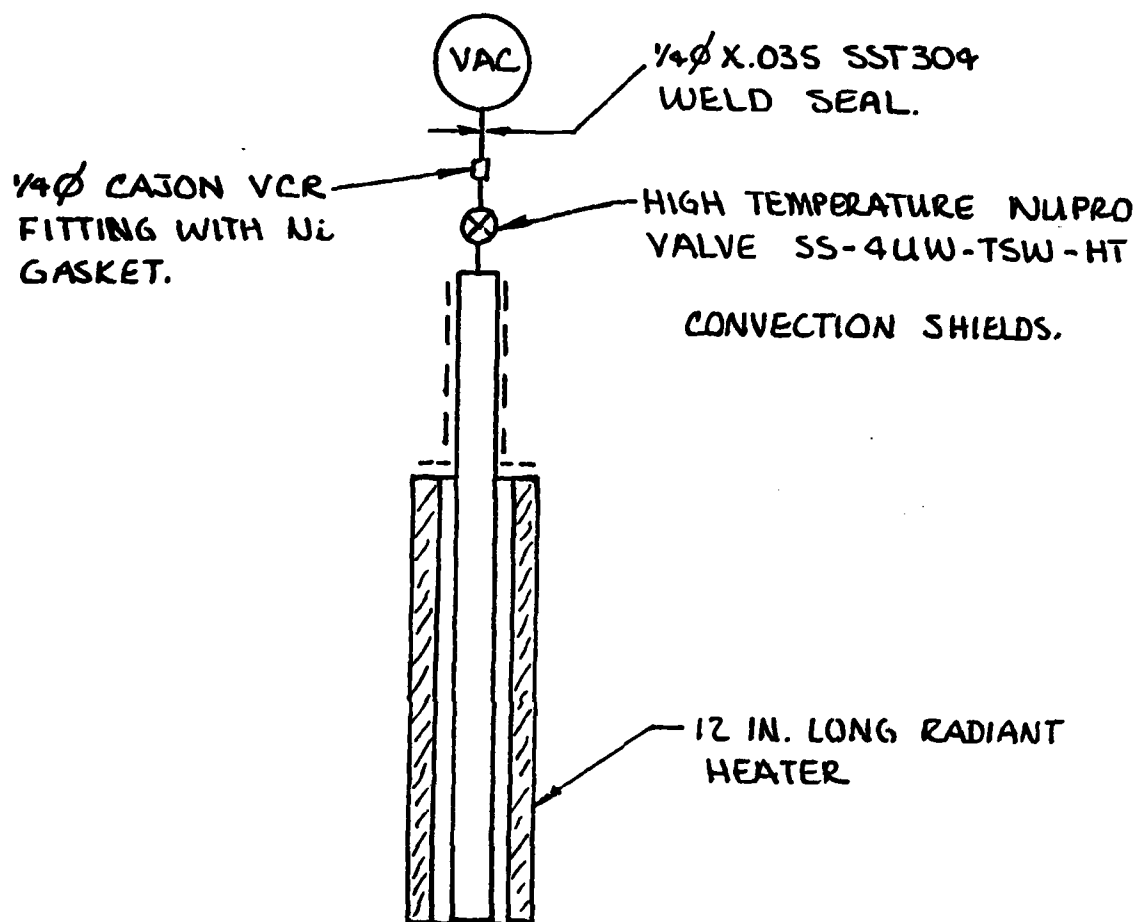
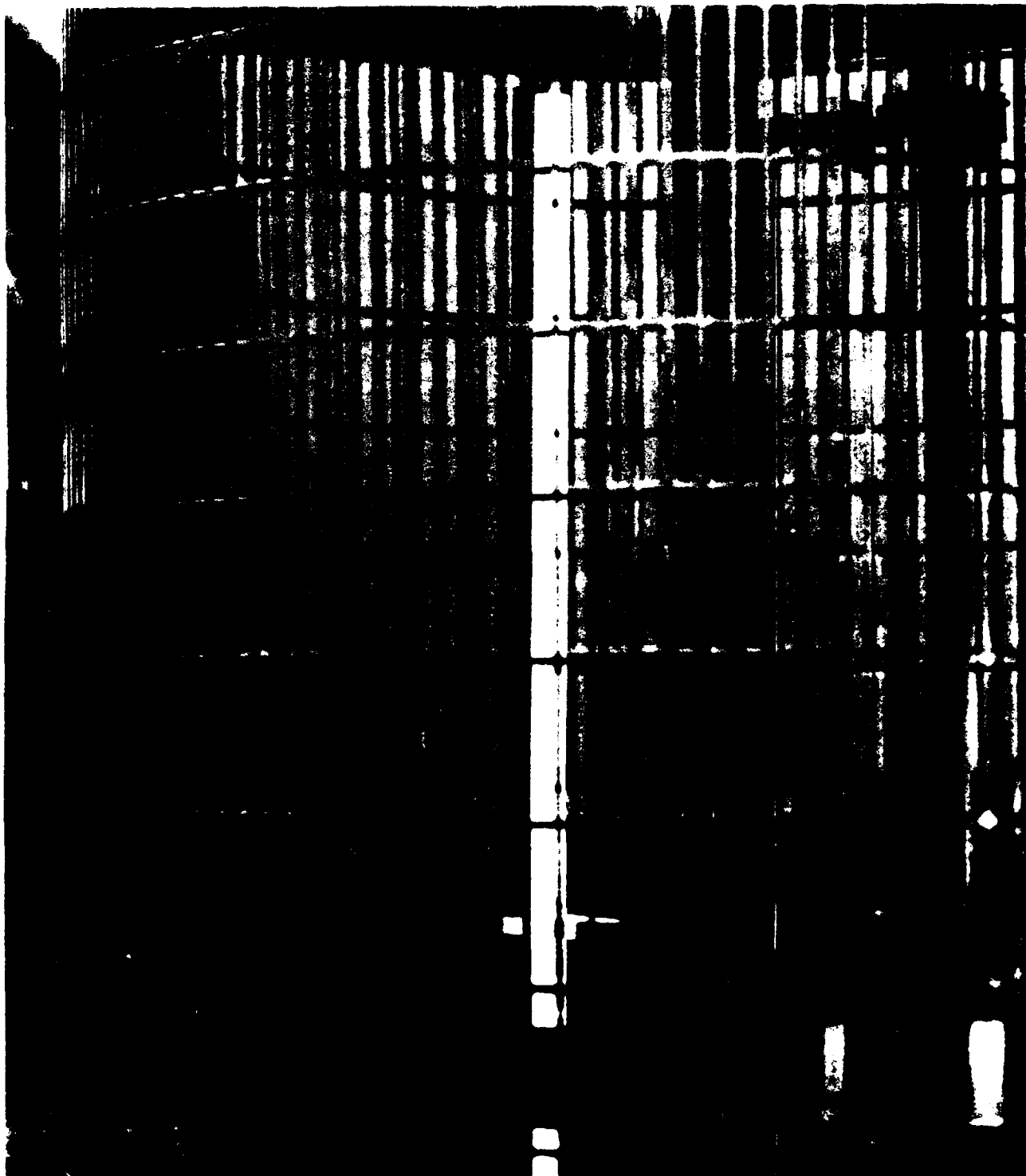Fig. A-4   PROCESSING SET-UP FOR S/N -001

Fig A-5   S/N -007 OPERATING AT 830°C FOLLOWING PROCESSING

191

A-9   TESTING

A-9.1   Test Apparatus

Each heat pipe was performance tested in a vacuum test chamber. The exterior of the test chamber is shown in Figure A-6. Figure A-7 shows details of the heater leads, supports, and radiation shields. The test layout is depicted schematically in Figure A-8.

A-9.2   Temperature Measurement

Initially, temperature measurements were made using four Type K thermo-couples. The locations were:

TC1:   0.25 inch from the evaporator end

TC2:   6.3   inches from the evaporator end

TC3:   9.0   inches from the condensor end

TC4:   0.25 inch from the condensor end

Tantalum straps were used to hold the thermocouples in place; however, the thermocouple readings tended to vary widely. The optical pyrometer was found to be more accurate for data collection. Thermocouples were still used to warn the operator of a dry-out condition in the evaporator.

A-9.3   Power Input and Output

Power input to the heat pipes was provided by a high current power supply (1000 amps, 10 volts). Water cooled high current leads penetrated through the end flange.

Attachment of the leads to heat pipes was done by two SST304 clamps. One clamp was rigidly supported by an OFHC bar clamped to the copper water cooled lead. The remaining clamp was attached to its lead via a flexible OFHC strap to prevent bending of the heat pipe by thermal expansion. Both high current leads were rigidly supported by ceramic standoffs mounted on 5/8 diameter SST304 tubes.

Power output was by radiation to the water cooled chamber wall. The cooling water temperature was maintained at 18°C.
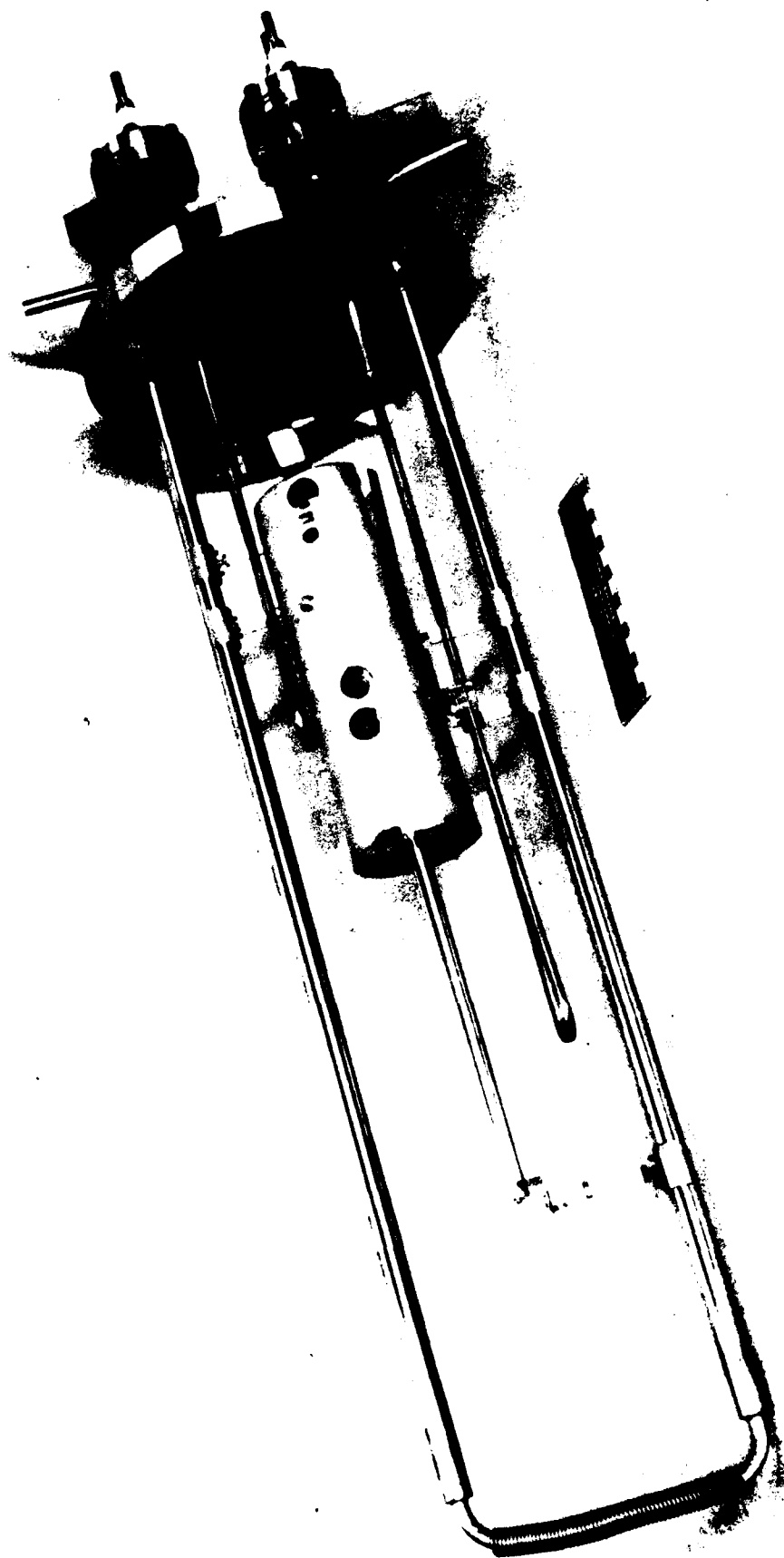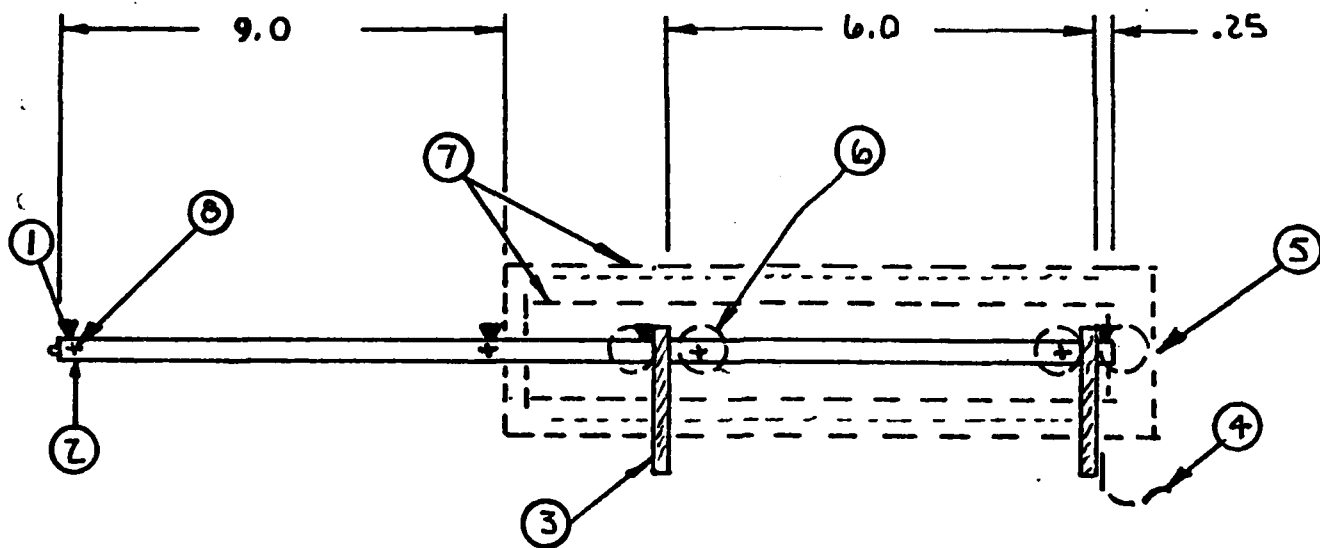
Fig. A-6 EXTERIOR DETAILS OF LIQUID METAL TEST CHAMBER

Fig. A-7 INTERIOR DETAILS OF LIQUID METAL HEAT PIPE TEST CHAMBER

194

1. INDICATES TYPE K THERMOCOUPLE LOCATIONS.
2. END SUPPORT
3. RIGID SST HIGH CURRENT CLAMP.
4. FLEXIBLE OFHC HIGH CURRENT STRAP.
5. VIEW HOLE THRU RADIATION SHIELD. FOR VIEW PORT IN FLANGE.
6. VIEW HOLE THRU RADIATION SHIELDS
7. SST RADIATION SHIELDS. 2" AND 3" DIA. WITH .005 THK SST FOIL BETWEEN.
8. + INDICATES OPTICAL PYROMETER TEMPERATURE MEASUREMENT POINTS.

FIGURE 8

Fig. A-8   TEST LAYOUT SCHEMATIC

A-9.4 **Test Method**

Power input to the heat pipes was increased slowly in increments of approximately 200 to 250 watts.

After stablization at each power level, the temperatures were measured at the points indicated by item 8 of Figure 8 and recorded on the data sheet.

When the heat pipes were mounted in the test chamber, they were observed to have a slight negative tilt (evaporator up). The tilt was estimated to be 0.15 inch.

A-10   REFERENCES

[A-1]   Feldman, K.T., Jr., ''The Heat Pipe: Theory, Design, and Applications,'' Notes presented at Short Course, University of New Mexico, Albuquerque, January 1974.

PalomarPrecisionTubesInc.

705 Greenfield Drive
El Cajon, California 92021
714) 444 2333

	Date
HUGHES AIRCRAFT COMPANY	JUNE 25, 1979
ELECTRON DYNAMICS DIVISION	
3100 WEST LOMITA BLVD.	
TORRANCE, CALIFORNIA 90509	

Certification of Customer Furnished Material

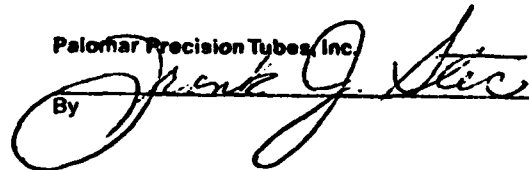| All material used on Purchase Order No.	Were furnished by
3-945411-U17	PALOMAR PRECISION TUBES INC.
Ref. Shipping Order No.	**All work was done in accordance with**
1311	PURCHASE ORDER
Quantity	**P/N** INCONEL 617 SEAMLESS TUBING
12 pcs. @ 40" lg. & 1 pc. @ 20" lg.	.500 O.D. x .050 WALL
Annealing Temperature	**Time at Temperature**
2150°F	5 MINUTES
Dew Point of Hydrogen	
-86 OR BETTER	

HUNTINGTON ALLOYS HEAT NO. XX05A3UK

Palomar Precision Tubes Inc.

By

Unique Wire Weaving Company
INCORPORATED

CERTIFICATION OF MATERIAL

RECEIVED
MATERIEL
APR 21 1980

April - 1980

Hughes Aircraft Co.
P. O. Box 2999
Bldg. 240, MS-115
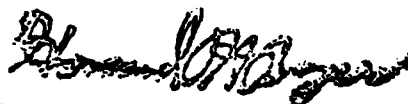Torrance, California 90509

Gentlemen:

This is to certify that to the best of our knowledge and belief the material shipped against your Purchase Order No. Q3-948615-U20 contains the following chemical analysis:

Inconel 617

C	.09	Mn	.02
S	.002	Si	.14
Cr	21.90	Ni(1)	54.82
Mo	8.94	Al	1.28
Fe	.44	Co	12.37

Very truly yours,
Unique Wire Weaving Company, Inc.

Howard H. Beyer
President

HHB:nhl

END